



National Library  
of Canada

Acquisitions and  
Bibliographic Services Branch

395 Wellington Street  
Ottawa, Ontario  
K1A 0N4

Bibliothèque nationale  
du Canada

Direction des acquisitions et  
des services bibliographiques

395, rue Wellington  
Ottawa (Ontario)  
K1A 0N4

*Your file* *Votre référence*

*Our file* *Notre référence*

## NOTICE

## AVIS

The quality of this microform is heavily dependent upon the quality of the original thesis submitted for microfilming. Every effort has been made to ensure the highest quality of reproduction possible.

La qualité de cette microforme dépend grandement de la qualité de la thèse soumise au microfilmage. Nous avons tout fait pour assurer une qualité supérieure de reproduction.

If pages are missing, contact the university which granted the degree.

S'il manque des pages, veuillez communiquer avec l'université qui a conféré le grade.

Some pages may have indistinct print especially if the original pages were typed with a poor typewriter ribbon or if the university sent us an inferior photocopy.

La qualité d'impression de certaines pages peut laisser à désirer, surtout si les pages originales ont été dactylographiées à l'aide d'un ruban usé ou si l'université nous a fait parvenir une photocopie de qualité inférieure.

Reproduction in full or in part of this microform is governed by the Canadian Copyright Act, R.S.C. 1970, c. C-30, and subsequent amendments.

La reproduction, même partielle, de cette microforme est soumise à la Loi canadienne sur le droit d'auteur, SRC 1970, c. C-30, et ses amendements subséquents.

**Optimum Performance of Solenoid Injectors  
for Direct Injection of Gaseous Fuels in IC Engines**

Henry Hong

A Thesis

in

The Department

of

Mechanical Engineering

Presented in Partial Fulfilment of the Requirements  
for the Degree of Doctor of Philosophy at  
Concordia University  
Montreal, Quebec, Canada

May 1995

© Henry Hong, 1995



National Library  
of Canada

Acquisitions and  
Bibliographic Services Branch

395 Wellington Street  
Ottawa, Ontario  
K1A 0N4

Bibliothèque nationale  
du Canada

Direction des acquisitions et  
des services bibliographiques

395, rue Wellington  
Ottawa (Ontario)  
K1A 0N4

*Your file* *Voire référence*

*Our file* *Notre référence*

THE AUTHOR HAS GRANTED AN IRREVOCABLE NON-EXCLUSIVE LICENCE ALLOWING THE NATIONAL LIBRARY OF CANADA TO REPRODUCE, LOAN, DISTRIBUTE OR SELL COPIES OF HIS/HER THESIS BY ANY MEANS AND IN ANY FORM OR FORMAT, MAKING THIS THESIS AVAILABLE TO INTERESTED PERSONS.

L'AUTEUR A ACCORDE UNE LICENCE IRREVOCABLE ET NON EXCLUSIVE PERMETTANT A LA BIBLIOTHEQUE NATIONALE DU CANADA DE REPRODUIRE, PRETER, DISTRIBUER OU VENDRE DES COPIES DE SA THESE DE QUELQUE MANIERE ET SOUS QUELQUE FORME QUE CE SOIT POUR METTRE DES EXEMPLAIRES DE CETTE THESE A LA DISPOSITION DES PERSONNE INTERESSEES.

THE AUTHOR RETAINS OWNERSHIP OF THE COPYRIGHT IN HIS/HER THESIS. NEITHER THE THESIS NOR SUBSTANTIAL EXTRACTS FROM IT MAY BE PRINTED OR OTHERWISE REPRODUCED WITHOUT HIS/HER PERMISSION.

L'AUTEUR CONSERVE LA PROPRIETE DU DROIT D'AUTEUR QUI PROTEGE SA THESE. NI LA THESE NI DES EXTRAITS SUBSTANTIELS DE CELLE-CI NE DOIVENT ETRE IMPRIMES OU AUTREMENT REPRODUITS SANS SON AUTORISATION.

ISBN 0-612-05075-0

Canada

Name HENRY HONG

Dissertation Abstracts International is arranged by broad, general subject categories. Please select the one subject which most nearly describes the content of your dissertation. Enter the corresponding four-digit code in the spaces provided.

MECHANICAL

SUBJECT TERM

0548

SUBJECT CODE

U·M·I

Subject Categories

**THE HUMANITIES AND SOCIAL SCIENCES**

**COMMUNICATIONS AND THE ARTS**

Architecture ..... 0729  
 Art History ..... 0377  
 Cinema ..... 0900  
 Dance ..... 0378  
 Fine Arts ..... 0357  
 Information Science ..... 0723  
 Journalism ..... 0391  
 Library Science ..... 0399  
 Mass Communications ..... 0708  
 Music ..... 0413  
 Speech Communication ..... 0459  
 Theater ..... 0465

**EDUCATION**

General ..... 0515  
 Administration ..... 0514  
 Adult and Continuing ..... 0516  
 Agricultural ..... 0517  
 Art ..... 0273  
 Bilingual and Multicultural ..... 0282  
 Business ..... 0688  
 Community College ..... 0275  
 Curriculum and Instruction ..... 0727  
 Early Childhood ..... 0518  
 Elementary ..... 0524  
 Finance ..... 0277  
 Guidance and Counseling ..... 0519  
 Health ..... 0680  
 Higher ..... 0745  
 History of ..... 0520  
 Home Economics ..... 0278  
 Industrial ..... 0521  
 Language and Literature ..... 0279  
 Mathematics ..... 0280  
 Music ..... 0522  
 Philosophy of ..... 0998  
 Physical ..... 0523

Psychology ..... 0525  
 Reading ..... 0535  
 Religious ..... 0527  
 Sciences ..... 0714  
 Secondary ..... 0533  
 Social Sciences ..... 0534  
 Sociology of ..... 0340  
 Special ..... 0529  
 Teacher Training ..... 0530  
 Technology ..... 0710  
 Tests and Measurements ..... 0288  
 Vocational ..... 0747

**LANGUAGE, LITERATURE AND LINGUISTICS**

Language  
 General ..... 0679  
 Ancient ..... 0289  
 Linguistics ..... 0290  
 Modern ..... 0291  
 Literature  
 General ..... 0401  
 Classical ..... 0294  
 Comparative ..... 0295  
 Medieval ..... 0297  
 Modern ..... 0298  
 African ..... 0316  
 American ..... 0591  
 Asian ..... 0305  
 Canadian (English) ..... 0352  
 Canadian (French) ..... 0355  
 English ..... 0593  
 Germanic ..... 0311  
 Latin American ..... 0312  
 Middle Eastern ..... 0315  
 Romance ..... 0313  
 Slavic and East European ..... 0314

**PHILOSOPHY, RELIGION AND THEOLOGY**

Philosophy ..... 0422  
 Religion  
 General ..... 0318  
 Biblical Studies ..... 0321  
 Clergy ..... 0319  
 History of ..... 0320  
 Philosophy of ..... 0322  
 Theology ..... 0469

**SOCIAL SCIENCES**

American Studies ..... 0323  
 Anthropology  
 Archaeology ..... 0324  
 Cultural ..... 0326  
 Physical ..... 0327  
 Business Administration  
 General ..... 0310  
 Accounting ..... 0272  
 Banking ..... 0770  
 Management ..... 0454  
 Marketing ..... 0338  
 Canadian Studies ..... 0385  
 Economics  
 General ..... 0501  
 Agricultural ..... 0503  
 Commerce-Business ..... 0505  
 Finance ..... 0508  
 History ..... 0509  
 Labor ..... 0510  
 Theory ..... 0511  
 Folklore ..... 0358  
 Geography ..... 0366  
 Gerontology ..... 0351  
 History  
 General ..... 0578

Ancient ..... 0579  
 Medieval ..... 0581  
 Modern ..... 0582  
 Black ..... 0328  
 African ..... 0331  
 Asia, Australia and Oceania ..... 0332  
 Canadian ..... 0334  
 European ..... 0335  
 Latin American ..... 0336  
 Middle Eastern ..... 0333  
 United States ..... 0337  
 History of Science ..... 0585  
 Law ..... 0398  
 Political Science  
 General ..... 0615  
 International Law and Relations ..... 0616  
 Public Administration ..... 0617  
 Recreation ..... 0814  
 Social Work ..... 0452  
 Sociology  
 General ..... 0626  
 Criminology and Penology ..... 0627  
 Demography ..... 0938  
 Ethnic and Racial Studies ..... 0631  
 Individual and Family Studies ..... 0628  
 Industrial and Labor Relations ..... 0629  
 Public and Social Welfare ..... 0630  
 Social Structure and Development ..... 0700  
 Theory and Methods ..... 0344  
 Transportation ..... 0709  
 Urban and Regional Planning ..... 0999  
 Women's Studies ..... 0453

**THE SCIENCES AND ENGINEERING**

**BIOLOGICAL SCIENCES**

Agriculture  
 General ..... 0473  
 Agronomy ..... 0285  
 Animal Culture and Nutrition ..... 0475  
 Animal Pathology ..... 0476  
 Food Science and Technology ..... 0359  
 Forestry and Wildlife ..... 0478  
 Plant Culture ..... 0479  
 Plant Pathology ..... 0480  
 Plant Physiology ..... 0817  
 Range Management ..... 0777  
 Wood Technology ..... 0746  
 Biology  
 General ..... 0306  
 Anatomy ..... 0287  
 Biostatistics ..... 0308  
 Botany ..... 0309  
 Cell ..... 0379  
 Ecology ..... 0329  
 Entomology ..... 0353  
 Genetics ..... 0369  
 Limnology ..... 0793  
 Microbiology ..... 0410  
 Molecular ..... 0307  
 Neuroscience ..... 0317  
 Oceanography ..... 0416  
 Physiology ..... 0433  
 Radiation ..... 0821  
 Veterinary Science ..... 0778  
 Zoology ..... 0472  
 Biophysics  
 General ..... 0786  
 Medical ..... 0760

Geodesy ..... 0370  
 Geology ..... 0372  
 Geophysics ..... 0373  
 Hydrology ..... 0388  
 Mineralogy ..... 0411  
 Paleobotany ..... 0345  
 Paleocology ..... 0426  
 Paleontology ..... 0418  
 Paleozoology ..... 0985  
 Palynology ..... 0427  
 Physical Geography ..... 0368  
 Physical Oceanography ..... 0415

**HEALTH AND ENVIRONMENTAL SCIENCES**

Environmental Sciences ..... 0768  
 Health Sciences  
 General ..... 0566  
 Audiology ..... 0300  
 Chemotherapy ..... 0992  
 Dentistry ..... 0567  
 Education ..... 0350  
 Hospital Management ..... 0769  
 Human Development ..... 0758  
 Immunology ..... 0532  
 Medicine and Surgery ..... 0564  
 Mental Health ..... 0347  
 Nursing ..... 0569  
 Nutrition ..... 0570  
 Obstetrics and Gynecology ..... 0380  
 Occupational Health and Therapy ..... 0354  
 Ophthalmology ..... 0381  
 Pathology ..... 0571  
 Pharmacology ..... 0419  
 Pharmacy ..... 0572  
 Physical Therapy ..... 0382  
 Public Health ..... 0573  
 Radiology ..... 0574  
 Recreation ..... 0575

Speech Pathology ..... 0460  
 Toxicology ..... 0383  
 Home Economics ..... 0386

**PHYSICAL SCIENCES**

Pure Sciences  
 Chemistry  
 General ..... 0485  
 Agricultural ..... 0749  
 Analytical ..... 0486  
 Biochemistry ..... 0487  
 Inorganic ..... 0488  
 Nuclear ..... 0738  
 Organic ..... 0490  
 Pharmaceutical ..... 0491  
 Physical ..... 0494  
 Polymer ..... 0495  
 Radiation ..... 0754  
 Mathematics ..... 0405  
 Physics  
 General ..... 0605  
 Acoustics ..... 0986  
 Astronomy and Astrophysics ..... 0606  
 Atmospheric Science ..... 0608  
 Atomic ..... 0748  
 Electronics and Electricity ..... 0607  
 Elementary Particles and High Energy ..... 0798  
 Fluid and Plasma ..... 0759  
 Molecular ..... 0609  
 Nuclear ..... 0610  
 Optics ..... 0752  
 Radiation ..... 0756  
 Solid State ..... 0611  
 Statistics ..... 0463  
 Applied Sciences  
 Applied Mechanics ..... 0346  
 Computer Science ..... 0984

Engineering  
 General ..... 0537  
 Aerospace ..... 0538  
 Agricultural ..... 0539  
 Automotive ..... 0540  
 Biomedical ..... 0541  
 Chemical ..... 0542  
 Civil ..... 0543  
 Electronics and Electrical ..... 0544  
 Heat and Thermodynamics ..... 0348  
 Hydraulic ..... 0545  
 Industrial ..... 0546  
 Marine ..... 0547  
 Materials Science ..... 0794  
 Mechanical ..... 0548  
 Metallurgy ..... 0743  
 Mining ..... 0551  
 Nuclear ..... 0552  
 Packaging ..... 0549  
 Petroleum ..... 0765  
 Sanitary and Municipal ..... 0554  
 System Science ..... 0790  
 Geotechnology ..... 0428  
 Operations Research ..... 0796  
 Plastics Technology ..... 0795  
 Textile Technology ..... 0994

**PSYCHOLOGY**

General ..... 0621  
 Behavioral ..... 0384  
 Clinical ..... 0622  
 Developmental ..... 0620  
 Experimental ..... 0623  
 Industrial ..... 0624  
 Personality ..... 0625  
 Physiological ..... 0989  
 Psychobiology ..... 0349  
 Psychometrics ..... 0632  
 Social ..... 0451



**CONCORDIA UNIVERSITY**  
**SCHOOL OF GRADUATE STUDIES**

This is to certify that the thesis prepared

By: **HENRY HONG**

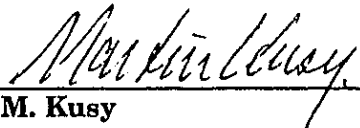
Entitled: *Optimum Performance of Solenoid Injectors for Direct Injection of Gaseous Fuels in IC Engines*

and submitted in partial fulfillment of the requirements for the degree of

**DOCTOR OF PHILOSOPHY (Mechanical Engineering)**

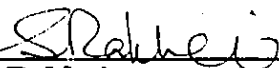
complies with the regulations of the University and meets the accepted standards with respect to originality and quality.


Signed by the final examining committee:


  
\_\_\_\_\_ Chair  
**Dr. M. Kusy**

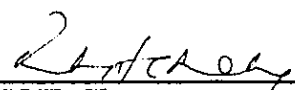
  
\_\_\_\_\_ External Examiner  
**Dr. B. Fijalkowski**

  
\_\_\_\_\_ External-to-Program  
**Dr. H. Jin**

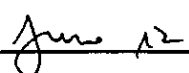
  
\_\_\_\_\_ Examiner  
**Dr. S. Rakheja**

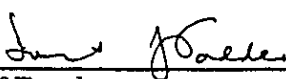
  
\_\_\_\_\_ Examiner  
**Dr. J. Svoboda**

  
\_\_\_\_\_ Thesis Co-Supervisor  
**Dr. T. Krepec**

  
\_\_\_\_\_ Thesis Co-Supervisor  
**Dr. R.M.H. Cheng**

Approved by   
\_\_\_\_\_ Chair of Department or Graduate Programme Director

 June 12 19 05

  
\_\_\_\_\_ Dean of Faculty

## ABSTRACT

### **Optimum Performance of Solenoid Injectors for Direct Injection of Gaseous Fuels in IC Engines**

Henry Hong, Ph.D.  
Concordia University, 1995

The growing environmental concerns have prompted the use of alternate fuels and a strong demand for electronically controlled gas injectors. This thesis investigates a solenoid operated fuel injector discharging gaseous fuel directly into the combustion chamber of an engine. A switching circuit is designed to boost the solenoid coil current for quick electromagnetic force generation to perform a fast injector opening. A capacitor incorporated in the switching circuit is used to oppose and to quickly diminish the coil current for fast injector closing. To accurately control the gas injection transient process, within fractions of a millisecond, a model of the solenoid magnetic circuit, including effects from eddy current and flux leakage losses in order to account for the hysteresis of the magnetization characteristics for force generation, is developed and matched with experimental results.

The performance studies showed that the stringent opening and closing timing requirements for the injector can be improved with proper selection of the design variables for the best performance. A systematic multivariable multiobjective constrained optimization procedure is developed to establish an optimal design. An optimized injection system could minimize the time delays and shape the profile of the injector needle motion in order to reduce the deviation between the expected and actual amount of the injected gas dose. A modified version of the Hooke and Jeeves unconstrained

optimization method is used. Boundary constraints are placed on the design variables to ensure that the design is confined within realizable physical limits. To account for these constraints, a procedure is introduced that tracks three successive objective functions as the optimization iteration progresses, and when a boundary is violated. The penalty function method accounts for all other constraints.

There are no known optimization methods that will result in a global minimum. Even if a global minimum is known to exist, then to determine the global minimum is to perform an exhaustive minimization search. The optimization method presented in this thesis results in a global minimization without the need to perform an exhaustive search on the design variables. This is because there is some "a priori" knowledge from the performance study about variable interactions, and about the trend of system performance for changes in the design variables.

The research shows that a solenoid operated injector with small size and weight, can operate fast enough and accurately in direct injection applications, after its design is optimized with the use of a comprehensive solenoid model for fast transient operations.

## DEDICATION

To Dr. Tadeusz Krepec, who always gives me support with persistent encouragement.



## ACKNOWLEDGEMENT

The author would like to express his gratitude and deep appreciation to his supervisors, Dr. T. Krepec and Dr. R.M.H. Cheng, for their suggestion of this research project and for guidance and inspiration throughout the author's graduate studies.

This work was supported by the Natural Science and Research Council, the Ministry of Energy Mines and Resources, Canada, and by Bendix Avelex Inc.

## TABLE OF CONTENTS

	PAGE
ABSTRACT .....	iii
DEDICATION .....	v
ACKNOWLEDGEMENTS .....	vi
LIST OF FIGURES .....	x
LIST OF TABLES .....	xiv
NOMENCLATURE .....	xv
CHAPTER 1 INTRODUCTION	
1.1 General .....	1
1.2 Review of Previous Work .....	4
1.2.1 Solenoid Operated Gasoline Injectors .....	5
1.2.2 Solenoid Operated Diesel Injection Systems .....	9
1.2.3 Solenoid Operated Gaseous Fuel Injectors .....	11
1.3 Thesis Objectives and Thesis Outline .....	15
CHAPTER 2 GAS INJECTOR AND METERING SYSTEM DESIGN	
2.1 Introduction .....	19
2.2 Pressure Unbalanced Gas Injector Design - First Generation .....	19
2.3 Pressure Balanced Gas Injector Design .....	22
2.4 Special Design of the Nozzle Seat .....	26
2.5 Incorporation of a Metering Valve Before the Injector .....	30
2.6 Design Optimization of Gas Injectors .....	32
2.7 Comments on Other Design Features of Solenoid Injectors .....	32
CHAPTER 3 MATHEMATICAL MODEL OF INJECTOR	
3.1 Introduction .....	35
3.2 Injector Dynamic Model .....	35
3.3 Gas flow Equations .....	36
3.4 Injected Gas Dose and Timing .....	39

CHAPTER	4	SOLENOID TRANSIENT FORCE AND CURRENT CHARACTERISTICS AND SWITCHING CIRCUIT DESIGN	
	4.1	Introduction . . . . .	42
	4.2	Experimental Set-up to Measure Solenoid Transient Characteristics . . . . .	44
	4.3	Discussion of Experimental Results . . . . .	47
	4.4	Derivation of Solenoid Coil Nonlinear Inductance, Velocity Induced Voltage, and Solenoid Electromagnetic Force . . . . .	79
	4.5	Mathematical Model of Solenoid Transient Characteristics . . . . .	85
	4.6	Parameter Estimation and Simulation Results . . . . .	87
	4.7	Switching Circuit Description . . . . .	104
	4.8	Mathematical Model of Switching Circuit . . . . .	106
	4.9	Summary . . . . .	107
CHAPTER	5	SIMULATION OF GASEOUS FUEL INJECTION PROCESS FOR VERIFICATION OF THEORETICAL CONCEPTS	
	5.1	Introduction . . . . .	112
	5.2	Mechanical and Electrical System Dynamic Performance . .	112
	5.3	Gas Flow Characteristics . . . . .	117
	5.4	Performance Index Study of System Variables . . . . .	120
	5.5	Summary . . . . .	125
CHAPTER	6	OPTIMIZATION OF SOLENOID OPERATED GASEOUS FUEL INJECTOR	
	6.1	Introduction . . . . .	127
	6.2	Selection of a Suitable Optimization Method . . . . .	128
	6.3	Introduction to the Optimization Method with the New Procedure to Account for Boundary Constraints . . . . .	134
	6.4	Formulation of the Multivariable Multiobjective Optimization Problem . . . . .	139
	6.5	Modifications to the Hooke and Jeeves Optimization Method to Account for Constraints . . . . .	140
	6.6	Introduction of a New Procedure to Account for Boundary Constraints to the One-Dimensional Optimization Problem to Determine Optimum Step Length . . . . .	145
	6.7	Global Optimality . . . . .	155

6.8	Optimization Results	157
6.9	Injector Transient Performance Comparison for Optimum and Typical Design Variables	167
6.10	Weight Assignment for Qualitative Comparison of System Performance	176
6.11	Summary	180
CHAPTER 7	CONCLUSION AND RECOMMENDATIONS	
7.1	Conclusions	184
7.2	Recommendations for Future Work	189
REFERENCES		191
APPENDIX A	CONICAL VALVE SEAT AND MINIMUM GEOMETRIC FLOW AREA	199
APPENDIX B	DESCRIPTION AND CALIBRATION OF PIEZO-CELL FORCE TRANSDUCER	202
APPENDIX C	DESCRIPTION OF CLAMP-ON CURRENT METER	204
APPENDIX D	DESCRIPTION OF SUBROUTINE MAXMIN	205

## LIST OF FIGURES

FIGURE	PAGE
1.1 Two methods of gaseous fuel supply: a) manifold gas injection b) direct gas injection . . . . .	2
2.1 Solenoid injector - first generation (left) Conventional diesel injector (right) . . . . .	20
2.2 Solenoid injector - second generation . . . . .	24
2.3 Comparison between the design features of first and second generation of solenoid operated gas injectors . . . . .	25
2.4 Conventional nozzle seat (left) and seat with reversed differential angle (right) . . . . .	27
2.5 Critical flow area characteristic for nozzle (a) for conventional nozzle seat (b) for reverse differential angle seat . . .	29
2.6 The utility shape of the nozzle orifice . . . . .	29
2.7 Solenoid injector interfaced by a metering valve operated by a stepper motor . . . . .	31
4.1 Schematic of the fixture to measure the solenoid force . . . . .	45
4.2 Switching circuit used in experimental set-up for solenoid current and force measurements . . . . .	46
4.3a Rise of current in solenoid coil, air-gap 0.635 mm . . . . .	49
4.3b Decay of current in solenoid coil, air-gap 0.635 mm . . . . .	50
4.4a Rise of solenoid force, air-gap 0.635 mm . . . . .	51
4.4b Decay of solenoid force, air-gap 0.635 mm . . . . .	52
4.5a Rise of current in solenoid coil, air-gap 0.535 mm . . . . .	53
4.5b Decay of current in solenoid coil, air-gap 0.535 mm . . . . .	54

4.6a	Rise of solenoid force, air-gap 0.535 mm . . . . .	55
4.6b	Decay of solenoid force, air-gap 0.535 mm . . . . .	56
4.7a	Rise of current in solenoid coil, air-gap 0.425 mm . . . . .	57
4.7b	Decay of current in solenoid coil, air-gap 0.425 mm . . . . .	58
4.8a	Rise of solenoid force, air-gap 0.425 mm . . . . .	59
4.8b	Decay of solenoid force, air-gap 0.425 mm . . . . .	60
4.9a	Rise of current in solenoid coil, air-gap 0.353 mm . . . . .	61
4.9b	Decay of current in solenoid coil, air-gap 0.353 mm . . . . .	62
4.10a	Rise of solenoid force, air-gap 0.353 mm . . . . .	63
4.10b	Decay of solenoid force, air-gap 0.353 mm . . . . .	64
4.11a	Rise of current in solenoid coil, air-gap 0.242 mm . . . . .	65
4.11b	Decay of current in solenoid coil, air-gap 0.242 mm . . . . .	66
4.12a	Rise of solenoid force, air-gap 0.242 mm . . . . .	67
4.12b	Decay of solenoid force, air-gap 0.242 mm . . . . .	68
4.13	Steady-state solenoid force as a function of coil current . . . . .	70
4.14	Transient force response at various air-gaps for 24 V input . . . . .	72
4.15	Solenoid force hysteresis loop for air-gap 0.635 mm . . . . .	74
4.16	Solenoid force hysteresis loop for air-gap 0.535 mm . . . . .	75
4.17	Solenoid force hysteresis loop for air-gap 0.425 mm . . . . .	76
4.18	Solenoid force hysteresis loop for air-gap 0.353 mm . . . . .	77
4.19	Solenoid force hysteresis loop for air-gap 0.242 mm . . . . .	78
4.20	Magnetic circuit for solenoid . . . . .	80

4.21	Equivalent circuit for solenoid . . . . .	86
4.22	Solenoid steady-state magnetization curve for air-gap 0.635 mm . . . . .	88
4.23	Solenoid steady-state magnetization curve for air-gap 0.535 mm . . . . .	89
4.24	Solenoid steady-state magnetization curve for air-gap 0.425 mm . . . . .	90
4.25	Solenoid steady-state magnetization curve for air-gap 0.353 mm . . . . .	91
4.26	Solenoid steady-state magnetization curve for air-gap 0.242 mm . . . . .	92
4.27	Material parameters $a_1$ and $a_2$ corresponding to Equation (4.2) . . . . .	93
4.28	Summary of solenoid steady-state magnetization curves and inductances for different air-gaps . . . . .	96
4.29	Solenoid flux dynamic hysteresis loop for air-gap 0.635 mm . . . . .	98
4.30	Solenoid flux dynamic hysteresis loop for air-gap 0.535 mm . . . . .	99
4.31	Solenoid flux dynamic hysteresis loop for air-gap 0.425 mm . . . . .	100
4.32	Solenoid flux dynamic hysteresis loop for air-gap 0.353 mm . . . . .	101
4.33	Solenoid flux dynamic hysteresis loop for air-gap 0.242 mm . . . . .	102
4.34	Switching circuit to control solenoid force generation . . . . .	105
5.1	Injection needle travel ( $h_{max}-h$ ) and solenoid force ( $F_s$ ) variations during simulated gas injection process . . . . .	113
5.2	Voltage applied to solenoid ( $V_s$ ), capacitor voltage ( $V_c$ ), voltage across the solenoid ( $V_{sol}$ ), and the exciting ( $i_e$ ) and magnetizing ( $i_m$ ) currents through the coil during simulated gas injection process . . . . .	115
5.3	Injector pressure and needle lift for two injection cycles . . . . .	118
5.4	Mass flow rate entering and mass flow rate exiting the injector chamber . . . . .	119
5.5	Sonic flow indication for metering valve orifice and injector orifice . . . . .	119
5.6	Performance Index vs. capacitance for different voltages . . . . .	122

5.7	Performance Index vs. spring rate for different spring preloads . . . . .	123
6.1a	Illustration of new procedure to account for boundary constraints, during Hooke and Jeeves exploratory moves . . . . .	135
6.1b	Illustration of new procedure to account for boundary constraints, two possible cases shown . . . . .	136
6.2	Normalized objective function w.r.t. iteration sequence . . . . .	161
6.3	Four time objectives ( $t_d$ , $t_r$ , $t_c$ , $t_f$ ) w.r.t. iteration sequence . . . . .	162
6.4	Change in voltage w.r.t. iteration sequence . . . . .	163
6.5	Change in spring preload w.r.t. iteration sequence . . . . .	164
6.6	Change in spring constant w.r.t. iteration sequence . . . . .	165
6.7	Change in capacitance w.r.t. iteration sequence . . . . .	166
6.8	Injector needle lift and solenoid force dynamic responses for optimized and typical systems . . . . .	168
6.9	Voltage transient characteristics for optimized and typical systems; for solid-state relay output, capacitor and across solenoid coil . . . . .	169
6.10	Exciting current $i_e$ and magnetizing current $i_m$ transient responses for optimized and typical systems . . . . .	170
6.11	Normalized objective function values for variations in weight assignment . . . . .	179
A.1	Valve seat with a conical angle greater than the needle angle . . . . .	200
B.1	Piezo-cell force transducer calibration curve . . . . .	203
D.1	Functional flow chart for subroutine MAXMIN . . . . .	206



## LIST OF TABLES

TABLE	PAGE
4.1 Air-gap positions and their corresponding current and force figures . . . .	48
6.1 Optimization results showing the 3 intermediate iteration sets and corresponding design vector values, the four time objectives, and the multiobjective function values . . . . .	159
6.2 Optimized and non-optimized systems. Comparison showing the design vector values, the four time objectives with time zero as reference, the injection time, and the peak boost current at corresponding time. . . .	172
6.3 Gas dosage comparison assuming: ideal square injection time corresponding to the pulse width, actual engine requirement, optimized and non-optimized system . . . . .	173
6.4 Optimization results from the application of different weights ( $w_1, w_2, w_3, w_4$ ) corresponding respectively to the four important individual time objectives ( $t_d, t_r, t_c, t_p$ ). For each set of weights, the corresponding design vector values, the four time objectives, and the multiobjective function values are indicated. . . . .	177

## NOMENCLATURE

- $a_1, a_2$  - experimentally determined constants for material reluctance (A/Wb, Wb)
- $a_{cof}$  - correction coefficient for continuity of material reluctance constants
- $b$  - constant in equivalent eddy current loss resistor ( $\Omega$ )
- $d$  - nozzle orifice / needle seat diameter (m)
- $c_1, c_2$  - constants in Froelich's equation (Wb/A-m, A/m)
- $g$  - acceleration due to gravity (9.806 m/s<sup>2</sup>)
- $g_j$  - constraints, of index  $j = 1, 2, \dots, n$
- $h$  - solenoid air-gap / injector needle displacement (mm)
- $h_{max}$  - maximum air-gap / maximum needle displacement (0.635 mm)
- $i$  - current (A)
- $i_e$  - exciting current (A)
- $i_m$  - magnetizing current (A)
- $i_{nom}$  - nominal solenoid current (7 A)
- $k$  - exploratory search index
- $m$  - mass of gas inside injector (kg)
- $m_a$  - mass of air in combustion cylinder (kg)
- $m_c$  - mass of solenoid core (kg)
- $m_n$  - mass of injector needle (kg)
- $m_{fg}$  - injected fuel dose for CH<sub>4</sub> (mg)
- $m_{fh}$  - injected fuel dose for hydrogen (mg)

- $m_s$  - mass of spring (kg)
- $m_i$  - injector total moving mass (0.02 kg)
- $\dot{m}_{12}$  - mass flow rate through orifice (kg/s)
- $\dot{m}_{cr}$  - critical mass flow rate through orifice (kg/s)
- $\dot{m}_{fg}$  - gas dose discharge rate for CH<sub>4</sub> (kg/s)
- $\dot{m}_{fh}$  - gas dose discharge rate for hydrogen (kg/s)
- $\dot{m}_{in}$  - mass flow rate supplied to injector (kg/s)
- $\dot{m}_{out}$  - mass flow rate exiting from injector (kg/s)
- $n$  - number of design variables
- $r$  - penalty parameter
- $r_1$  - radius of base, for frustum of a right cone (mm)
- $r_2$  - radius of top, for frustum of a right cone (mm)
- $t$  - time (ms)
- $t_c$  - delay time in injector closing (ms)
- $t_d$  - delay time in injector opening (ms)
- $t_f$  - time duration for injector fall (ms)
- $t_i$  - injection time (ms)
- $t_r$  - time duration for injector lift (ms)
- $\bar{u}_i$  - unit coordinate direction for design variable of index  $i$
- $w_1, w_2$   
 $w_3, w_4$  - subjective weights assigned to the four time objectives
- $x_i$  - design variable of index  $i$

$x_{i,max}$	- maximum of boundary constraint for design variable $i$
$x_{i,min}$	- minimum of boundary constraint for design variable $i$
$y$	- boss end fixed air-gap (0.5 mm)
$z$	- altitude, for frustum of a right cone (mm)
$A_1$	- effective area normal to magnetic flux path at pole end ( $4.9265 \times 10^{-5} \text{ m}^2$ )
$A_2$	- effective area normal to magnetic flux path at boss end ( $10.733 \times 10^{-5} \text{ m}^2$ )
$A_{12}$	- orifice area between chamber volumes ( $\text{m}^2$ )
$A_g$	- required nozzle flow area for $\text{CH}_4$ ( $\text{m}^2$ )
$A_h$	- required nozzle flow area for hydrogen ( $\text{m}^2$ )
$A_m$	- orifice minimum geometric flow area ( $\text{m}^2$ )
$B$	- magnetic flux density ( $\text{Wb}/\text{m}^2$ )
$C$	- capacitance ( $\mu\text{F}$ )
$C_v$	- orifice flow coefficient
$D$	- coefficient of viscous damping ( $\text{Ns}/\text{m}$ )
$F$	- spring preload force (N)
$F_g$	- gas momentum force acting on injector needle (N)
$F_s$	- solenoid force of attraction (N)
$H$	- magnetic field intensity ( $\text{A}/\text{m}$ )
$H_p(\bar{X})$	- penalty function to account for current constraint and injector opening conditions, $p = 1 \text{ to } 4$
$H_v(\phi, h)$	- nonlinear velocity induced voltage coefficient ( $\text{V}\cdot\text{s}/\text{m}$ )
$J^*$	- optimum value of objective function (ms)

- $J^+$  - objective function after design vector positive perturbation (ms)
- $J^-$  - objective function after design vector negative perturbation (ms)
- $J'_0, J'_1, J'_2$  - three consecutive objective functions (ms)
- $J'_{temp}$  - temporary storage of objective function value (ms)
- $J(\bar{X})$  - unconstrained multiobjective function (ms)
- $J'(\bar{X})$  - constrained multiobjective function (ms)
- $J_E(\bar{X}, r)$  - reformulated objective function to account for constraints (exterior)
- $J_I(\bar{X}, r)$  - reformulated objective function to account for constraints (interior)
- $K$  - spring constant (kN/m)
- $K_c$  - constant term in orifice subsonic mass flow rate equation
- $L$  - side length, for frustum of a right cone (mm)
- $L_l$  - inductance to account for flux leakage (mH)
- $L(\phi, h)$  - nonlinear coil inductance (mH)
- $N$  - number of coil turns (230)
- $N_{I2}$  - ratio of mass flow rate to critical mass flow rate
- $P$  - injector chamber absolute pressure (Pa)
- $P_1$  - upstream absolute pressure from orifice (Pa)
- $P_2$  - downstream absolute pressure from orifice (Pa)
- $P_i$  - intake absolute pressure of combustion cylinder (Pa)
- $P_r$  - pressure ratio, cylinder pressure to gas supply pressure
- $PI$  - performance index (ms)

- $R$  - gas constant, hydrogen = 4125.6; CH<sub>4</sub> = 518 (J/kg-K)  
 $R_a$  - air constant (0.287 J/kg-K)  
 $R_c$  - equivalent resistor to account for eddy current losses ( $\Omega$ )  
 $R_l$  - leakage resistor (3.5  $\Omega$ )  
 $R_i$  - internal coil resistance (1.7  $\Omega$ )  
 $\bar{S}$  - pattern search direction  
 $T_1$  - upstream absolute temperature from orifice (K)  
 $T_2$  - downstream absolute temperature from orifice (K)  
 $T_i$  - absolute temperature of combustion cylinder (K)  
 $V$  - general volume (m<sup>3</sup>) or source voltage (V)  
 $V_c$  - capacitor voltage (V)  
 $V_{ch}$  - volume of combustion cylinder (m<sup>3</sup>)  
 $V_{sol}$  - voltage across coil, including internal resistance (V)  
 $V_s$  - source voltage (V)  
 $V_z$  - zener diode voltage (V)  
 $V_A$  - solid-state relay output voltage (V)  
 $V_\phi$  - voltage across coil model, less internal resistance (V)  
 $W(\phi, h)_{mag}$  - stored magnetic energy (J)  
 $\bar{X}$  - design vector  
 $\bar{X}^*$  - optimum design vector  
 $\bar{X}_{1, mem}$  - temporary storage of design vector

- $\bar{X}_{k,0}$  - exploratory search starting or new base design vector
- $\bar{X}_{k,i-1}$  - current base design vector
- $\bar{X}_{k,n}$  - base design vector after  $n$  variable perturbations
- $\bar{X}_{temp}$  - temporary storage of design vector
- $\gamma$  - ratio of specific heats, hydrogen = 1.409; CH<sub>4</sub> = 1.299
- $\delta$  - established incremental value for scalar step length
- $\varepsilon$  - small number ( $\varepsilon \ll 1$ )
- $\theta$  - half the angle of the needle conical tip (°)
- $\lambda$  - scalar step length
- $\lambda^*$  - optimum scalar step length
- $\lambda_0, \lambda_1, \lambda_2$  - three consecutive step lengths
- $\mu_0$  - permeability of free space ( $4\pi \times 10^{-7}$  Wb/A-m)
- $\nu$  - specific volume (m<sup>3</sup>/kg)
- $\phi$  - magnetic flux (Wb)
- $\Delta x_i$  - prescribed step length for design variable  $i$
- $\Gamma$  - exterior penalty function
- $\Xi$  - interior penalty function
- $\mathfrak{R}_1$  - reluctance at pole plus boss end (A/Wb)
- $\mathfrak{R}_2$  - reluctance of core material (A/Wb)

# CHAPTER 1

## INTRODUCTION

### 1.1 General

Two areas of transportation technology deserve special attention in our fast developing world. These are the use of electronic controls and the prevention of air pollution. The research topic presented in this thesis is to benefit these two goals. It is related to the use of alternative gaseous fuels: natural gas and hydrogen, in order to reduce the air pollution caused by vehicular engines. It is also in the field of mechatronics, featuring the conventional mechanical systems now being enhanced by the fast development in microprocessor control technology.

The objective of the research is to develop an advanced engine injector, for direct injection of a gaseous fuel into the cylinder of an internal combustion engine. Existing systems for gaseous fuels deliver the gas to the intake manifold of the combustion engine, similar to the way as it is realized for gasoline supply with the use of a carburettor or with port injectors. However, this technology is not the most advantageous one because it reduces the amount of air delivered to the engine cylinders, and thus the power of the engine. It also limits the engine efficiency by not allowing the use of a high compression ratio because of the "knock" phenomenon. Therefore, injecting fuel directly into the cylinder of an internal combustion engine allows for increased compression ratio and for higher mean effective pressure, as compared with manifold fuel injection. Figure 1.1 is a schematic diagram illustrating the differences between the manifold gas injection



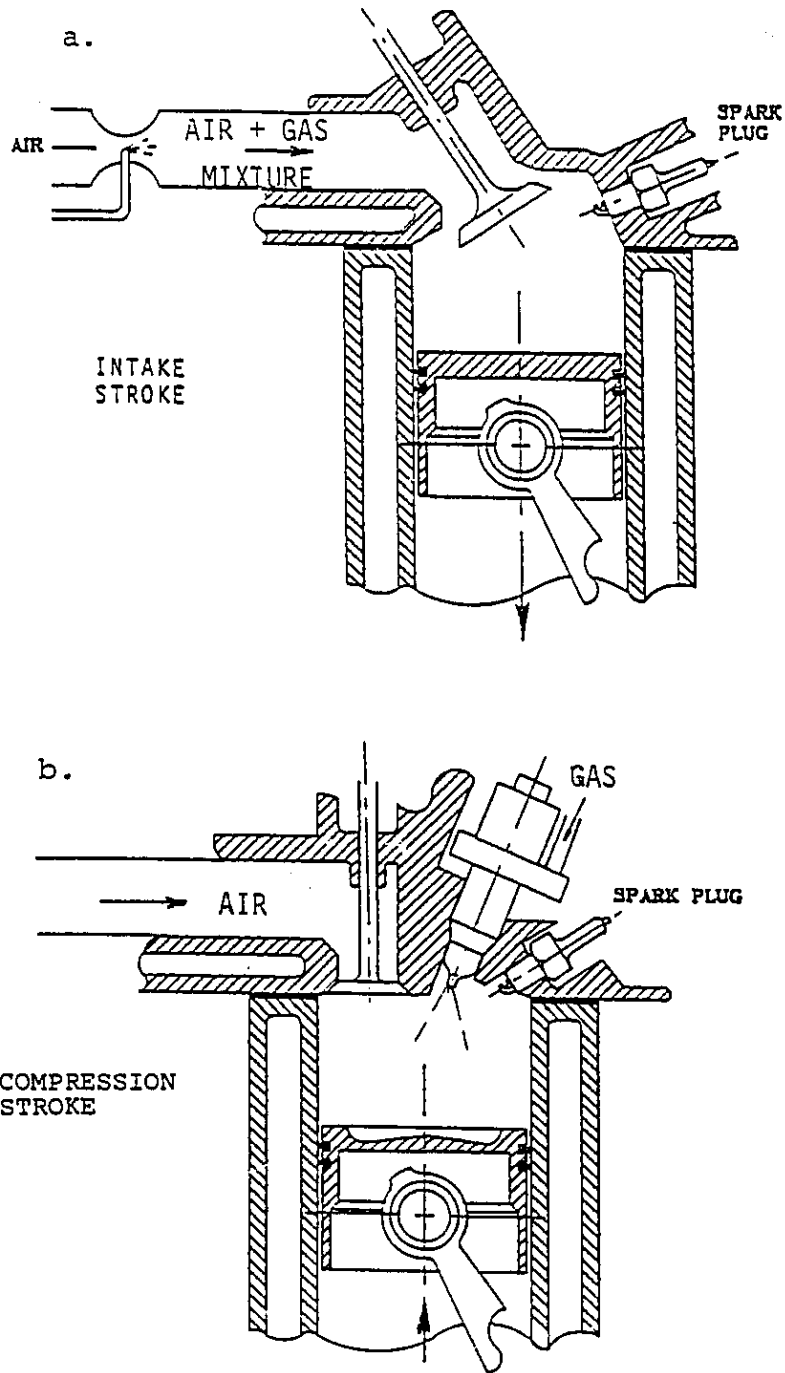


Fig. 1.1 Two methods of gaseous fuel supply  
 (a) - manifold gas injection  
 (b) - direct gas injection

system and the direct gas injection system for an internal combustion engine [1]. However, direct fuel injection creates several challenges which are described as follows:

1. The need to inject gaseous fuels instead of diesel oil or gasoline, which are liquid fuels used currently in internal combustion engines, requires to create a very different fuel delivery system. Because of the high compressibility of gaseous fuels, it is not possible to open the injector precisely at the selected injection point in time by using the gas pressure wave, as it is done in diesel fuel injection systems. Therefore, the development of a new fuel injection concept suitable for highly compressed gaseous fuels is required.
2. The electronically controlled solenoid operated injectors which are widely used for gasoline injection in spark ignition engines cannot be accepted for high pressure direct injection of gaseous fuels. This is because these injectors are unable to withstand the high temperatures and pressures of the engine's combustion chamber. The operating pressure of gasoline injection systems is about 100 times lower than that of the diesel system, and about 10 times lower than that required for direct gas injection systems. Therefore, the gasoline injectors could neither sustain such a high pressure nor assure the tight sealing of gas connections. Furthermore, the use of gaseous, instead of liquid fuel creates a challenge for the cooling and lubrication of such injectors, in which these conditions must also be met by the new injector design. Finally, while high speed of operation is not required for gasoline injectors because the spark

ignition engine has its fuel intake time several times longer than that required for direct fuel injection, the solenoids used in gasoline injectors are not strong enough to open fast an injector charged with high pressure.

3. Injection of gaseous fuel directly into the cylinder of an internal combustion engine is a very complex process that requires a good compromise amongst various design and performance factors. For such an injector, the design must be properly and systematically optimized. The development and application of an effective multivariable multiobjective computer optimization method is, therefore, an ultimate goal to meet these design and performance criteria.

It should be emphasized that the above discussions are primarily related to the dynamic transients of the solenoid operated injector and gas injection process. After the design of the injector is completed, the injector must next be tested on an actual engine and more development work would be required before it can be considered finalized as a commercially viable product.

## **1.2 Review of Previous Works**

The review of previous research studies presented in this section is mainly concerned with the solenoid operated fuel injectors for spark ignition engines and for compression ignition engines, as well as for stratified charge (hybrid) engines [2].

### 1.2.1 Solenoid Operated Gasoline Injectors

Solenoid operated gasoline injectors represent a technology that is already being used in mass production for reliable and durable automotive components. However, this technology cannot be fully utilized in the production of injectors for direct gas injection in internal combustion engines. The reasons are a result from the following differences in system requirement:

1. The direct gas injectors are installed in the cylinder of a piston engine with the injector nozzle protruding into the combustion chamber where the temperature, during the combustion process, exceeds 2000 °C. In contrary, the gasoline injectors are installed in the intake manifold where the temperature does not exceed 200 °C. Thus, the component parts of the direct gas injector must be fabricated to be resistant to the extreme high temperatures.
2. The direct injection of gas must occur within a very short time span of approximately 3 to 5 ms, and the time of injector opening and closing must be extremely short. In addition, the injected fuel dose must be strictly coordinated with the crankshaft position and must be highly repeatable. In gasoline injectors, the time of injection can be much longer, as it is not synchronized with the crankshaft position; as a result, the time of opening and closing of the injector is not critical, while it should be repeatable.

3) The working fluid of direct gas injectors are gaseous fuels which have lower viscosity and heat absorption capability when compared to the liquid fuels used in gasoline injectors. Therefore, the worst lubricating and cooling effects of gaseous fuels have to be taken into consideration.

Still, there is some expertise in gasoline injection technology that could be relevantly applied to high pressure direct injectors. The appropriate topics are reviewed in the following discussions.

The concept of using the solenoid operated gasoline injectors have been first proposed and patented by Bendix, USA in 1973 [3]. However, the first reliable injector design was introduced by Robert Bosch from Germany in 1975, based on the Bendix patents [4] and used in D-Jetronic, L-Jetronic and Motronic gasoline injection systems [5]. These systems were later adapted by Bendix [6], Lucas [7] and other producers with various modifications, all over the world. Custom made solenoids have been used, installed in a metal sheet shell, with its core attached to a pintle type needle which was opening and closing the discharge orifice in the nozzle body. Because of relatively low ambient temperature, soft "O" rings could be applied for sealing of the injector body in the engine intake manifold ports.

Modelling of the solenoid dynamic response for the purpose of design improvements and for development of new fuel injectors, was first attempted by D.H. Smith and D.A. Spinweber from Ford Motor Co in 1980 [4]. The model for liquid fuel injectors included flux density changes resulting from a magnetization curve equation,

to estimated reluctance changes caused by different fixed and variable air-gap lengths and component materials. A leakage reluctance was also included to account for flux leakages. The non-constant reluctance was used to calculate the solenoid coil inductance for their current model, and to determine the magnetic flux affecting the force generated by the solenoid. However, it was not described how the parameters were obtained to model the magnetization curve. Experimental results of the current rise and pintle dynamics for a pulse width of 3 ms were shown, while simulation results at a pulse width of 3.5 ms were reported. Although, the objective of the paper was to study the adequacy of solenoid injector dynamic control for short pulse widths, the results from experiments and simulation indicated a slow rise in the system current which would result in a slow generation of solenoid force. These important delays were not commented upon. Although the time delays in nozzle opening and closing and the rate of needle rise were stated numerically, no other comments were reported. This leads one to conclude that, as long as the nozzle opens and closes following the command pulse width signal and the injector supplies sufficient fuel dose, the delays inherent to the system are unimportant when port injection is considered.

Predicting of solenoid transient performance by computer simulation was next attempted in Delco Remy Division of GM by R.V. Esperti [9] in 1981 and J.P. Henry and D.S. Denis in 1987 [10]. The solenoid was modelled as a spring-mass-damper system with solenoid force as an external input. There was no attempt to predict the solenoid force because the authors stated that this was to be a user supplied input. An equation was given to model the transient current through the solenoid coil. But, the

model was over simplified by neglecting the changes in inductance due to changing air-gaps. Included in the model was a linear approximation of the velocity induced voltage. This term accounts for the electrical energy that is converted into mechanical energy as the air-gap is reduced, and when mechanical energy is converted to electrical energy as the air-gap is increased. The authors stated clearly that the model will be in error for solenoid response times that are less than about one millisecond.

Sensitivity analysis of the Bendix Electronics DEKA pulse-driven gasoline injector has been presented by G. Bata and M. Sosa from Bendix Electronics Division of Allied Automotive in 1987 [11]. The Taguchi Method of fractional factorial experimentation was used in the study. The method is a statistical analysis of the performance of the injector from changing dimension values from their low level to high level values, but only for a limited number of parameter combinations from the seven selected that were considered to influence the performance. Some of the fifty-five performance measurements were, made such as, the operating pulse width which gave information on its relationship to fuel flow linearity; the minimum amount of current needed to open the injector; the maximum current at which the injector starts to close; the inductance of the coil, which gave relation between lift and coil turns; the amount of time it took the injector to completely open, as well as to completely close; the endurance test, where the conclusion was made that the main factor affecting the life cycling is the spring force which should be as large as possible and the lift which should be as small as possible. The study obtained gave an estimation on system optimum performance and about the

parameter values which can then be applied to improve the existing injector design, as well as about simplifying the manufacturing process of certain injector parts.

All the solenoids that have been used in gasoline injectors are very similar in design. They operate with the maximum needle lift between 0.3 to 0.5 mm, and are immersed in gasoline that provides a cooling effect for the solenoids, thus preventing them from overheating.

There is a new trend in gasoline injection that is promoting direct fuel injection systems. This new advancement is presently in its early stage, where solenoid injectors are being developed mainly for the application in the new generation of 2-stroke spark ignition engines. This new development is described by T. Lake et al. as the research work made jointly between Ricardo Consulting Engineers, Ltd. and Isuzu Motors, Ltd. in 1993 [12]. However, the implementation of this new technology is aimed rather for the next century.

### **1.2.2 Solenoid Operated Diesel Injection Systems**

Solenoid operated diesel injectors are a very rare species due to the fact that the present use of hydraulically operated injectors is already representing a proven technology for high pressure injection of liquid fuels. Use of solenoid operated injectors, while simplifying the hardware, would create several problems in obtaining precise amount of the fuel dose and timing accuracy, in the avoidance of post-injection, as well as in fuel leakage at the very high injection pressures which in many cases can approach



and exceed 100 MPa. However, there are some attempts to use solenoids for the control of diesel fuel injection, particularly in the new electronically controlled fuel injection pumps.

Application of solenoid to diesel unit-injectors has been tried for the 2-stroke Detroit Diesel engines since 1985 by GM [13,14]. In the modified electronically controlled unit-injectors, the fuel delivery is still provided by a mechanically operated plunger. However, the injection timing and the injected fuel dose is controlled by a solenoid operated valve that spills back to the tank the excess of fuel delivered by the plunger. The design and application of the solenoid is very different, when compared with the gasoline injectors, where the solenoid has a more conventional cylindrical shape and controls directly the fuel discharge to the engine with the needle lift in the range of 0.3 to 0.5 mm. The solenoid in the GM unit-injector has a flat design that limits the stroke of the core to about 0.15 mm. To improve the closing of the solenoid operated valve, a laminated core is used to realize an instant decay of the solenoid force after shut-down of the current.

Similar unit-injectors have been recently introduced also by Lucas [15] and by Bosch [16]. The concept of spilling the fuel pumped by the plunger has been also used by Bosch in the electronically controlled unit-pumps [16].

In rotary-distributor fuel injection pumps, the solenoid operated spill-valves have been used for fuel metering and timing for several years by Nippondenso [17], Diesel Kiki [18], by Ford [19], by Toyota [20] and recently by Caterpillar [21] and Bosch [22].

In all these cases, the solenoid operated valves are incorporated in the fuel injection pumps and are spilling the excess of fuel delivered by the pump plunger back to the tank in a similar way as the DDEC unit-injector described above.

In the above applications, the solenoids actuating the spill valves have a rather flat custom made design, with the lifts in the range of 0.2 mm. They are operated while immersed in diesel fuel that is helping to absorb the heat released by the solenoid.

### **1.2.3 Solenoid Operated Gaseous Fuel Injectors**

The injection of gaseous fuels is a new technology recently developed for natural gas and hydrogen fuelled engines that are less pollutant and contribute to the protection of the environment. There are two very different types of such injectors: for manifold gas injection and for direct gas injection use. The injectors used in manifold gas injection do not differ much from gasoline injectors, except that in the former, the gas pressure is higher, in the range from 0.8 to 1.5 MPa and the nozzle discharge flow area is larger. While direct injectors are a new technology in its development stage, they are also very different from diesel fuel injectors. This difference is mainly related to the following two factors:

1. Gaseous fuel is much more compressible than the liquid fuel and cannot be discharged to the combustion chamber by the movement of a plunger. It has to be discharged from a common rail containing the gas under pressure, by

opening the solenoid operated injectors according to the firing sequence of the engine cylinders.

2. Gaseous fuel does not need to be atomized during injection and, therefore, it does not require such high injection pressures as the diesel fuel. Still, the pressure must be much higher than that for manifold injection, i.e. in the range of 10 MPa, to provide the proper gas distribution inside the combustion chamber and adequate mixing with the air.

Therefore, special solenoid operated injectors must be developed for direct injection of gaseous fuels that conform to the following requirements:

- high pressure gas injection,
- injector nozzle protruding into the combustion chamber,
- fast opening and closing of the nozzle with precise timing,
- size and shape conforming to the existing diesel injectors.

To operate such injectors, special solenoid driving circuits had to be developed.

A concept of direct injection of hydrogen in internal combustion engines using solenoid operated injectors was proposed by T. Krepec et al. in 1984 [23]. This was followed by the design and development work on a prototype injector, first for hydrogen in 1985-1987 [24,25,26] and next for natural gas in 1988 [27]. The injector was based on a Bosch size "S" conventional diesel injector, and was equipped with a Lendex Model 5-SF solenoid. The solenoid force did help the gas pressure force to open the injector at the right time and for the required amount of fuel dose injected. The injector was also

fitted with a metering valve allowing to vary the injected gas dose by throttling the gas flow to the injector. Thus, with the pulse width included to regulate solenoid operation, a double control of the gas dose was provided. A special driving circuit was used to cut-off the current at the end of the gas discharge and to rapidly close the injector.

In 1989, Green and Wallace [28] developed two different injectors for the injection of hydrogen and natural gas; both operated by solenoids. These injectors were very different in design and application, because they were aimed at different engines. The first one, was for direct injection of hydrogen in a 4-stroke diesel engine. It had a flat type solenoid immersed in the gas which operated the injector needle through a long pull-rod. The solenoid acted in one direction only and a spring was installed near the needle tip to ensure injector closing. The design was aimed at high flow rates of hydrogen, due to the large volumetric dose required to be injected during full power operation of the engine. The second injector was made for a 2-stroke Detroit Diesel engine with the operating pressure much lower because it was injecting gas when the engine piston was near the BDC position. It had a similar solenoid, but was much shorter due to the fact that it was not installed in the engine cylinder head. Both injectors were able to open for a time period not longer than 1 ms. To achieve this goal, a special capacitive discharge circuit of 100 V supplying a boost current of short duration was developed to drive the solenoid for the injector opening. The circuit also provided quick current cut-off when the injector had to be closed. This reduced the closing time period.

An improved concept of the 2-nd generation gas injectors was developed by T. Krepec et al. for Allied Signal Aerospace Inc. between 1990-92 [29]. In these injectors, the large and heavy solenoid of the 1-st generation was replaced by a small high performance Lisk L-5 solenoid. Also, the injector needle was pressure balanced to avoid gas leakage and needle seizure. A family of solenoids with different length and various nozzles was manufactured and tested with natural gas and hydrogen. The design of the solenoid injectors was next optimized in 1993 by H. Hong [30,31,32] and improved by H. Kekedjian in 1993 as 3-rd generation with the use of a Lisk L7 solenoid [33].

A different type of high pressure solenoid operated hydrogen injector has been presented by N. Glasson et al. in 1992 [34]. A soft material was used for the sealing of the nozzle seat and to eliminate hydrogen leakage; however, the soft seat proved not to remain durable. Also introduced was a very short stroke (0.15 mm) of the injector needle to reduce the time of the needle lift; however, due to severe needle bouncing, the nozzle critical flow area at full lift was varying and caused the gas discharge rate to be unsteady that resulted in variations in injected gas dose.

The overview of the previous work and the above discussions show clearly that the problems related to the direct injection of gaseous fuels are far from being solved. In addition, as stated by one of the researchers [12], "the development of direct injection technology is a logical step in the process to further improve the engine cold and transient operation". This statement was related to the gasoline engines and shows

clearly that the research work in the field of the direct gas injection for diesel engines is equally relevant to its application for the spark ignition engines, particularly to the 2-stroke engines.

### **1.3 Thesis Objectives and Thesis Outline**

The first objective of this thesis is to develop a comprehensive mathematical model for the solenoid to provide a computer simulation of the solenoid/injector systems dynamic response for design improvement purposes. The model describing the solenoid dynamic characteristics, with the introduction of a flux leakage inductance and an eddy current loss resistance terms, is innovative and has been validated by experimentation. With a better comprehension of the solenoid characteristics, it is the goal to apply the solenoid to applications and performances beyond its nominal intended use. This is the second objective of the thesis, where a novel design for a solenoid switching circuit is used to demonstrate that small off-the-shelf solenoids can function in an "over-powered" mode to give a rapid rise in force without causing solenoid damage, provided that electric power is brought back to nominal conditions rapidly. The third objective of the thesis is to have an injection system that operates at optimum performance. Since the dynamic performance of the injection process is complex and depends on many design parameters, a systematic and computerized method is required. The Hooke and Jeeves unconstrained optimization method is selected to evaluate for the optimum set of system variables. For the design to be physically realizable, boundary constraints are imposed on the design

variables. A new approach to account for boundary constraints are introduced to complement the Hooke and Jeeves method.

Based on the literature review and on the analysis of the available options, the research program leading to the development of the solenoid operated gas injectors for diesel engines can be described as follows:

1. The injector should be equipped with a strong but light-weight solenoid; it should represent a compromise between the strong opening force and the small inertia of the solenoid core; also, it would be advantageous to use commercially available solenoids to reduce the cost of the injector.
2. The solenoid driving circuit should be designed with the objective that it would accelerate the opening and make shorter the closing time of the injector.
3. A multivariable design optimization procedure should be developed to determine the optimum values of the design variables so as to minimize the opening and closing time of the injector, bringing this time close to that of a diesel engine, i.e. well below 1 ms.

It has to be mentioned that there is no attempt found in the literature to thoroughly optimize a solenoid operated injector. One of the possible reasons may be the lack of a valid solenoid model for the simulation of the fast transient responses. Some mathematical models found in the literature used to simulate the dynamic response of a solenoid [8,10,30,32,33] are either based on not very accurate primitive models or are

derived from the data obtained from specific experiments, without creating a more general mathematical model responding to a voltage step input.

Regarding the driving circuit for the solenoid, allowing for faster opening and closing of the injector, there are some concepts in the literature that are worthy of consideration [28,29,30,31,33]; however, they again require the development of a more valid solenoid model which would be included in the mathematical model of the injector.

The design of the injector under investigation is already known. The framework has been developed in a research contract for Allied Signal Aerospace Inc. [29]. The mathematical model for this injector is partly based on the expertise related to diesel injectors; however, several modifications had to be made which reflect the application of gaseous fuels.

The research program of this thesis will concentrate on the following items:

1. Development and experimental validation of the mathematical model for fast dynamic response of the solenoid.
2. Development of a fast acting driving circuit for the solenoid and a model for simulation of the fast transient driving processes.
3. Creation of a comprehensive mathematical model for the fast operating gas injectors.
4. Development of a computer program for simulation of fast dynamic response of the gas injector.



5. Development of a multivariable multiobjective optimization procedure for the gas injector, including all the important design parameters.
6. Optimization of the gas injector design.
7. Drawing conclusions and making recommendations for further injector modifications.

## CHAPTER 2

### GAS INJECTOR AND METERING SYSTEM DESIGN

#### 2.1 Introduction

The design of the gaseous injectors is a result of the research work done at Concordia University's Centre for Industrial Control at the Fuel Control Systems Laboratory, in the framework of an industrial contract for Allied Signal Aerospace Inc. [29]. The contributions from this author to the research work was in the designing and testing of driving circuits and its application to solenoids, as well as proposing design requirements to improve the injector performance. This research has led to the design and testing of the 2-nd configuration of solenoid operated injectors for gaseous fuels (natural gas and hydrogen), as described in this chapter.

#### 2.2 Pressure Unbalanced Gas Injector Design - First Generation

The basic concept of the 2-nd generation of solenoid operated gas injector design is derived from the 1-st generation of injectors developed and tested a few years earlier in the Fuel Control Systems Laboratory at Concordia University [35]. Figure 2.1 is a schematic comparing the differences between the 1-st generation of injectors and a conventional diesel injector.

As the figure illustrates, the gas injector design was based on the commercially available diesel injectors of size "S", according to the classifications given by Bosch. The injector corresponds to the DIN Standards, except the size of the upper portion

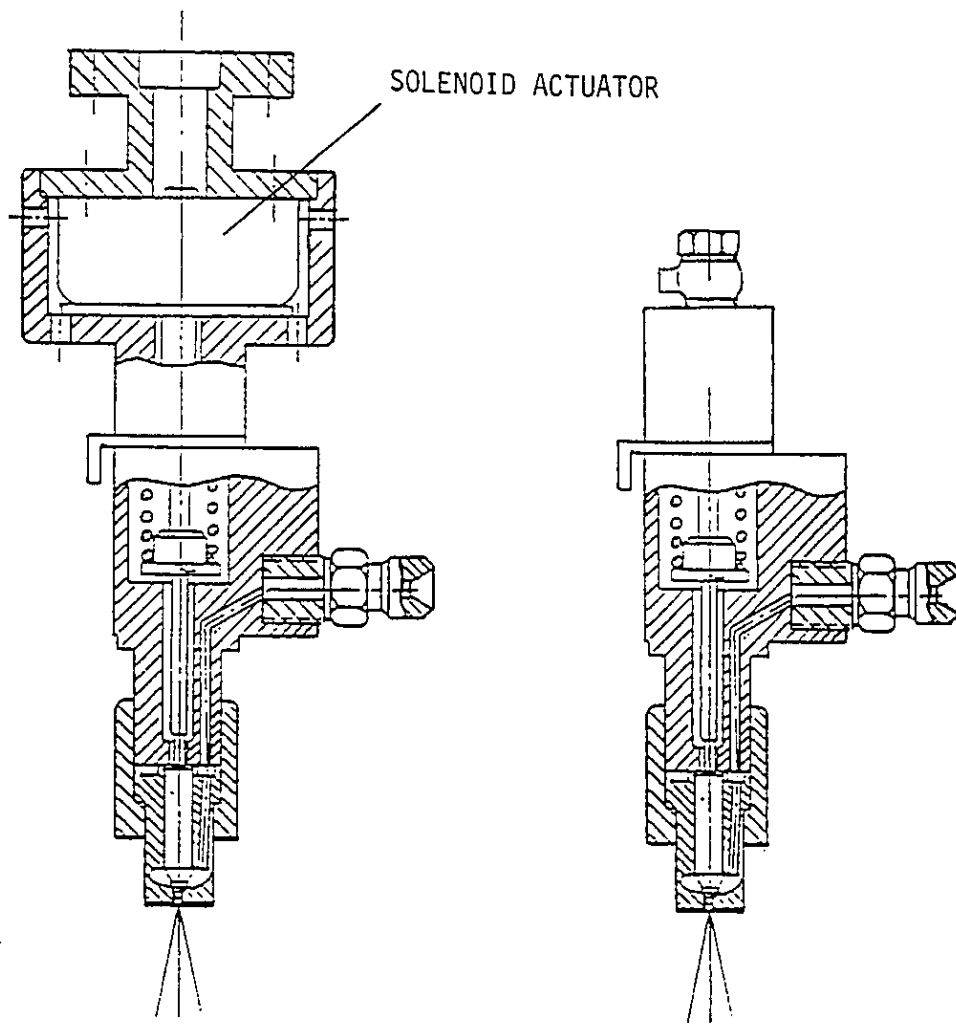


Fig. 2.1 Solenoid injector - first generation (left)  
Conventional diesel injector (right)

which became quite "bulky", due to the large solenoid used. Unfortunately, smaller solenoids were not available during that time period of research; while small solenoids already started to appear, their availability was very restricted [36]. Despite the large size and weight of the solenoid, the injectors could be installed on the diesel engine without modification of the cylinder head, and they have been tested on the Peugeot "Idenor" diesel engine for direct hydrogen injection [35].

The gas injectors of the 1-st generation were operated both by the solenoid force and by the gas pressure. This principle of operation was, to some extent, similar to the operation of the conventional diesel injectors. The gas pressure inside the injector housing acted on one side of the injector needle only, while the second side was under the atmospheric pressure. The solenoid force was used to initiate the injection process by starting the needle movement against the injector spring; this allowed the gas to enter the nozzle seat and thus provided the addition of pressure force to help the solenoid to lift the needle even faster. Certain advantages and disadvantages of such an injector design are as follows:

- The use of the unbalanced gas force to help the solenoid force in lifting the needle, resulted in very fast opening of the injector, and was comparable to the opening time of conventional diesel injectors.
- The pressure unbalanced injector needle lead to a substantial leak of gas from the pressure side of the needle to the atmospheric side. Such a situation, although acceptable with liquid diesel fuel, is not acceptable with gas, especially

with hydrogen fuel of much lower viscosity. This is due to the following two reasons:

- 1) the leaking gas could not be re-used for injection because the injected gas had to be under high pressure,
- 2) the close machining tolerance between the needle and injector housing had to be used to separate the high pressure side from the atmospheric side; low gas viscosity provides poor lubrication and leads to a seizure hazard of the needle.

The progress made in recent years in the development of high performance solenoids, which became commercially available, allowed to modify the gas injector design, in order to make its size and weight more compatible with conventional diesel injectors.

### **2.3 Pressure Balanced Gas Injector Design**

There are several main differences in the design of the 2-nd generation of gas injectors as compared with the 1-st generation.

The 2-nd generation of solenoid operated gas injectors has the gas pressure acting on both sides of the injector needle; however, at the bottom of the needle, where it touches the seat, the gas pressure is not acting on the needle surface which is limited by the outer seat diameter. Therefore, the needle is only partly pressure balanced and the degree of balancing depends on the ratio of the seat diameter to the needle diameter.

The design of the 2-nd generation injector is shown in Figure 2.2, and Figure 2.3 is a schematic diagram comparing the differences between the 1-st and 2-nd generation of gas injectors.

It is clearly seen from the schematic diagram that the gas pressure in the 2-nd generation of injectors is the same on both sides of the needle because of the common gas supply at these two volume locations and because of the grooves cut longitudinally along the needle axis. The only different pressure occurs underneath the needle seat surface. As a result from these design changes, the needle fit in the nozzle body does not require close tolerances which gives a more free movement of the needle. This is because the needle-body is no longer required to act as a seal, and the beneficial effect is that the seizure hazard is avoided. Still, the piloting of the needle is required in order to bring the conical tip of the needle axially and accurately into the conical seat in the nozzle body; in case of greater misalignment, the seat would leak and wear faster. This concentricity is provided by the lands on the peripheral diameter of the needle.

The solenoid used in the 2-nd generation of gas injectors is much smaller than that used in the 1-st generation. An off-the-shelf, high performance Lisk L5 solenoid with an armature made of rare earth material, is used. However, because the gas pressure is not fully balanced on the needle when the injector is closed, a substantial force has to be created by the solenoid to start open the injector. Because of the small size of the solenoid, the gas injectors of the 2-nd generation can have the same external size as the

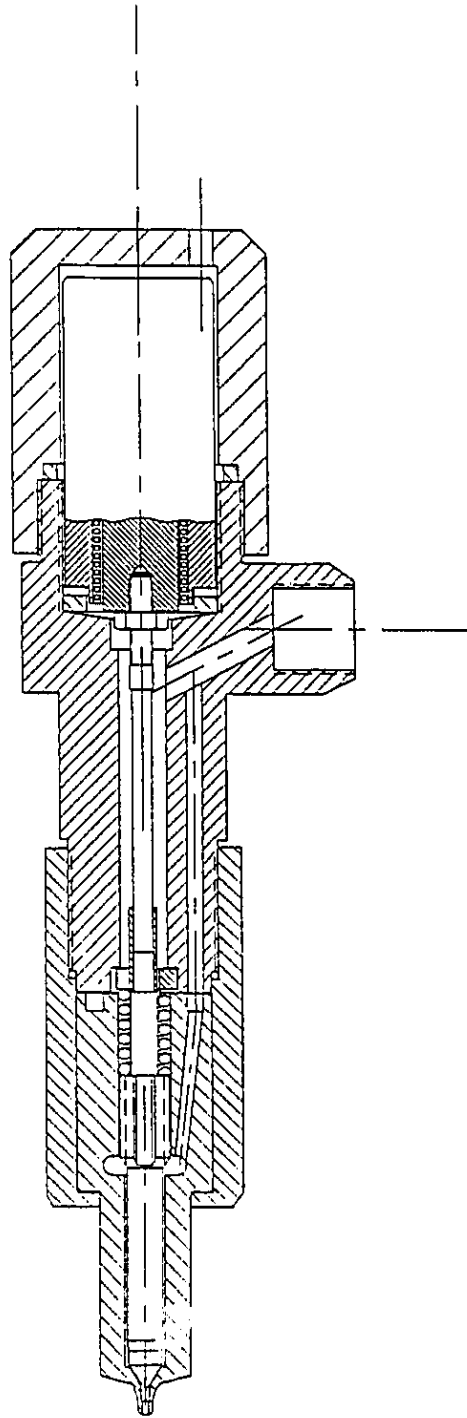


Fig. 2.2 Solenoid injector - second generation

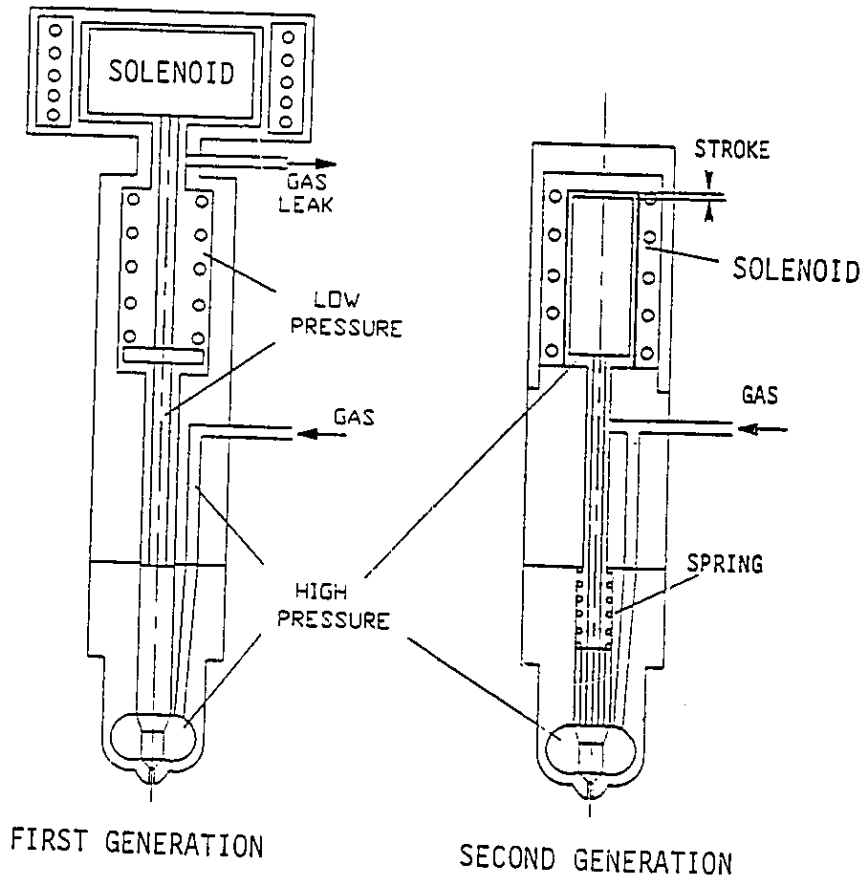


Fig. 2.3 Comparison between the design features of first and second generation of solenoid operated gas injectors



conventional diesel injectors of size "S", and can be directly installed into the existing diesel engines.

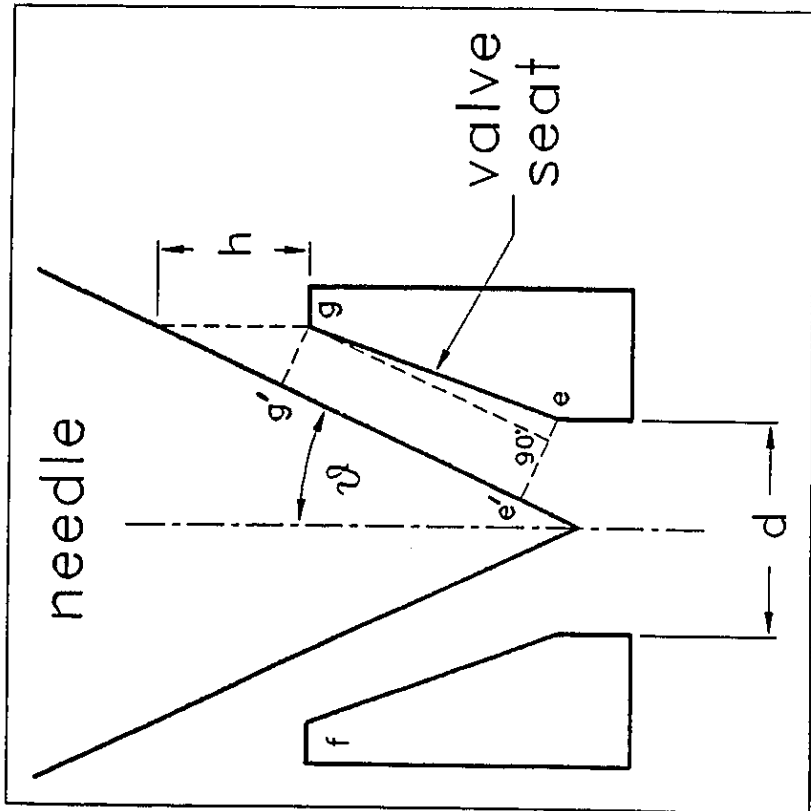
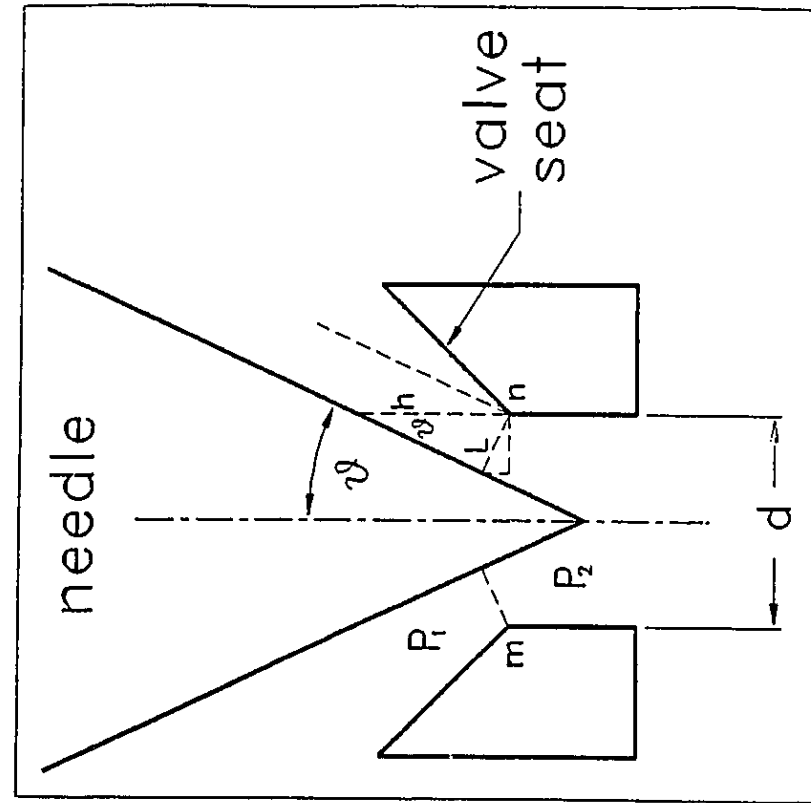
As experienced during the injector testing [29], the solenoid core remains attracted to the solenoid pole when the two comes into contact even when the applied voltage is removed. To avoid such a situation which results in a big delay for the core return movement, two remedies were used:

- 1) A gap was set at the end of the core stroke so that it would not come into contact with the solenoid pole
- 2) An insulation layer was placed at the core end to avoid contact with the solenoid pole (refer to Figure 2.3)

#### **2.4 Special Design of the Nozzle Seat**

As mentioned in the previous section, the nozzle seat occupies part of the needle conical tip and causes a partial unbalance of the pressure forces acting on the needle. The unbalanced force to open the injector, must be overcome by the solenoid force and is creating a limit for the maximum gas pressure supplying the injector. The existing situation is illustrated in Figure 2.4 and is explained as follows.

The conventional design of the diesel nozzle seat is shown in Figure 2.4a, with the seat cone angle smaller than the needle tip cone angle by approximately 40 minutes. Such a configuration yields the seat sealing circumferential line of contact at the outer seat diameter, given by the points f & g. When the injector is closed, the gas pressure



(a)

(b)

Fig. 2.4 Conventional nozzle seat (left) and seat with reversed differential angle (right)

is acting only on the needle surface that is outside the outer seat diameter, thus limiting the pressure force acting on the needle from the seat side.

At the beginning of the needle lift, the gas starts to flow into the seat through the gap between the needle and the seat. The critical flow area of the edge-like gap, determined from the distance  $gg'$ , increases with the needle lift, as shown in Figure 2.5a. At some lift value, the flow area switches from the outer seat diameter to the inner seat diameter, and the critical flow area becomes determined by line  $ee'$ . The flow area continues to grow with the needle lift.

It is obvious that when the critical flow area is at the inner seat diameter, there is a substantial increase in the seat pressure due to the throttling of the gas flow at the seat exit circumference. This, of course, contributes to the increase of the pressure force acting on the needle from the seat side and is beneficial to the needle acceleration. Finally, when the inner seat flow area reaches the size of the nozzle orifice area of diameter  $d$ , the critical flow area becomes constant, as shown in Figure 2.5a. The pressure force acting on the needle in the seat will depend only on the orifice size; however, at this needle position, the needle lift reaches its maximum and the pressure force in the seat is becoming irrelevant to the injector opening process.

As proposed [29], the seat design could be changed, by reversing the direction of the differential seat angle; the cone angle on the needle tip can be made smaller than the seat cone angle, as shown in Figure 2.4b. In this case, the seat sealing circumferential contact line would be at the inner seat diameter marked  $mn$  when the

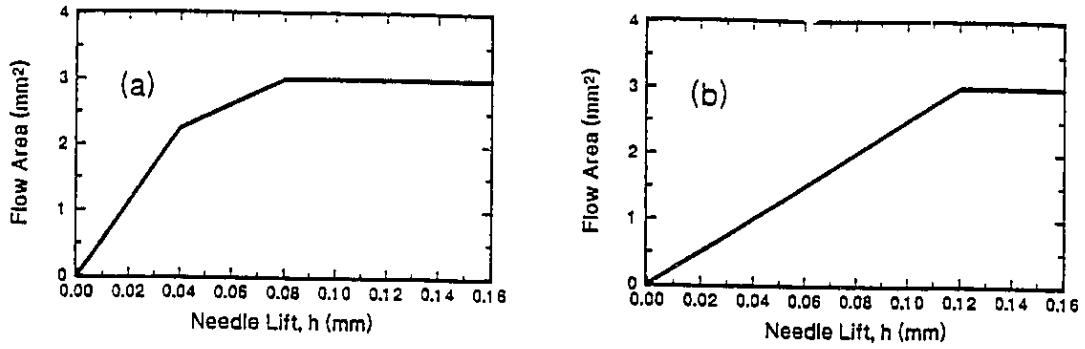


Fig. 2.5 Critical flow area characteristic for nozzle  
 (a) - for conventional nozzle seat  
 (b) - for reverse differential angle seat

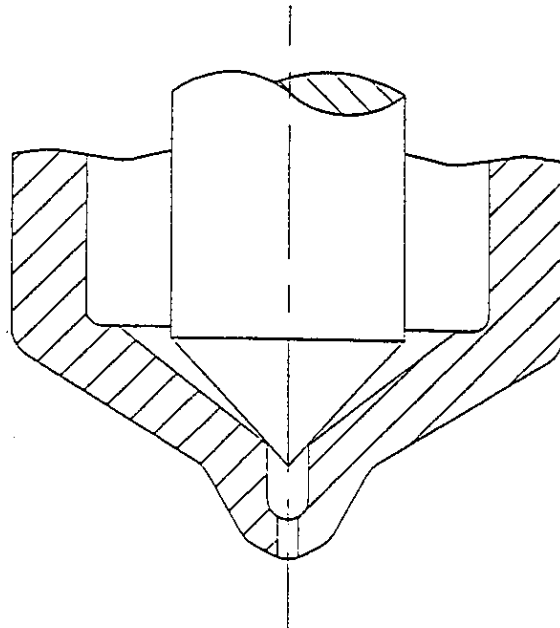


Fig. 2.6 The utility shape of the nozzle orifice

injector is closed. The increase in the critical flow area versus needle lift is shown in Figure 2.5b. The seat pressure would be equal to the gas supply pressure from the beginning of the injection process and the pressure force acting on the needle conical tip would be much greater when the injector is closed. Thus, this allows the operation of the same injector (equipped with the same solenoid) with a much higher gas supply pressure. Also, gas flow calculations for the injection process for the reversed differential angle nozzle would be much simpler, as compared with the conventional nozzle injector.

It has to be pointed out that, for practical applications, the nozzle must be designed as shown in Figure 2.6. The shape of the exit orifice allows to maintain a constant injector flow area that is not affected by the maximum needle lift (stroke) and by the dimensional tolerances of the seat which are much more difficult to maintain during manufacturing than the orifice diameter. It also eliminates the variation in gas discharge from the injector due to the needle bouncing on its seat, as well as from the discharge variations due to the seat wear. The effect of the end-orifice diameter size on the critical flow characteristics is shown, as a horizontal line, in Figure 2.5b.

## **2.5 Incorporation of a Metering Valve Before the Injector**

To increase the operational flexibility of the gas injector, the gas flow entering the injector could be throttled by a metering valve operated by a stepper motor, as illustrated in Figure 2.7. This concept was already investigated with the 1-st generation

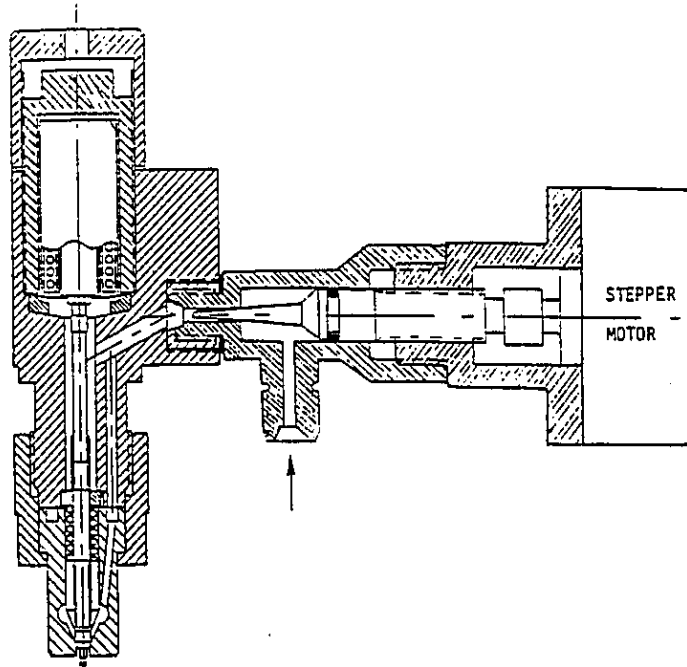


Fig. 2.7 Solenoid injector interfaced by a metering valve operated by a stepper motor

of the gas injectors, however, with the increase of the injector volume resulting from the pressure balancing of the needle, this concept needs to be re-examined.

## **2.6 Design Optimization of Gas Injectors**

There are so many factors affecting the performance of the solenoid operated gas injectors that a proper choice of the design parameters would require a multivariable optimization procedure. The ones presented in references [30,31,32] were made based on a simplified model of the solenoid, where its fast transient characteristic was not adequately simulated. A development of a more accurate solenoid transient model would allow to obtain better optimization results for this thesis; it would also fill-up the gap in the literature regarding the modelling of fast dynamic response of solenoids, thus contributing to the engineering know-how.

## **2.7 Comments on Other Design Features of Solenoid Injectors**

The design of the second generation of solenoid operated injectors developed for Allied Signal Aerospace Inc., was a subject of thorough investigation involving particular components of the injector and its driving circuit, as well as their behaviour at different operating conditions [29]. This involved:

- 1) The solenoid driving circuit, which was first designed in an H-configuration, used four solid-state relays. This design, although functionally satisfactory, was criticized by Allied Signal Aerospace Inc. as being overly expensive. To satisfy

the company, a driving circuit was proposed, by the author of this thesis, which consisted of only one solid-state relay switch. The circuit is presented in Chapter 4 of this thesis.

- 2) The control of the gas dose was realized by two methods: by changing the pulse width command signal and by controlling the opening of the metering valve orifice. The impact of the two control strategies for gas dose variations has been investigated by Miele [27]. The objective for the optimization of the injector design presented in Chapter 6 of this thesis considers only one pulse width and one metering valve opening. The optimization procedure is general and is applicable to any combinations of pulse command signal and valve setting.
- 3) The impact of the operating frequency, as well as the damping of the injector needle system and the related spring-back phenomena resulting in so the called "bouncing" of the needle, have been examined by Kekedjian [33], together with the dynamic forces acting on the needle seat which contributes to its wear.
- 4) The impact of temperature on the performance of the injector has been, to some extent, investigated during the research made for Allied Signal Aerospace Inc. [29]. In this thesis, however, the temperature factor has been neglected (i.e. the ambient laboratory isothermal conditions have been assumed). This assumption can be justified by the fact that the impact of temperature is primarily related to the injector operating on a particular engine and at particular working conditions, which can be very different and very difficult to generalize. Thus, for the



optimization of an injector dedicated to a particular engine at specific working conditions, the same optimization technique, as presented in this thesis, can still be used. However, the solenoid dynamic response data should be corrected for each particular temperature level.

- 5) The possible improvement of the solenoid cooling conditions has been proposed by Kekedjian in his third generation design [33] through directing the natural gas inflow to the injector from above the solenoid. In this way, the gas flow can surround and cool the solenoid walls.

## CHAPTER 3

### MATHEMATICAL MODEL OF INJECTOR

#### 3.1 Introduction

To optimize the injector design, a mathematical model for the injector discharging gaseous fuel should be developed and the basic data for the gas injection process should be derived.

#### 3.2 Injector Dynamic Model

The dynamic model of the injector needle is considered to be a mass-spring-damper system, with positive velocity pointing away from the solenoid pole. The injector motion equation, where  $h$  represents the needle vertical travel, is described by:

$$m_t \frac{d^2h}{dt^2} + D \frac{dh}{dt} + K \cdot h = F_s + F + F_g + m_t \cdot g \quad (3.1)$$

where  $m_t$  represents the total moving mass which consists of the solenoid core  $m_c$ , the injector needle  $m_n$  and the effective spring mass  $\frac{1}{3}m_s$ .  $D$  is the coefficient of viscous damping, and is experimentally derived from a similar injector operating on natural gas [33]:

$$D = 2.0 \times 10^{-6} \cdot P \quad (3.2)$$

where  $P$  is the pressure inside the injector chamber.  $K$  and  $F$  represent respectively the spring constant and spring preload force.  $F_s$  is the electromagnetic force of attraction created by the electrical solenoid.  $F_g$  is the gas pressure force acting on the injector

needle and resulting from the pressure drop across the injector nozzle orifice; it is approximated by:

$$F_g = A_m \cdot (P - P_e) \quad (3.3)$$

The pressure is assumed uniformly equal to  $P$  above the minimum geometric flow area  $A_m$  at the seat inner diameter and uniformly equal to the exit pressure  $P_e$  below this area, as explained in Section 2.3. The minimum geometric flow area  $A_m$  after the needle has lifted to height  $h$  is derived in Appendix A, and is expressed as:

$$A_m = \pi \cdot (h \cdot \sin\theta) (d - h \cdot \sin\theta \cdot \cos\theta) \quad (3.4)$$

where  $d$  is the seat diameter of the nozzle orifice and  $\theta$  is the half the angle of the needle conical tip.

### 3.3 Gas flow Equations

Gas flow through orifices is considered to undergo an isentropic process and can be subsonic or sonic [37,38]. Sonic flow corresponds to maximum mass flow rate and is established from the "critical" pressure ratio across the orifice given by:

$$\left( \frac{P_2}{P_1} \right)_{cr} = \left( \frac{2}{\gamma + 1} \right)^{\frac{\gamma}{\gamma - 1}} \quad (3.5)$$

where  $P_1$  and  $P_2$  are respectively the pressure upstream and downstream from the orifice, and  $\gamma$  is the ratio of specific heats for the gas. For sonic flow, the critical mass flow rate is:

$$\dot{m}_{cr} = \frac{C_v A_{12} P_1}{\sqrt{T_1}} \left[ \frac{\gamma}{R} \left( \frac{2}{\gamma+1} \right)^{\frac{\gamma+1}{\gamma-1}} \right]^{\frac{1}{2}} \quad (3.6)$$

where  $A_{12}$  is the orifice area between chamber volumes,  $T_1$  is the upstream absolute temperature, and  $R$  is the gas constant. For subsonic flow, the mass flow rate is expressed by:

$$\dot{m}_{12} = \frac{C_v A_{12} P_1}{\sqrt{T_1}} \left\{ \frac{2\gamma}{(\gamma-1)R} \left[ \left( \frac{P_2}{P_1} \right)^{\frac{2}{\gamma}} - \left( \frac{P_2}{P_1} \right)^{\frac{\gamma+1}{\gamma}} \right] \right\}^{\frac{1}{2}} \quad (3.7)$$

A flow coefficient  $C_v$  of 0.7 is assumed for all orifice areas, and the relationship between upstream  $T_1$  and downstream  $T_2$  temperature of an orifice is given by the isentropic process equation:

$$\frac{T_2}{T_1} = \left( \frac{P_2}{P_1} \right)^{(\gamma-1)/\gamma} \quad (3.8)$$

Equation (3.7) can be rewritten as:

$$\dot{m}_{12} = \frac{K_c C_v A_{12} P_1 N_{12}}{\sqrt{T_1}} \quad (3.9)$$

where

$$N_{12} = \frac{\dot{m}_{12}}{\dot{m}_{cr}} = \left[ \frac{\left( \frac{P_2}{P_1} \right)^{\frac{2}{\gamma}} - \left( \frac{P_2}{P_1} \right)^{\frac{\gamma+1}{\gamma}}}{\frac{\gamma-1}{2} \left( \frac{2}{\gamma+1} \right)^{\frac{\gamma+1}{\gamma-1}}} \right]^{\frac{1}{2}} \quad (3.10)$$

and the constant term  $K_c$  is:

$$K_c = \left[ \frac{\gamma}{R} \left( \frac{2}{\gamma+1} \right)^{\frac{\gamma+1}{\gamma-1}} \right]^{\frac{1}{2}} \quad (3.11)$$

Equation (3.10) is used to track the sonic or subsonic flow status through the orifices.

It should be noted that for subsonic flow

$$N_{12} < 1$$

and for the limiting case of sonic flow

$$N_{12} = 1$$

The pressure within the injector chamber can be determined from the equation of state for an ideal gas,  $PV=mRT$ , where  $V$ ,  $m$ , and  $T$  are respectively the chamber volume, gas mass, and gas absolute temperature. Differentiating the state equation with respect to time gives:

$$\frac{1}{P} \frac{dP}{dt} = \frac{1}{m} \frac{dm}{dt} - \frac{1}{V} \frac{dV}{dt} + \frac{1}{T} \frac{dT}{dt} \quad (3.12)$$

It is assumed that the chamber pressure and temperature is related by the isentropic process equation  $P\nu^\gamma = \text{constant}$ , where  $\nu$  is the specific volume. Substituting the specific volume term by  $RT/P$  from the equation state and differentiating the isentropic equation with respect to time, results in:

$$\frac{1}{T} \frac{dT}{dt} = \frac{\gamma-1}{\gamma} \cdot \frac{1}{P} \cdot \frac{dP}{dt} \quad (3.13)$$

Substituting Equation (3.13) into (3.12) yields the chamber pressure as:

$$\frac{1}{\gamma P} \frac{dP}{dt} = \frac{1}{m} \frac{dm}{dt} - \frac{1}{V} \frac{dV}{dt} \quad (3.14)$$

The rate of gas mass accumulation inside the chamber volume is determined from the application of the continuity equation:

$$\frac{dm}{dt} = \dot{m}_{in} - \dot{m}_{out} \quad (3.15)$$

where  $\dot{m}_{in}$  represents the mass flow rate supplied to the injector from the metering valve, and  $\dot{m}_{out}$  represents the mass flow rate discharging from the injector into the combustion chamber. Substituting Equation (3.15) into (3.14) and assuming that the pressure change due to the volume change is negligible because the injector needle has very small displacement, the rate of change in the chamber pressure is determined as:

$$\frac{dP}{dt} = \frac{\gamma RT}{V} (\dot{m}_{in} - \dot{m}_{out}) \quad (3.16)$$

### 3.4 Injected Gas Dose and Timing

For the four stroke engine with the displacement volume  $V_{ch}$  of 1 litre per cylinder, the injector discharges gas at every two revolutions of engine rotation. The injected gas dose is assumed at maximum engine torque and the corresponding engine speed of 2000 rpm. Hence, the time corresponding to one cycle is:

$$\frac{(60 \text{ s}) \times (2 \text{ rev.})}{2,000 \text{ rpm}} = 0.06 \text{ s} \quad (3.17)$$

To find the opening time of the injector, the following assumptions have been made:

For the injection of natural gas, the air/fuel ratio is 14.5 [2]. Then the injected fuel dose is:

$$m_{fg} = \frac{m_a}{14.5} = \frac{1}{14.5} \frac{P_i V_{ch}}{R_a T_i} \quad (3.18)$$

where  $m_a$  is the mass of air inside the cylinder. Assuming that the intake pressure  $P_i$  for the cylinder air is 100 kPa, the temperature  $T_i$  is 300 K, and the air constant  $R_a$  is given as 287 kJ/kg-K, the gas dose will be:

$$m_{fg} = \frac{(100) \cdot (0.001)}{(14.5) \cdot (0.287) \cdot (300)} = 80 \text{ mg of natural gas}$$

The calculated fuel dose must be injected during 60° of crankshaft revolution. This corresponds to an injection time of:

$$t_i = \frac{60^\circ}{720^\circ} \times 0.06 \text{ s} = 5 \text{ ms}$$

Then, the gas discharge rate should be:

$$\dot{m}_{fg} = \frac{80 \text{ mg}}{5 \text{ ms}} = 16 \frac{\text{mg}}{\text{ms}} \text{ or } 0.016 \frac{\text{kg}}{\text{s}}$$

The natural gas will be injected with the pressure ratio:

$$P_r = \frac{\text{cylinder pressure}}{\text{gas supply pressure}}$$

Assuming that the gas supply pressure is 100 bar and that the cylinder pressure is 40 bar, the pressure ratio  $P_r$  is 0.4 and the gas discharge will be sonic. Then, Equation (3.6) can be used to calculate the required nozzle orifice flow area for natural gas as:

$$A_g = 1.3507 \times 10^{-6} \text{ m}^2$$

Similar calculations can be made for hydrogen for the air/fuel ratio of 34.3 [2]. The required fuel dose for a 1 litre cylinder, the gas discharge rate over 5 ms, and the required nozzle orifice flow area, are respectively:

$$m_{fh} = 34 \text{ mg}$$

$$\dot{m}_{fh} = 0.0068 \frac{\text{kg}}{\text{s}}$$

$$A_h = 1.5748 \times 10^{-6} \text{ m}^2$$



## CHAPTER 4

### SOLENOID TRANSIENT FORCE AND CURRENT CHARACTERISTICS AND SWITCHING CIRCUIT DESIGN

#### 4.1 Introduction

As reported in the literature, there has been several attempts to design solenoid operated injector systems and to evaluate their performances. However, there is a lack of a generalized mathematical model of the solenoid, which would allow to simulate accurately enough its fast dynamics and transient force characteristics. A comprehensive mathematical description, based on a better understanding of the solenoid capabilities, allows to extract more benefit from the component function when applied to a system's design.

The design of an electrical solenoid has some similarities to that of a power transformer, except that the solenoid has a moving air-gap. The model of the transformer iron core can be approximated by an equivalent circuit [39,40], consisting of the alternating voltage source in series with a resistance term representing the coil winding and an inductance term representing the flux leakages through air and through the winding. These components are then modelled in parallel with the coil inductance and with a core-loss resistance term. This last term accounts for the losses due to the induced eddy currents in the ferromagnetic material and hysteresis. In the study of power transformers, the values assigned to the flux leakage inductance and core-loss resistance parameter terms are based on a steady-state voltage source and current rms values since power losses are of concern.

In this chapter, the model of a solenoid is selected similar to the equivalent circuit of the power transformer. Since the solenoid transient force and current characteristics for different applied voltages are of concern, the numerical values assigned to the model parameters will be representative of the time response requirements. This approach to the modelling of the dynamic behaviour of solenoids is novel. The subject presented in this chapter has been reported in reference [41].

Once the characteristics of the solenoid has been established, the next goal is to design a driving circuit to take advantage these properties for fast injector opening and closing. Presented in this chapter is a simple but effective, solenoid driving switching circuit that has been designed for this purpose. The circuit is quite simple because only seven components are used in its design. It should be noted that the switching transistor, solid-state relay, pull-up resistor and flyback diode are general components in most switching circuit applications; however, the proposed innovative sub-circuit introduced consists only of three components, the capacitor, leakage resistor and zener diode. From the manufacturer's point of view, using off-the-shelf solenoids and few electronic components is quite cost effective.

The switching circuit of the solenoid is instrumental for achieving a good performance of the gas injector. The special design of such a circuit, as compared with those for conventional "on-off" solenoids, is providing the injector with fast opening and closing capabilities. In addition, the driving circuit demonstrates that off-the-shelf high performance compact-sized solenoids can be used where their power rating can be

increased above their nominal value for a short period of time without causing overheating damage.

#### **4.2 Experimental Set-up to Measure Solenoid Transient Characteristics**

The experimental set-up to measure the solenoid transient force and current characteristics is illustrated in Figure 4.1. Measurements are taken at various fixed air-gap positions for different applied voltages. The set-up consists of a threaded fixture which mounts the injector on its upside down position. By threading-in the solenoid housing onto the fixture, the piezo-cell force transducer and a brass spacer can be secured between the solenoid outer casing and threaded fixture. The spacer is disk shaped with a cylindrical pin at its centre. A hole is drilled through the solenoid casing at the magnetic pole in such a way that the protruding pin comes in contact with the solenoid movable core. When the disk face is in contact with the solenoid casing, the length of the pin ensures the length of the air-gap between the solenoid core and solenoid pole. By changing the pin length, different lengths of fixed air-gaps are attained. When the solenoid is energized, the core does not move but the pulling force is transmitted from the core onto the disk and compresses the piezo-cell transducer that rests on top of the fixture. The specifications and calibration curve of the load cell are described in Appendix B.

The electronic switching circuit used to energize the solenoid coil is shown in Figure 4.2. A solid state relay with DC output manufactured by GORDOS is totem

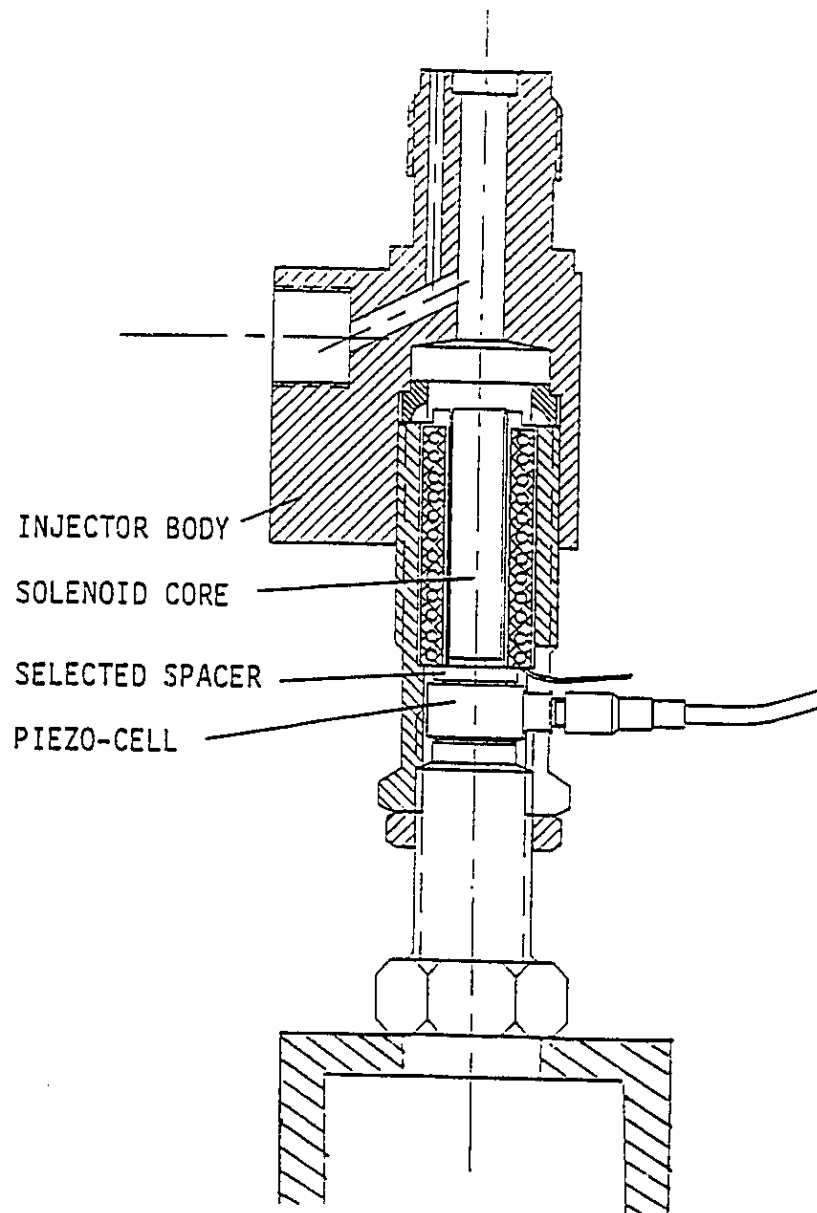


Fig. 4.1 Schematic of the fixture to measure the solenoid force

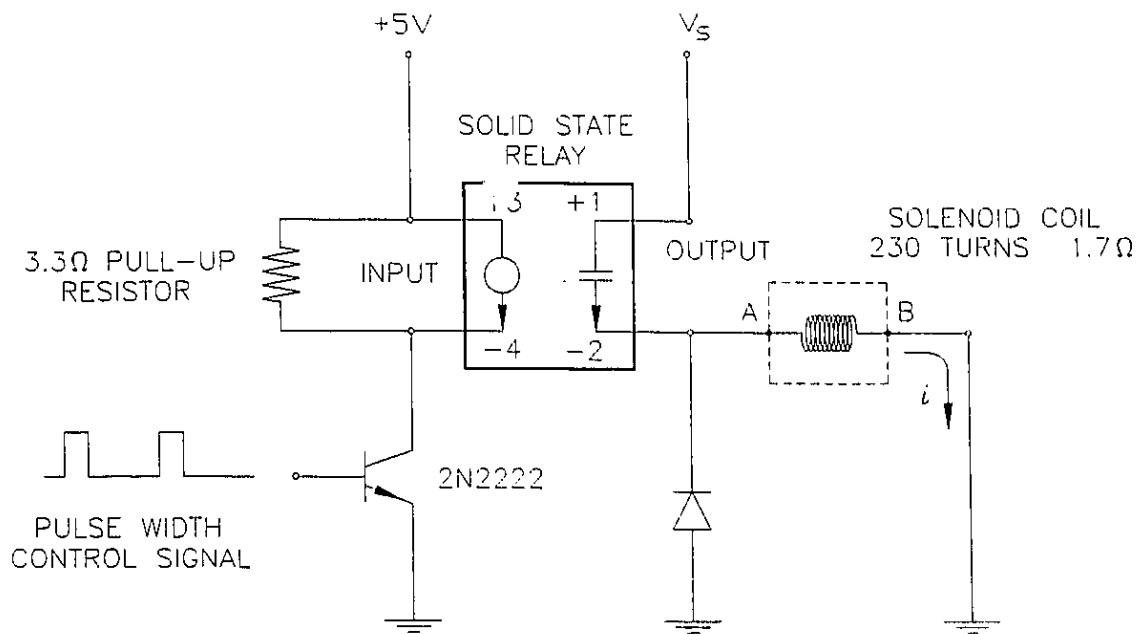


Fig. 4.2 Switching circuit used in experimental set-up for solenoid current and force measurements

poled with a 2N2222 NPN bipolar junction transistor. A voltage of single step provides the control signal applied to the base of the transistor to turn it on and off. When the transistor is turned on, terminal 4 of the relay input is pulled low. In turn, the relay is closed and current from the voltage supply  $V_s$  energizes the solenoid coil. The rise in transient force is measured with the piezo-cell transducer, and the corresponding coil currents are measured with a clamp-on current meter. Appendix C describes the specifications of the clamp-on current meter.

When the control signal is stepped to zero voltage, the transistor is turned off and terminals 3 and 4 of the relay are at equal potential. The relay is next opened, and the free wheeling diode is used in order to protect the relay by providing a path to the current and to avoid the back EMF spike from the solenoid coil. The decay of transient force and current are then measured.

### **4.3 Discussion of Experimental Results**

Transient force and current are measured for the solenoid core fixed at five different air-gap positions. At each air-gap, the voltage is applied from 6 V to 27 V at the increments of 3 V. The figures of the test results with their corresponding air-gap positions are summarized in Table 4.1. Each figure is indicated for the variable of current or force with respect to its rise or decay, which corresponds to the source voltage being applied when the relay is closed, or removed when the relay is opened. Also indicated in the table are figure numbers of force versus current for each air-gap. The

points in the figures are from experimental measurements. The lines passing through the points are made from the simulation results of the solenoid model, and will be presented in Section 4.6.

AIR-GAP (mm)	FIGURE NUMBER				
	Current (A)		Force (N)		Force (N) vs. Current (A)
	rise	decay	rise	decay	
0.635	4.3a	4.3b	4.4a	4.4b	4.15
0.535	4.5a	4.5b	4.6a	4.6b	4.16
0.425	4.7a	4.7b	4.8a	4.8b	4.17
0.353	4.9a	4.9b	4.10a	4.10b	4.18
0.242	4.11a	4.11b	4.12a	4.12b	4.19

Table 4.1 Air-gap positions and their corresponding current and force figures.

With reference to Figure 4.3a for a 0.635 mm air-gap, the transient and steady-state current through the solenoid coil increases as the applied voltage across its terminals is increased. For applied voltages below 15 V, the rise in current with respect to time is exponential in shape. Above this applied voltage, the current has a steep rise and next bends rapidly to its steady-state value. These differences in the shape of the current time response is an indication of a changing coil inductance, which is a function of flux magnitude. This trend is seen in all the test results of current rise at all air-gap positions (Figures 4.3a, 4.5a, 4.7a, 4.9a, 4.11a). Current effects due to air-gap positions are not

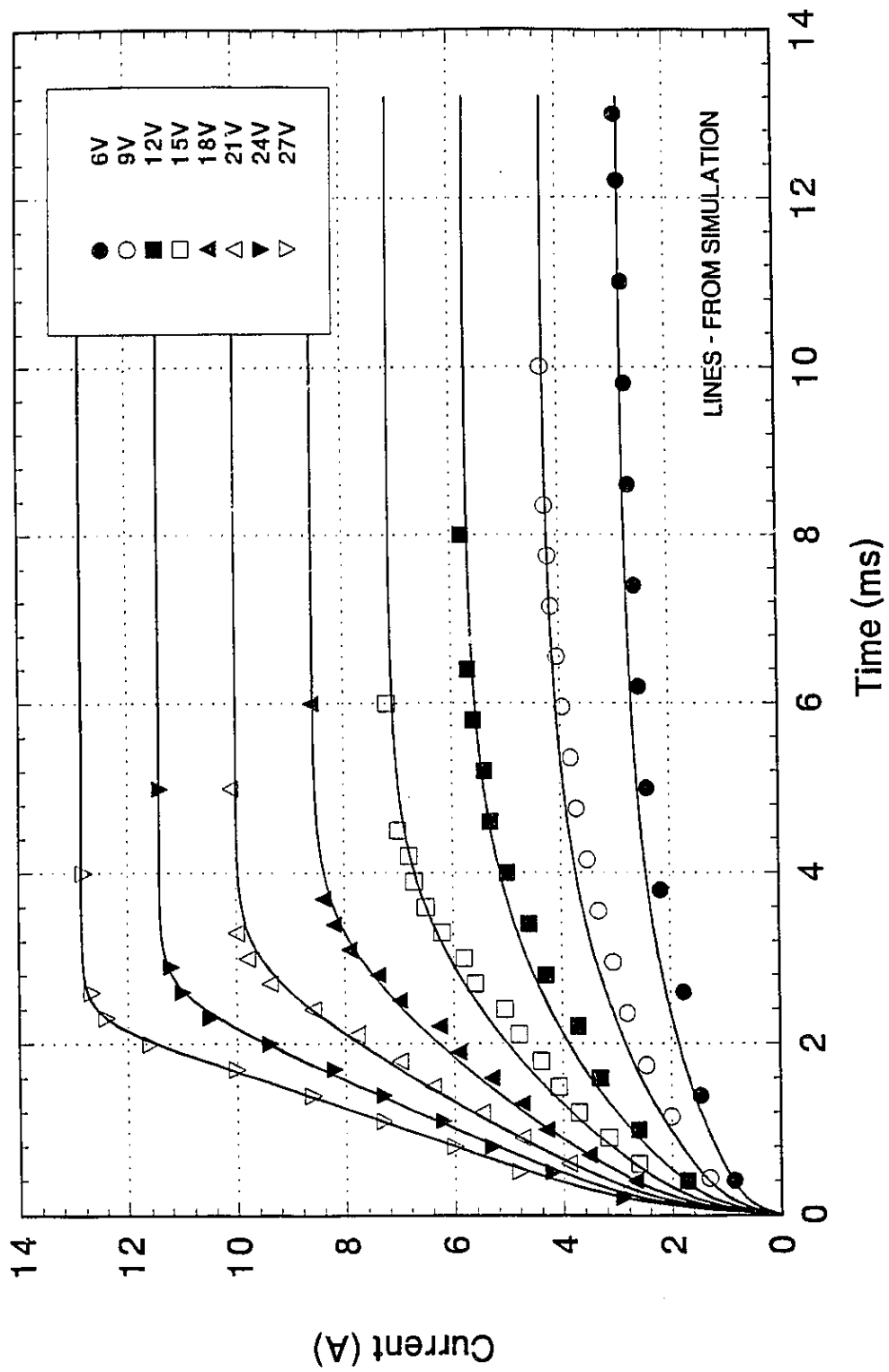


Fig. 4.3a Rise of current in solenoid coil, air-gap 0.635 mm



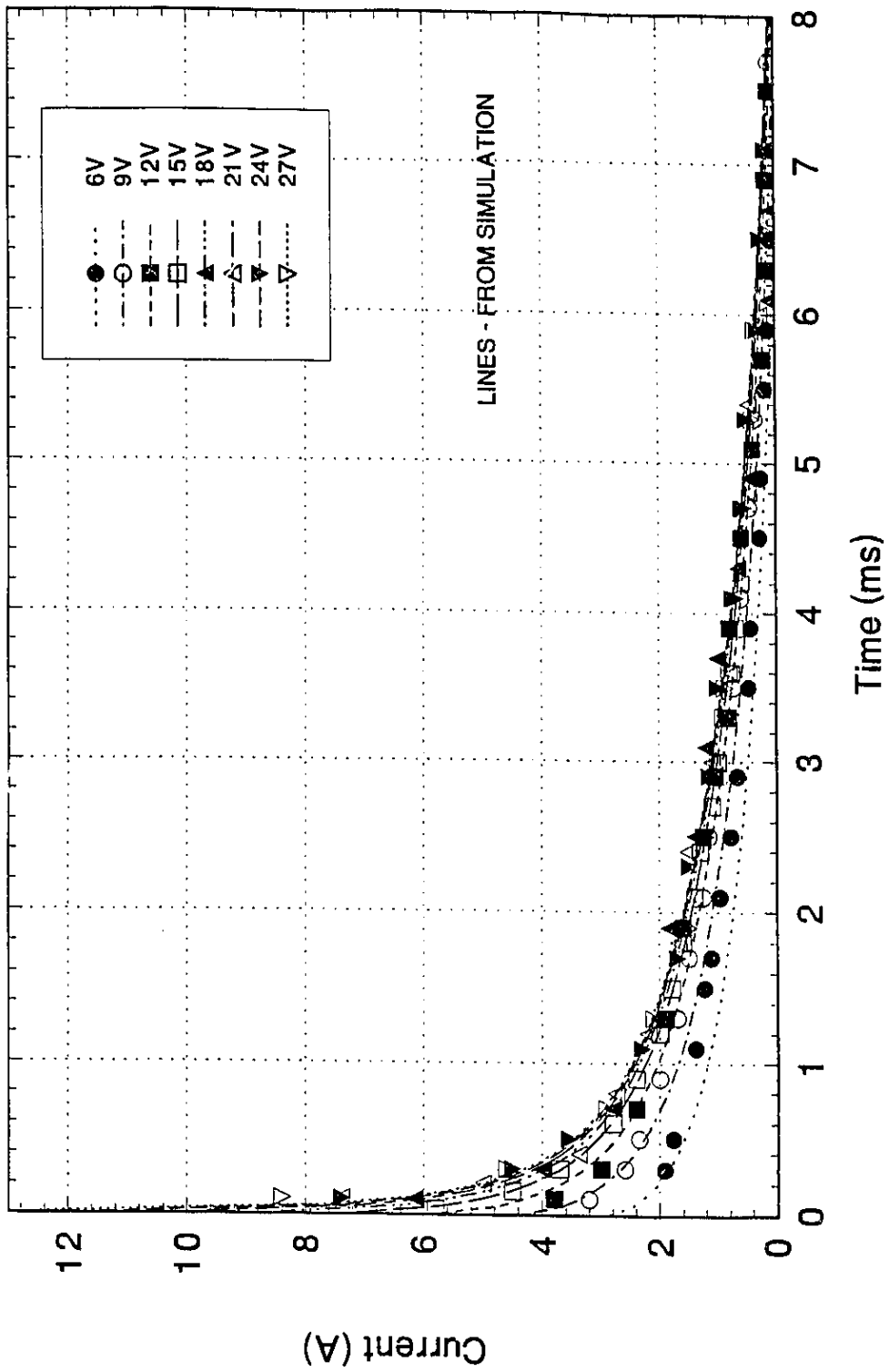


Fig. 4.3b Decay of current in solenoid coil, air-gap 0.635 mm

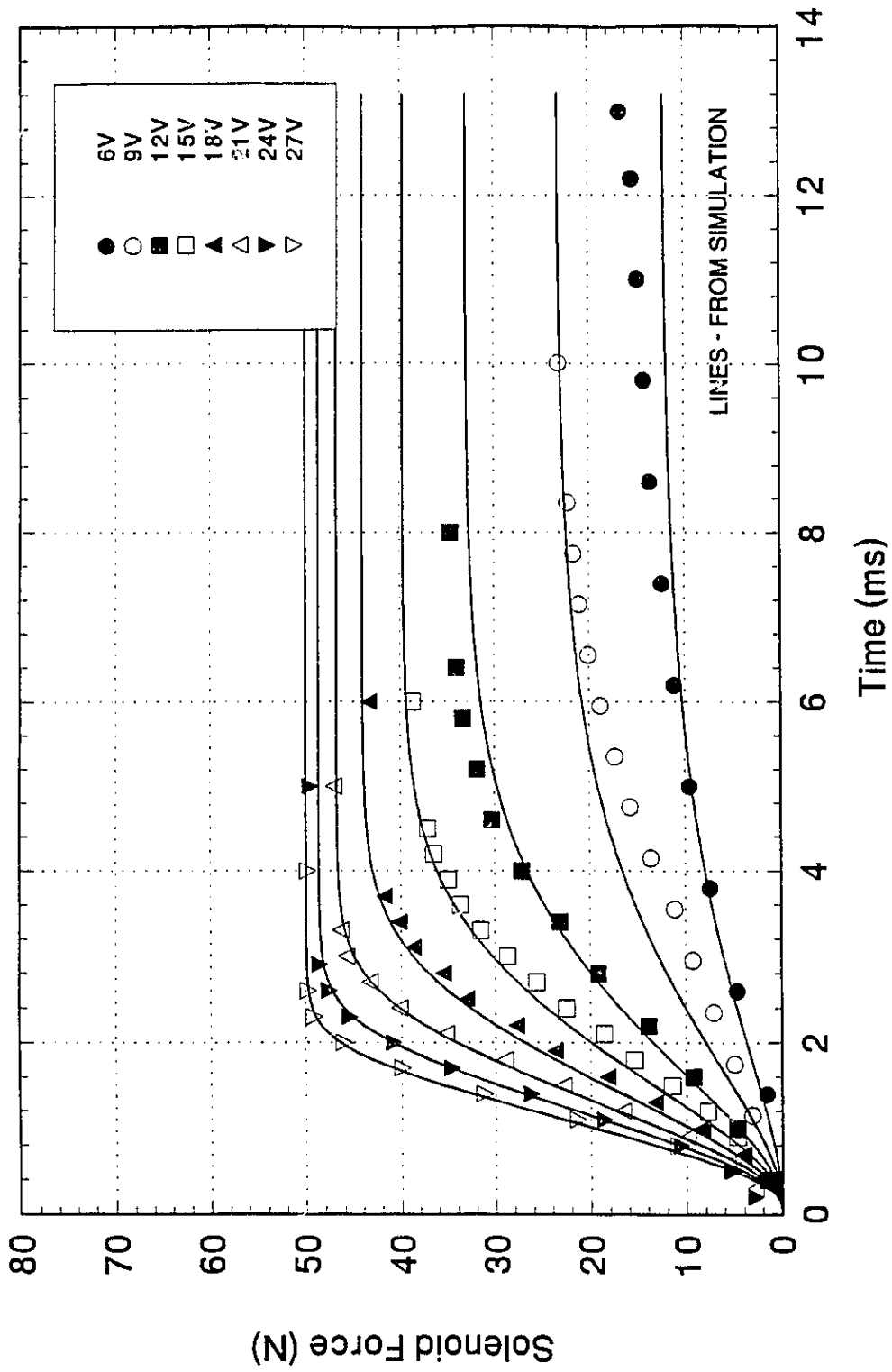


Fig. 4.4a Rise of solenoid force, air-gap 0.635 mm

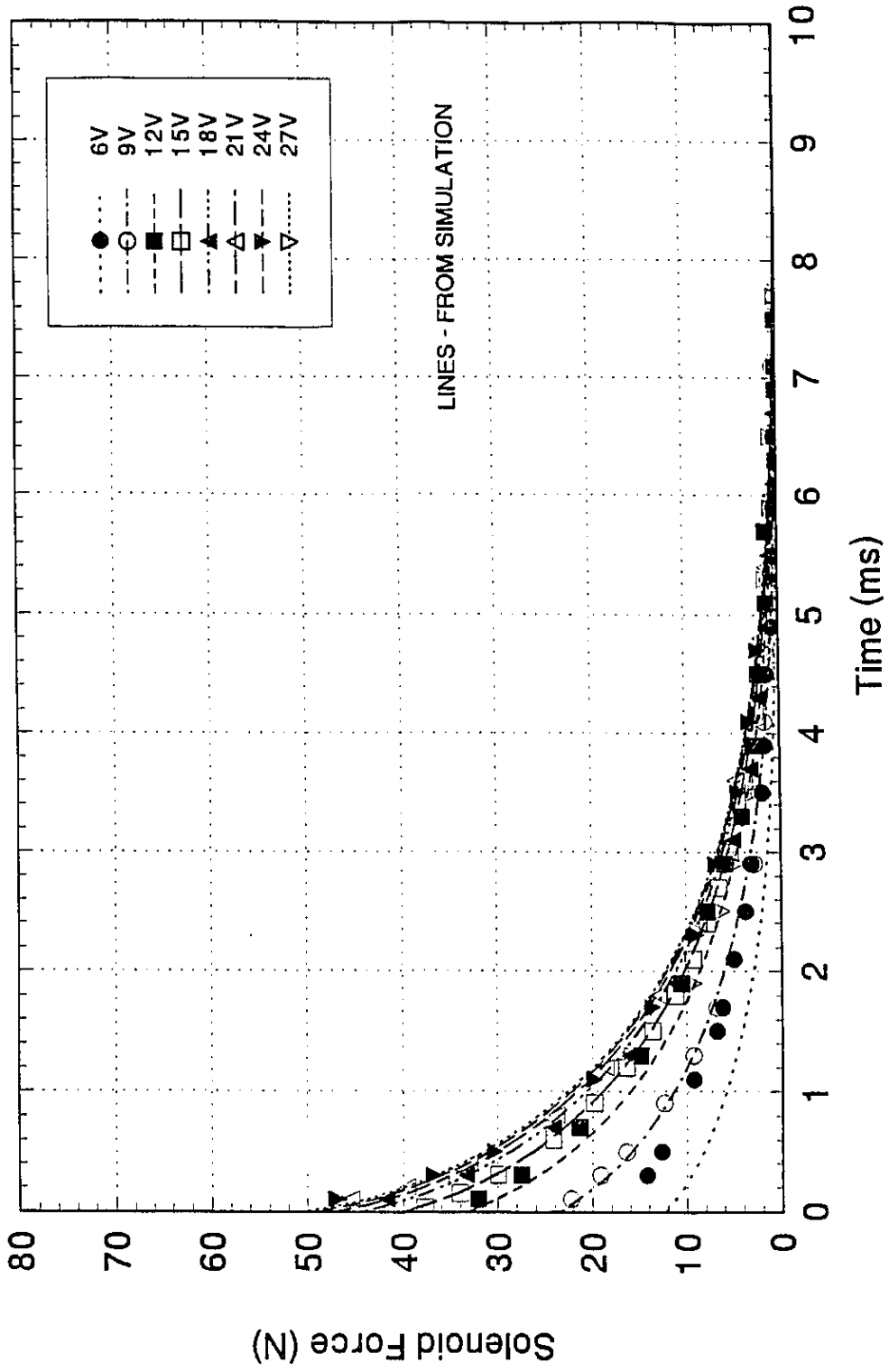


Fig. 4.4b Decay of solenoid force, air-gap 0.635 mm

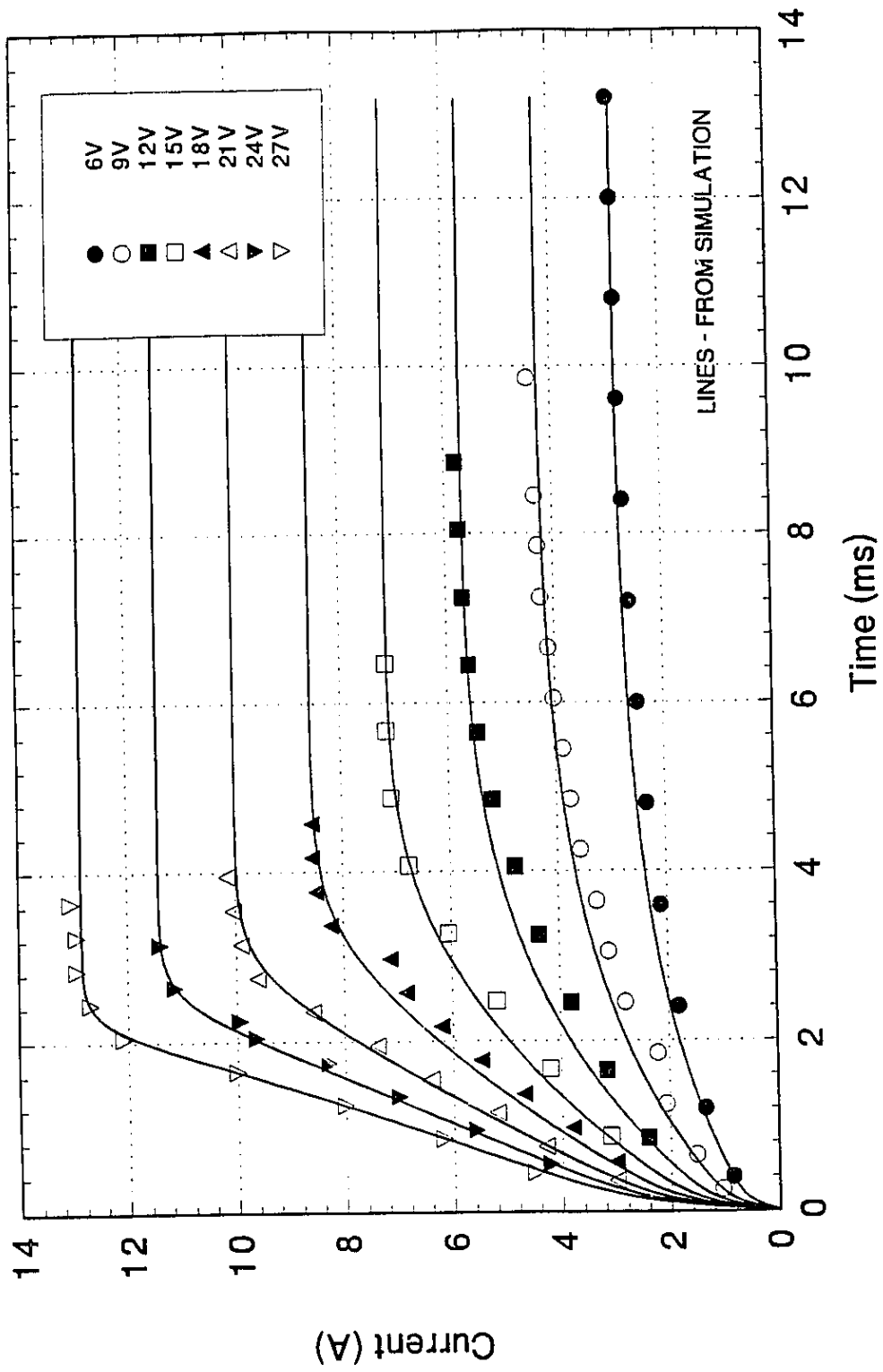


Fig. 4.5a Rise of current in solenoid coil, air-gap 0.535 mm

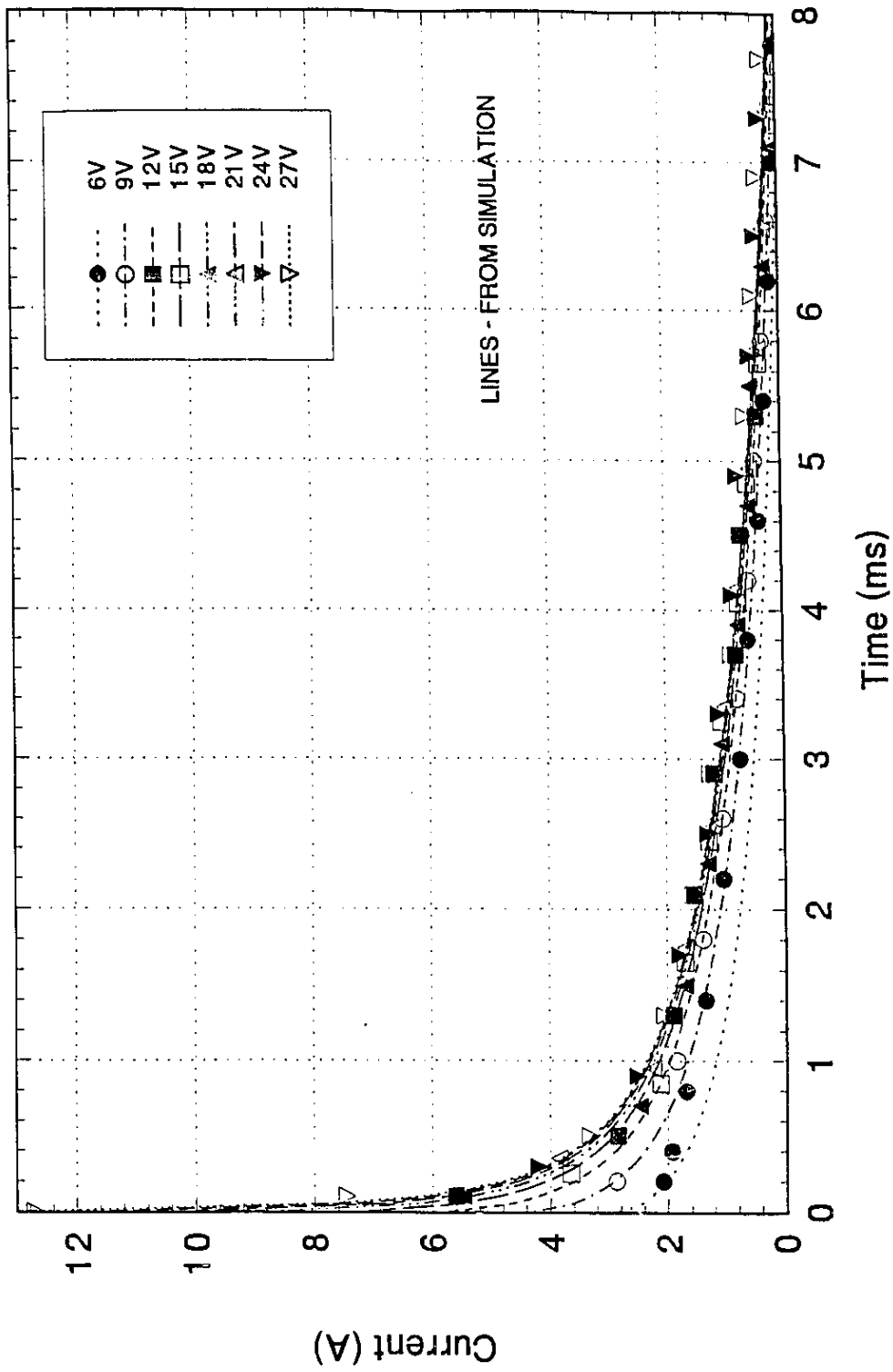


Fig. 4.5b Decay of current in solenoid coil, air-gap 0.535 mm

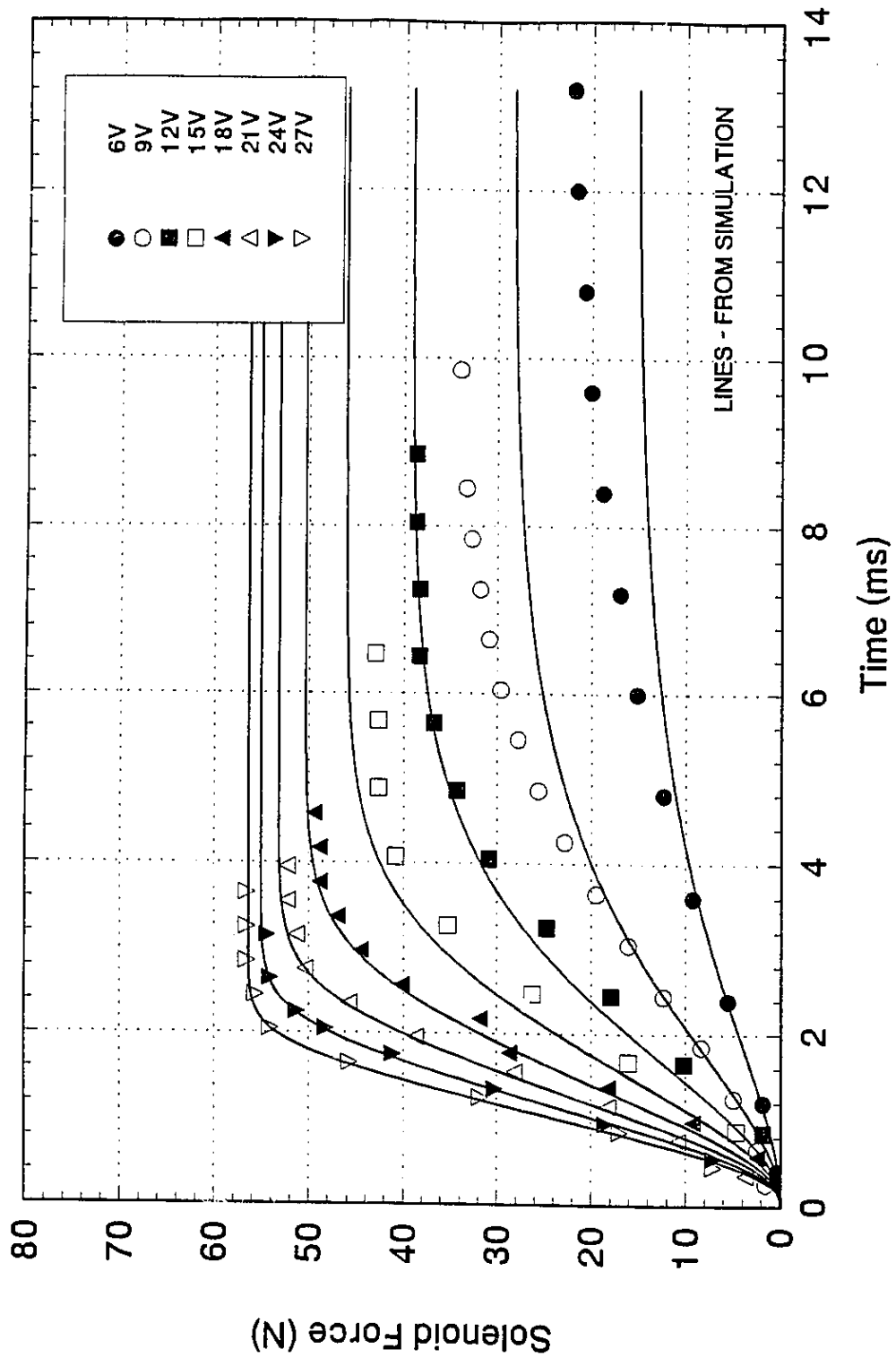


Fig. 4.6a Rise of solenoid force, air-gap 0.535 mm

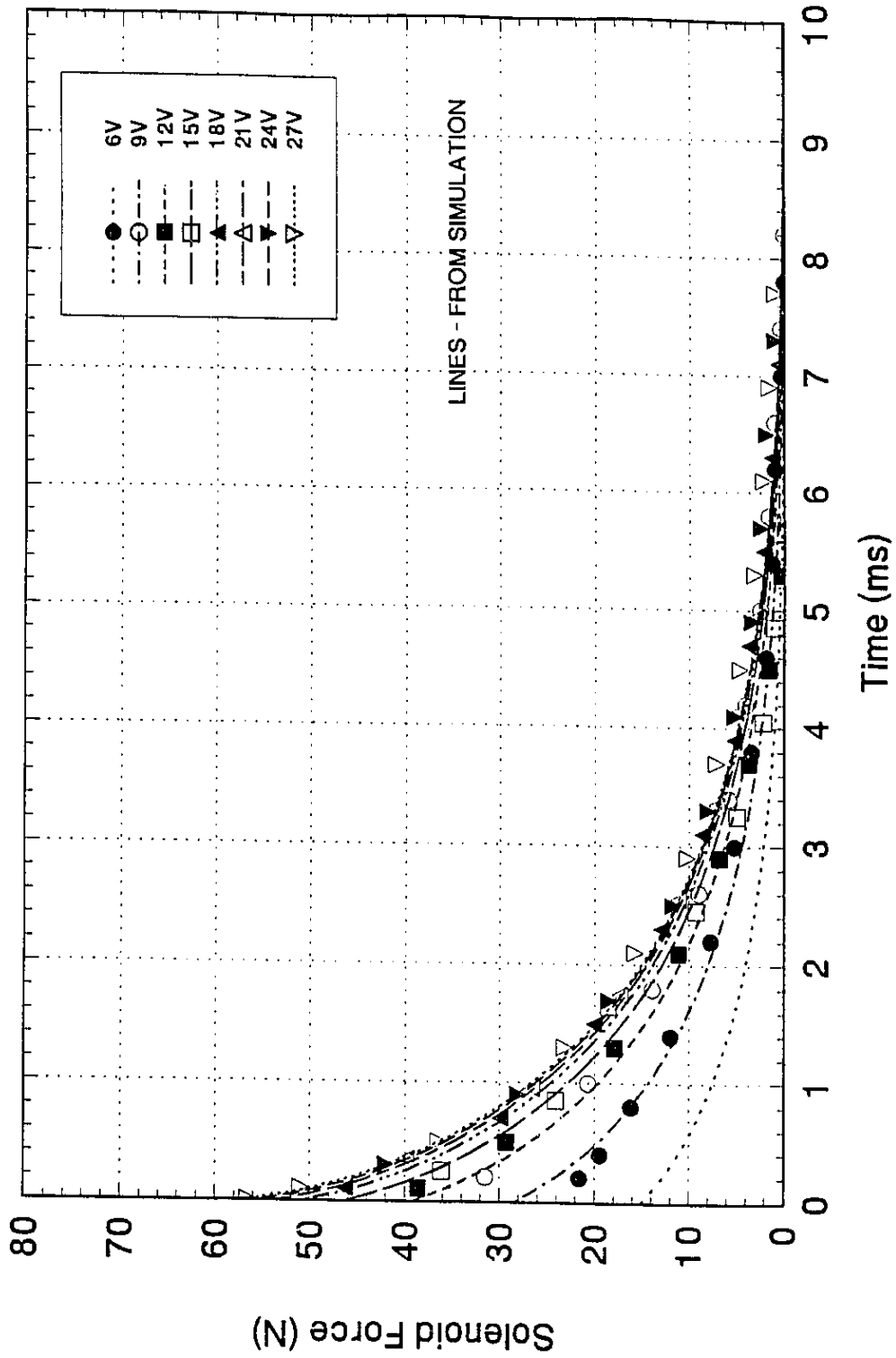


Fig. 4.6b Decay of solenoid force, air-gap 0.535 mm

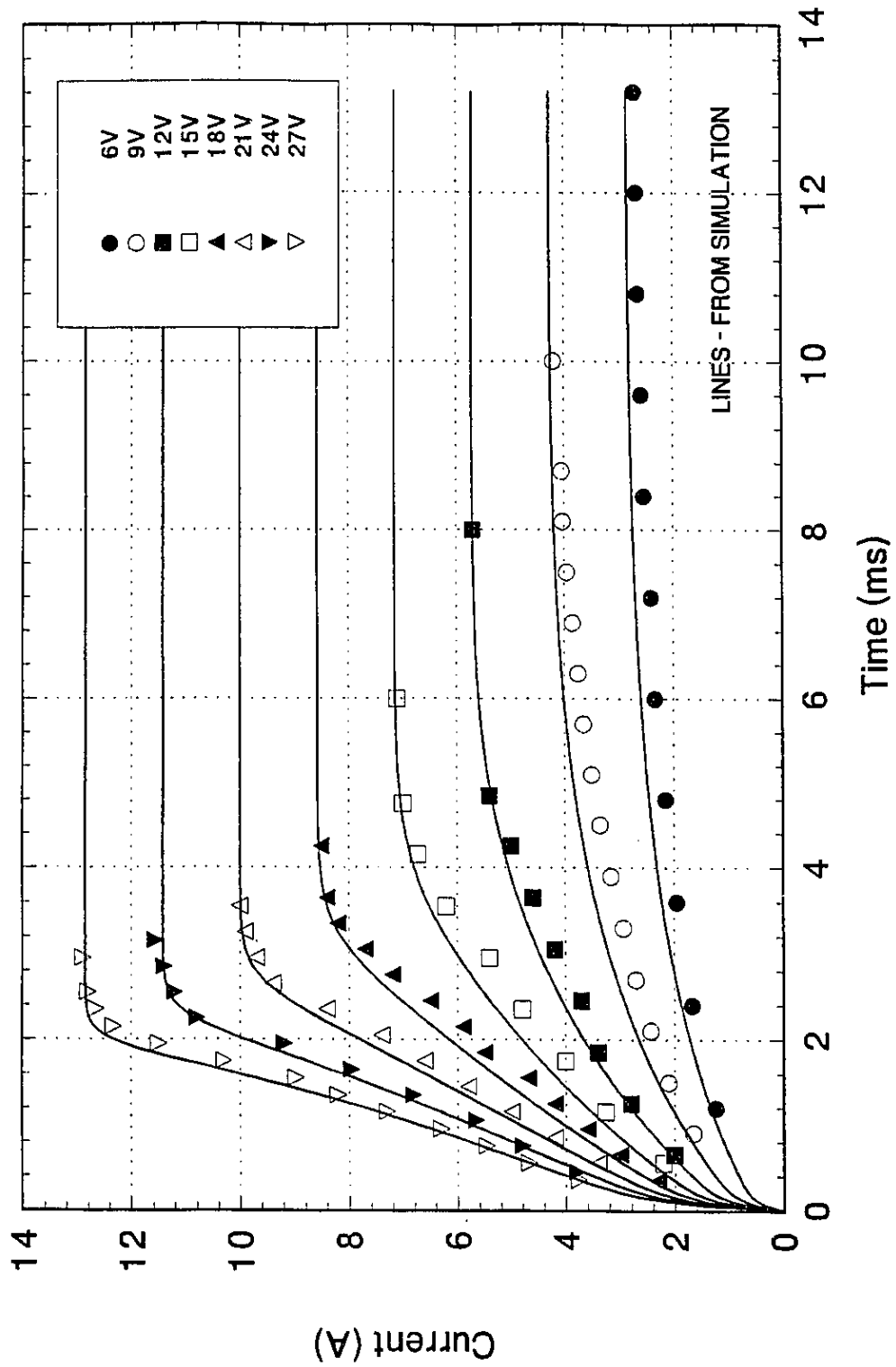


Fig. 4.7a Rise of current in solenoid coil, air-gap 0.425 mm



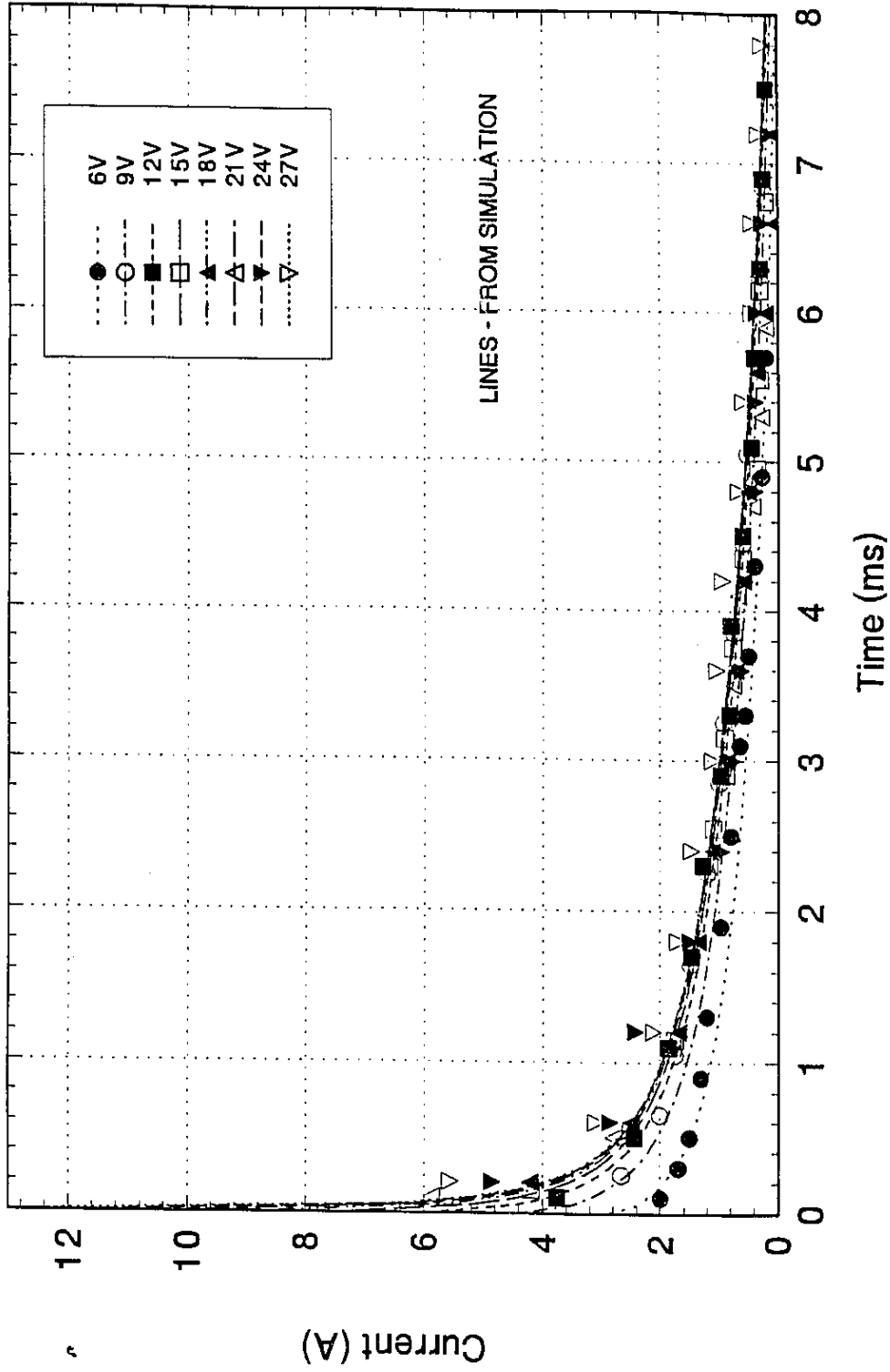


Fig. 4.7b Decay of current in solenoid coil, air-gap 0.425 mm

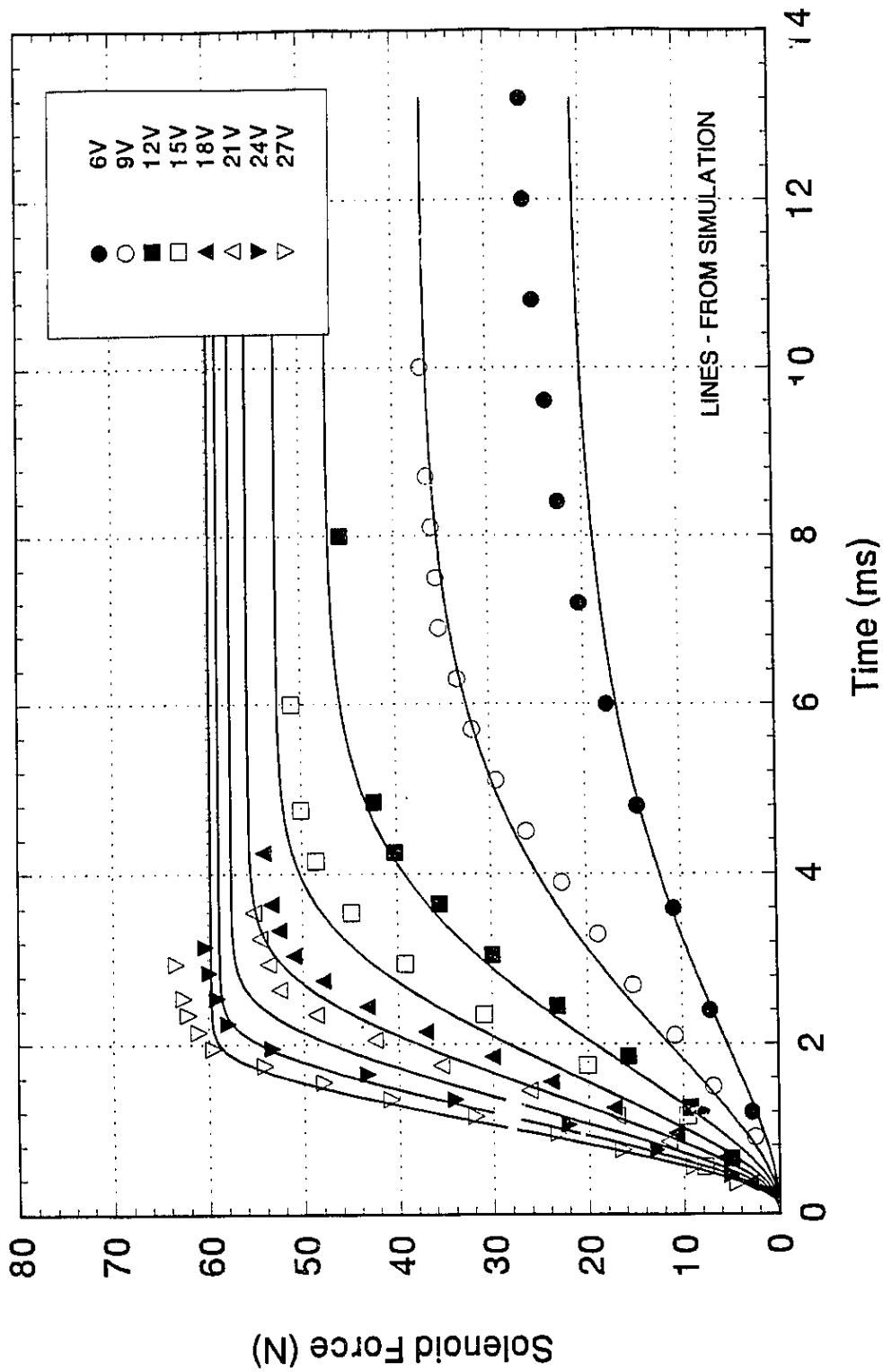


Fig. 4.8a Rise of solenoid force, air-gap 0.425 mm

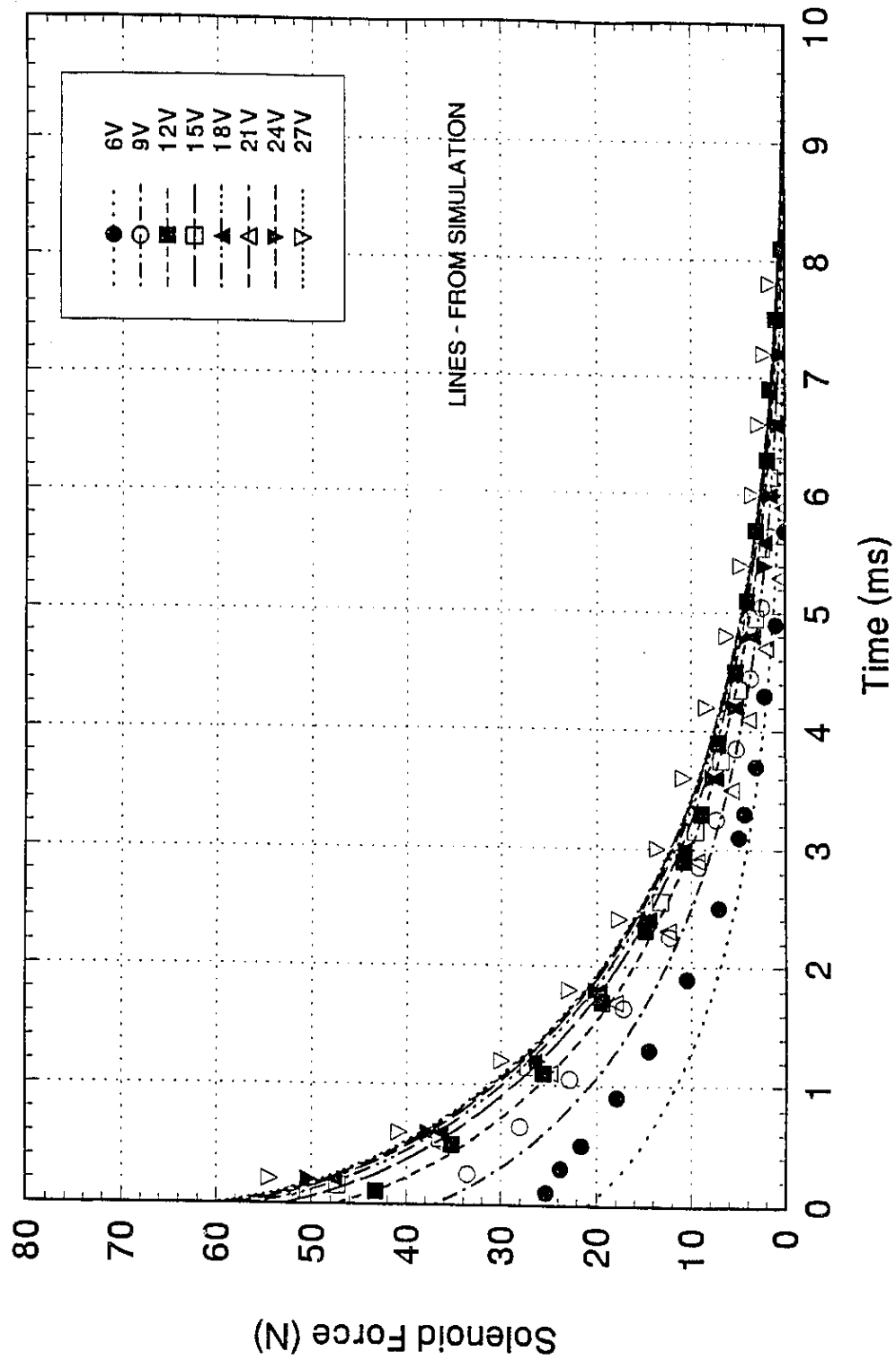


Fig. 4.8b Decay of solenoid force, air-gap 0.425 mm

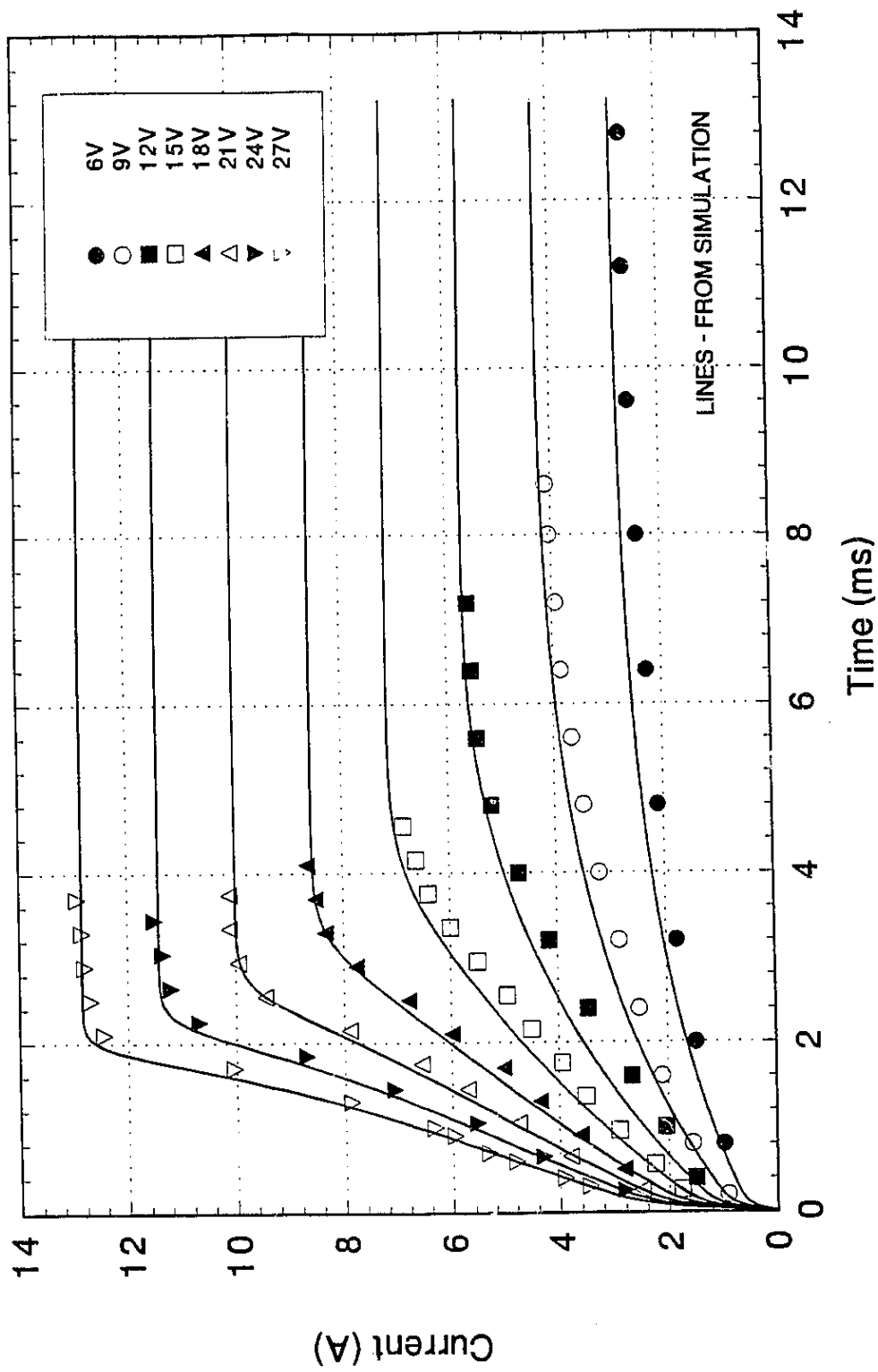


Fig. 4.9a Rise of current in solenoid coil, air-gap 0.353 mm

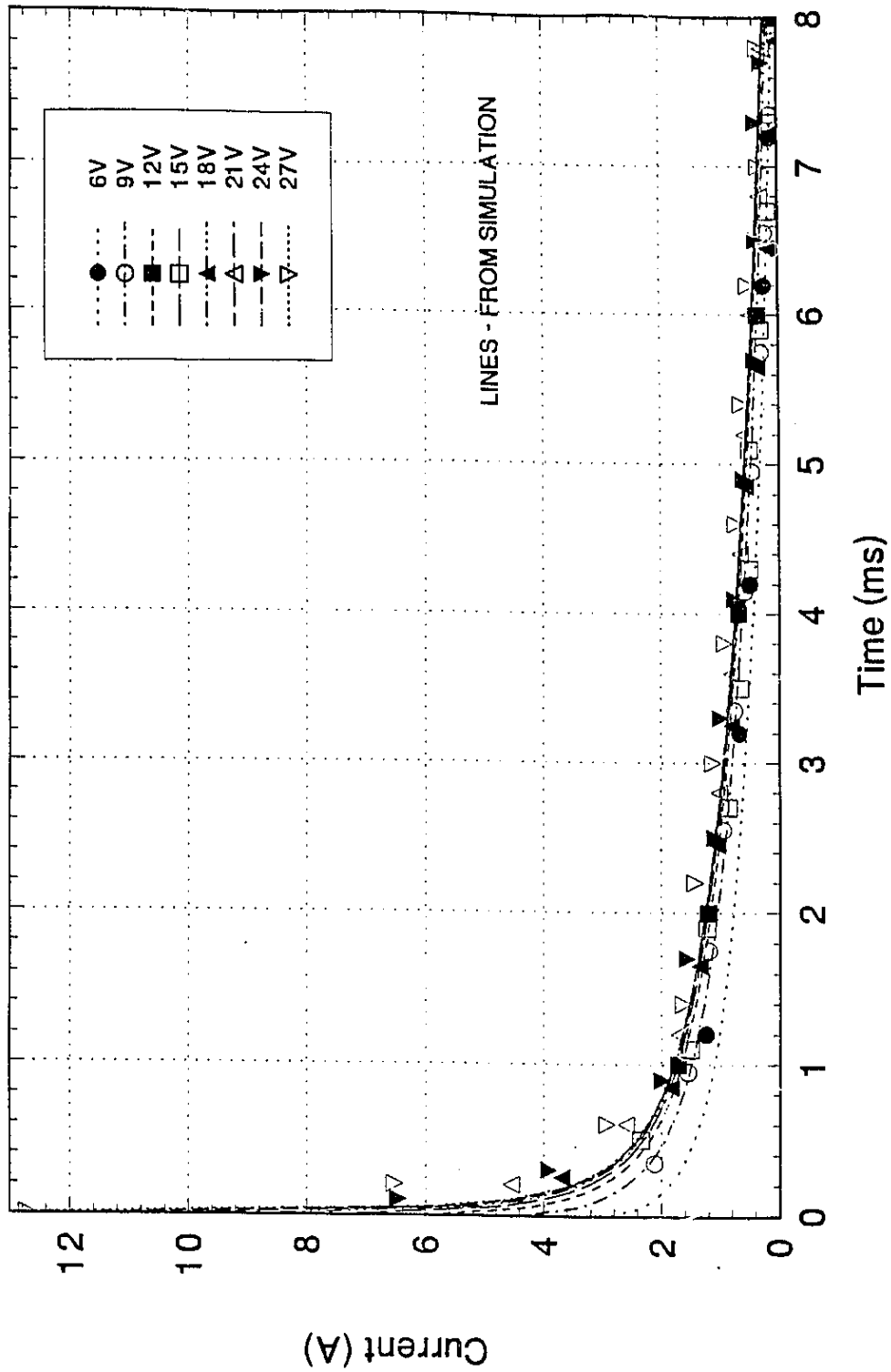


Fig. 4.9b Decay of current in solenoid coil, air-gap 0.353 mm

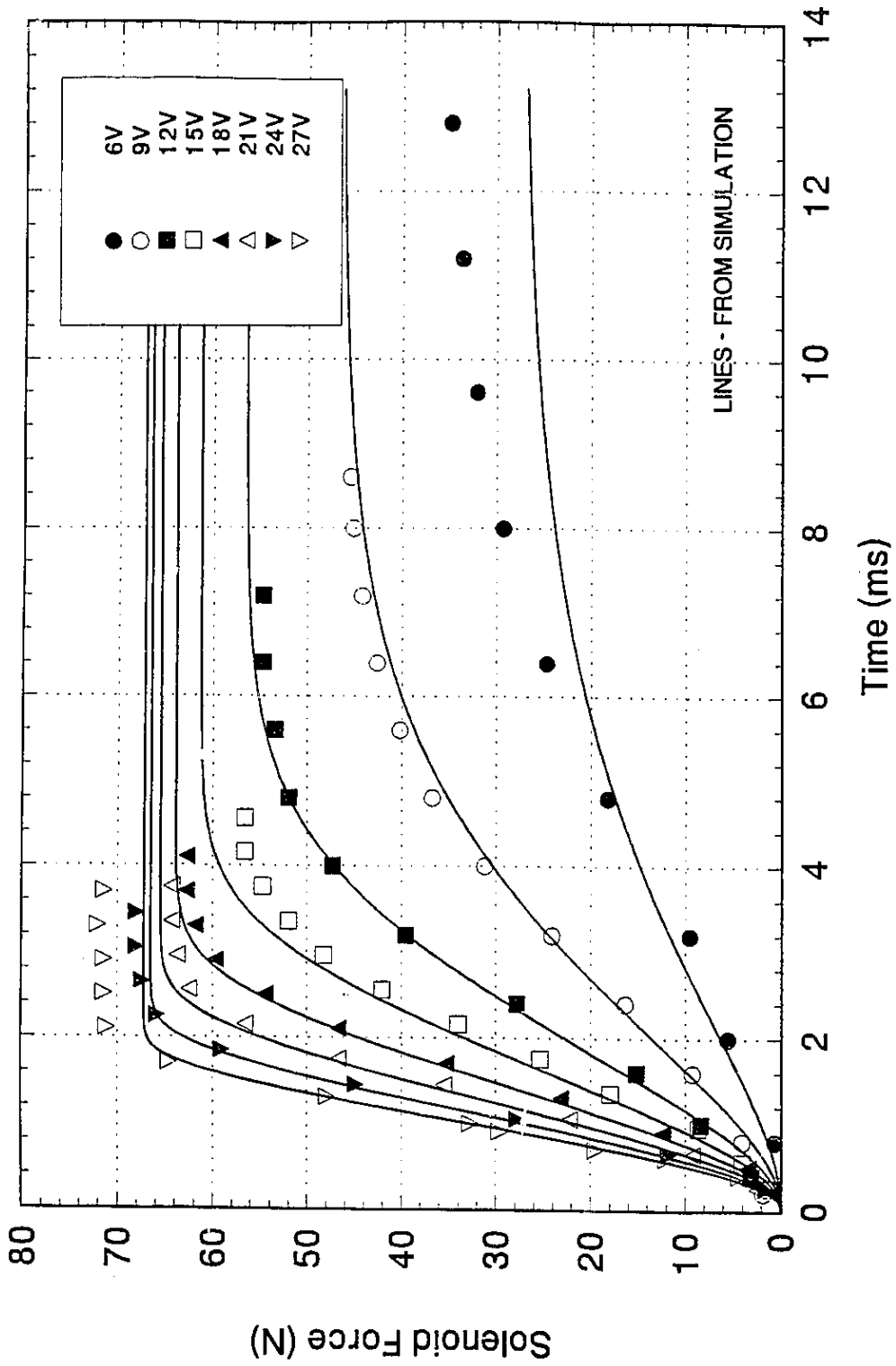


Fig. 4.10a Rise of solenoid force, air-gap 0.353 mm

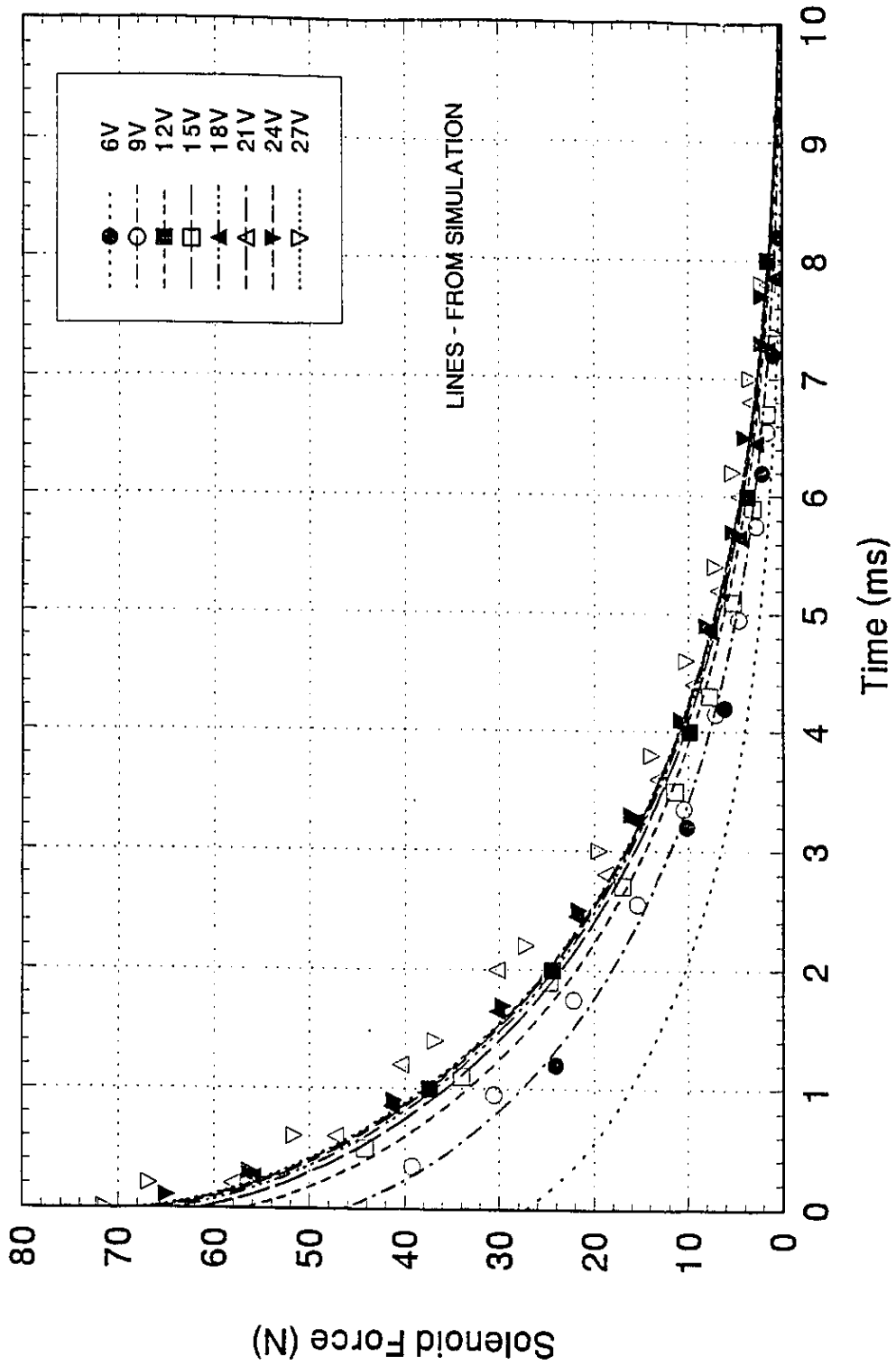


Fig. 4.10b Decay of solenoid force, air-gap 0.353 mm

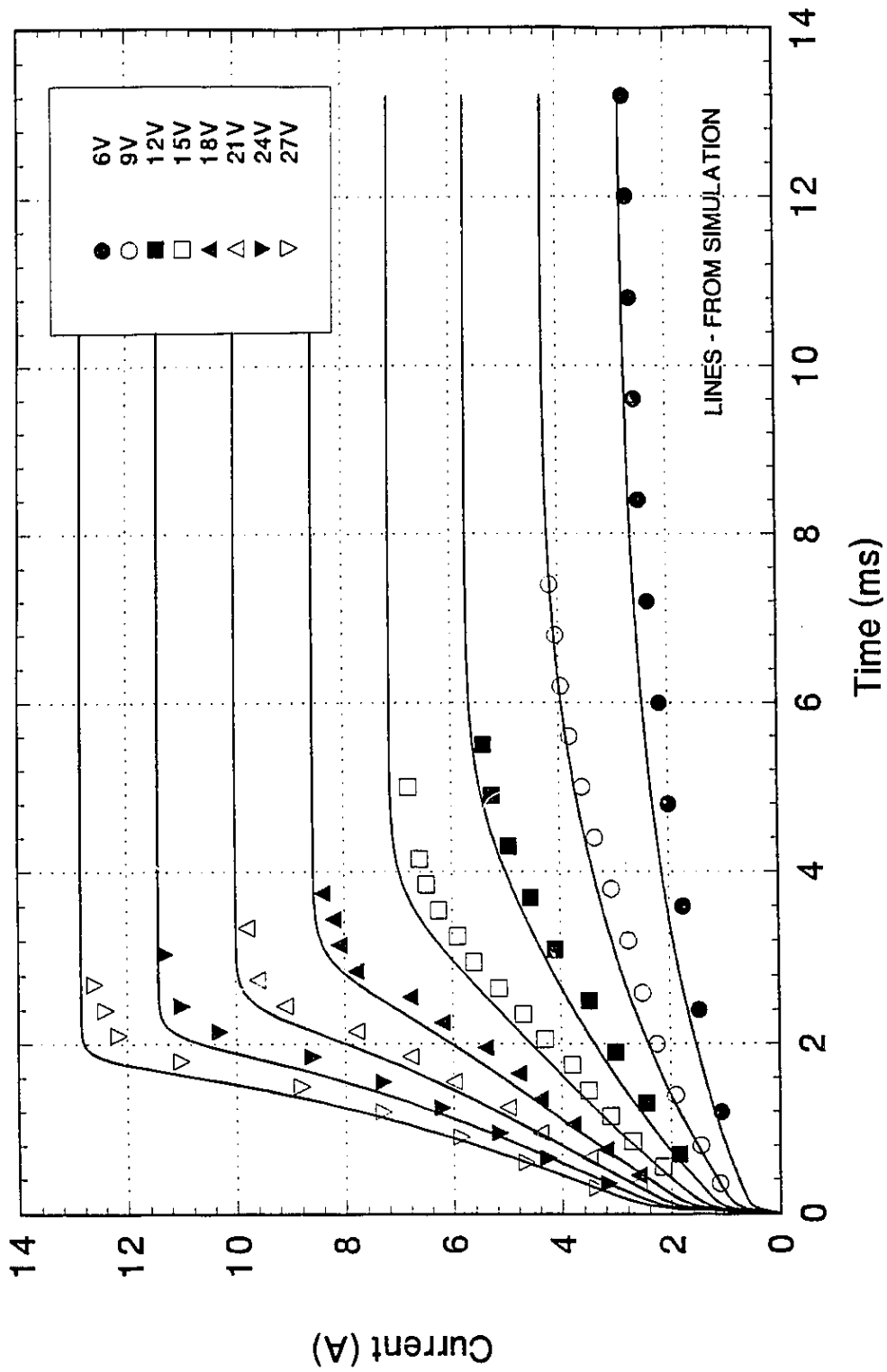


Fig. 4.11a Rise of current in solenoid coil, air-gap 0.242 mm



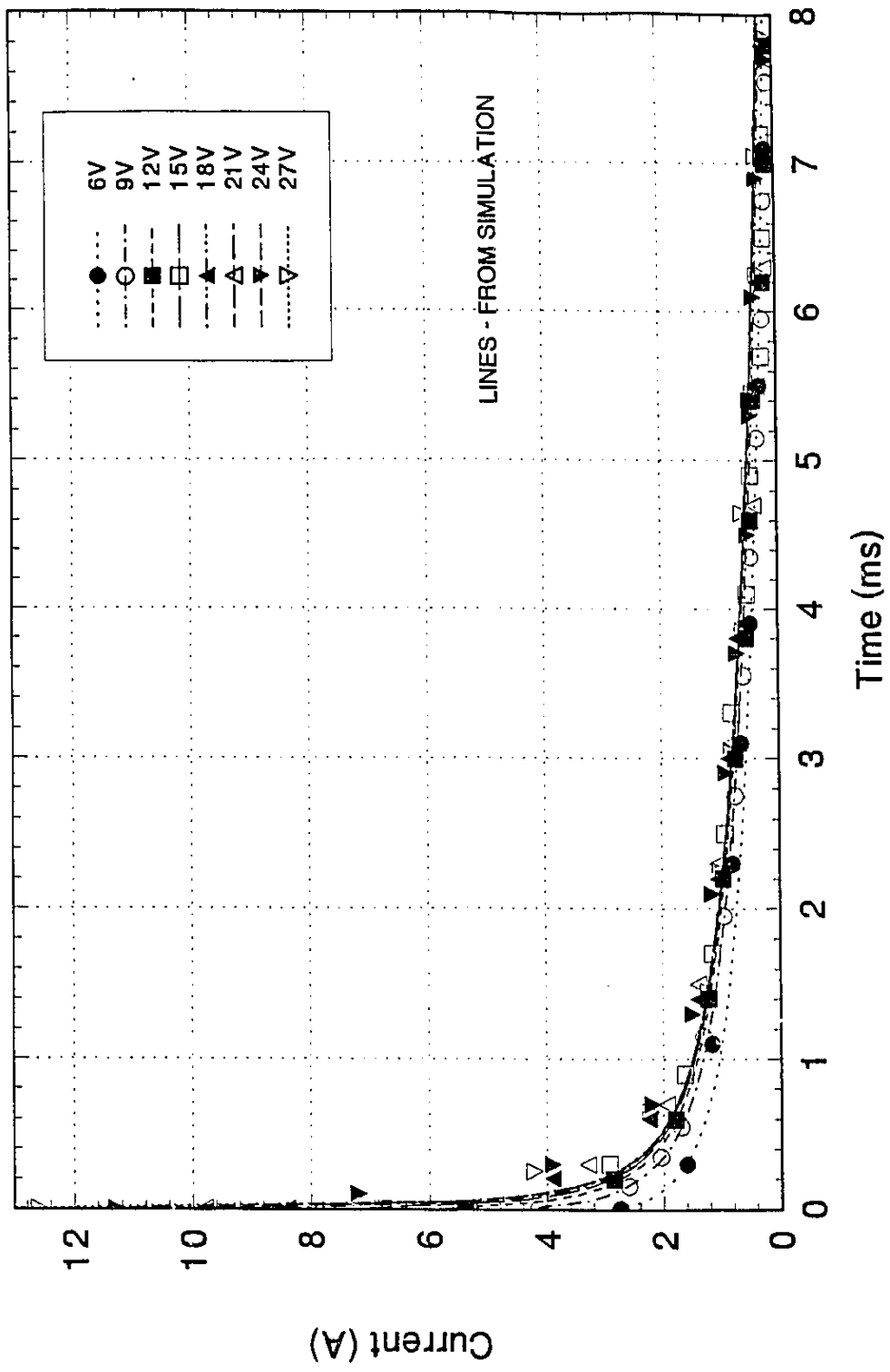


Fig. 4.11b Decay of current in solenoid coil, air-gap 0.242 mm

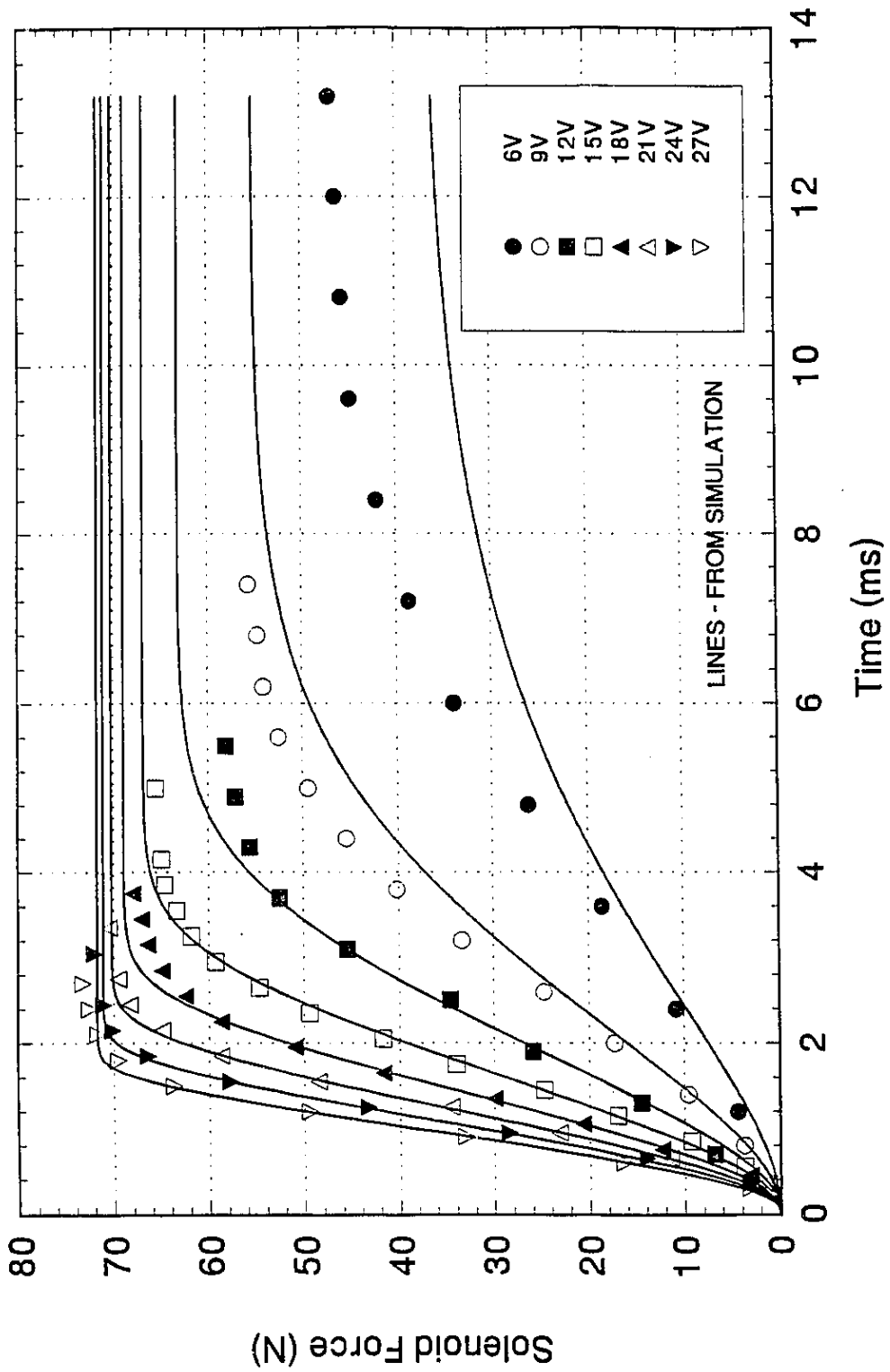


Fig. 4.12a Rise of solenoid force, air-gap 0.242 mm

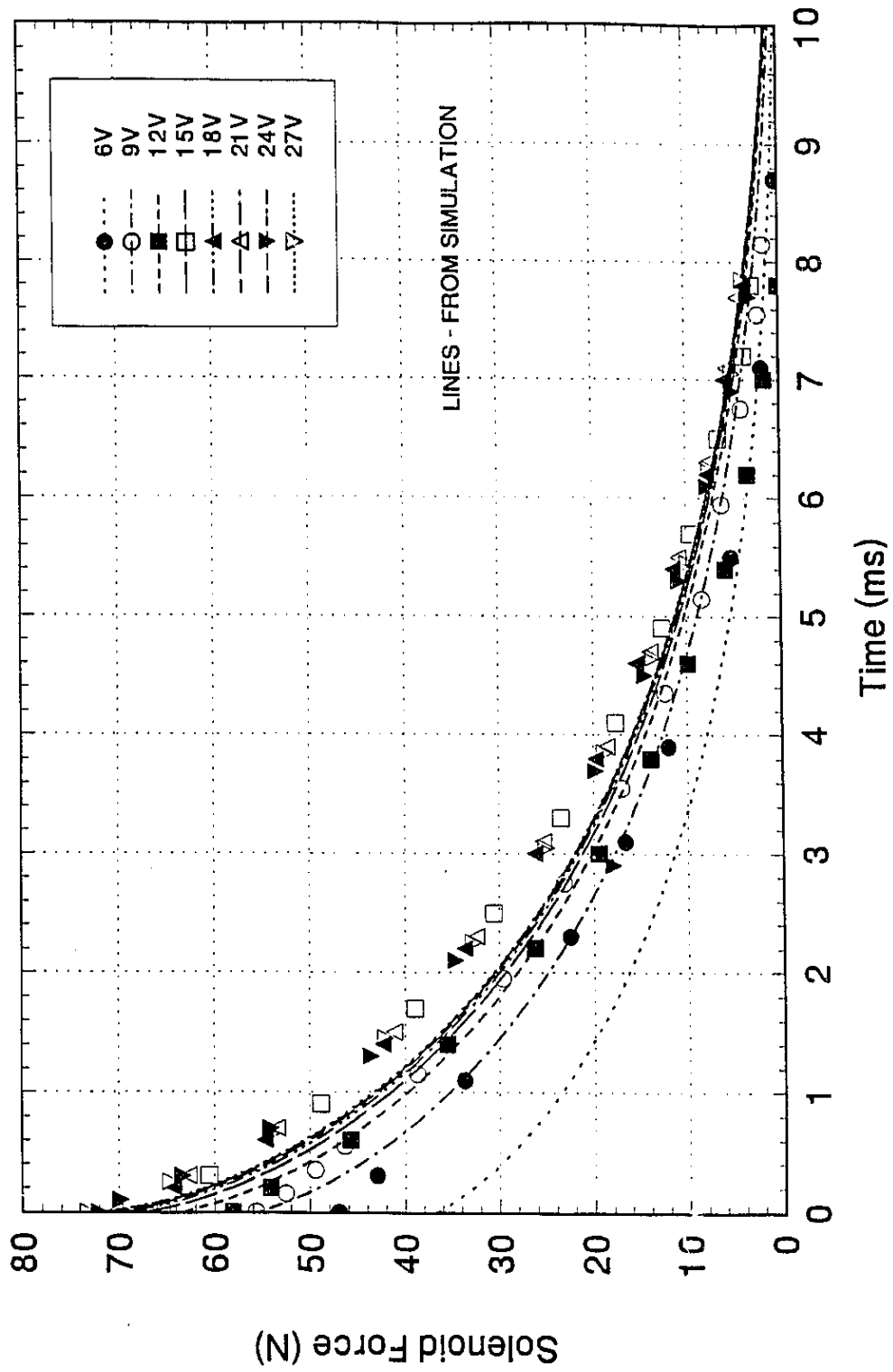


Fig. 4.12b Decay of solenoid force, air-gap 0.242 mm

perceivable from the test results, although from theory it is expected that the inductance decreases for an increase in the air-gap.

The corresponding transient force measurements for the 0.635 mm air-gap are shown in Figure 4.4a. The shape of the force rise for an increase in applied voltage are similar to that of the current time responses. This is expected since the solenoid force of attraction is generated from the coil current. The major difference observed between the current and force responses is at steady-state values. The current steady-state values are separated successively by the incremental voltage difference of 3 V divided by the internal resistance of the coil ( $1.7 \Omega$ ) plus resistance of the solid state relay ( $0.4 \Omega$ ). The steady-state force measurements are not consistently separated, but tend to approach a maximum force. This trend in force is seen in all five sets of air-gap positions (Figures 4.4a, 4.6a, 4.8a, 4.10a, 4.12a), and is attributed to the force saturation. Steady-state solenoid force saturation as a function of coil current is summarized in Figure 4.13. Moreover, the figure shows that larger solenoid forces can be attained when the air-gap is reduced.

Since the solenoid force is generated from the coil current, force saturation suggests that there is a maximum effective current to produce a maximum force. Any current above this maximum is not effective since no larger force can be generated. This indicates that there should be a limit to the voltage applied across the solenoid coil to produce this maximum coil current. These statements are true if only steady-state forces are considered. With reference to any relationship of force rise, such approach to force

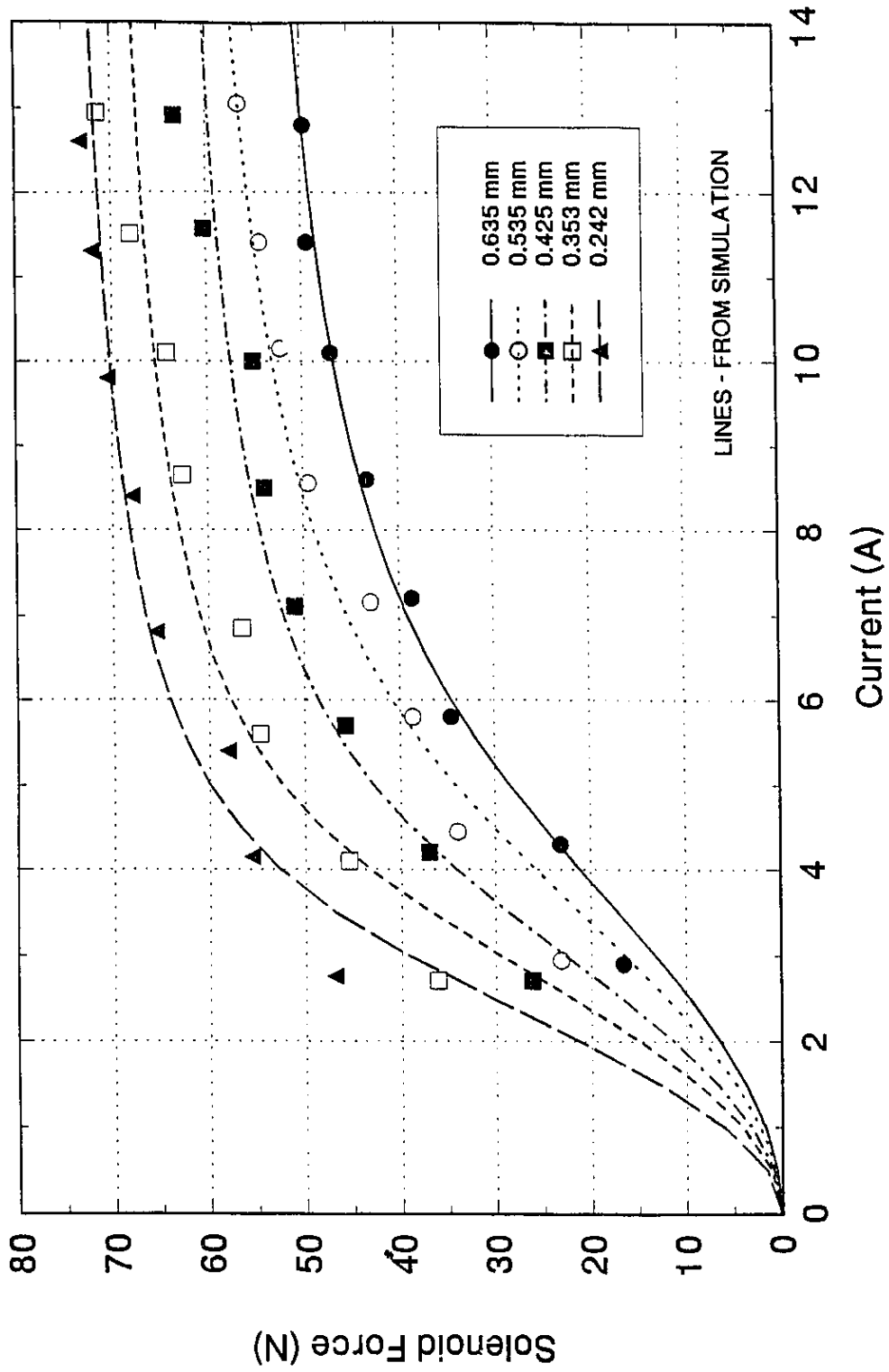


Fig. 4.13 Steady-state solenoid force as a function of coil current

saturation is obvious. However, as the applied voltage is increased, the rate of the force increase is augmented. This indicates that a high applied voltage across the coil is constructive to produce a large solenoid force 'rapidly'. Thus, the applied voltage across the solenoid coil should not be limited regarding the current saturation and a high voltage is desirable to generate a rapid force increase at the beginning of the injector opening when it is particularly needed.

Figure 4.14 shows the effect of air-gap on the transient forces for an applied voltage set at 24 V. A faster force increase occurs for smaller air-gaps, although the inductance is larger. This is because a larger magnetic flux is being generated at smaller air-gaps for the same voltage.

Figure 4.3b shows the experimental data for current decay at an air-gap of 0.635 mm. It can be observed that the current decay starting from a higher steady-state current, has a shorter response time. This similarity is seen in all the figures of current decay for the air-gaps at all fixed positions (4.3b, 4.5b, 4.7b, 4.9b, 4.11b). In addition, when the graphs showing the current decay curves are compared, as the air-gap progressively gets smaller, the beginning of the current decay is earlier for smaller air-gaps. These observations are attributed to the variable inductance that is becoming smaller at larger flux magnitudes. Therefore, more flux is attained at smaller air-gaps at a given current, and also more flux occurs at higher current values.

Since the solenoid force is also dependent on the magnetic flux, the force decay at a fixed air-gap position has a shorter response time when higher steady-state current

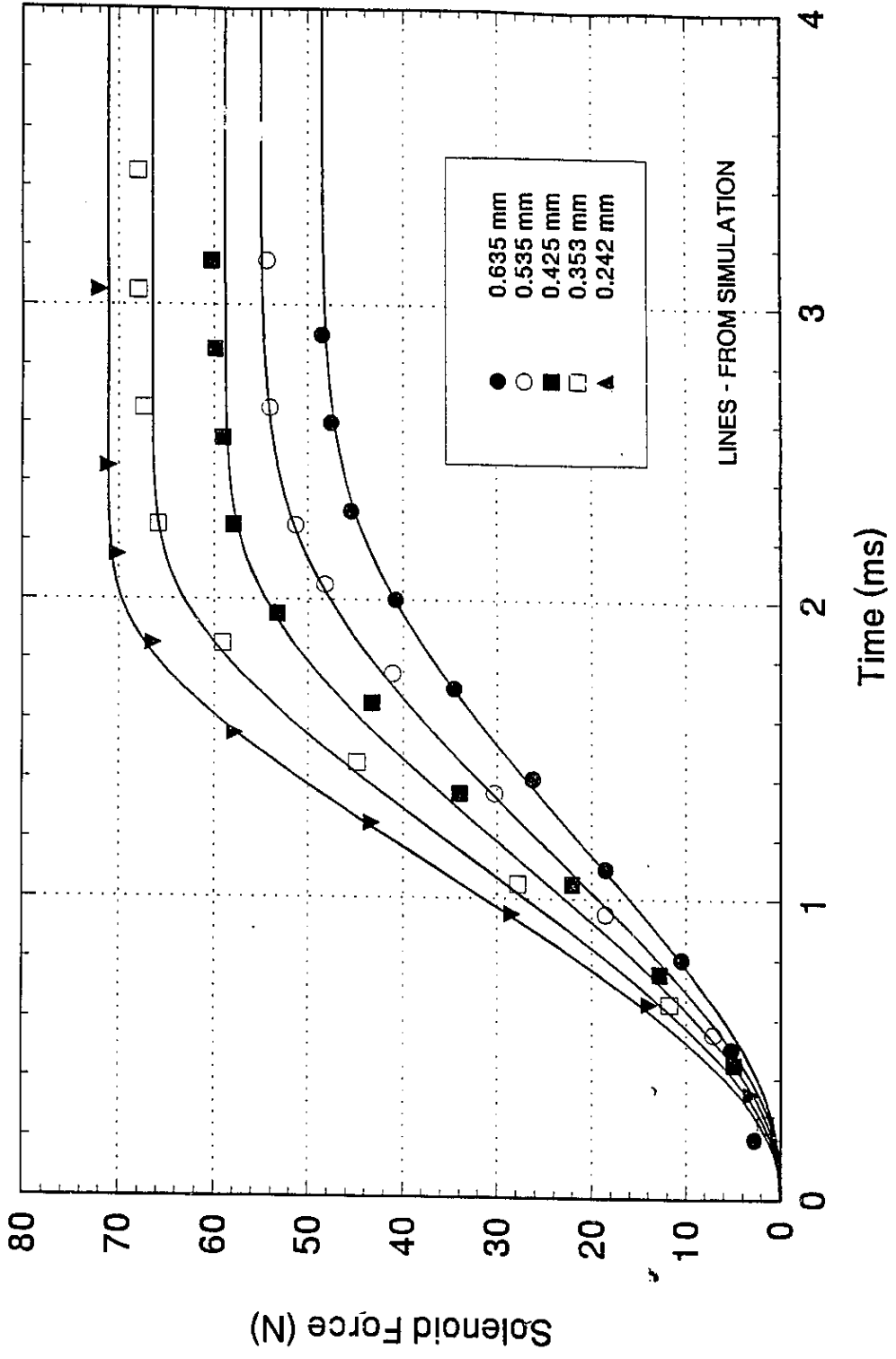


Fig. 4.14 Transient force response at various air-gaps for 24 V input

values are attained. This phenomenon is seen in all the figures of the force decay (4.4b, 4.6b, 4.8b, 4.10b, 4.12b). A comparison of forces obtained with the air-gap being decreased, indicates that it takes more time for the force to decay for smaller air-gaps, although all the initial currents started at the same value. This is because of the fact that larger steady-state forces are obtained for the same current if the air-gap is reduced, and the force starts to decay from an initially higher value which takes more time to reach the zero value.

The experimental data are re-plotted in Figures 4.15 to 4.19 to show the force versus current for the five air-gap positions. With reference to Figure 4.15, for an air-gap of 0.635 mm, the transient force as a function of transient current forms a hysteresis loop around the steady-state force versus current curve, which is shown as the solid line. The transient current and the resulting transient force increase is towards the right of the steady-state curve due to the voltage application. Towards the left of the steady-state curve, the variables are decreasing due to the removal of the applied voltage.

As the applied voltage is being increased, the hysteresis loop gets larger. The transient curves shift towards the right which is an indication of a faster force and current response. Also, the steady-state force increases as the steady-state current increases. However, the final force asymptotically approaches the saturation value. When the applied voltage is being removed, both, the steady-state current and the force decay. Independently of the initial steady-state force, all force decays eventually converge



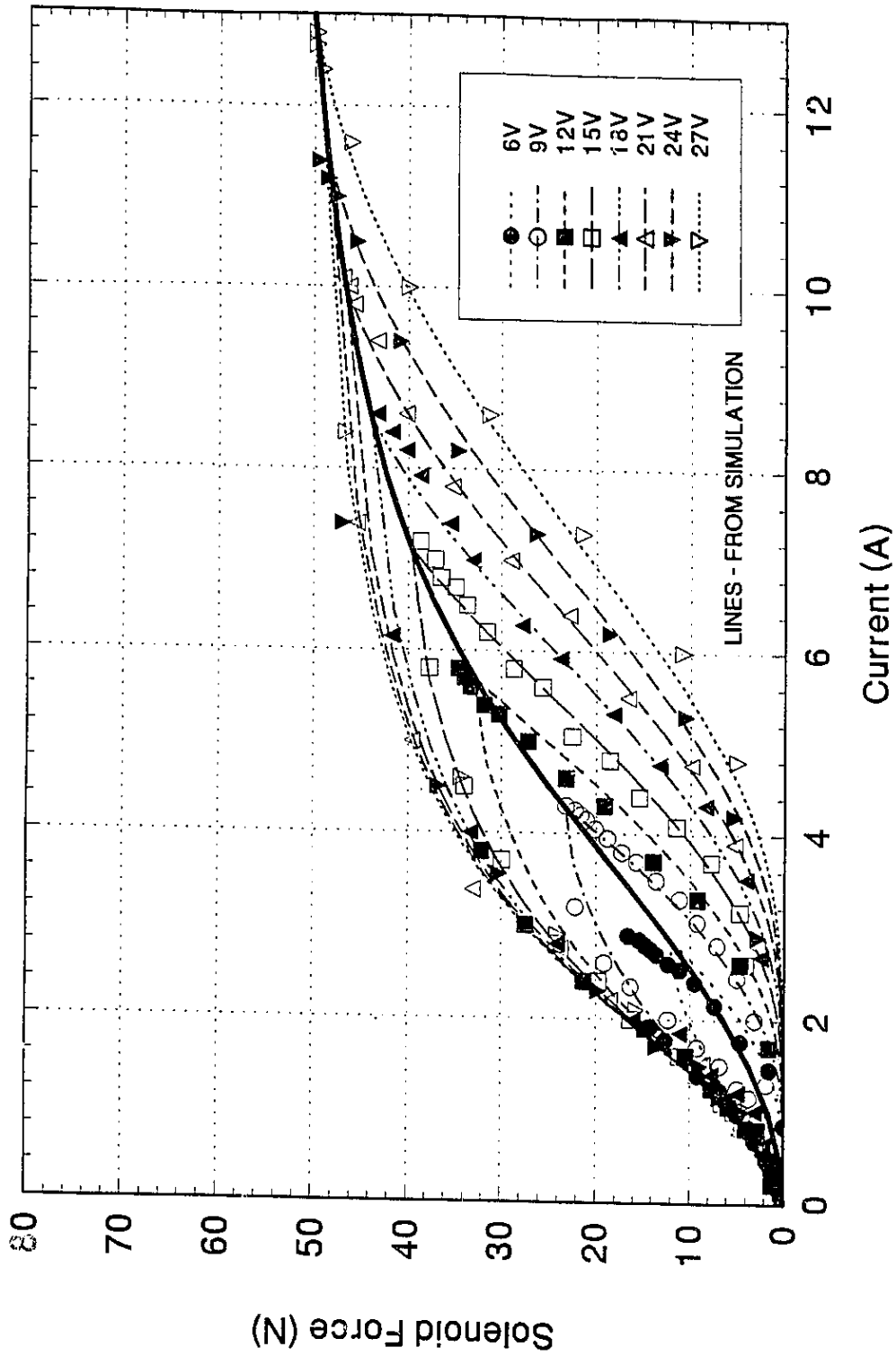


Fig. 4.15 Solenoid force hysteresis loop for air-gap 0.635 mm

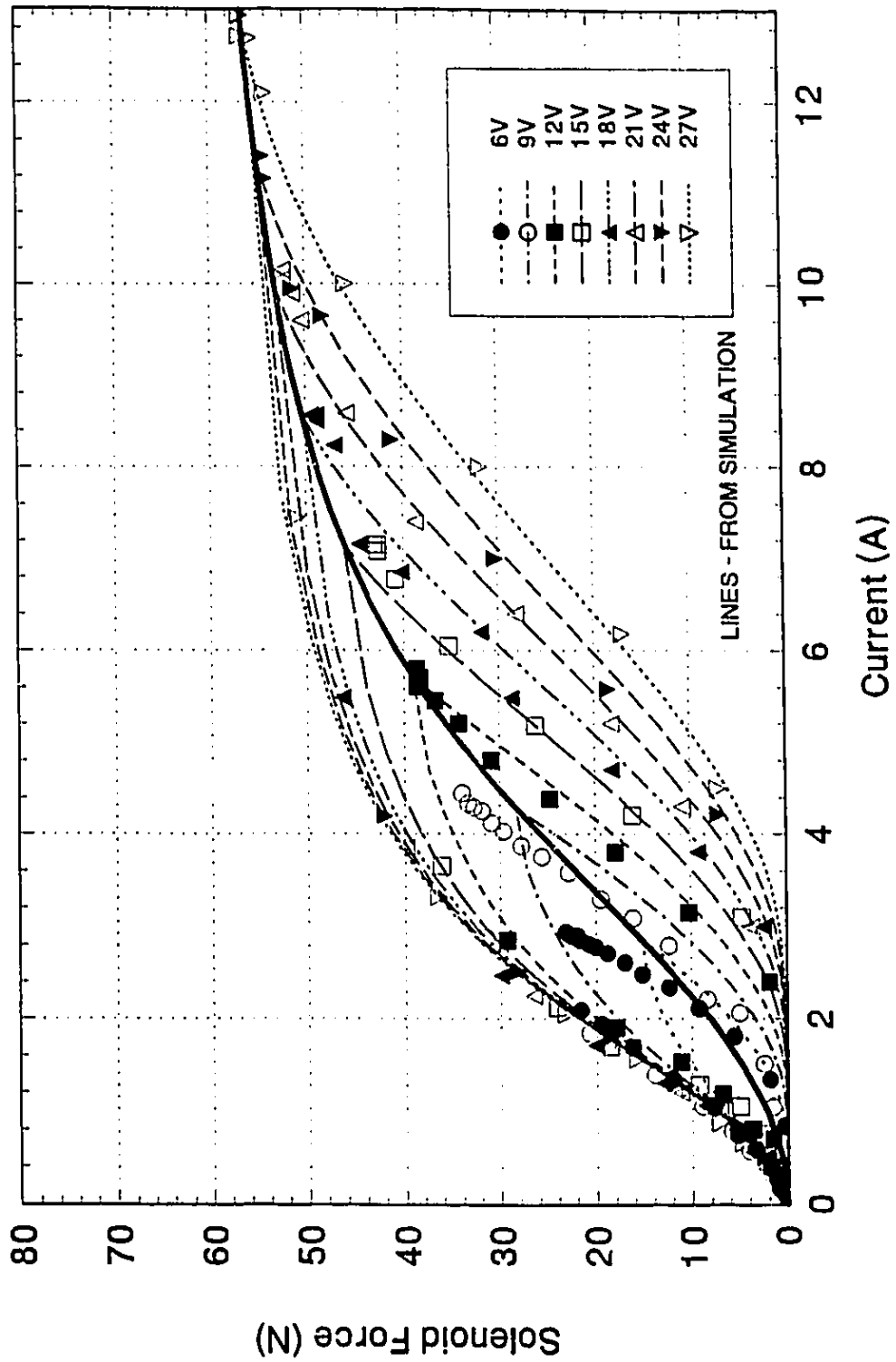


Fig. 4.16 solenoid force hysteresis loop for air-gap 0.535 mm

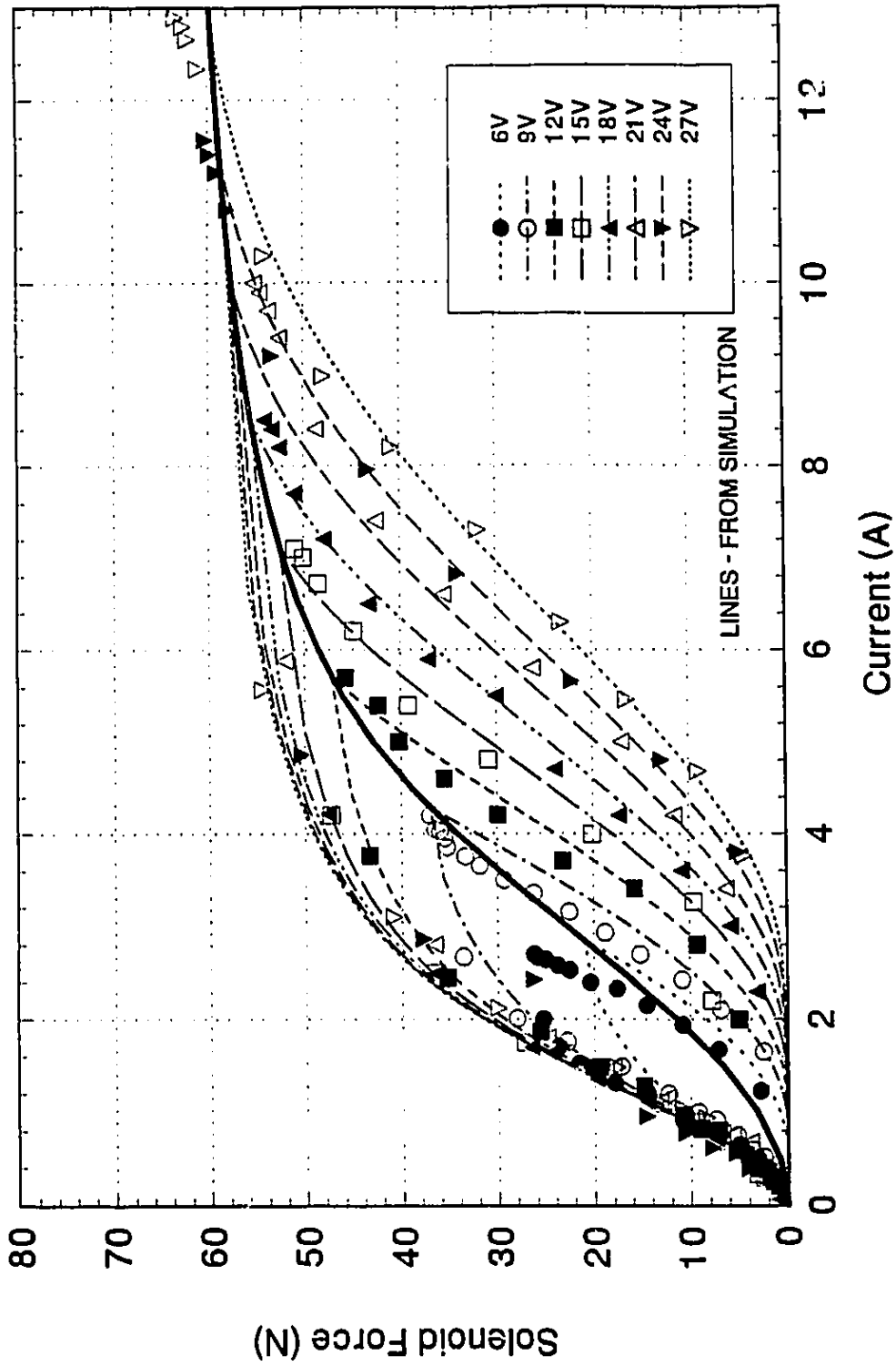


Fig. 4.17 Solenoid force hysteresis loop for air-gap 0.425 mm

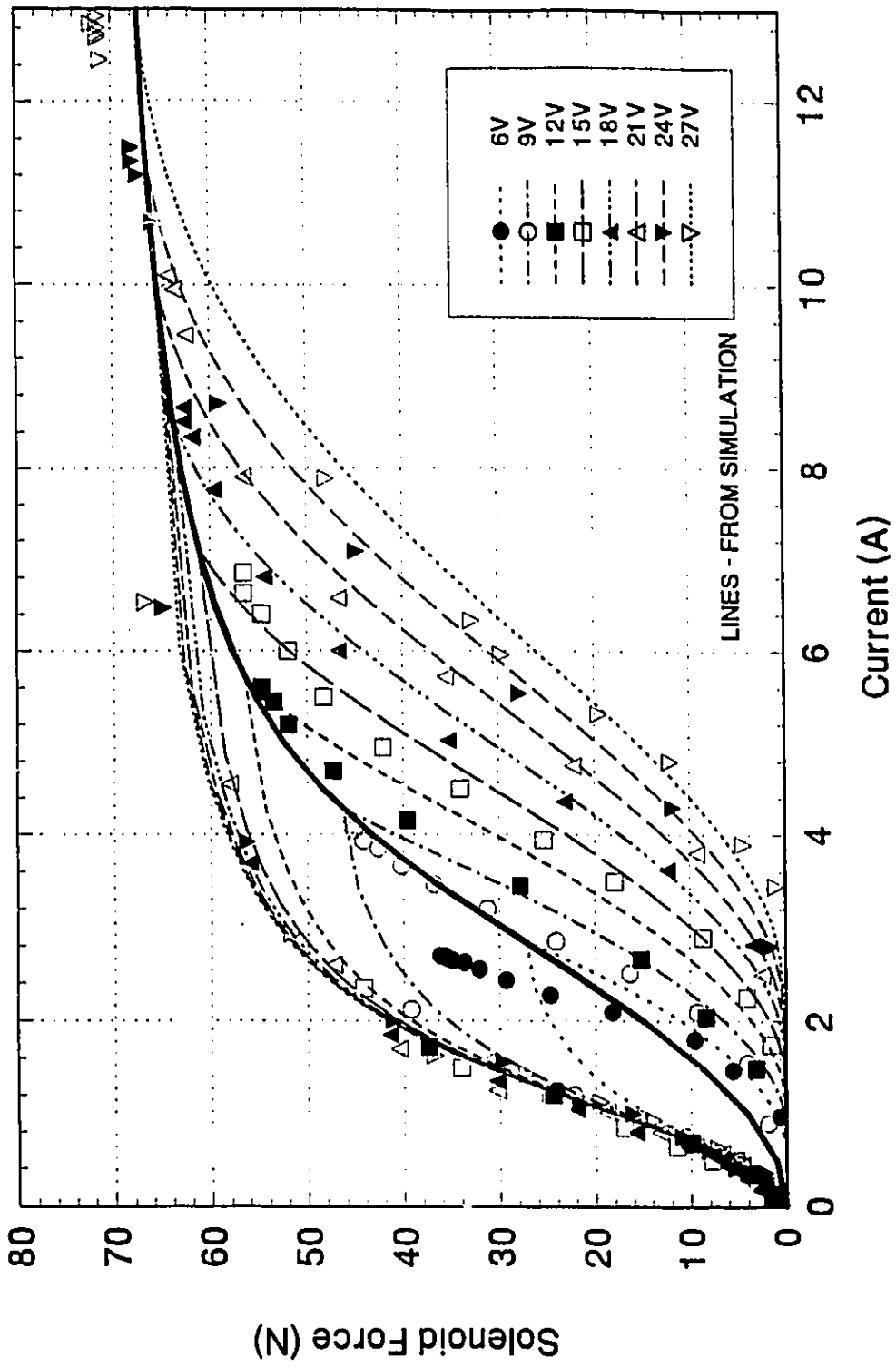


Fig. 4.18 Solenoid force hysteresis loop for air-gap 0.353 mm

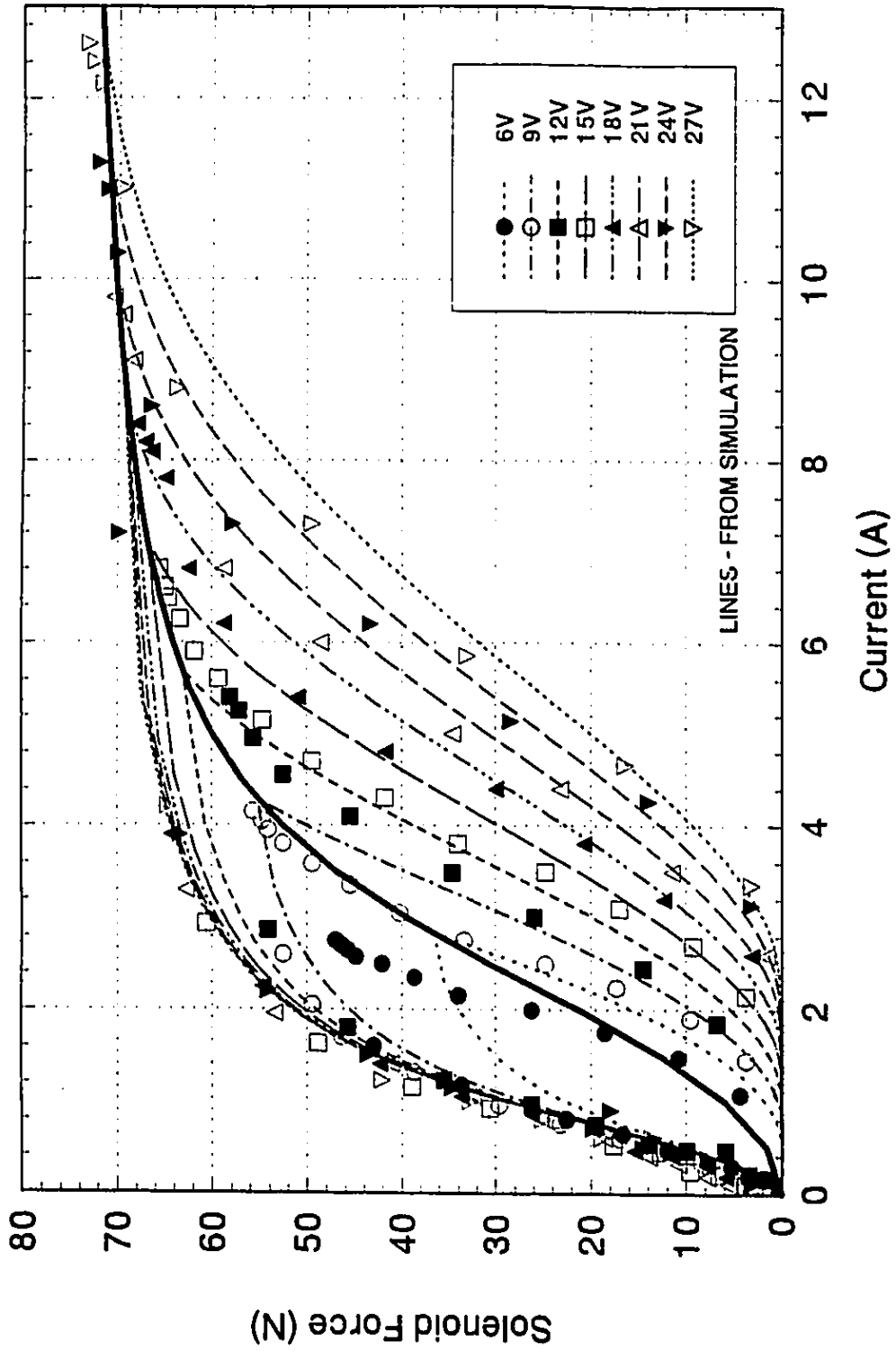


Fig. 4.19 Solenoid force hysteresis loop for air-gap 0.242 mm

asymptotically towards a common limit line. Similar characteristics are observed for all the force hysteresis loops at fixed air-gap positions as shown in Figures 4.16 to 4.19.

#### 4.4 Derivation of Solenoid Coil Nonlinear Inductance, Velocity Induced Voltage, and Solenoid Electromagnetic Force

Figure 4.20 is an illustration of the magnetic circuit for the cylindrical solenoid. Positive force and displacement of the solenoid core are in the direction away from the magnetic pole. The path of the magnetic flux passes through the coil windings, the solenoid movable core and casing, and through two air-gaps. The reluctance at the pole end with variable air-gap  $h$  and the reluctance at the boss end with fixed air-gap  $y$ , is given by:

$$\mathfrak{R}_1 = \frac{h}{\mu_0 A_1} + \frac{y}{\mu_0 A_2} \quad (4.1)$$

where  $\mu_0$  is the permeability of the free space.  $A_1$  and  $A_2$  are respectively the pole end and the boss end effective areas that are normal to the magnetic flux path.

Although, the material of the core is known to be 1215 carbon steel, the reluctance of the core is expressed by a simple model in order to ease the mathematical manipulation and to circumvent the necessity to correct its value due to any unknown contributions. The equation representing the reluctance of the core and casing material is dependent on the magnitude of the magnetic flux  $\phi$  and on the length of the core that the flux traverses through; it accounts for flux saturation by the material properties. The

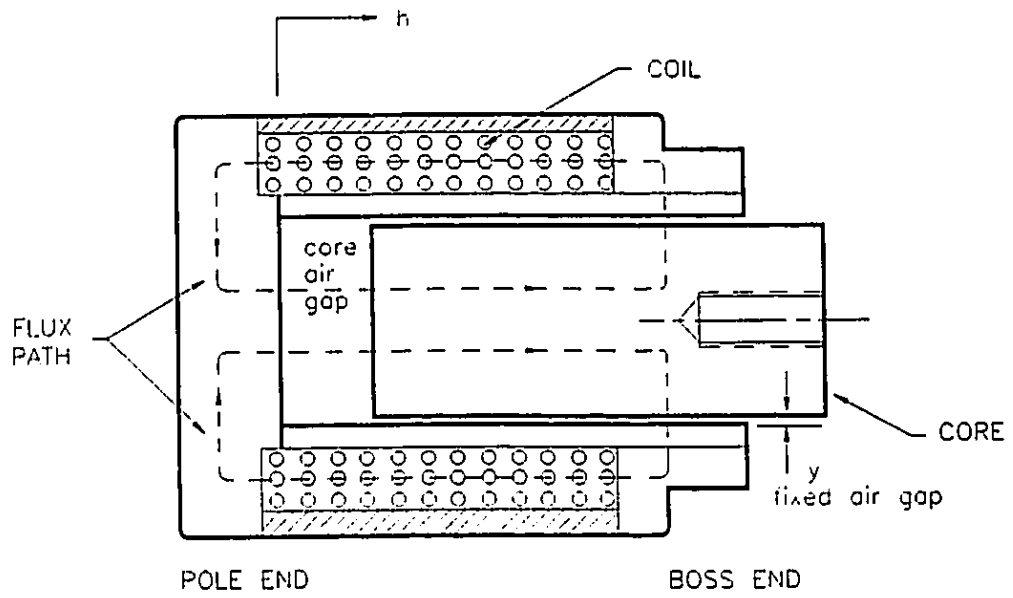


Fig. 4.20 Magnetic circuit for solenoid

mathematical model, where the material parameters  $a_1$  and  $a_2$  are to be determined from an experiment, is expressed by:

$$\mathfrak{R}_2 = \frac{a_1}{a_2 - \phi} \quad (4.2)$$

The material reluctance, as described by Equation (4.2) is derived from Froelich's [42] equation which is a mathematical approximation to the magnetization curve relating the magnetic flux density  $B$  to the field intensity  $H$ ; it is expressed as:

$$B = \frac{c_1 \cdot H}{c_2 + H} \quad (4.3)$$

Equation (4.3) embodies two asymptotes. For low field intensities  $H$  (or equivalently low current  $i$ ), the flux density  $B$  (or equivalently flux  $\phi$ ) is linearly related to the ratio  $c_1/c_2$  ( $c_1$  and  $c_2$  being material constants). For large  $H$ , the flux density  $B$  is saturated at a value that is proportional to the constant  $c_1$ . Between the two asymptotes the magnetization curve is exponential in shape. The parameters  $a_1$  and  $a_2$  in Equation (4.2) may be shown to be related to the constants  $c_2$  and  $c_1$ . Summarizing:

$$\begin{aligned} H \rightarrow 0 & \quad B \rightarrow \frac{c_1}{c_2} H \\ H \rightarrow \infty & \quad B \rightarrow c_1 \end{aligned}$$



From Equations (4.1) and (4.2), the current  $i$  through a simple coil as shown in Figure 4.2, is related to the magnetic flux as the sum of the reluctances in series, given by:

$$N \cdot i = \frac{h}{\mu_0 A_1} \cdot \phi + \frac{y}{\mu_0 A_2} \cdot \phi + \frac{a_1}{a_2 - \phi} \cdot \phi \quad (4.4)$$

where  $N$  is the total number of coil windings. The total derivative of Equation (4.4) with respect to  $h$  and  $\phi$ , after rearranging the terms, is:

$$d\phi = \frac{N}{\mathfrak{R}_1 + \frac{a_1 a_2}{(a_2 - \phi)^2}} \cdot di - \frac{\phi / (\mu_0 A_1)}{\mathfrak{R}_1 + \frac{a_1 a_2}{(a_2 - \phi)^2}} \cdot dh \quad (4.5)$$

The general form of Equation (4.5) for the flux, as a nonlinear function of the coil current  $i$  and the core air-gap  $h$ , is:

$$\phi = \phi(i, h) \quad (4.6)$$

and the total derivative of Equation (4.6) is:

$$d\phi = \left( \frac{\partial \phi}{\partial i} \right) \cdot di + \left( \frac{\partial \phi}{\partial h} \right) \cdot dh \quad (4.7)$$

A comparison of the coefficients from Equations (4.5) and (4.7) shows that the partial derivatives are:

$$\frac{\partial \phi}{\partial i} = \frac{N}{\mathfrak{R}_1 + \frac{a_1 a_2}{(a_2 - \phi)^2}} \quad (4.8)$$

and

$$\frac{\partial \phi}{\partial h} = \frac{-\phi / (\mu_0 A_1)}{\mathfrak{R}_1 + \frac{a_1 a_2}{(a_2 - \phi)^2}} \quad (4.9)$$

The induced voltage across the coil due to the changes from the magnetic flux, based on the Faraday's law and on the substitution from Equation (4.7), is:

$$V_\phi = N \cdot \frac{d\phi}{dt} = N \cdot \left( \frac{\partial \phi}{\partial i} \right) \cdot \frac{di}{dt} + N \cdot \left( \frac{\partial \phi}{\partial h} \right) \cdot \frac{dh}{dt} \quad (4.10)$$

The equation can be rewritten, after substitution of the partial derivatives from Equations (4.8) and (4.9), as:

$$V_\phi = L(\phi, h) \cdot \frac{di}{dt} - H_v(\phi, h) \cdot \frac{dh}{dt} \quad (4.11)$$

where the nonlinear inductance of the coil and the nonlinear velocity coefficient, as a function of flux magnitude and air-gap length, are respectively:

$$L(\phi, h) = \frac{N^2}{\mathfrak{R}_1 + \frac{a_1 a_2}{(a_2 - \phi)^2}} \quad (4.12)$$

$$H_v(\phi, h) = \frac{L(\phi, h) \cdot \phi}{\mu_0 A_1 N} \quad (4.13)$$

The second term on the right side of Equation (4.11) is the velocity induced voltage which is dependent on the magnitude of the core velocity. When the core is moving

towards the magnetic pole, the velocity induced voltage is negative in magnitude. This indicates that the source is supplying the electrical energy for the conversion into mechanical energy. When the core moves away from the magnetic pole, the velocity induced component is positive, indicating that the mechanical energy is converted to the electrical energy and is returned to the source.

Equation (4.12) indicates that the coil inductance increases as the air-gap is reduced, or as the magnetic flux is reduced. Equation (4.13) shows that the velocity coefficient increases with the coil inductance that results from a reduction in the air-gap. The coefficient also increases with an increase in flux, and then it would decrease as the flux approaches saturation due to the fact that the inductance reduces at a faster rate.

The electromagnetic force of the core attraction created by the solenoid is determined from the stored magnetic energy [43]  $W(\phi, h)_{mag}$ :

$$F_s = - \frac{\partial W(\phi, h)_{mag}}{\partial h} = - \frac{\partial}{\partial h} \left( \int_0^\phi N i \cdot d\psi \right) = - \frac{\phi^2}{2 A_1 \mu_0} \quad (4.14)$$

where the integrand is given by Equation (4.4) and  $\psi$  is a dummy variable for integration. The negative sign indicates that the force is directed towards the magnetic pole, and it tends to reduce the air gap reluctance.

#### 4.5 Mathematical Model of Solenoid Transient Characteristics

The equivalent circuit for the solenoid coil is shown in Figure 4.21. The variable resistor  $R_c$  across the coil inductance accounts for eddy current losses in the core, which are ohmic in nature. By considering eddy current losses, hysteresis is introduced into the magnetization curve of the solenoid model. The leakage inductance  $L_l$  in series with the coil accounts for flux leakages, which tends to increase the overall system inductance. The series resistor  $R_l$  represents the internal resistance of the coil. The number of  $N$  coil windings is applied in order to obtain the resistance  $R_l$  for rated power. The current supplied from the source is termed the "exciting current"  $i_e$ , while the current through the coil that produces the magnetic flux, as given by Equation (4.4) is termed the "magnetizing current"  $i_m$ . The difference,  $i_e - i_m$ , is the core-loss component of current.

With reference to Figures 4.2 and 4.21, the governing equations for the solenoid model are written as follows. The voltage across the solenoid coil is:

$$V_\phi - V_c = (i_e - i_m) \cdot R_c \quad (4.15)$$

where the voltage  $V_c$  at node- $B$  is at zero potential. The exciting current from the voltage source through the flux leakage inductance is:

$$i_e = \frac{1}{L_l} \int (V_s - i_e \cdot R_l - V_\phi) dt \quad (4.16)$$

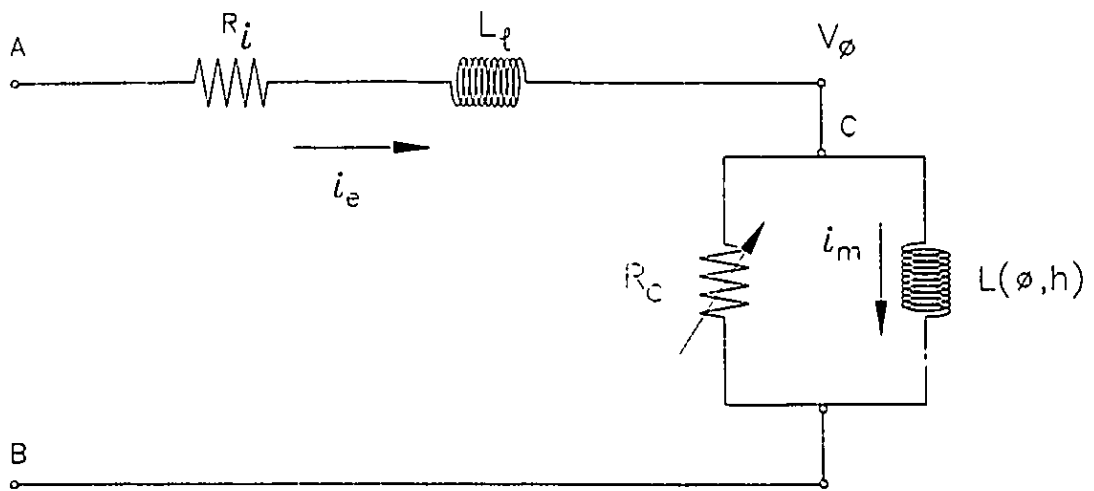


Fig. 4.21 Equivalent circuit for solenoid

The magnetizing current through the coil, including the effects of core velocity, is:

$$i_m = \frac{1}{L(\phi, h)} \int (V_\phi - V_c + H_v(\phi, h) \cdot \frac{dh}{dt}) dt \quad (4.17)$$

#### 4.6 Parameter Estimation and Simulation Results

The internal resistance  $R_i$  of the solenoid coil has been measured and was found to be  $1.7 \Omega$ , with the number of coil windings  $N$  counted as 230 turns by cutting open the solenoid. The pole end and boss end effective areas,  $A_1$  and  $A_2$ , obtained from measurements of the solenoid geometry, are estimated to be  $4.9265 \times 10^{-5} \text{ m}^2$  and  $10.733 \times 10^{-5} \text{ m}^2$ , respectively. The length of the fixed air-gap  $y$  is measured to be 0.5 mm.

The material parameters,  $a_1$  and  $a_2$  from Equation (4.2), are dependent on the length of the variable air-gap  $h$  and are estimated from the force and current measurements. Figure 4.22 shows the magnetization curve of flux versus current for the 0.635 mm core air-gap. Flux values are calculated from Equation (4.14) since the solenoid forces are known. The flux versus current at steady-state conditions after voltage application, is plotted as the eight square points. The first two terms on the right side of Equation (4.4), representing the effects of the pole and boss end air-gaps and their combined effects, are shown as straight line permeance (reciprocal of reluctance). To isolate the effect due only to the material reluctance at these eight measurements, the

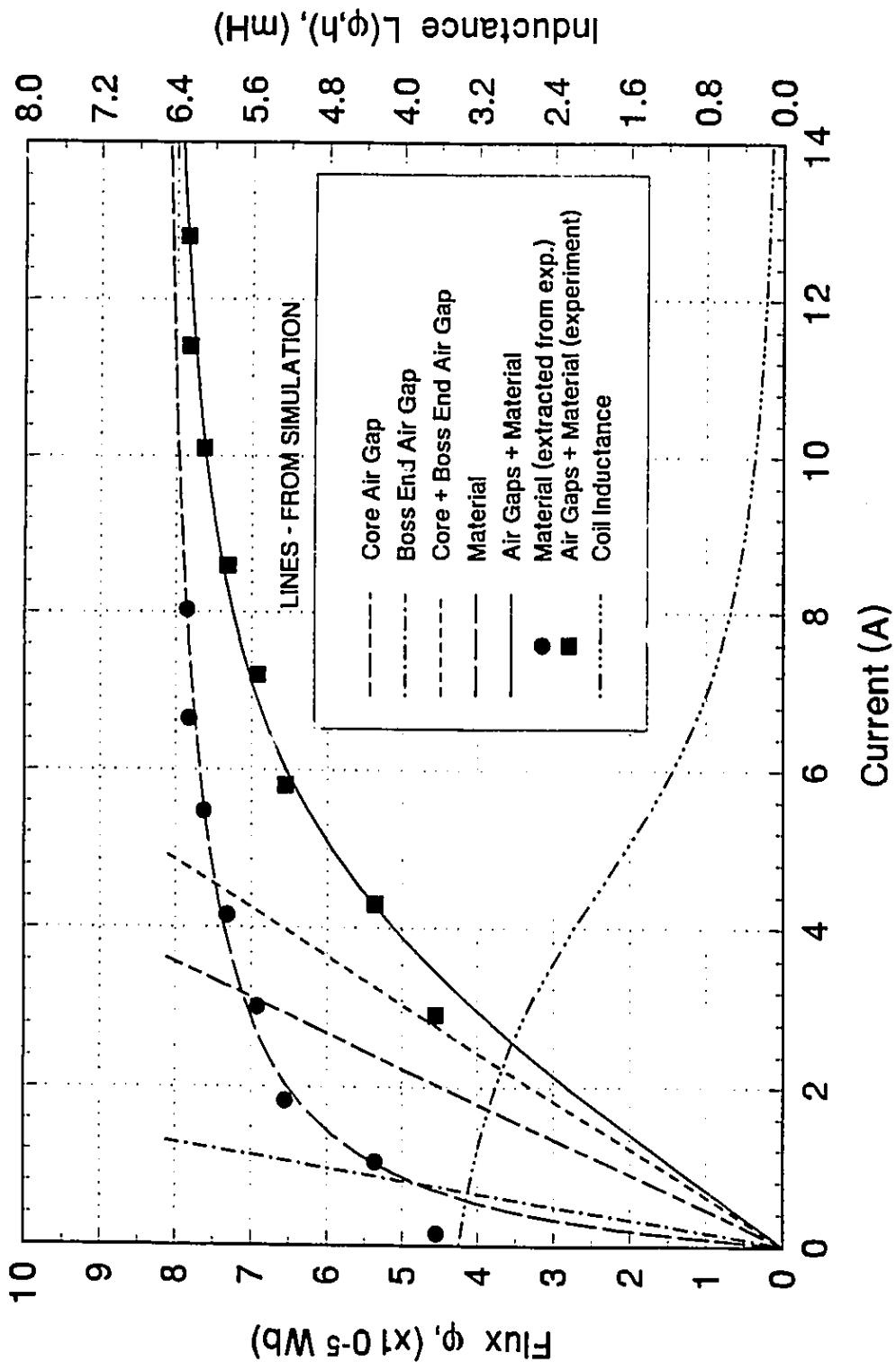


Fig. 4.22 Steady-state magnetization curve for air-gap 0.635 mm

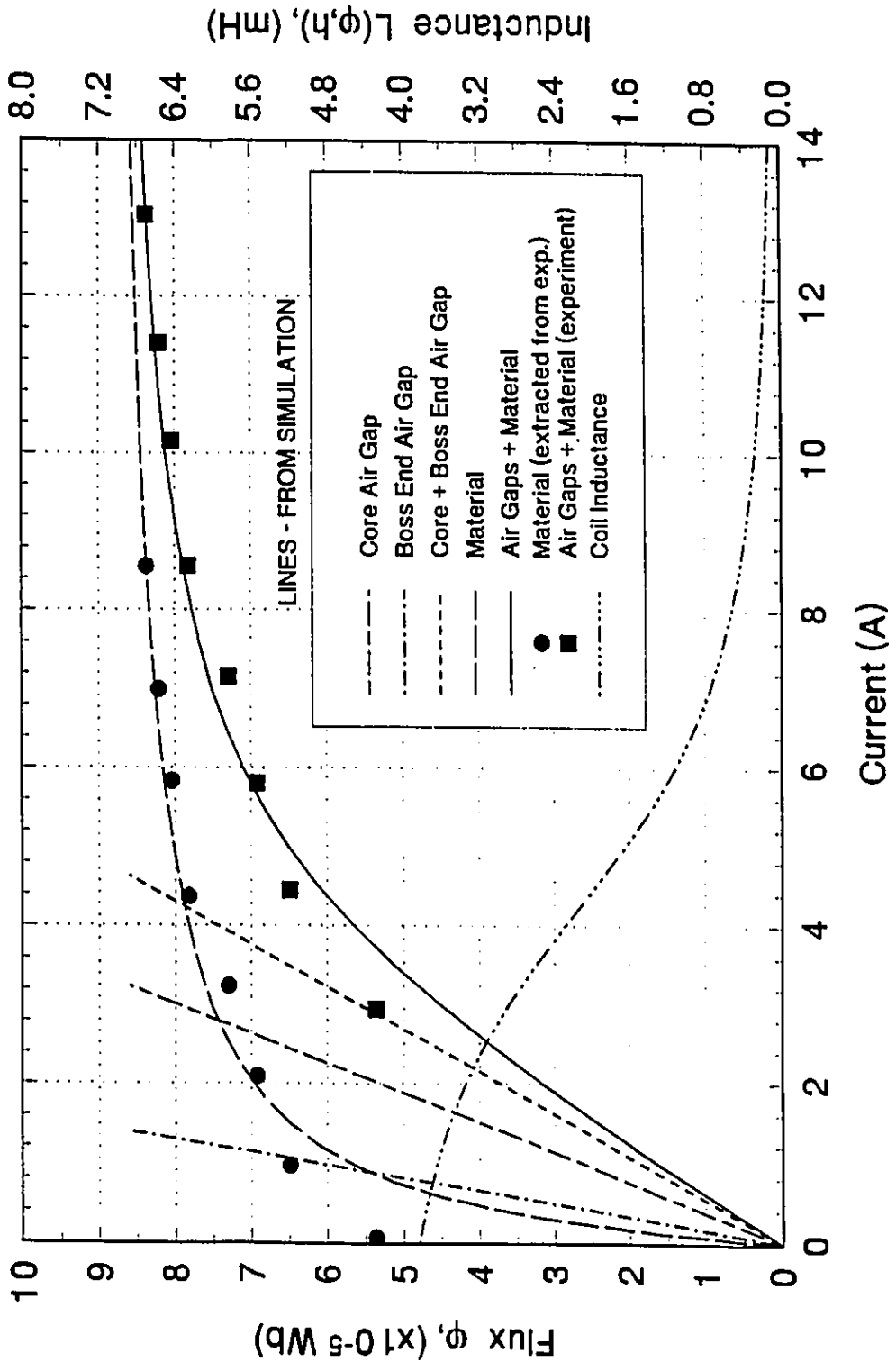


Fig. 4.23 Steady-state magnetization curve for air-gap 0.535 mm



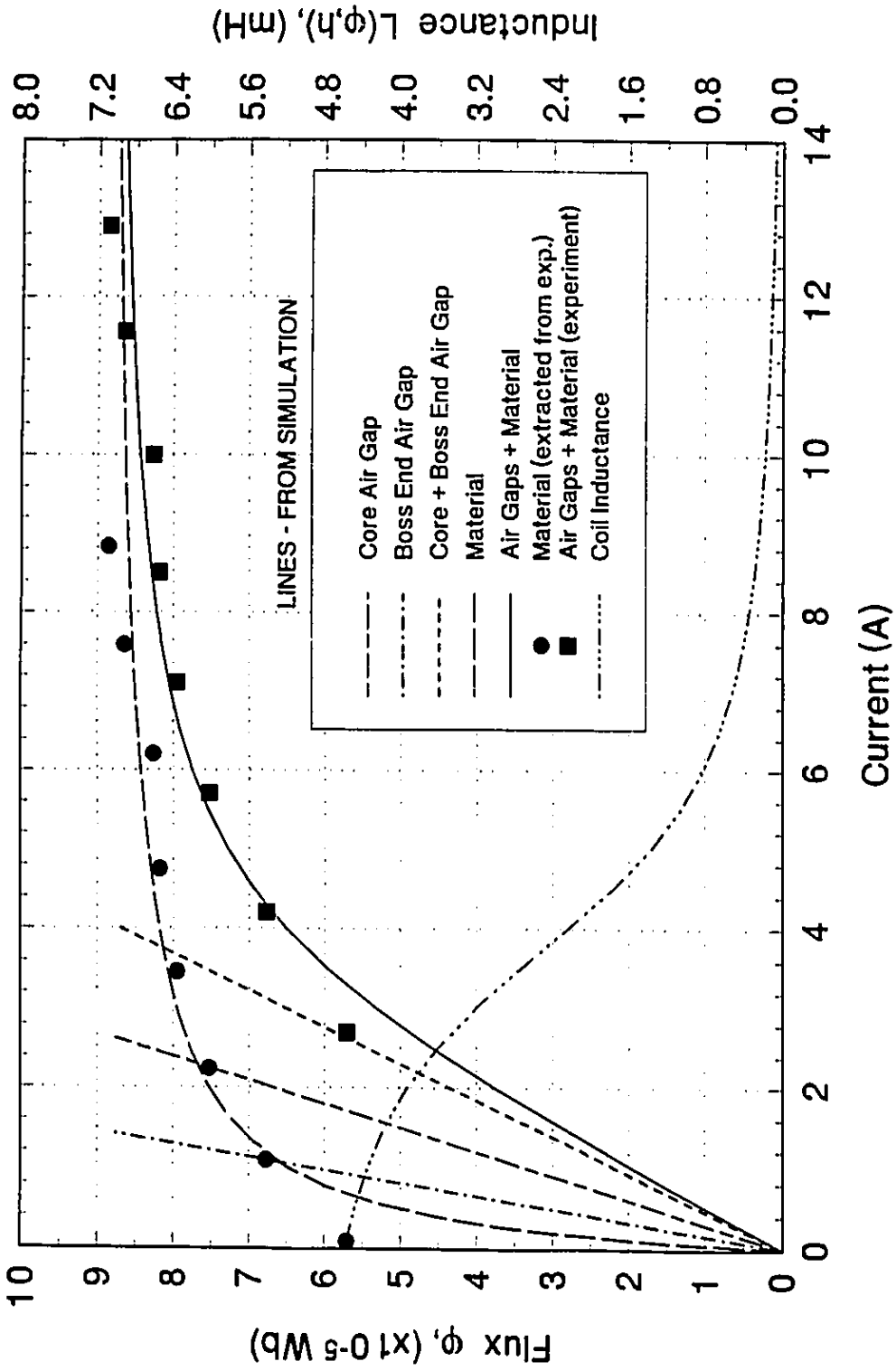


Fig. 4.24 Steady-state magnetization curve for air-gap 0.425 mm

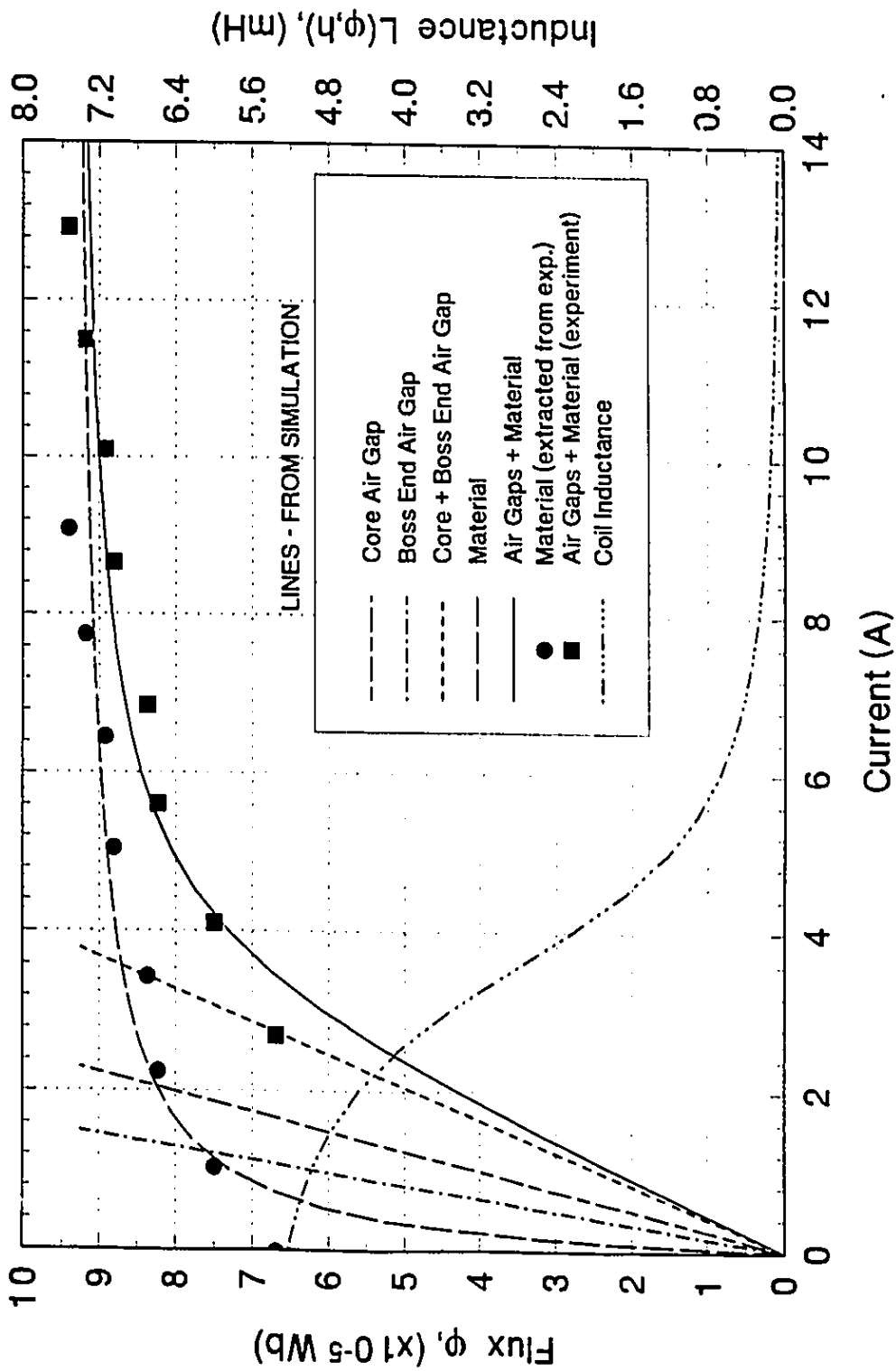


Fig. 4.25 Steady-state magnetization curve for air-gap 0.353 mm

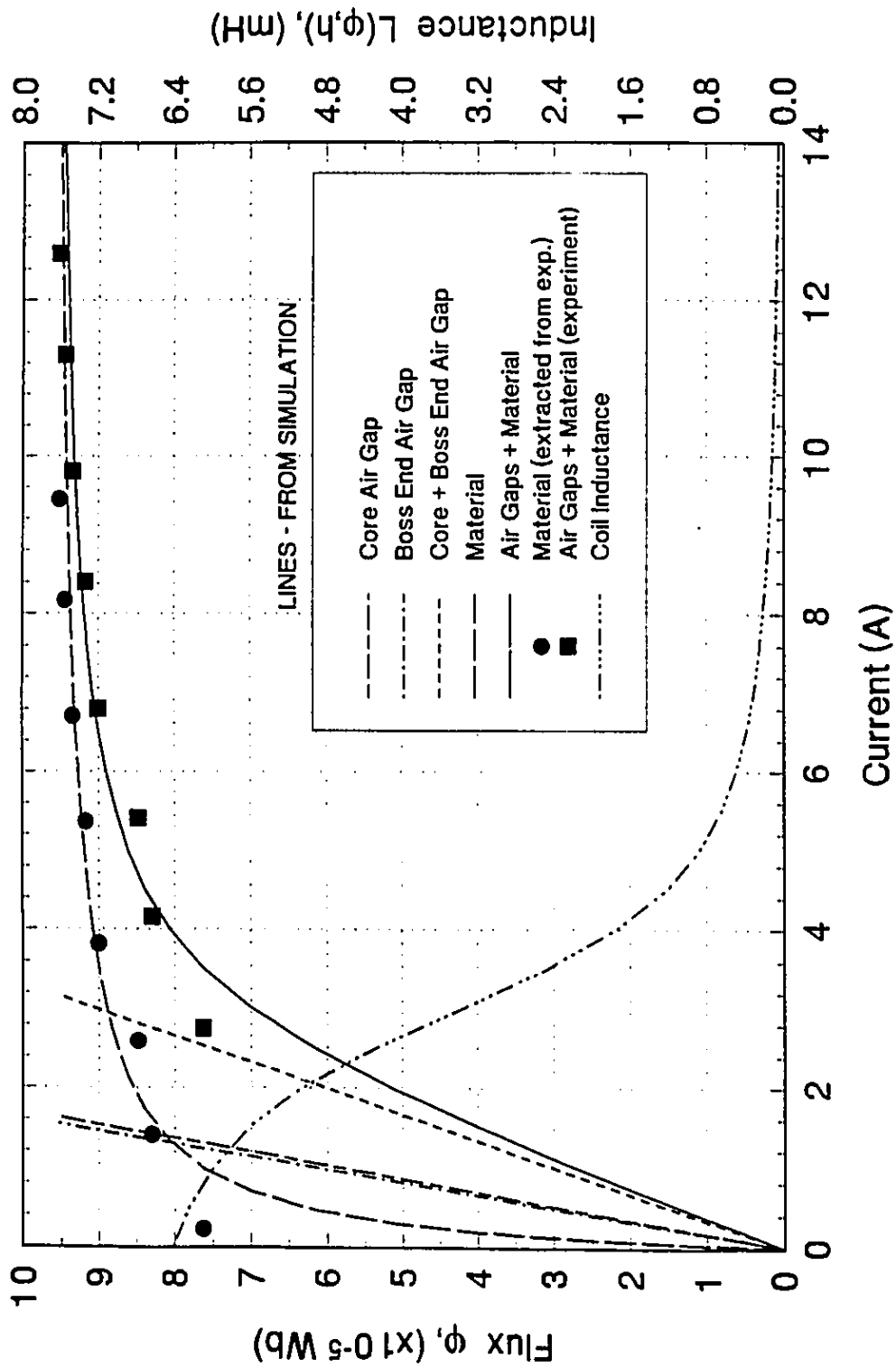


Fig. 4.26 Steady-state magnetization curve for air-gap 0.242 mm

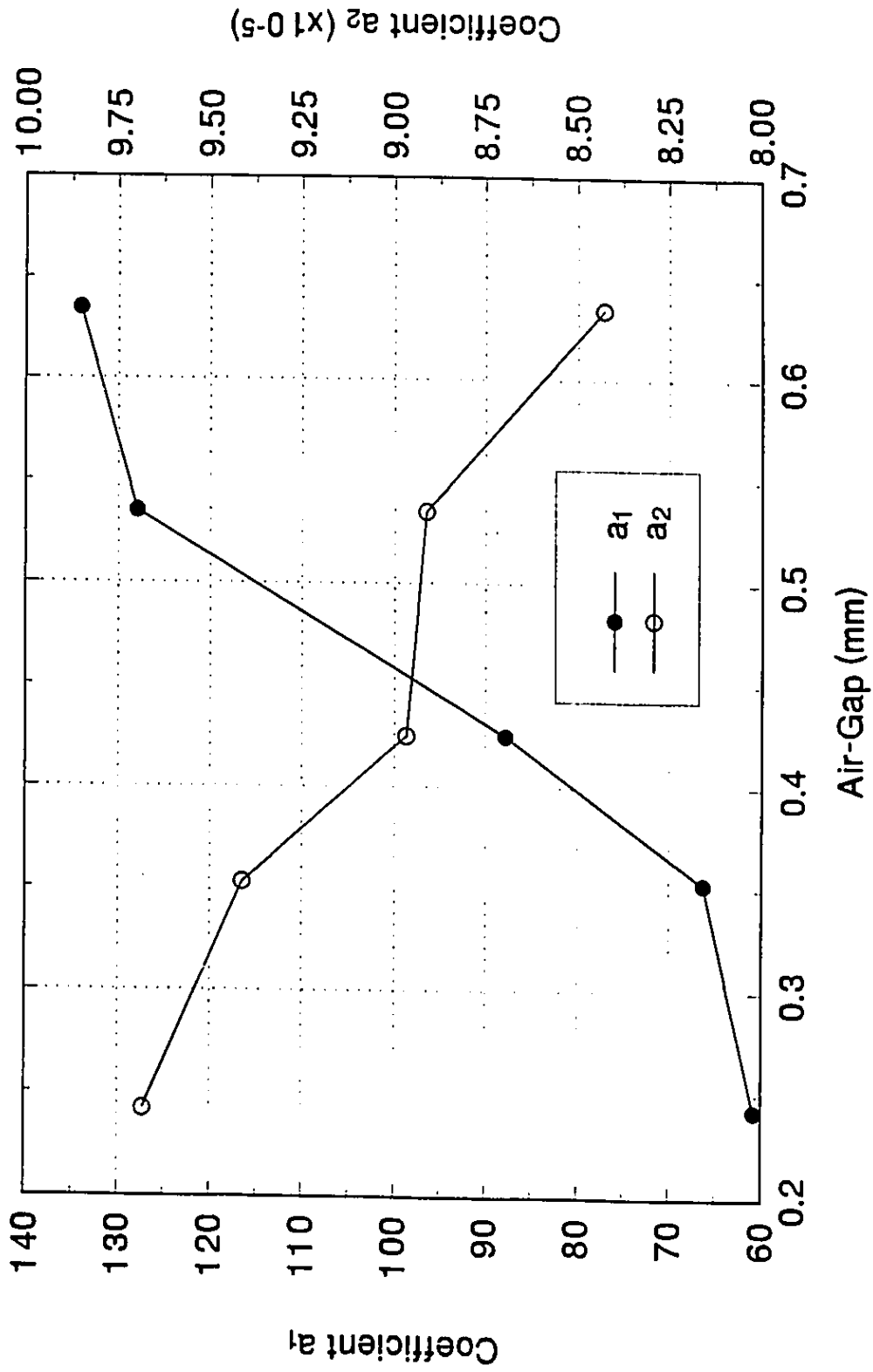


Fig. 4.27 Material parameters corresponding to Equation (4.2)

values contributing to the two air-gaps are calculated and are subtracted from the right side of the magnetomotive force ( $Ni$ ) values. The results divided by the number of coil turns  $N$  is the current contribution to produce the flux through the core material only. The eight flux points are then plotted against these current values, and are shown as circle-points on the figure.

With the current contribution and flux known for the core material, the parameters  $a_1$  and  $a_2$  which are constant for a particular fixed air-gap, can be determined from Equation (4.4). Using the values from the last seven measurements (refer to Figure 4.22), the curve fitted through these points determines the values of the two constants. A plot of the values representing the last term from Equation (4.4), using the constants now known, is shown in the figure as a curve passing through the circular points. This curve will be termed the "steady-state" magnetization curve for the core material. The effect of flux saturation as the current rises is clearly shown, and is limited by the constant  $a_2$ . As shown in the Figure 4.22, the first point deviates much from the curve and was not taken into consideration in the curve fitting process. This is because the Equation (4.2) is only a good approximation for the values above the bend of the magnetization curve. This does not diminish the merit of Equation (4.2) since the objective is to obtain a fast current rise.

The complete effect due to the two air-gap and material reluctance can now be evaluated from Equation (4.4) and is plotted as the curve passing through the original experimental (square) points. This curve will be termed the "steady-state" magnetization

curve for the solenoid. Flux saturation now occurs at higher current values because the air-gaps have the effect of shifting the magnetization curve of the core to the right.

At low flux values, the reluctance is essentially a combined reluctance of the two air-gaps. As the flux increases, the material reluctance dominates and approaches infinity. Also shown in the figure is the effect of the flux on the coil inductance of Equation (4.12). The inductance decreases with an increase in flux, which indicates faster current and force responses.

A similar procedure is applied to determine the material parameters for the other four sets of steady-state magnetization curves, that are shown in Figures 4.23 to 4.26. The material parameters are summarized in Figure 4.27 as a function of the air-gap. Parameters between the points evaluated from experiment can be interpolated. Parameters for the air-gap values from zero to minimum can be extrapolated.

The steady-state magnetization curves derived for the solenoid for the five sets of fixed air-gaps, are summarized in Figure 4.28. As the air-gap is reduced, higher steady-state magnetic flux values are attained at a given current. The flux saturates at a higher value but it takes less current to obtain the flux saturation. Also shown in the figure is a summarization of the inductances for changes occurring in the air-gap. At low flux values, the inductance is larger at smaller air-gaps. As the flux increases, the inductance decreases. When the flux has increased to such an extent that the saturation comes into effect, near the bend of the magnetization curve, the inductance at smaller air-gaps is becoming lower than that for larger air-gaps.

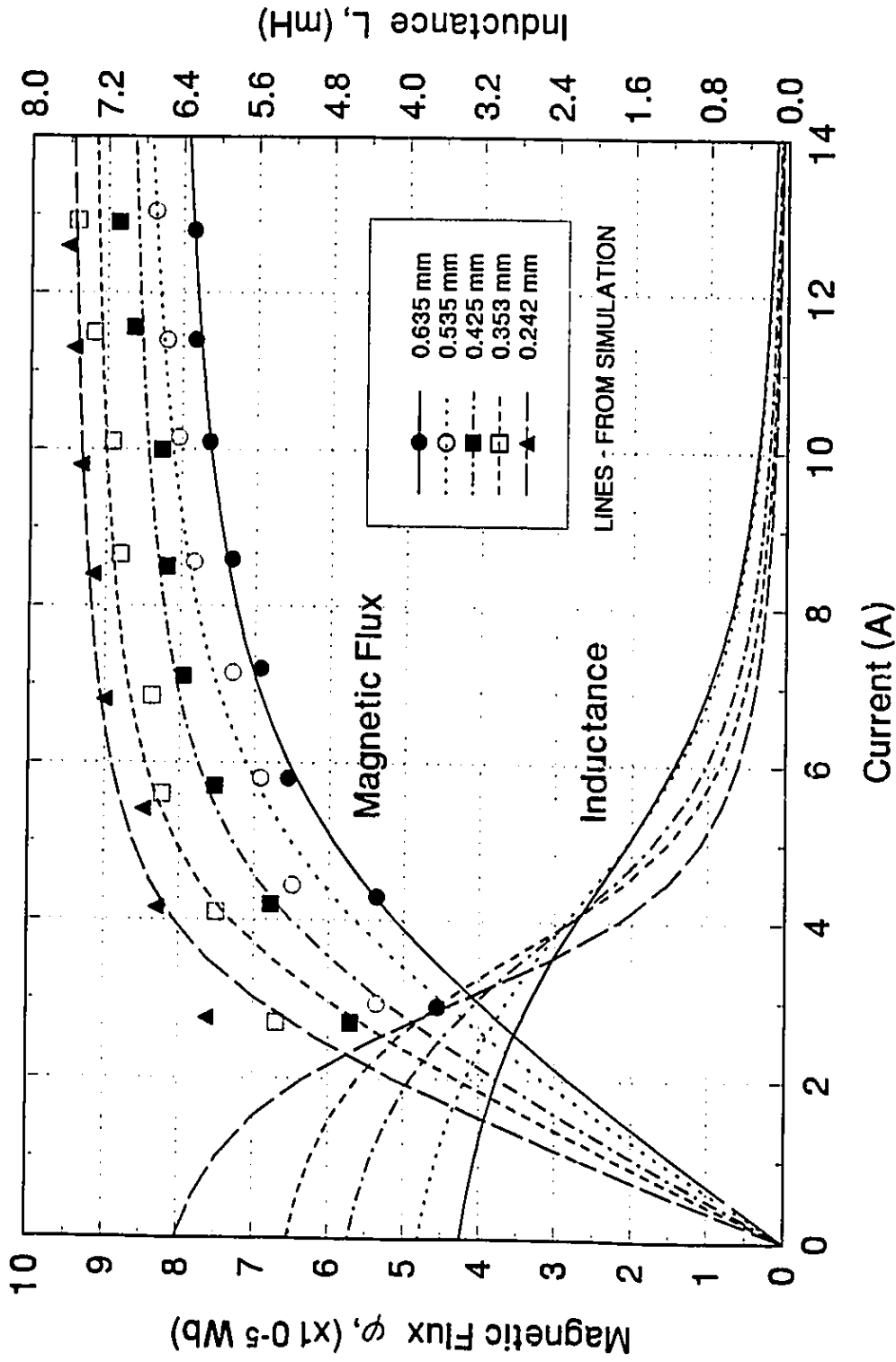


Fig. 4.28 Summary of solenoid steady-state magnetization curves and inductances for different air-gaps

The experimental data points from Figures 4.3 to 4.4 for the 0.635 mm air-gap are re-plotted in Figure 4.29 in the form of a magnetization curve. Similar re-plots are performed for the other four air-gap positions from their experimental data, as shown in Figures 4.30 to 4.33. The solid line is the steady-state magnetization curve for the solenoid. The transient points obtained from experiments form a hysteresis loop around the steady-state magnetization curve. To the right of the curve are the transient results after the source voltage is applied, while to the left of the curve are shown the results after the source voltage is removed. When the voltage is removed, the decay of all flux values converges to a reluctance asymptote. As well, the hysteresis loop grows larger as the applied voltage is increased.

The curves passing through the experimental data points are simulation results of the solenoid coil equivalent circuit model shown in Figure 4.21. When the source voltage is applied, the shape of the hysteresis loop depends on the resistor value  $R_r$  in Equation (4.14), and the curves can be shifted left or right depending on the value of the flux leakage inductance  $L_l$  in Equation (4.15). For the voltage removal, one constant resistance value is sufficient to create the model. In summary, the values for  $R_r$  and  $L_l$ , that are sufficient to model the solenoid eddy current and flux leakage losses in the equivalent circuit to produce the desired shape of the hysteresis loop, are respectively:



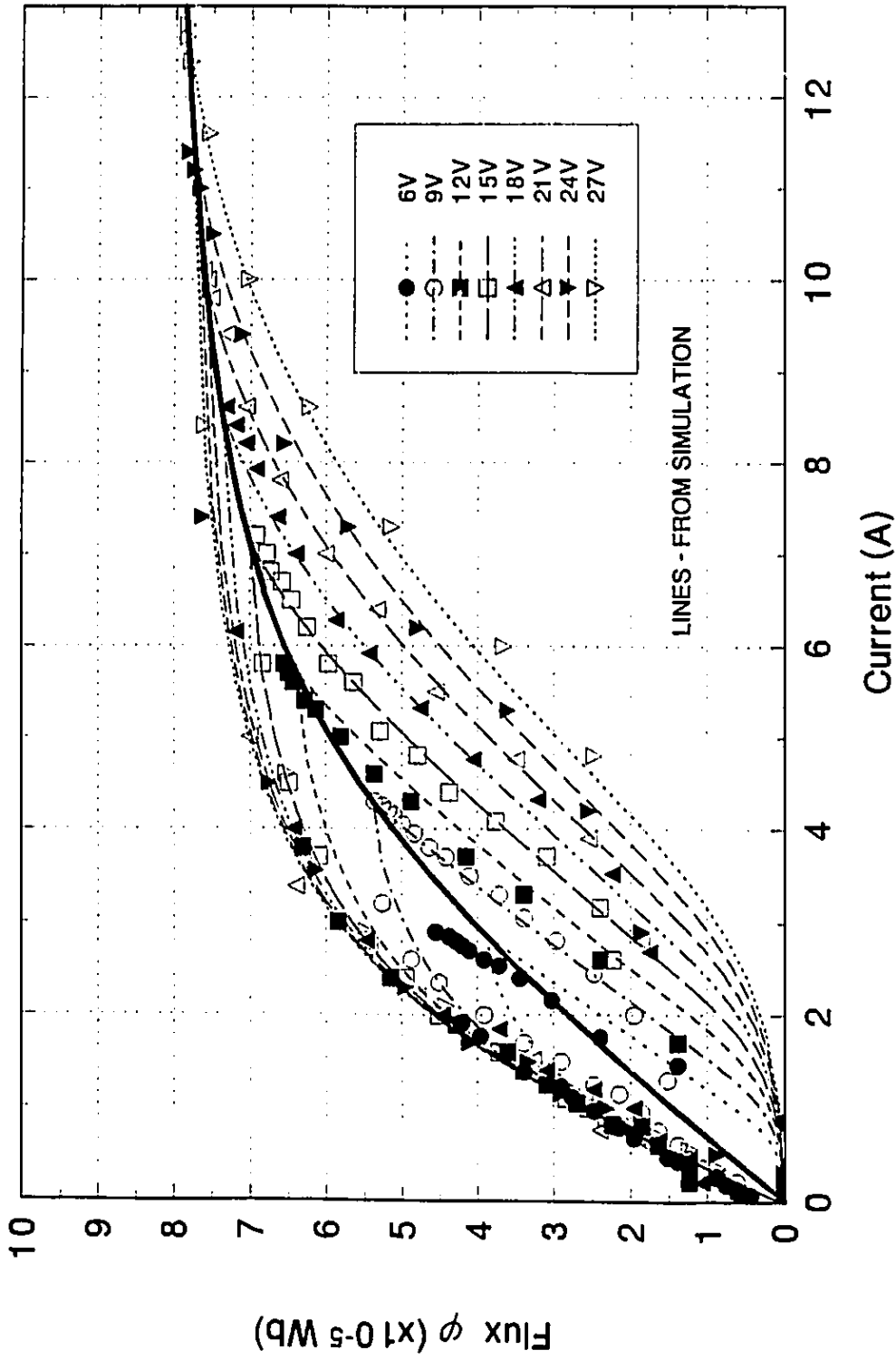


Fig. 4.29 Solenoid flux dynamic hysteresis loop for air-gap 0.635 mm

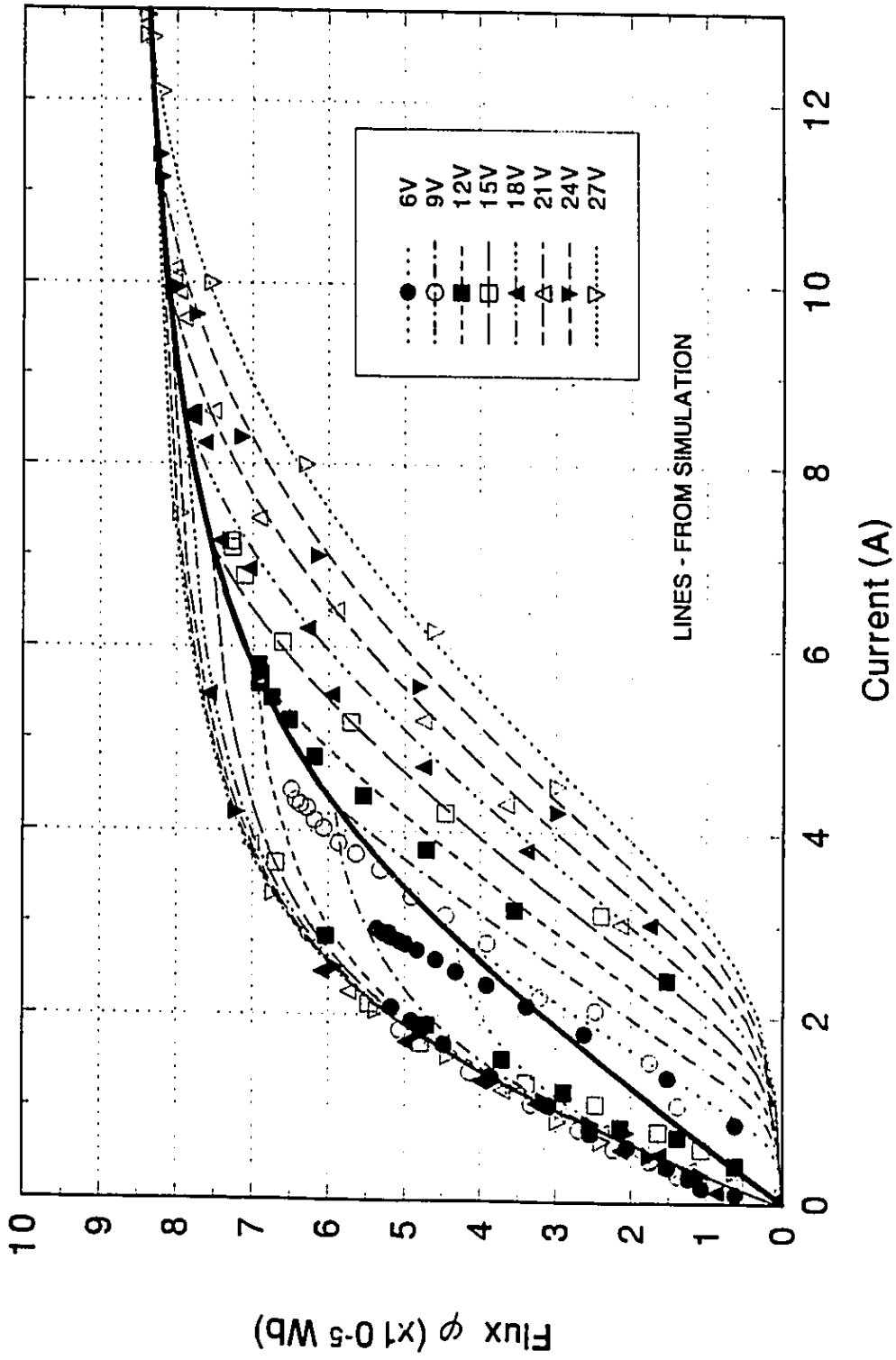


Fig. 4.30 Solenoid flux dynamic hysteresis loop for air-gap 0.535 mm

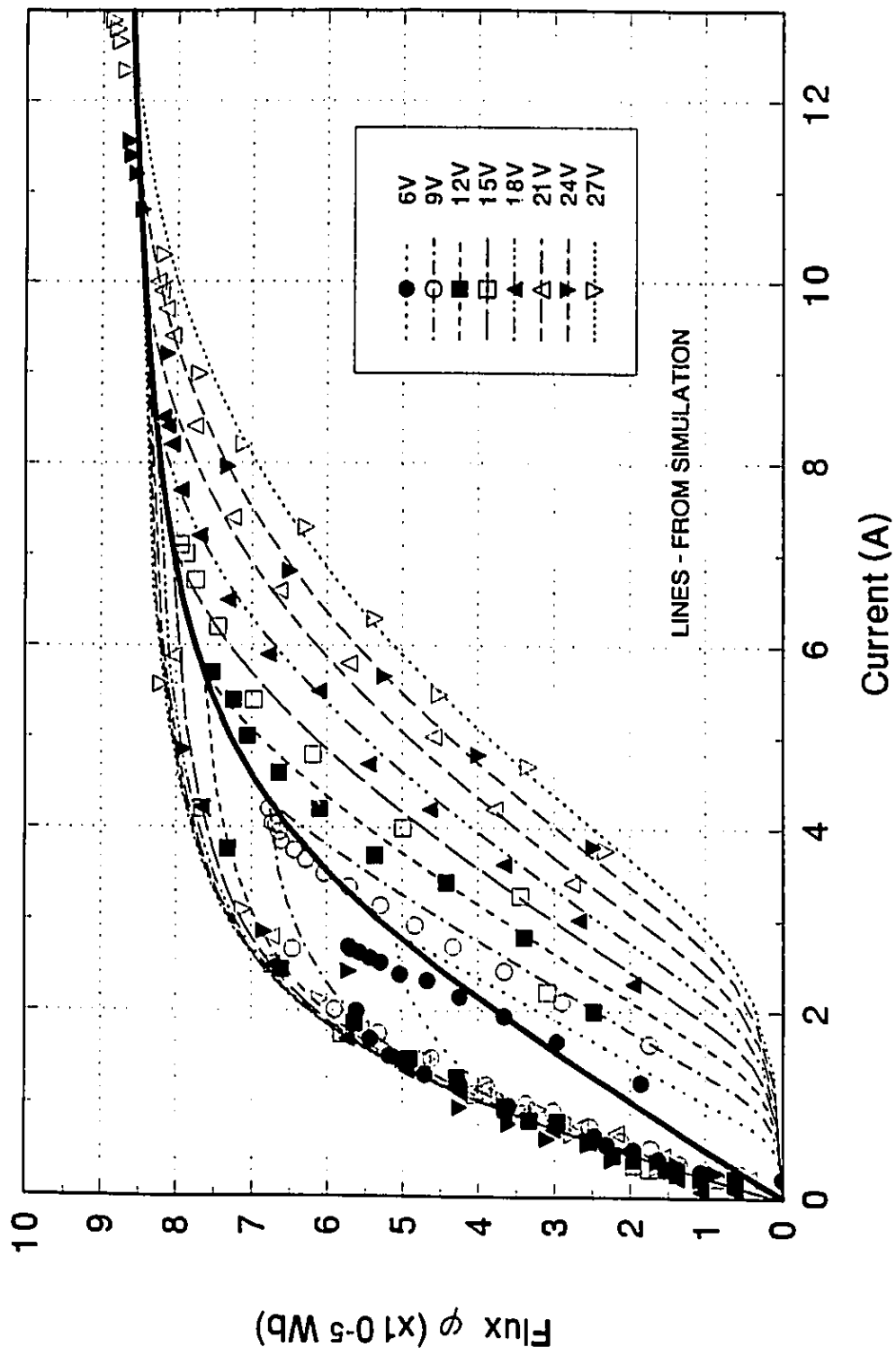


Fig. 4.31 Solenoid flux dynamic hysteresis loop for air-gap 0.425 mm

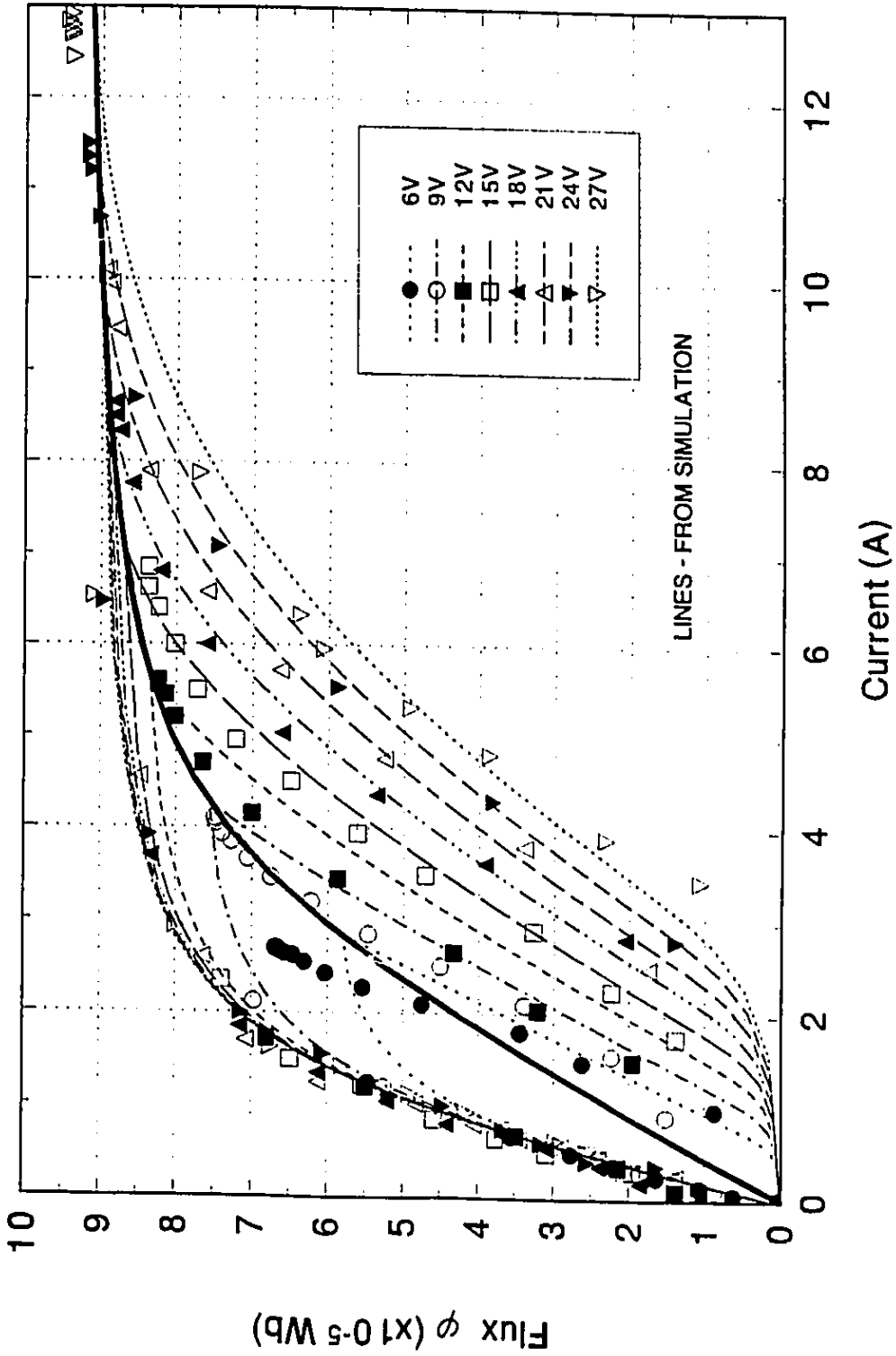


Fig. 4.32 Solenoid flux dynamic hysteresis loop for air-gap 0.353 mm

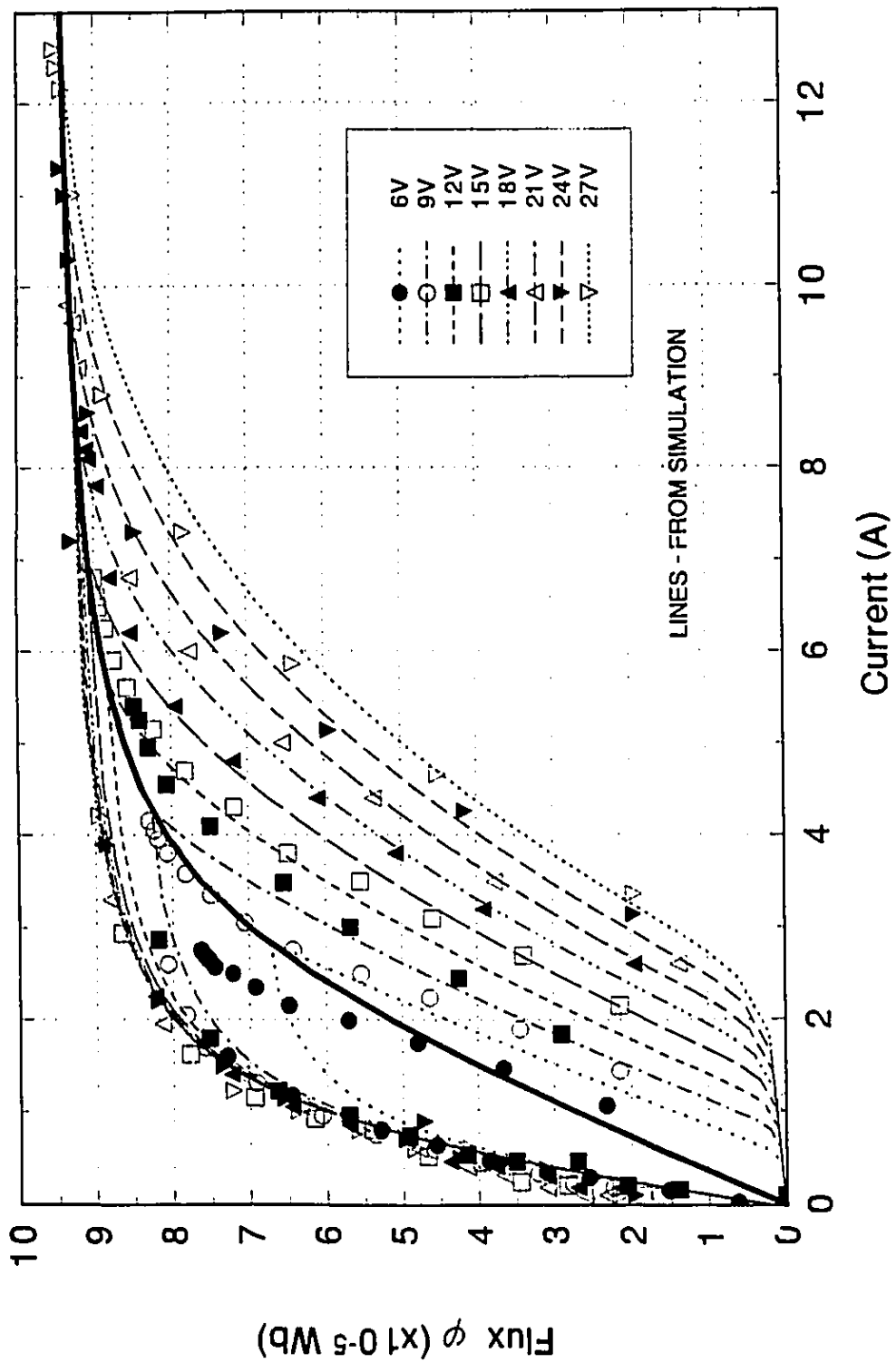


Fig. 4.33 Solenoid flux dynamic hysteresis loop for air-gap 0.242 mm

$$R_c = b - (b - 1) \cdot \frac{\phi}{a_2}$$

$$\text{where } R_c = 20 \Omega \quad \text{for } \frac{di_m}{dt} < 0 \quad (4.18)$$

$$\text{and } b = -7633.6 \cdot h + 10.85 \quad \text{for } \frac{di_m}{dt} \geq 0$$

$$L_l = (763.4 \cdot h + 0.0653)^2 \cdot L(\phi, h) \quad (4.19)$$

Equations (4.18) and (4.19) are generalized to account for all air-gap lengths. It should be noted that a discontinuity arises when the current condition in equation (4.18) are changed from the application to the removal of the source voltage. When this condition change occurs, both constants  $a_1$  and  $a_2$  must be multiplied by the following coefficient for continuity:

$$a_{cof} = 443.2 \cdot h + 0.2518 \quad (4.20)$$

Referring back to the current and force time responses of Figures 4.3 through 4.12, and to Figures 4.15 to 4.19 for the force versus current hysteresis graphs, the curves from the simulation results agree well with the test results. This demonstrates the adequacy of the electrical and magnetic mathematical model for the solenoid driving circuit and the coil characteristics.

#### 4.7 Switching Circuit Description

The electrical switching circuit used to enhance the speed of injector solenoid opening and closing is shown in Figure 4.34. Part of the driving circuit is similar to that shown in Figure 4.2 and its function is described in Section 4.2. Instead of the node-B of the solenoid coil being at ground potential, it is now connected to the parallel circuit consisting of a capacitor  $C$ , a resistor  $R_I$ , and a zener diode.

During the injector opening phase, the solid-state relay is switched into its closed position while the capacitor is initially discharged. This allows the complete charge of the voltage source  $V_S$  to be supplied across the solenoid coil which creates a large current "boost" of short duration through the coil. This generates a rapid rise in the solenoid force which is required only at the beginning of the injector opening to overcome the spring preload force and the inertia force to quickly accelerate the injector needle before its fully open position. While the capacitor is being charged to its maximum voltage that is limited by the zener diode, the "boost" current peaks and then decays. The value of the zener diode is selected so that at steady-state conditions the voltage across the coil will be at its nominal 12 V and the current will be at 7 A, approximately. Returning fast the solenoid voltage and the current to their nominal values protects the coil from excessive heating and reduces the possibility of damage. In addition, once the injector needle is almost fully lifted, a large solenoid force is no longer required. A much smaller force is only required to balance the spring force that tends to close the injector.

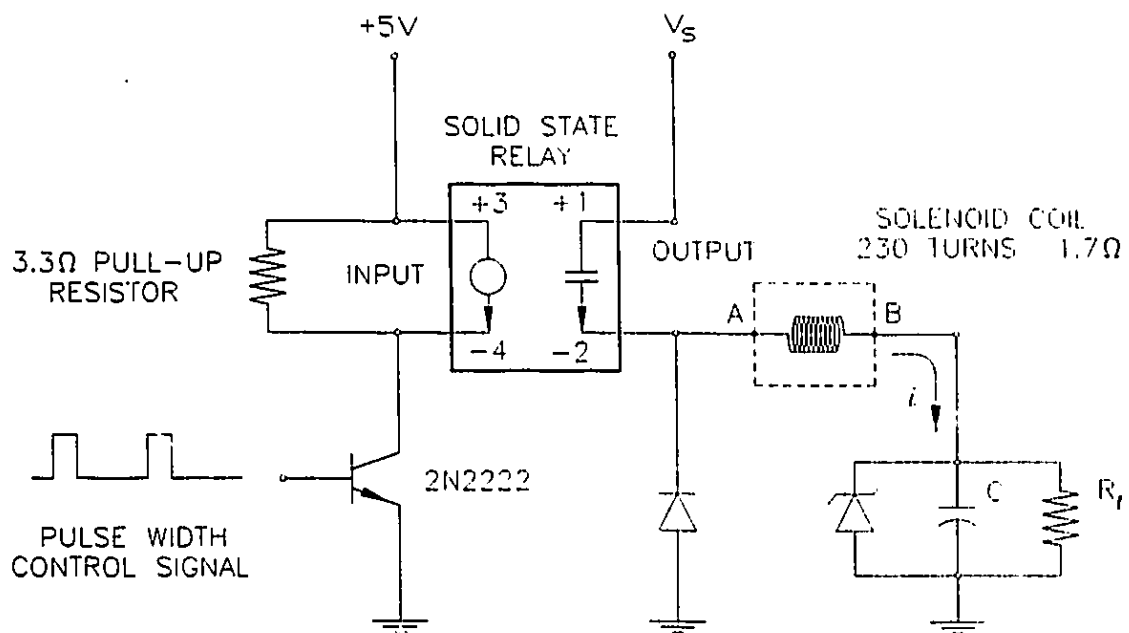


Fig. 4.34 Switching circuit to control solenoid force generation



When the solid-state relay is switched to its open position, the applied voltage is instantly removed but the current continues to flow through the solenoid because of the coil inductance. Hence, the protection diode connecting the solid-state relay output to the ground is to protect the relay from the resulting negative voltage spike. Since the capacitor is already fully charged, the capacitor voltage helps to oppose the continuation of the current flow. This expedites the current deceleration and results in a fast decay of solenoid force, helping the injector needle to close rapidly. The resistor  $R_l$  is provided for the capacitor to discharge before the start of the next injection cycle.

#### 4.8 Mathematical Model of Switching Circuit

Equations (4.15), (4.16) and (4.17) can be considered, respectively, as valid mathematical descriptions of the voltage across the solenoid coil, the exciting current through the flux leakage inductance, and the magnetizing current through the coil. The voltage at node-B, is described by the capacitor voltage that is limited by the zener diode expressed as:

$$V_c = \int_0^t \left( \frac{i_c R_l - V_c}{R_l C} \right) d\tau \quad \text{for} \quad V_c < V_z \quad (4.21)$$

$$\text{and} \quad V_c = V_z \quad \text{for} \quad V_c \geq V_z$$

where  $V_z$  is the zener diode voltage and  $\tau$  is a dummy variable for integration.

## 4.9 Summary

A comprehensive mathematical model of the solenoid has been presented. The model is derived from fundamental electromagnetic concepts which include the consideration of the ferromagnetic material reluctance (combined material effects of the solenoid core and casing); it is based on an equivalent circuit similar to that used in the study of power transformers. The solenoid study with the consideration of eddy current and flux leakage losses, which leads to the presentation of a steady-state magnetization curve and a dynamic hysteresis loop in the description of the electrical solenoid with step voltages as input, is both innovative and contributing to a better understanding of solenoid transient behaviour.

The mathematical model is general, and can be applied to describe any electromagnetic solenoid. It must be pointed out that both, the steady-state and the transient experimental force and current measurements, are required to complete the solenoid model. This is because the parameters of the model are specific to a particular class of solenoids.

The steady-state measurements, at various air-gap lengths, are needed to determine the material reluctance parameters  $a_1$  and  $a_2$  of Equation (4.2). The procedure to determine these two parameters is straight-forward, and can be reviewed as described in Section 4.6. With reference to Figures 4.22 to 4.26 for illustrative purposes, the material reluctance is the reciprocal of the slope of the steady-state magnetization curve for the core. At very low current values, Equation (4.22) is not a good representation

of the experimentally extracted flux values. This modelling deficiency would reflect in obtaining incorrect values of the solenoid steady-state forces generated, as shown in Figure 4.13 at current values of approximately 3 A. This does not diminish the validity of the material reluctance equation since its objective is to provide solutions for a large current and a fast transient response. In other words, low current values are not sustained long enough to significantly affect the system responses.

With reference to Figure 4.13, deviations between the model and experimental steady-state forces are most likely due to the test set-up and testing procedure. During the experiments, it was noted that the consistency of the force measurements were to some extent affected by the amount of preload applied to the piezo-cell force transducer. To circumvent this problem, a micrometer with its ratchet effect that supplied a constant low force was used to preload the transducer. Another problem occurred when the injector was placed on its test-stand, in that the wire connecting the force transducer tended to move the lightly preloaded transducer while it was being moved. This in turn would upset the initial preload setting and would affect the force measurements. It can be suggested for the future work, that a more controlled test environment be established to eliminate these effects. However, the experimental values shown in Figure 4.13 indicate that the data are quite consistent in curvature shape and approach the force saturation as expected.

For a given air-gap, the solenoid transient force and flux forms a hysteresis loop as a function of current. When the voltage is applied, the shape of the simulated flux

curve can be controlled by the value assigned to the eddy current resistance parameter  $R_e$ . As well, this flux curve can be shifted left or right depending on the value assigned to the flux leakage inductance  $L_l$ . In addition, when the applied voltage is removed, the material reluctance parameters  $a_1$  and  $a_2$  have to be multiplied by a coefficient for continuity. These parameters and coefficient were adjusted until the simulated force and current transient responses matched the data obtained from experiments. It must be admitted that although the parameters and coefficient are described by continuous equations in order to be valid for all air-gap lengths, they were determined on a trial and error basis. For future work, a more systematic method should be established to determine these equations in a more comprehensive manner.

The dynamic hysteresis loop for the solenoid generated force, or similarly for the magnetic flux at a given air-gap, expands horizontally along the current axis as the applied voltage is increased. For example, this characteristic is shown in Figure 4.15 for the solenoid force and in Figure 4.29 for the magnetic flux at a fixed air-gap of 0.635 mm. It can be seen that the time rate of current and force rise decreases towards the right of the steady-state curve, which happens also when the inputs of applied step voltages are larger. This characteristic of fast force time response is desirable to result in a quick injector opening. It must be pointed out that as the curves shift toward the right, the coil inductance also increases. This is because at a given fixed current value, the magnetic flux decreases for larger applied voltages. As verified by Equation (4.12), a decrease in magnetic flux increases the coil inductance. Thus, the improvement in transient force and current responses cannot be attributed to the inductance getting

smaller, but is rather due to the fact that the potential difference across the coil is larger. This leads to the conclusion that an expanding hysteresis loop is undesirable, not just from the energy loss considerations but also because of the simultaneous coil inductance increase. Thus, the solenoid characteristics study can provide solenoid manufacturers some insight into the means of producing a faster responding solenoid. It can be concluded that the width of the dynamic hysteresis loop should be limited so that the increase in the coil inductance is kept to smaller values. A small inductance allows fast current response and thus force generation will also be faster. This can be achieved by reducing the flux leakage (i.e. shifting the flux transient curves towards the left, closer to the steady-state magnetization curve) and by reducing the amount of eddy current losses (reshaping the flux transient curves more towards the steady-state magnetization curve). An approach similar to that taken in power transformers can be applied to reduce eddy currents by lamination of the iron-core [8].

For any fixed air-gap, it is interesting to note that when the applied voltage is removed, the magnetic flux (and equivalently the solenoid force) decays toward a common asymptote independent of the initial current. An example of this phenomenon is illustrated in Figure 4.29 for flux at an air-gap of 0.635 mm. With reference to Equation (4.12), the common flux at the asymptote line indicates that eventually a constant inductance is reached. Since this asymptote line is to the left of the steady-state magnetization curve, the constant inductance is also of the smallest magnitude for this air-gap. With reference to Figure 4.33 for a smaller air-gap of 0.242 mm, the asymptote line lies even further to the left of the graph which indicates that the

inductance is also smaller. These characteristics of a small inductance are desirable for fast current decay which leads to a fast force decay to close the injector quickly.

## CHAPTER 5

### SIMULATION OF GASEOUS FUEL INJECTION PROCESSES FOR VERIFICATION OF THE THEORETICAL CONCEPTS

#### 5.1 Introduction

The developed mathematical model of the solenoid injector is tested by substituting the design parameters and investigating their impact on the gas injection characteristics. This evaluation is to provide some 'a priori' knowledge to what values the design variables should approximately have before the system is optimized for optimum performance.

#### 5.2 Mechanical and Electrical System Dynamic Performance

The dynamics of a solenoid-operated injector discharging natural gas directly into the combustion chamber of a diesel engine is computer simulated to verify the mechanical and electrical performances and control concepts. Simulation is performed for a typical set of variables consisting of the voltage source  $V$  (36 V), spring constant  $K$  (80 kN/m), spring preload  $F$  (10 N) and capacitor charge  $C$  (640  $\mu$ F). These variables have been chosen since they have significant influence on the performance of the injector.

Figure 5.1 shows the needle motion ( $h_{max}-h$ ) and solenoid force ( $F_s$ ) variations with respect to the time. Application of the pulse width command voltage to open the injector is at time zero and removal of the voltage to close the injector is at 5.0 ms.

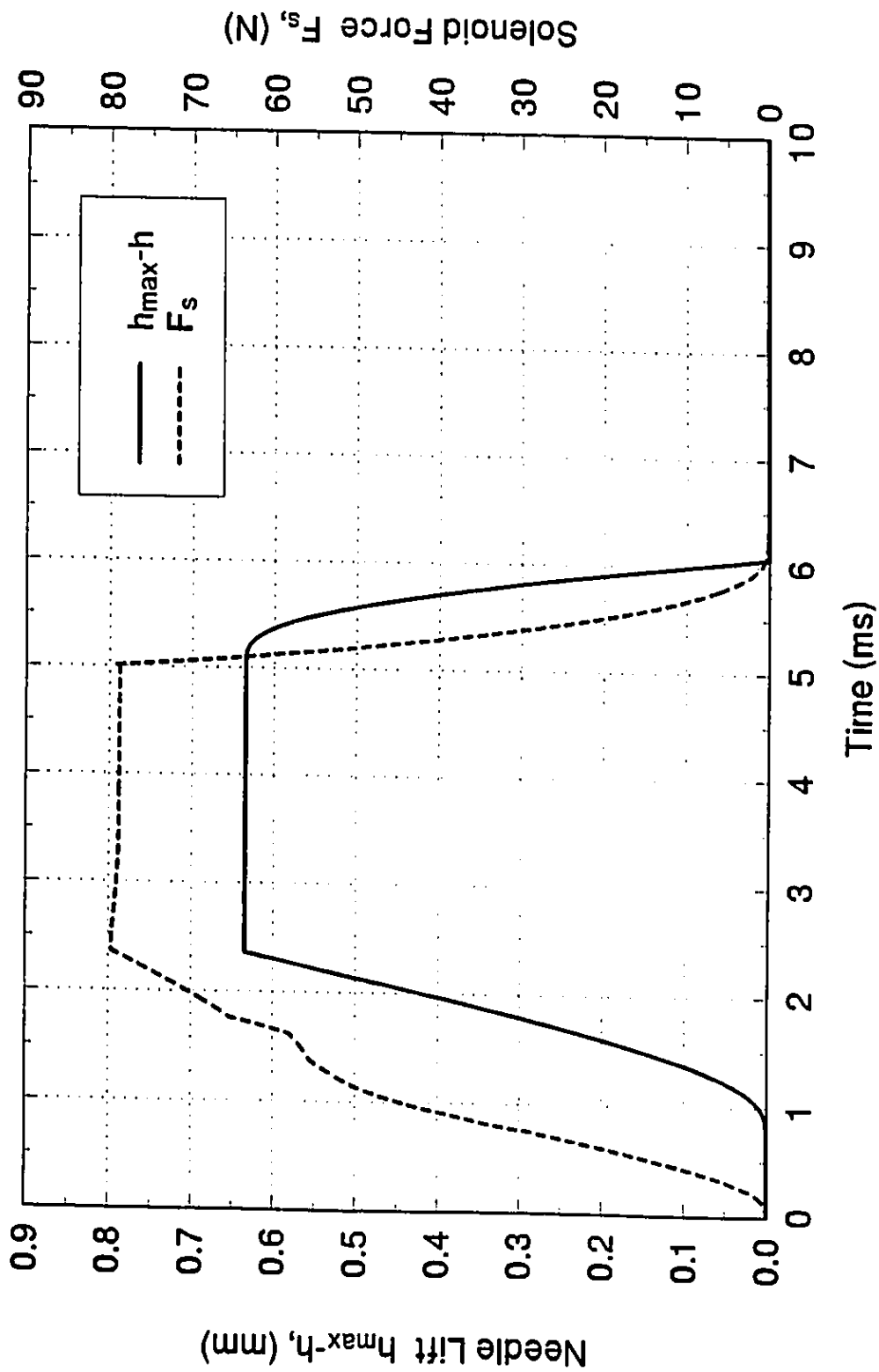


Fig. 5.1 Injector needle travel ( $h_{max-h}$ ) and solenoid force ( $F_s$ ) variations during simulated gas injection process



Figure 5.2 shows the voltage applied to the solenoid ( $V$ ), the capacitor voltage ( $V_C$ ), voltage across the solenoid ( $V_{sol}$ ), and the exciting ( $i_e$ ) and magnetizing ( $i_m$ ) currents through the coil. These variables can be identified from the circuit diagram of Figure 5.1 and from the solenoid coil equivalent circuit of Figure 4.21.

At the beginning of the injection process, the capacitor is initially discharged, when the 36 V across the solenoid is applied. As the exciting current initiates, the solenoid force starts to increase. The capacitor begins to charge that results in gradual decrease of the voltage across the solenoid. However, the current continues to rise due to the solenoid coil inductance and peaks at about 12 A at 1.28 ms. After a delay of 0.75 ms, the needle starts to rise as the solenoid force balances the combined effect of the spring preload and the gas pressure forces acting on the needle. Then, within 1.60 ms, the needle rapidly accelerates and reaches its full lift position. During this acceleration period, the increase in solenoid force is due to the rise in current and to the reduction in the air-gap. Even after the current has reached its maximum, the solenoid force continues to rise because of the progressing reduction in the air-gap. The solenoid force attains its maximum when the injector becomes fully open; then, it decreases due to decaying current.

The voltage across the capacitor is limited by the zener diode to protect the solenoid coil from excessive heating in such a manner that at steady-state conditions the voltage and current will return to their nominal values of 12 V and 7 A. The large current "boost" applied provides a rapid increase in solenoid force in order to reduce the

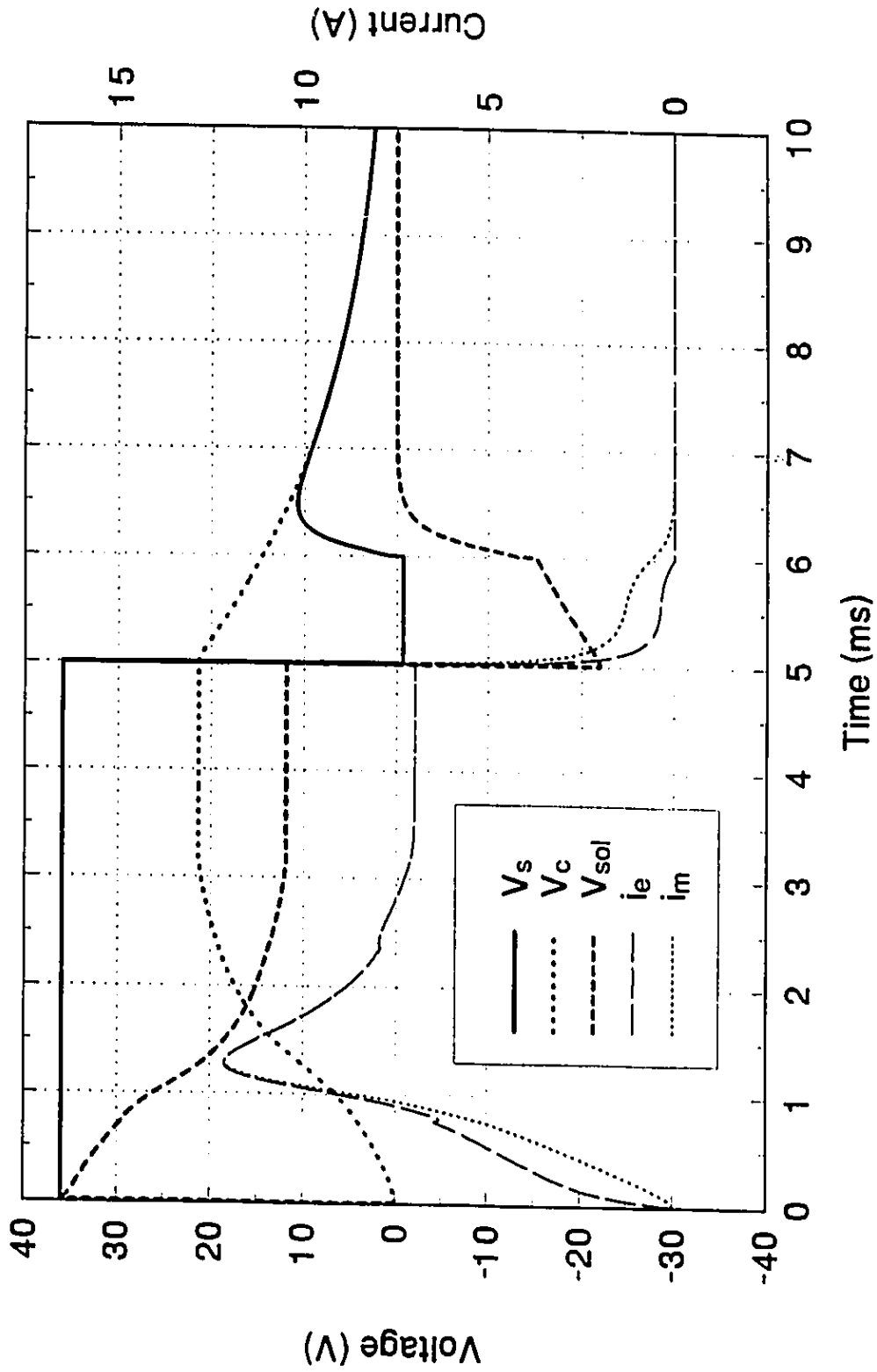


Fig. 5.2 voltage applied to solenoid ( $V_s$ ), capacitor voltage ( $V_c$ ), voltage across the solenoid ( $V_{sol}$ ) and the exciting ( $i_e$ ) and magnetizing ( $i_m$ ) currents through the coil during simulated gas injection process

time delay to overcome the spring preload force. This helps in accelerating the needle to its fully open position.

When the relay is opened, the relay protection diode limits the negative voltage spike to  $-0.7\text{ V}$  since the current continues to flow through the solenoid due to the coil inductance. The next function of the capacitor is to provide an opposing voltage across the solenoid to decelerate the current through the coil. This, in turn results in a rapid reduction of the solenoid force, so that the spring force can close the injector with minimum closing delay and fall time. The solenoid force is next seen to decay instantly as the relay opens. The needle starts to move down after  $0.05\text{ ms}$  of delay, and then rapidly falls within  $1.0\text{ ms}$ .

The capacitor voltage could be maintained at its zener diode limit ( $12\text{ V}$ ) until the drop in current through the solenoid becomes insufficient to sustain the limiting voltage across the resistor. At this current value, the capacitor begins to discharge through the resistor and the current opposing voltage across the solenoid starts to decrease. When there is no more current flowing through the solenoid, the voltage across the protection diode equals that of the capacitor voltage. Eventually the capacitor will totally discharge before the next injection cycle.

The magnetizing current lags behind the exciting current because of the flux leakage inductance. The velocity-induced voltage has negligible effect, except for a slight increase in the time taken for the current to reach zero during the needle closing phase.

### 5.3 Gas Flow Characteristics

Figure 5.3 shows the status of the pressure within the injector for the opening and closing of the injector orifice. When the needle lifts up, the injector pressure drops exponentially from its initial pressure of 10 MPa. This is because the injector nozzle is discharging gas to the combustion chamber. This pressure drop can be reduced by increasing the metering valve orifice opening. When the solenoid is de-energized and the needle closes the exit orifice, the injector pressure recovers exponentially to its original value before the next injection occurs. The time required for the pressure recovery can be reduced by increasing the metering valve orifice opening.

Figure 5.4 illustrates the gas mass flow rate entering the injector chamber from the gas supply remaining at constant pressure and the mass flow rate exiting the injector into the combustion chamber where the constant pressure is assumed. As soon as the needle starts lifting, the mass flow exiting the injector rises rapidly to a maximum. Then it starts to decrease at a slow rate due to the injector pressure decrease. When the solenoid is de-energized the exit mass flow rate decreases to zero when the needle closes the injector.

The mass flow rate entering the injector chamber from the gas supply source rises exponentially when the needle is lifted off its seat. When the needle is closed, this mass flow continues until the pressure within the injector chamber returns to its initial pressure which is equal to the supply pressure.

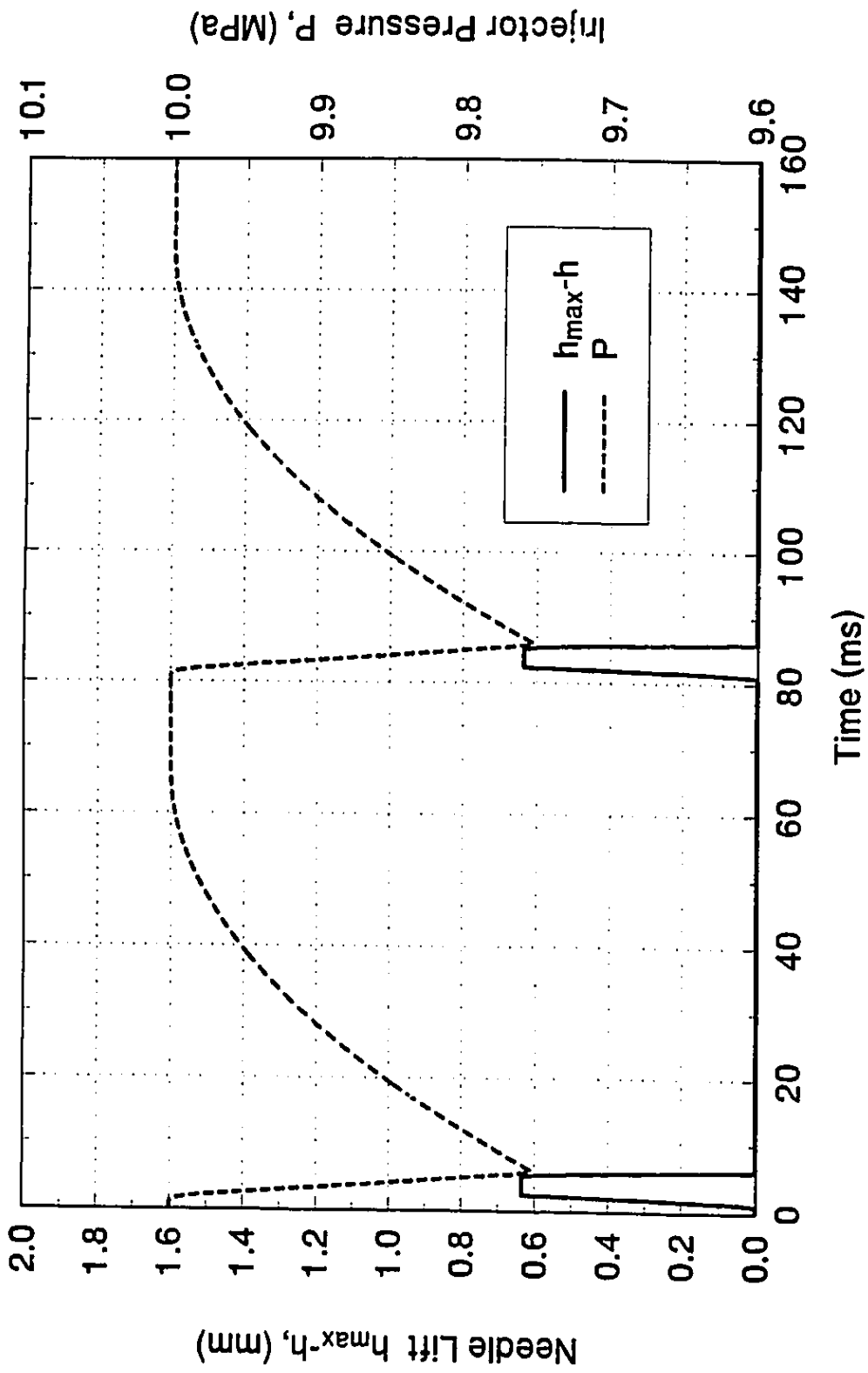


Fig. 5.3 Injector pressure and needle lift for two injection cycles

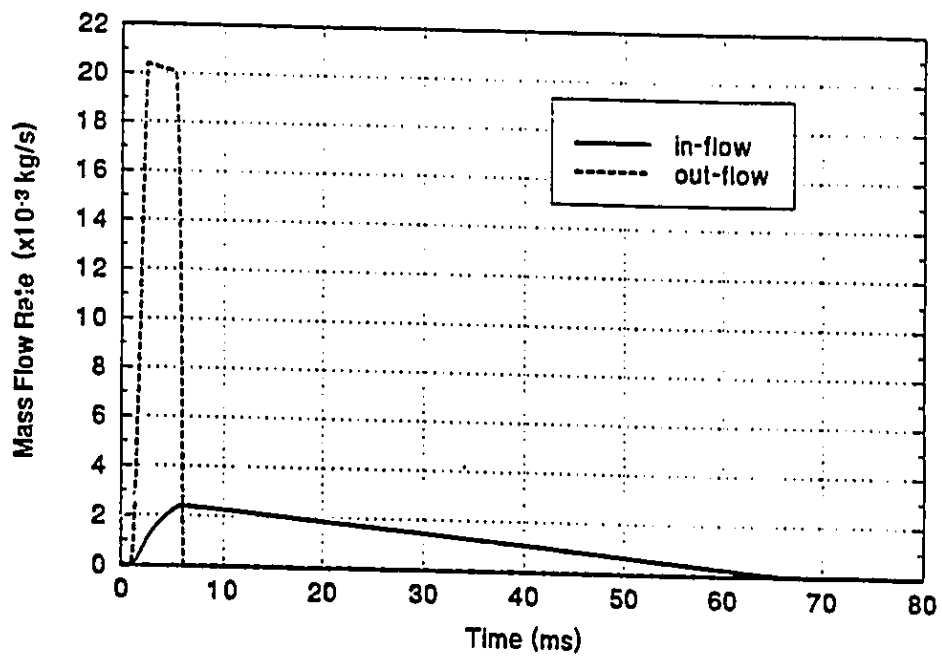


Fig. 5.4 Mass flow rate entering and mass flow rate exiting the injector chamber

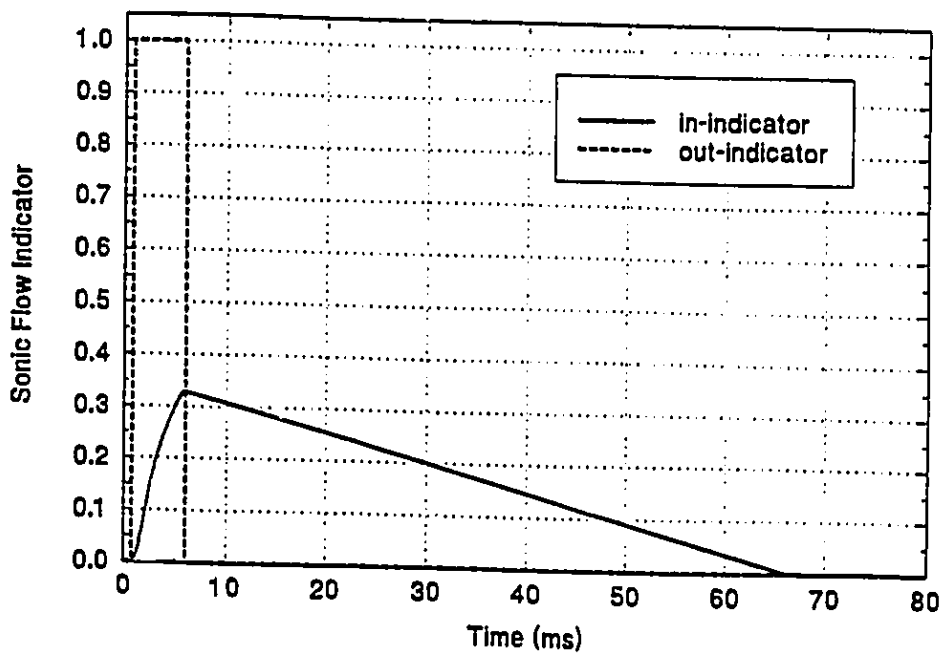


Fig. 5.5 Sonic flow indication for metering valve orifice and injector orifice

Figure 5.5 is a plot of Equation (3.10), which is an indicator of sonic or subsonic orifice flow. As illustrated in the figure, as soon as the injector needle is lifted off its seat, the nozzle exit orifice is always at sonic flow conditions until it closes. The metering valve orifice is never at sonic flow conditions.

#### 5.4 Performance Index Study of System Variables

Variations of a set of design variables that greatly influence the injector dynamic performance is studied. The design variables are selected as the voltage source  $V$ , spring preload  $F$ , spring constant  $K$  and capacitor  $C$ . Changes to the design variables are limited to ranges that are considered physically realizable, given as:

$$\begin{aligned} 18 \text{ V} &\leq V \leq 36 \text{ V} \\ 5 \text{ N} &\leq F \leq 25 \text{ N} \\ 20 \text{ kN/m} &\leq K \leq 140 \text{ kN/m} \\ 100 \text{ } \mu\text{F} &\leq C \leq 1120 \text{ } \mu\text{F} \end{aligned}$$

The performance of the injector dynamics due to variations from the design vector is measured by a time performance index defined as:

$$PI = t_d + t_r + t_c + t_f \quad (5.1)$$

where the four important time objectives for a minimum performance index are taken to be:

- $t_d$  - delay time in injector opening
- $t_r$  - time duration for injector lift
- $t_c$  - delay time in injector closing
- $t_f$  - time duration for injector fall

Results obtained from the design variable changes are shown in Figures 5.6 and 5.7. Figure 5.6 shows variations in the performance index for changes in capacitance. Each curve shown is for a different voltage value while the spring rate and preload are the same at their mid-range values of 80 kN/m and 15 N.

For small capacitances, the performance index has large values because the capacitor charges up too quickly to provide sufficient current "boost" to generate a large solenoid force to open the injector. When the capacitance are at even lower values, the injector cannot open because of this quick capacitor charging effect.

For a fixed voltage, as the capacitance increases, the performance of the injector improves. This is because the boost current becomes more effective in generating a sufficient solenoid force to decrease the opening delay  $t_d$  and to increase the acceleration of the needle opening thereby reducing the time duration for the injector lift  $t_l$ .

As the capacitance continues to increase, the injector performance for all the curves of different voltage input improves and then level off. With reference to the 36 V supply voltage curve, after the current boost attains a peak value the current eventually returns to its 7 A nominal value before the voltage is removed to close the injector. This was also observed for all the other curves from their simulation results. However, for the 36 V curve, for capacitor values starting at between 800 and 900  $\mu\text{F}$  and greater, the current is greater than the nominal value when the injector starts to close. It is expected that the performance curve will worsen and will start to increase again after some capacitor value greater than 1120  $\mu\text{F}$ . The shape of the performance index curve will



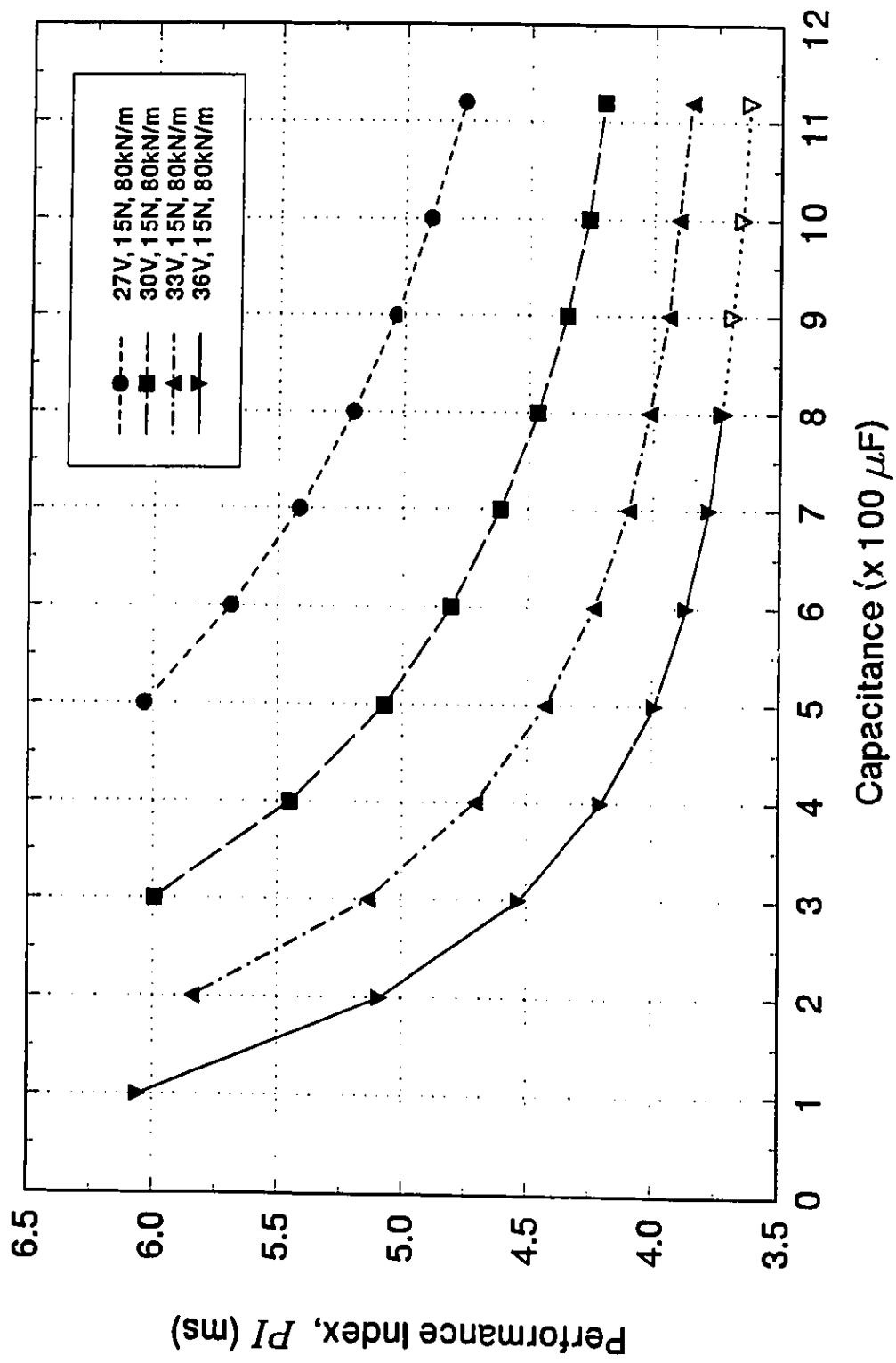


Fig. 5.6 Performance Index vs. capacitance for different voltages

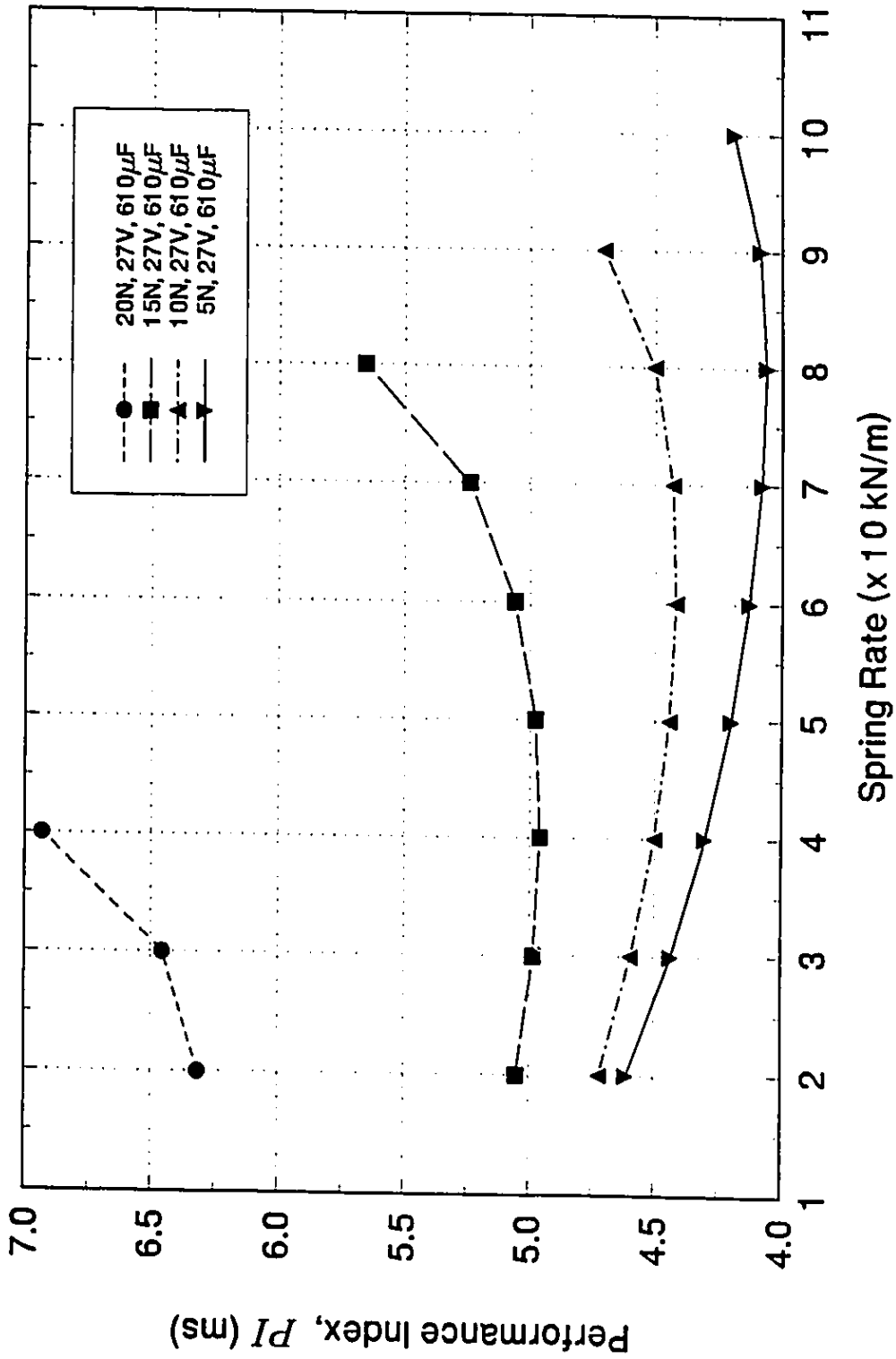


Fig. 5.7 Performance Index vs. spring rate for different spring preloads

then be concave. Thus, for larger capacitor values the performance index will increase because both the delay before closing time  $t_c$  and the duration of injector fall time  $t_f$  will increase. This effect is attributed to the greater voltage differential across the solenoid which results in a larger current flow. Then, after the current reaches its peak and decays, it would end at a larger value than for a smaller capacitor, at the instant when the command signal is removed. This larger current takes longer time to decay even though there is an opposing voltage. In turn, the solenoid force which is a function of current, will also take a longer time to decay.

Figure 5.7 shows the results of the performance index for variations of the spring rate. Each curve represents a different spring preload, while the voltage and capacitor variables are held at their mid-range values of 27 V and 610  $\mu\text{F}$ .

For a large spring preload (20 N curve), increasing the spring rate deteriorates the injector performance because there is more compression force to oppose the needle opening acceleration. Eventually, the spring compression force becomes so great that it only allows the needle to pop open briefly.

For small spring preloads, the shape of the performance curves are concave. Increasing the spring stiffness starting at low values improves the injector performance. This is because the compromise for a decrease in both the delay in injector closing  $t_c$  and duration of fall  $t_f$  times are more beneficial although the time duration of needle lift  $t_r$  increases. Thus, a stiffer spring provides a higher closing force to accelerate the needle closing. But eventually, increasing the spring rate further results in the compromise

becoming no longer feasible and the injector performance deteriorates. This limit occurs at the minimum of the performance versus spring rate curves, and this point shifts to higher stiffness values as the preload is decreased. Inevitably, a large spring stiffness is reached that only allows the needle to pop open for too short a time duration to be considered effective in supplying fuel to the engine.

## **5.5 Summary**

Simulation of the complete injection system model for a typical set of design variables has shown that the system performs as intended for direct gaseous fuel discharge into the cylinder of an internal combustion engine. An injection duty cycle of 5 ms over a 60 ms period is sufficient for the electrical circuitry to recover to steady-state conditions before the start of the next injection, as shown in Figure 5.2. The sample system simulation illustrated in Figure 5.3 shows that the pressure inside the injector is very close to recovery at 60 ms. Adjustment for full pressure recovery can be accomplished easily by increasing the metering valve orifice opening. Figure 5.5 shows that the mass flow through the injector orifice into the combustion chamber is always sonic. This design is intended so that the mass flow will only be a function of pressure differential across the exit orifice.

The study of the injector performance by varying the important design variables is for the purpose of attaining an estimate of the variables that will produce an optimum system performance, as a starting point for the system optimization process. In addition,

a knowledge of how the system performs can be used to verify the solution from the optimization process.

From the system performance study, it can be concluded that an optimum injector design can be achieved by:

- The supply voltage should be high, to provide a large current to overcome the spring preload and quickly accelerate the needle to its full open position.
- The capacitor value should not be small. A small capacitance charges up too quickly to provide a sufficient current boost to generate an initially large solenoid force during the injector opening stage.
- The capacitor value should not be too large. A large capacitance creates too large a current that results in an increase in injector closing delays because the solenoid force is sustained longer. It takes more time for a large current to decay than for a current of smaller value. In addition, the large current is only required during the initial opening of the injector, and should return to nominal values to protect the solenoid from overheating.
- The spring preload should be small, so that the injector opening delay is kept short.
- The value of the spring stiffness should provide the best compromise between the time of needle rise and delays from the start of needle closing and needle fall time. A stiffer spring provides a higher closing force to accelerate the needle closing.

## CHAPTER 6

### OPTIMIZATION OF SOLENOID OPERATED GASEOUS FUEL INJECTOR

#### 6.1 Introduction

Simulation based studies outlined in Chapter 6 have confirmed the feasibility of using the investigated gaseous fuel injector for direct fuel discharge into internal combustion engines, since the stringent timing requirements for its opening and closing could be achieved. Performance index studies show that the timing requirements can be still improved with proper selection of the design variables. However, the study would be time consuming because many data points are required, while the final results can only show the performance trends for particular design parameter changes. Therefore, an optimal set of the design variables cannot be concluded from such a study.

In this chapter, a systematic multivariable multiobjective constrained injector optimization procedure is described to establish an optimal set of the design variables. The Hooke and Jeeves unconstrained optimization method [44<sup>(1)</sup>] is used with the introduction of a novel approach to account for boundary constraints. The procedure keeps track of three successive objective function values and their corresponding step lengths. Algorithm logic control is used to determine whether the optimum design variable solution lies on the boundary. The design variables are restricted to within the feasible region, and the constraint procedure may be classified as a 'self-bounding' [46<sup>(1)</sup>] technique. A penalty function is used to account for the behaviour constraint imposed

on the current and status checking of whether the injector opens, completely opens, and completely closes at the prescribed time requirements.

An earlier optimization study made for determining an optimal set of design variables for solenoid-operated gaseous fuel injectors has been already reported [30,31]. The univariate optimization method was applied, in which at each iteration, only one variable from the set of design variables was optimized, while the remaining variables were held fixed. Although, this method resulted in an optimum solution set, the sequence in applying particular variables affected the optimization results. The optimization method presented in this chapter avoids such situation.

From the optimization study of the injection system, it can be concluded that an optimized injector design minimizes the time delays and improves the profile of the needle motion. This in turn, diminishes the deviation between the ideal and actual amount of the gas dosage supplied to the engine.

## **6.2 Selection of a Suitable Optimization Method**

Application of optimization techniques requires the evaluation of an objective function. To obtain the function value for the solenoid/injection system, the complete dynamic model must be simulated to include the injector opening and closing time periods. Any adjustment to one or more system parameters during the optimization procedure requires the complete model to be simulated again. In addition, information about the derivatives of the objective function cannot be expressed explicitly and

analytically. Methods that require the derivatives of the objective function would result in approximations through finite difference methods and the calculation of these estimates may involve lengthy computation, as well as possible numerical rounding errors that could affect estimation of the gradient and interact with the convergence criteria [45<sup>(1)</sup>, 46<sup>(2)</sup>]. The injector system under consideration falls into the optimization category where the function value itself and the gradient of the function is difficult or costly to evaluate. The optimization method used for the class of problems that do not require information about the function derivatives are often termed 'direct search techniques' [45<sup>(2)</sup>].

Optimization of the system is further complicated by system constraints. Inequality boundary constraints must be imposed on the injector design variables so that the solution set is physically realizable. The penalty function methods, or otherwise called the transformation methods, "have proved most popular and most successful" in constrained optimization by direct search techniques [46<sup>(3)</sup>], and "are of great importance in solving real life problems" [44<sup>(2)</sup>].

There are two penalty function methods. One is termed the 'exterior penalty' function method and the other is termed the 'interior penalty' function method. The latter method is also called the 'barrier function' method.

The method of approach to solve a constrained optimization problem is to reformulate the problem into an unconstrained one by the addition of a penalty term to the objective function. Then, an unconstrained optimization method is used to solve the problem. The last terms on the right side of Equations (6.1) and (6.2) describe



respectively the exterior and interior penalty functions, where  $\bar{X}$  is the set of design variables to be optimized,  $r$  is a positive constant known as the penalty parameter,  $J(\bar{X})$  is the unconstrained objective function and,  $J_E(\bar{X}, r)$  and  $J_I(\bar{X}, r)$  are the reformulated objective functions to account for the constraints [44<sup>(3)</sup>, 47].

$$J_E(\bar{X}, r) = J(\bar{X}) + r \sum_{j=1}^n \Gamma[g_j(\bar{X})] \quad (6.1)$$

$$J_I(\bar{X}, r) = J(\bar{X}) - \frac{1}{r} \sum_{j=1}^n \Xi[g_j(\bar{X})] \quad (6.2)$$

The number of  $n$  inequality constraints are given by

$$g_j \leq 0 \quad \text{for } j = 1, 2, \dots, n \quad (6.3)$$

Some of the more common  $\Gamma$  and  $\Xi$  penalty functions are [44<sup>(4)</sup>]:

$$\Gamma = \max[0, g_j(\bar{X})] \quad (6.4)$$

$$\Gamma = \{\max[0, g_j(\bar{X})]\}^2$$

and

$$\Xi = -\frac{1}{g_j(\bar{X})} \quad (6.5)$$

$$\Xi = \log[-g_j(\bar{X})]$$

Equations (6.1) and (6.4) describe the applications of the exterior penalty function method. It can be seen that optimizing for the solution vector is exactly the same as

optimizing for an unconstrained system when no boundaries have been violated since the penalty function has a value of zero. In this situation, it is said that the design vector is within the feasible region. Whenever the design vector goes beyond its constraints which is outside the feasible region, the penalty function returns a value greater than zero. This positive value multiplied by a sufficiently large penalty parameter  $r$ , will drive the solution away from the infeasible region back towards the boundary.

Equation (6.2) is for the application of the interior penalty function method. When the design vector is away from the boundary, but well within the feasible region, the penalty term is small. The reformulated objective function  $J_r(\bar{X}, r)$  is always greater than  $J(\bar{X})$  because the penalty function given by Equation (6.5) is negative. As a design variable approaches the boundary (i.e.  $g_j$  approaches zero), the penalty function tends to infinity. The start of function increase depends on the selected value of the penalty parameter  $r$ . Thus, subsequent large objective function values which always lie within the feasible region, act as a 'barrier' to keep the design vector from going beyond the constraint boundary.

Although the penalty function methods are the most widely used technique for constrained optimization, the methods have certain weaknesses. To determine the appropriate penalty parameter  $r$  for the interior penalty method [44<sup>(6)</sup>], the parameter must first be selected at some suitable value greater than zero. The system is optimized using an unconstrained optimization method and the solution must be tested for optimality. If not, the complete system must again be optimized by decreasing the

penalty parameter  $r$ . The test for optimality requires two consecutive optimization runs to compare the differences between the objective functions or design vectors for a termination criterion. Obviously, the drawback to this method for systems that require model simulation for the objective function, may require much computation before an appropriate penalty parameter is reached.

Another drawback that can occur is when the constraints are different by several orders of magnitude. The contribution of the larger constraint will be greater than that of the smaller constraint in the formulation of the penalty function. Trouble arises when one constraint changes more rapidly than the other and hence will be overpowering [48]. The usual procedure to avoid this problem is to normalize the constraints between -1 and 0, or by defining a different penalty parameter for each constraint in Equations (6.1) and (6.2) [44<sup>(6)</sup>].

In multivariable optimization procedures using the direct search methods, once the direction of search is known, the optimization reduces to a one-dimensional search for the optimum step length along this direction. The usual algorithm to evaluate this step length is by fitting quadratic or cubic extrapolation and interpolation functions to the objective function values. These curve fitting algorithms cannot accurately model the penalty functions with its singularity at the boundary of the feasible region [46<sup>(4)</sup>].

These are only some of the drawbacks described which are more appropriate to the systems that require model simulation for the objective function. These deficiencies apply to both the interior and exterior penalty function methods, where for the latter

method the appropriate penalty parameter is adjusted by increasing its value from an initially smaller one.

In this thesis, the unconstrained direct search technique of Hooke and Jeeves is selected to optimized the fuel injector system. This is because the method is not difficult to implement as an algorithm, and because the other accepted direct search techniques are extensions of this method as a basis for their modifications [44<sup>(7)</sup>].

From the review of the methods to account for boundary constraints, the natural selection is to implement the interior penalty function method since a design variable going outside the feasible region may have no physical meaning (i.e. negative spring preload). But still, this method is not used because of the drawbacks described, which are related to the following reasons:

- 1) To determine the penalty parameter  $r$  may require many optimization runs before it is considered appropriate. Each simulation of the injector dynamic model to evaluate the objective function is already time consuming. The combined computation time of the system dynamics and search for the final penalty parameter may be excessive.
- 2) The constraints must be normalized, or different penalty parameters must be assigned to each constraint. This is because the design variables have large orders of magnitude differences. For example, the spring constant is of the order of  $10^5$  N/m, while the capacitor is  $10^{-4}$  F.

3) A quadratic interpolation method [44<sup>(6)</sup>] for the one-dimensional search to determine the optimum step length is selected for implementation. Analytical methods cannot be used because the objective function cannot be expressed explicitly. As well, the cubic interpolation method cannot be used because first derivatives of the objective function are required. Using the interior penalty function method could result in very large function values near the boundary and the quadratic interpolation method can be rendered inapplicable.

In Section 6.3, a novel approach to account for boundary constraints that avoids the pitfalls as described above will be introduced. The procedure keeps track of three successive objective function values and their corresponding step lengths. These values are used for: 1) to determine if a boundary has been reached, and if so, the algorithm decides if this corresponds to the optimum design vector, and 2) the bracketing of three function values that is required for the quadratic interpolation method. The technique to account for boundary constraints can be considered similar to a 'self-bounding' method, since the design variables are restricted to remain within the feasible region. Implementation of this new procedure requires some modifications to the Hooke and Jeeves unconstrained optimization method.

### **6.3 Introduction to the Optimization Method with the New Procedure to Account for Boundary Constraints**

A graphical interpretation of the procedure to account for boundary constraints is illustrated in Figure 6.1a. To simplify the explanation, the objective function  $J$  is

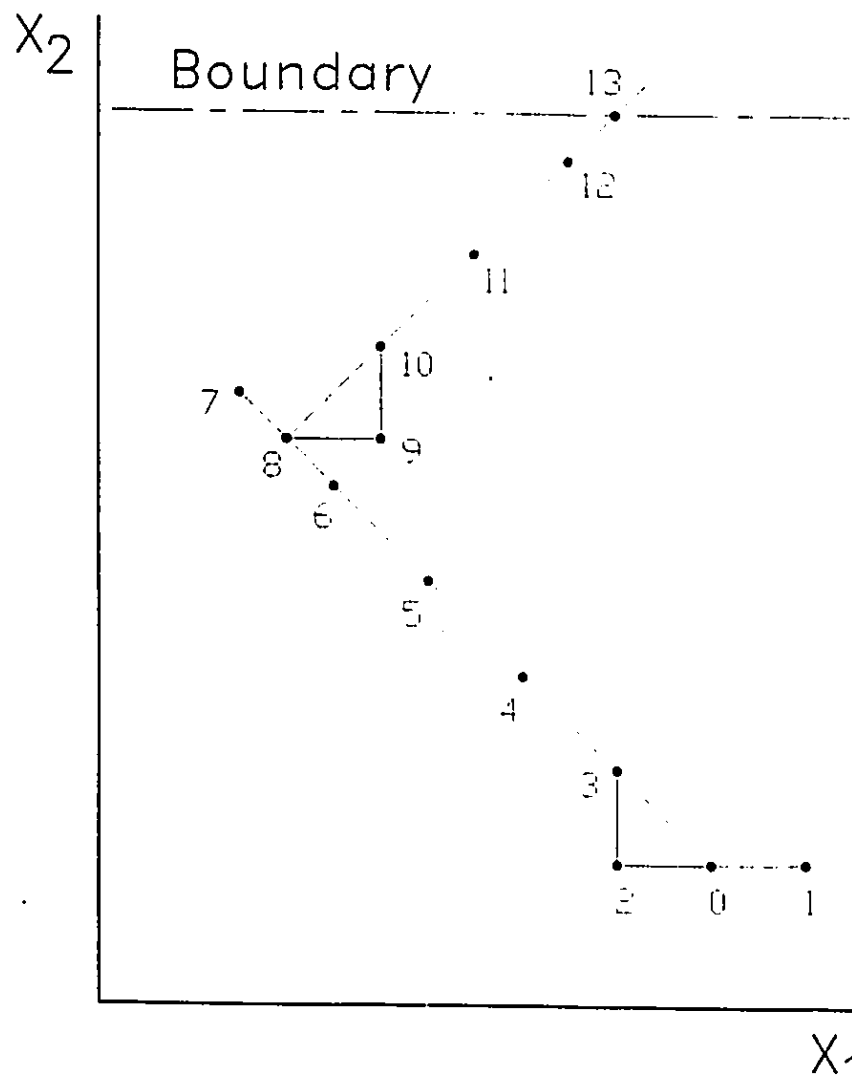


Fig. 6.1a Illustration of new procedure to account for boundary constraints, during Hooke and Jeeves exploratory moves

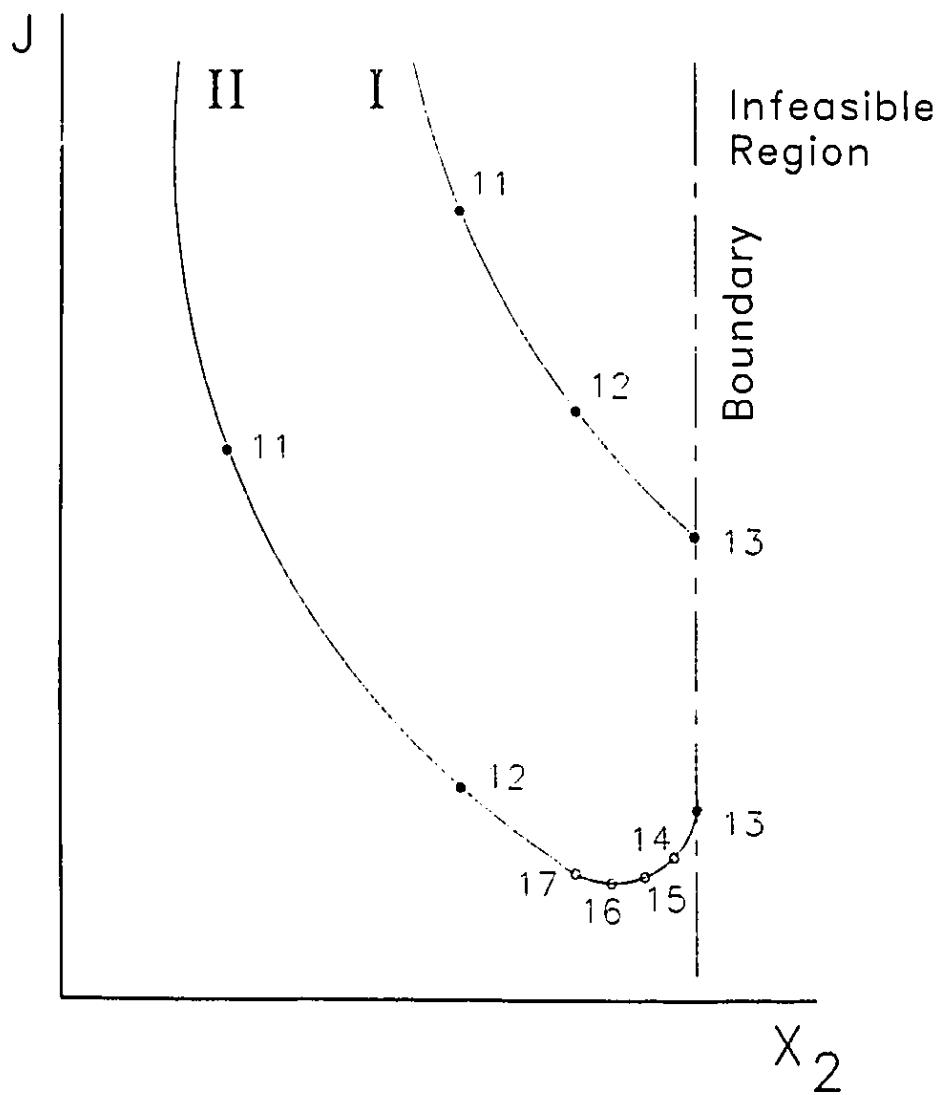


Fig. 6.1b Illustration of new procedure to account for boundary constraints, two possible cases shown

considered to be a function of only two design variables  $x_1$  and  $x_2$ . The Hooke and Jeeves unconstrained optimization method starts with an arbitrarily chosen base vector  $\mathbf{X}_0$  within the feasible region, and begins by probing (called the exploratory moves) along each of the coordinate axes to determine the direction of search (called the pattern direction). As shown in the figure, the variable  $x_1$  is probed, at some prescribed length for each variable, in the positive direction to point 1 and the objective function is found to be greater than its initial value. Thus, this is not a valid point and the variable is probed in the negative direction and is found to be valid. Next, the second variable  $x_2$  is probed in the positive direction to point 3 and the function value is found to be less. The pattern direction is established to be along the vector direction from  $\mathbf{X}_0$  to  $\mathbf{X}_3$ . The pattern direction is usually multiplied by a scalar step length  $\lambda$ , but to simplify the description of the optimization procedure, it is assumed a value of 1. To account for constraints during the exploratory moves, the design variables are simply limited to their maximum or minimum values. This procedure acts as a barrier and restricts the design variables to within the feasible region.

The optimization search continues along the pattern direction with decreasing objective function values to points 4, 5 and 6. At point 7, the function value increases. Since no boundary conditions have been violated, the three function values ( $J_5, J_6, J_7$ ) and their corresponding step lengths ( $\lambda_5, \lambda_6, \lambda_7$ ), which form a concave function, are used in the quadratic interpolation method to determine the optimum step length relative to the starting point, and are used to establish the minimizing design variable set along the direction as point 8.



Starting at point 8, the application of the exploratory moves establishes the pattern direction as along the vector direction from  $X_8$  to  $X_{10}$ . The function decreases along this direction at points 11 and 12. The design variable  $x_2$  attempts to go beyond its boundary but is barred from the infeasible region by its maximum limit. Thus, point 13 is a possible minimum.

Figure 6.1b illustrates the two possible objective function variations as the design variable  $x_2$  changes along this pattern direction. If the changes are along path-I, then a comparison of objective functions  $J_{12}$  and  $J_{13}$  establishes point 13 as a minimum and the next exploratory move starts from this point. More probe moves are required because  $x_1$  could produce further minimization and  $x_2$  could then change as well.

The second possible changes are shown in the figure as path-II. The prescribed step lengths could have been too coarse, and therefore, the points 11, 12 and 13 are monotonically decreasing and do not form a concave function with their  $\lambda$  values; the minimum between points 12 and 13 has been bypassed. Since point 13 is a base point for the exploratory move, we can assume that the first probe of the two variables with the prescribed lengths produce function values greater than that for point 13. Then the second exploratory move, which is part of a convergence criterion, reduces the prescribed probe lengths by 1/10 th. Thus, after starting again at point 13, the smaller probe lengths find the function value decreasing along points 14, 15 and 16. At point 17, the function value increases, and the three point bracketing is established by the points 15, 16 and 17. The quadratic interpolation method determines the optimum  $\lambda$

value relative to point 13 and the minimum point, as point 14, for the next exploratory move.

Thus, the essence of the new procedure to account for boundary constraints has been briefly described. Sections 6.5 and 6.6 give a full description of the procedure.

#### 6.4 Formulation of the Multivariable Multiobjective Optimization Problem

The design vector,  $\bar{X}$ , consists of a set of design variables which have significant influence on the performance of the injector. Thus, the design vector, consisting of the voltage source  $V$ , spring preload  $F$ , spring constant  $K$  and capacitor  $C$ , is defined as:

$$\bar{X} = [ V, F, K, C ]^T \quad (6.6)$$

Consequently, the unconstrained multiobjective function  $J(\bar{X})$  to be minimized is:

$$J(\bar{X}) = w_1 \cdot t_d + w_2 \cdot t_r + w_3 \cdot t_c + w_4 \cdot t_f \quad (6.7)$$

where the four important time objectives are chosen to be:

- $t_d$  - delay time in injector opening
- $t_r$  - time duration of injector lift
- $t_c$  - delay time in injector closing
- $t_f$  - time duration of injector fall

Each objective is assigned a weight  $w_i$ , selected according to its relative importance.

Boundary constraints have been placed on each design variable to ensure that the design is confined within realizable physical limits. This results in the constrained optimization problem posed as:

$$\text{Minimize } [J(\bar{X})] \quad (6.8)$$

subject to side constraints:

$$\begin{aligned} 18 \text{ V} &\leq V \leq 36 \text{ V} \\ 5 \text{ N} &\leq F \leq 25 \text{ N} \\ 20 \text{ kN/m} &\leq K \leq 140 \text{ kN/m} \\ 100 \mu\text{F} &\leq C \leq 1120 \mu\text{F} \end{aligned} \quad (6.9)$$

A behaviour constraint is next imposed on the optimization problem by requiring that the exciting current  $i_e$  must reduce to the solenoid steady-state nominal 7 A current before the solid-state relay is turned off to close the injector after 5 ms; it is stated as:

$$i_e \leq i_{nom} = 7 \text{ A} \quad \text{for} \quad t \leq 5 \text{ ms} \quad (6.10)$$

This steady-state current constraint also ensures that the capacitor is fully charged within the allocated time. Without this constraint, if the closing time is greater than the design objective of 5 ms, the decreased current may not be sufficient to overcome the spring forces and the injector would close prematurely.

### 6.5 Modifications to the Hooke and Jeeves Optimization Method to Account for Constraints

The unconstrained optimization method of Hooke and Jeeves is a direct search method that does not require derivatives of the objective function. Only objective function evaluations are required. The method first performs an exploratory move sequentially along each coordinate of its design vector to determine the direction of search. Once the direction of search is established, the second move is along this pattern

direction which is determined by the vector of the univariate moves. Searching along the pattern direction results in a faster solution than always optimizing along the direction being parallel to the coordinate axes.

Two different approaches are applied to account for each of the current constraint, injector opening status and boundary constraints. During the exploratory and pattern searches, the current constraint is accounted for by reformulating the constrained optimization problem to an unconstrained one by the addition of a penalty term to the objective function. The optimization problem is then restated as:

$$J'(\bar{X}) = \text{Minimize} \left( J(\bar{X}) + \sum_{p=1}^4 (H_p(\bar{X})) \right) \quad (6.11)$$

where index  $p=1$  refers to the current constraint, which is checked up to the solid-state closing time at 5 ms, as:

$$\text{for } p=1; \text{ if } i_e - i_{nom} > 0, \text{ then } H_1(\bar{X}) = 10.0, \text{ else } H_1(\bar{X}) = 0 \quad (6.12)$$

At each iteration for a given design vector  $\bar{X}$ , the dynamic response of the solenoid is simulated and the unconstrained objective function  $J(\bar{X})$  is evaluated. Whenever the current requirement is satisfied, the penalty function returns to a value of zero. Otherwise,  $H_1$  will be positive when the constraint is violated. A penalty value of 10, which is approximately 3 times the expected objective function value, is sufficient to indicate that the current constraint has been violated.

Indices  $p=2, 3, 4$  are not for constraints, but for the condition checking if the injector opens at all, if it fully opens within the 5 ms duty time, and if the injector

completely closes within the simulation time period, respectively. This leads to a sequential checking, stated as:

$$\begin{aligned}
 &H_2 = H_3 = H_4 = 10 \quad \text{initialize the penalty functions} \\
 &dummy = 0 \quad \text{and initialize the dummy variable "dummy"} \\
 &\text{(injector opens)} \\
 &\text{if } h_{\max} - h > 0, \text{ then } H_2 = 0 \text{ and } dummy = 1 ; \\
 &\text{(injector is fully open)} \\
 &\text{if } dummy = 1 \text{ and } h = 0, \text{ then } H_3 = 0 \text{ and } dummy = 2 ; \\
 &\text{(injector is fully closed)} \\
 &\text{if } dummy = 2 \text{ and } h = h_{\min}, \text{ then } H_4 = 0 \text{ and } dummy = 3 ;
 \end{aligned} \tag{6.13}$$

The air-gap  $h$  is equal to zero when the injector needle is fully open.  $h_{\max}$  is the maximum needle lift at 0.635 mm, and  $h_{\min}$  is the minimum opening which is when the needle is closed at 0.0 mm.

To account for the boundary constraints, as given by Equation (6.9), during the exploratory moves, a simple approach is taken in which the design variables are assigned to their maximum or minimum values whenever that variable goes beyond its limit. This maximum and minimum specification is the only change required to the method to account for the boundary constraints. During the pattern search, three consecutive step lengths and their corresponding objective function values are tracked, and programming logic control determines if the solution lies on the boundary. The pattern search method will be fully explained in Section 6.6.

The modifications to the Hooke and Jeeves optimization method to take into account the constraints is described as follows:

step 1: For  $k = 1$ , start the exploratory search by selecting an arbitrarily chosen design vector  $\bar{x}_{k,0} = [x_1, x_2, \dots, x_n]^T$ , called the starting base point, where  $n$  is the number of design variables, within the feasible region. Evaluate the corresponding objective function  $J(\bar{x}_{k,0})$ . Specify the boundary constraints of each variable, given by its maximum  $x_{i,max}$  and minimum  $x_{i,min}$  values. Establish prescribed probe lengths  $\Delta x_i$  for each unit coordinate directions  $\bar{u}_i$ , defined as:

$$\bar{u}_1 = [1, 0, 0, \dots, n]^T$$

$$\bar{u}_2 = [0, 1, 0, \dots, n]^T$$

$$\bar{u}_3 = [0, 0, 1, \dots, n]^T$$

.

.

$$\bar{u}_n = [0, 0, 0, \dots, 1]^T$$

step 2: Perturbate each variable  $x_i$  about the current base point  $\bar{x}_{k,i-1}$ , sequentially for  $i = 1, 2, \dots, n$  to obtain the point  $\bar{x}_{k,n}$ . If any variable is perturbed beyond its constraint, set that variable to its maximum  $x_{i,max}$  or minimum  $x_{i,min}$  value. The exploratory search algorithm is as follows, where the double underlined statements are the only changes to the Hooke and Jeeves optimization method:

$$\bar{X}_{k,i} = \left\{ \begin{array}{l} \bar{X}_{k,i-1} + \Delta x_i \bar{u}_i \quad \underline{\text{limited by } x_{i,\max}} \\ \text{if } J^+ = J'(\bar{X}_{k,i-1} + \Delta x_i \bar{u}_i) < J'(\bar{X}_{k,i-1}) \\ \bar{X}_{k,i-1} - \Delta x_i \bar{u}_i \quad \underline{\text{limited by } x_{i,\min}} \\ \text{if } J^- = J'(\bar{X}_{k,i-1} - \Delta x_i \bar{u}_i) < J'(\bar{X}_{k,i-1}) \\ \bar{X}_{k,i-1} \\ \text{if } J'(\bar{X}_{k,i-1}) < \min(J^+, J^-) \end{array} \right. \quad (6.14)$$

step 3: At the end of  $n$  exploratory moves, the point  $\bar{X}_{k,n}$  is compared to the base point  $\bar{X}_{k,0}$ . If there has been no change between the two points, the probe lengths  $\Delta x_i$  are reduced, and step 2 is repeated. The optimization process is considered to have converged to a solution whenever each probe length is reduced below a corresponding small value of  $\varepsilon_i$ . The program is terminated when the following criteria is satisfied:

$$\Delta x_i < \varepsilon_i \quad \text{for } i = 1, 2, \dots, n \quad (6.15)$$

step 4: If the two points compared in step 3 are different, then the pattern search direction is taken as:

$$\bar{S} = \bar{X}_{k,n} - \bar{X}_{k,0} \quad (6.16)$$

The pattern search is to find the new base point:

$$\bar{X}_{k+1,0} = \bar{X}_{k,n} + \lambda \bar{S} \quad (6.17)$$

where  $\lambda$  is a scalar step length. The multivariable optimization problem is now reduced to a one-dimensional search for the optimal scalar  $\lambda^*$  that minimizes the objective function:

$$J'(\lambda) = J'(\bar{X}_{k,n} + \lambda \bar{S}) \quad (6.18)$$

When the solution to the one-dimensional optimization problem is concluded, the new base point given by Equation (6.17) is updated by  $\lambda = \lambda^*$ , the exploratory search index  $k$  is incremented by 1, and the multivariable optimization problem is repeated starting at step 2.

## 6.6 Introduction of a New Procedure to Account for Boundary Constraints to the One-Dimensional Optimization Problem to Determine Optimum Step Length

The one-dimensional search for the optimum scalar step length  $\lambda^*$  is calculated relative to the starting base point  $\bar{X}_{k,n}$ . A maximum of three consecutive scalar step lengths ( $\lambda_0, \lambda_1, \lambda_2$ ) and their corresponding objective function values ( $J'_0, J'_1, J'_2$ ) are tracked to determine the optimal step length and to determine if any design variables have violated boundary constraints. The program is described as follows:

step 1: The program is initiated with known values from the  $k^{\text{th}}$  exploratory search, which are (step 1a):



**STEP 1a**

- $\bar{X}_{k,n}$  - the base point design vector
- $J'_0 = J'(\bar{X}_{k,n})$  - the objective function evaluated at the base point
- $\bar{S}$  - the pattern search direction

Next, establish a prescribed incremental change  $\delta$  for the step length  $\lambda$ , and search for the temporary base point  $\bar{X}_1$  along the pattern direction  $\bar{S}$  (step 1b):

**STEP 1b**

- $\lambda_0 = 0$  - the initial step length set at zero
- $\delta$  - establish incremental value for the step length
- $i = 1$  - initialize pattern search index
- $\lambda_1 = \lambda_0 + \delta$  - increment the step length
- $\bar{X}_1 = \bar{X}_{k,n} + \lambda_1 \bar{S}$  - evaluate temporary base point
- call **MAXMIN** - if any boundary constraints are violated,  
 $\lambda_1$  is returned to bring variable at boundary  
(**BORDER** returned)

Once the temporary base point is evaluated, the design vector is checked for any boundary violations by calling subroutine **MAXMIN** (the subroutine will be fully described in Appendix D). The subroutine returns two values for constraint violations. The first is a logic indicator **BORDER** set to **TRUE** if any violations have occurred. The second value returned is the re-evaluation for the

magnitude of the largest step length  $\lambda_j$ , calculated from the variable that went the "most" beyond its constraint. If no borders have been violated, *BORDER* is set to FALSE and the step length  $\lambda_j$  remains unchanged.

The step length  $\lambda_j$  is then checked if the pattern search was started from a boundary. In such a case, recalculation from the subroutine would have returned  $\lambda_j = 0$ . Since the search cannot go beyond any constraints, the pattern direction  $\bar{S}$  is reversed and the temporary base point  $\bar{X}_1$  is recalculated with the original  $\lambda_j$ . Subroutine MAXMIN is called to examine if any design variables have violated boundary constraints after reversal of the pattern direction (step 1c):

**STEP 1c**

*if*  $\lambda_1 = 0$

$\lambda_1 = \lambda_0 + \delta$                     - *reset step length*

$\bar{S} = -\bar{S}$                                 - *reverse pattern direction*

$\bar{X}_1 = \bar{X}_{k,n} + \lambda_1 \bar{S}$                 - *recalculate temporary base point*

*call MAXMIN*                            - *check for boundary violations*  
   ( $\lambda_1$  and *BORDER* returned)

Next, after either of the three step length cases discussed above, *BORDER* is tested for variables laying on the boundary. If FALSE, continue the program at step 2, otherwise, calculate the temporary base point  $\bar{X}_1$  and evaluate the

corresponding objective function  $J'_1$ . The objective  $J'_1$  is then compared to the previous objective  $J'_0$ . If the comparison is  $J'_0 > J'_1$  and since  $J'_1$  is on the boundary, then the solution lies on the boundary and a logic indicator  $SAB$  is set to TRUE and the program continues at step 2. Otherwise  $J'_0 \leq J'_1$ . Thus, the step length  $\lambda_j$  is reset, the pattern direction  $\bar{S}$  is reversed, the temporary base point  $\bar{X}_1$  is recalculated, and the subroutine MAXMIN is called to determine boundary conditions (step 1e):

**STEP 1e**

**if BORDER = TRUE**

$\bar{X}_1 = \bar{X}_{k,n} + \lambda_1 \bar{S}$                       - recalculate temporary base point  
using  $\lambda_1$  returned from MAXMIN

$J'_1 = J'(\bar{X}_1)$                                 - calculate objective function at  $\bar{X}_1$

**else continue programme at step 2**

**if  $J'_0 \leq J'_1$**

$\lambda_1 = \lambda_0 + \delta$                                 - reset the step length

$\bar{S} = -\bar{S}$                                         - reverse pattern search direction

$\bar{X}_1 = \bar{X}_{k,n} + \lambda_1 \bar{S}$                         - evaluate temporary base point

**call MAXMIN**                                    - check for boundary violations  
( $\lambda_1$  and BORDER returned)

**else set SAB = TRUE and continue programme at step 2**

After the pattern direction reversal, *BORDER* is checked again for boundary conditions. If the temporary base point  $\bar{x}_1$  is not beyond any constraints, the program continues at step 2. Otherwise, the solution lies on the boundary and *SAB* is set to *TRUE*,  $\bar{x}_1$  is calculated from the step length  $\lambda_1$  returned from subroutine *MAXMIN*, and the objective  $J'_1$  is evaluated at  $\bar{x}_1$ . If  $J'_0 > J'_1$ , the solution at the boundary is  $\bar{x}_1 = \bar{x}_{k,n} + \lambda_1 \bar{s}$  corresponding to the objective  $J'_1$ , otherwise the boundary solution is  $\bar{x}_1 = \bar{x}_{k,n}$  corresponding to the objective  $J'_0$  (step 1f):

***STEP 1f***

*if BORDER = TRUE*

$$\bar{x}_1 = \bar{x}_{k,n} + \lambda_1 \bar{s} \quad - \lambda_1 \text{ returned MAXMIN}$$

$$J'_1 = J'(\bar{x}_1)$$

*SAB = TRUE*                    - set logic indicator

*else continue programmeat step 2*

*if J'\_0 > J'\_1*

$$\bar{x}_1 = \bar{x}_{k,n} + \lambda_1 \bar{s} \quad - \text{solution at boundary}$$

*else*  $\bar{x}_1 = \bar{x}_{k,n}$                     - solution at boundary,  $\lambda_1 = 0$

step 2: First, the logic state  $SAB$  must be determined. If  $SAB=TRUE$ , then the solution for the temporary base point  $\bar{x}_1$  and step length  $\lambda_1$  are known and lie on the boundary. Therefore, the pattern search is completed and the exploratory search is restarted at index  $k$  incremented by 1. The new base point is set to  $\bar{x}_{k,0} = \bar{x}_1$ , and the program continues at step 2 of Section 6.5.

Otherwise, entry at this point of the program is from the result of  $BORDER$  being tested as  $FALSE$ . Thus, from the known step length  $\lambda_1$ , the objective  $J'_1$  is calculated and compared to the previous objective  $J'_0$ . If  $J'_1 > J'_0$ , then the pattern search must be reversed. Next a logic indicator  $FINISH$  is set to  $FALSE$  indicating that a third temporary base point must be sought for, and the second point  $\bar{x}_1$  is memorized in  $\bar{x}_{1,mem}$ . At this stage in the program, two of the three points being tracked are known, namely the step lengths  $(\lambda_0, \lambda_1)$  and their corresponding objective functions  $(J'_0, J'_1)$ .

step 3: The search for the third temporary base point starts by determining the state of the logical variable  $FINISH$ . If  $TRUE$ , then the exploratory index  $k$  is incremented by 1, the new base point is set to  $\bar{x}_{k,n} = \bar{x}_2$ , and the program continues at step 2 of Section 6.5. Otherwise, the step length  $\lambda_2$  is incremented by  $\delta$ , the third temporary base point is calculated as  $\bar{x}_2 = \bar{x}_{k,n} + \lambda_2 \bar{s}$ , and the subroutine  $MAXMIN$  is called to determine boundary conditions. If any design variables have gone beyond its constraint, the subroutine returns  $\lambda_2$  so that any

**STEP 2**

*if SAB = TRUE*                      - *solution at boundary*

*k = k+1*                                - *increment exploratory index*

$\bar{X}_{k,0} = \bar{X}_1$                         - *new base point equal to temporary base point, return to and perform next exploratory search*

*else*

$\lambda_1$                                     - *known from BORDER calls*

$J'_1 = J'(\bar{X}_1)$                         - *calculate objective function at  $\lambda_1$*

*if  $J'_1 > J'_0$*                         - *reverse pattern direction and variable indices*

$\bar{S} = -\bar{S}$                               - *reverse pattern direction*

*swap variable indices*

$J'_{temp} = J'_0$                          $\bar{X}_{temp} = \bar{X}_{k,n}$

$J'_0 = J'_1$                                $\bar{X}_{k,n} = \bar{X}_1$

$J'_1 = J'_{temp}$                          $\bar{X}_1 = \bar{X}_{temp}$

*else no pattern direction and index changes*

**FINISH = FALSE**                    - *set logic indicator, search for third point*

$\bar{X}_{1,mem} = \bar{X}_1$                         - *memorize second temporary base point*

### STEP 3

if *FINISH* = *TRUE*

- pattern search is finish

$k = k+1$

- increment exploratory search index

$\bar{X}_{k,0} = \bar{X}_2$

- new base point equal to temporary base point, return to and perform next exploratory search

else

$\lambda_2 = \lambda_1 + \delta$

- increment the step length

$\bar{X}_2 = \bar{X}_{k,n} + \lambda_2 \bar{S}$

- calculate temporary base point

call *MAXMIN*

- determine boundary conditions

if *BORDER* = *TRUE*

- if boundaries have been exceeded

use  $\lambda_2$  from *MAXMIN*

$\bar{X}_2 = \bar{X}_{k,n} + \lambda_2 \bar{S}$

- recalculate temporary base point

continue

$J'_2 = J'(\bar{X}_2)$

- calculate objective function corresponding to  $\lambda_2$

if  $[(J'_0 > J'_1) \text{ AND } (J'_1 < J'_2)]$

AND  $[(\lambda_0 < \lambda_1) \text{ AND } (\lambda_1 < \lambda_2)]$  - convex bounded

enter Quadratic Interpolation Routine to calculate optimum  $\lambda^*$

$\bar{X}_2 = \bar{X}_{k,n} + \lambda^* \bar{S}$

- new base point

*FINISH* = *TRUE*

- return to beginning of step 3 to perform next exploratory search

variable of  $\bar{x}_2$  will be recalculated at its boundary value. Next, the objective function  $J'_2$  corresponding to  $\bar{x}_2$  is evaluated. If the objective function  $J'_1$  is bounded by the objectives  $J'_0$  and  $J'_2$  and is convex, and if the three step lengths increase consecutively, then the optimum scalar step length  $\lambda^*$  can be found by a quadratic interpolation method.

step 4: If the objective function  $J'_1$  is not bounded, then the logical variable *BORDER* is tested. If TRUE, and if  $J'_1 \leq J'_2$ , then the solution does not lie on the boundary and is  $\bar{x}_2 = \bar{x}_{1,mem}$ . Otherwise  $J'_1 > J'_2$ , and the solution is  $\bar{x}_2$  which lies on the boundary. If *BORDER* = FALSE, and if both  $J'_0 = J'_1$  and  $J'_1 \leq J'_2$  are TRUE, then the solution is  $\bar{x}_2 = \bar{x}_{1,mem}$ . For all cases, *FINISH* is set to TRUE and the program continues at step 3. Otherwise, the objective function gradually decreases as the step length is increased. The indices of objective functions and step lengths are shifted, and the temporary base point  $\bar{x}_2$  must again be re-evaluated starting from step 3.



**STEP 4**

if *BORDER* = *TRUE*      - compare  $J'_1$  and  $J'_2$

if  $J'_1 \leq J'_2$  then  $\bar{X}_2 = \bar{X}_{1,mem}$

if  $J'_1 > J'_2$  then  $\bar{X}_2 = \text{boundary value}$

*FINISH* = *TRUE*

continue programme at step 3

if *BORDER* = *FALSE*

and if ( $J'_0 = J'_1$ ) AND ( $J'_1 \leq J'_2$ )

$\bar{X}_2 = \bar{X}_{1,mem}$

*FINISH* = *TRUE*

continue programme at step 3

else                      - swap indices

$\lambda_0 = \lambda_1$        $\lambda_1 = \lambda_2$

$J'_0 = J'_1$        $J'_1 = J'_2$

$\bar{X}_{1,mem} = \bar{X}_2$

continue programme at step 3

and search for next  $\lambda_1, \bar{X}_2, J'_2$

## 6.7 Global Optimality

The optimization method described in Sections 6.5 and 6.6 does not guarantee that the solution vector will result in a global minimum objective function. A global minimum is achieved if and only if the objective function is known to be concave, in which case it is also a local minimum. In addition, the Weierstrass Theorem [49] can prove the existence of a global minimum, but the existence theorem does not show how to achieve this minimum. Thus, even if a global minimum is known to exist, and especially if the design variables are not independent but interact, then the only way to determine the global minimum is to perform an exhaustive minimization search for all variable combinations and permutations. There are no known optimization methods that will result in a global minimum.

For the optimization problem under consideration, the only known fact is that there is interaction between variables. But, there is no need to perform an exhaustive search on the design variables since there is some 'a priori' knowledge about variable interactions, and about the trend of the objective function for design variable changes obtained from the performance index study of Section 5.4.

From the performance index study, it can be seen that the objective function tends to decrease for larger applied voltages and for larger capacitor values. This voltage and capacitor combination provides an almost instant high current boost to create a rapid rise in solenoid force and quick opening of the injector. The interaction between the applied voltage and the capacitor change is that a large capacitance has a tendency to limit the

maximum applied voltage. As a result, the capacitor value is influenced by the constraint on the exciting current to reach its nominal value at steady-state conditions, before it is cut off to close the injector, as imposed by Equation (6.10).

It can also be concluded that the objective function decreases for smaller spring preload values because less solenoid force is required to overcome the initial force during the injector opening. In addition, the objective function decreases as the spring constant increases because the compressed spring provides more force increase to balance the solenoid force and quickly close the injector. The interaction between these two variables shows that a given spring preload force limits the maximum spring rate value when the injector is fully opened, and vice versa. For the small spring rate values, it is the spring preload value that provides a trade-off between the injector opening delay and closing delay periods.

If the variable interactions are not considered in an optimization program, there is a possibility that the single solution provides a local minimum instead of a global minimum. To ensure that the result is a global minimum, the optimization program described in Sections 6.5 and 6.6 is executed in such a manner as to obtain a first set of design vector solutions and the objective function values. Next, the optimization programme is executed again, with the solution vector used as the starting base point and modified by decreasing the spring rate and capacitor change by one half of their values, while the applied voltage and spring preload values are unchanged. Once the second solution vector is evaluated, the procedure of decreasing the spring rate and capacitor

values by one half is repeated, and the optimization programme is then executed again. By applying such a procedure, the limits on variables resulting from their interaction, are avoided. The program is terminated when the difference between the present objective function value and the previous iteration value remains within 0.5 %. A comparison of the smallest value with the local minimum objective function values, results in the global minimum and the corresponding optimum design vector.

## 6.8 Optimization Results

The system undergoing the optimization process is a solenoid operated injector developed for natural gas discharging directly into the combustion chamber of an internal combustion engine. The optimization procedure starts with the base point design vector selected arbitrarily within the feasible region as:

$$\bar{X}_{k,0} = [27 V, 15 N, 80 kN/m, 610 \mu F]^T$$

In this optimization program, an equal weight of 1.0 is initially assigned to each of the four time objectives, as defined by Equation (6.7). This signifies that all these objectives have equal importance.

The simulation process revealed that the application of the optimization technique required a total of 306 iterations. The number of iterations is equal to the number of objective function (or system simulation) calls, which included the exploratory moves, pattern direction moves, and quadratic interpolations. To ensure that a global minimum

is reached, independent of the starting base point, three optimization solution sets were obtained, as shown in Table 6.1. Included in the table and corresponding to each optimization set, are the optimum design vector  $\bar{x}^*$ , the four important time objectives  $(t_d, t_r, t_c, t_f)$  and the optimum objective function  $J^*$ . The optimization is automatically terminated after set 3 because the difference between the objective function value and that of the previous set 2, is within the termination criterion of 0.5 %. The objective function value for the optimization set 3 is actually 0.9  $\mu\text{s}$  less than that for the set 2, however, the values shown in the table are the same because of fourth decimal round-offs. Therefore, quantitatively, the design vector from optimization set 3 is being considered as the optimum solution.

If the global optimality, as described in Section 6.5 was not considered, the solution set 1 would have been mistakenly accepted as the optimum result. The capacitor value has interacted and limited the maximum applied voltage to 33.85 V. The corresponding objective function value is 3.274 ms, which is greater than the value for the global minimum of 3.184 ms corresponding to the set 3.

With respect to the global optimum design vector, it is only the voltage design variable that has reached its higher boundary constraint of 36 V. All other design variables remain within their constraints, although the spring preload is very close to its lower constraint value. From a comparison between the iteration sets 2 and 3, it is interesting to note that the 8.06% increase in spring constant and the 3.80% increase in

SET		1	2	3	% change of set 2 w.r.t. set 3
ITERATIONS		108	40	158	
$\bar{X}^*$	$V$ (V)	33.85	36.0	36.0	0.0
	$F$ (N)	5.0	5.0	5.19	3.80
	$K$ (kN/m)	90.430	83.471	90.786	8.06
	$C$ ( $\mu$ F)	976	813	820	0.87
$t_d$ (ms)		0.711	0.668	0.671	0.45
$t_r$ (ms)		1.482	1.414	1.463	3.31
$t_c$ (ms)		0.038	0.062	0.033	-87.74
$t_f$ (ms)		1.043	1.040	1.017	-2.29
$J^* = J'(\bar{X}^*)$ (ms)		3.274	3.184	3.184	-0.03

Table 6.1 Optimization results showing the 3 intermediate iteration sets and corresponding design vector values, the four time objectives, and the multiobjective function values.

spring preload significantly reduce the delay period before the needle fall  $t_c$  by -87.74%. It can be also seen that the combined time period increase in opening delay  $t_d$  and the rise time  $t_r$  is compensated by the combined time period decrease for the delay before fall  $t_c$  and the fall time  $t_f$ . This indicates that the overall objective function value is not as sensitive to the spring variable changes, as it is to the individual delay time period changes.

A graph of the objective function being normalized by the optimum value of 3.184 ms for increasing iteration steps is shown in Figure 6.2. A normalized objective function value of 1 indicates optimality. Large function values are not indicated, since the graph is magnified to show the function values of interest. The dashed vertical lines indicate a large jump in objective function values because the current constraint has been violated. A note is added on the figure stating the number of iterations required to converge to each of the three solution sets.

Figure 6.3 illustrates the variations in the four important time objectives ( $t_d$ ,  $t_r$ ,  $t_c$ ,  $t_f$ ) for the progressing iteration. Again, large time values are not shown because the graph is enlarged to amplify the time values of interest. The large time values, as shown by the dashed-line vertical jumps on the delay before fall time  $t_c$  and fall time  $t_f$  curves, result from the injector not closing within the prescribed 5 ms duty time.

The design variables of voltage, spring preload, spring constant and capacitor values for increasing number of iterations, are shown in Figures 6.4 to 6.7, respectively. The spikes indicated on these graphs are due to the univariate exploratory moves, where

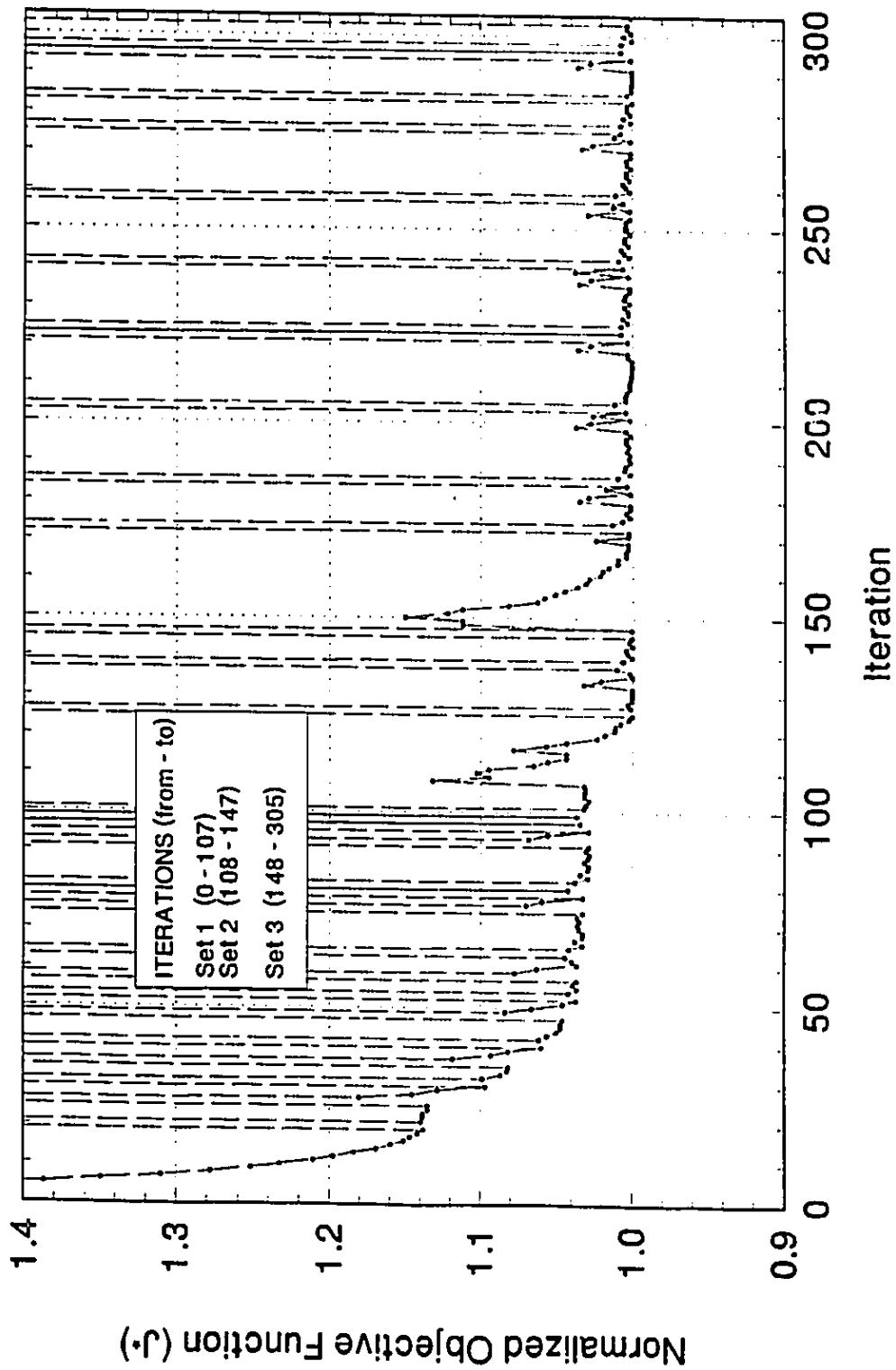


Fig. 6.2 Normalized objective function w.r.t. iteration sequence



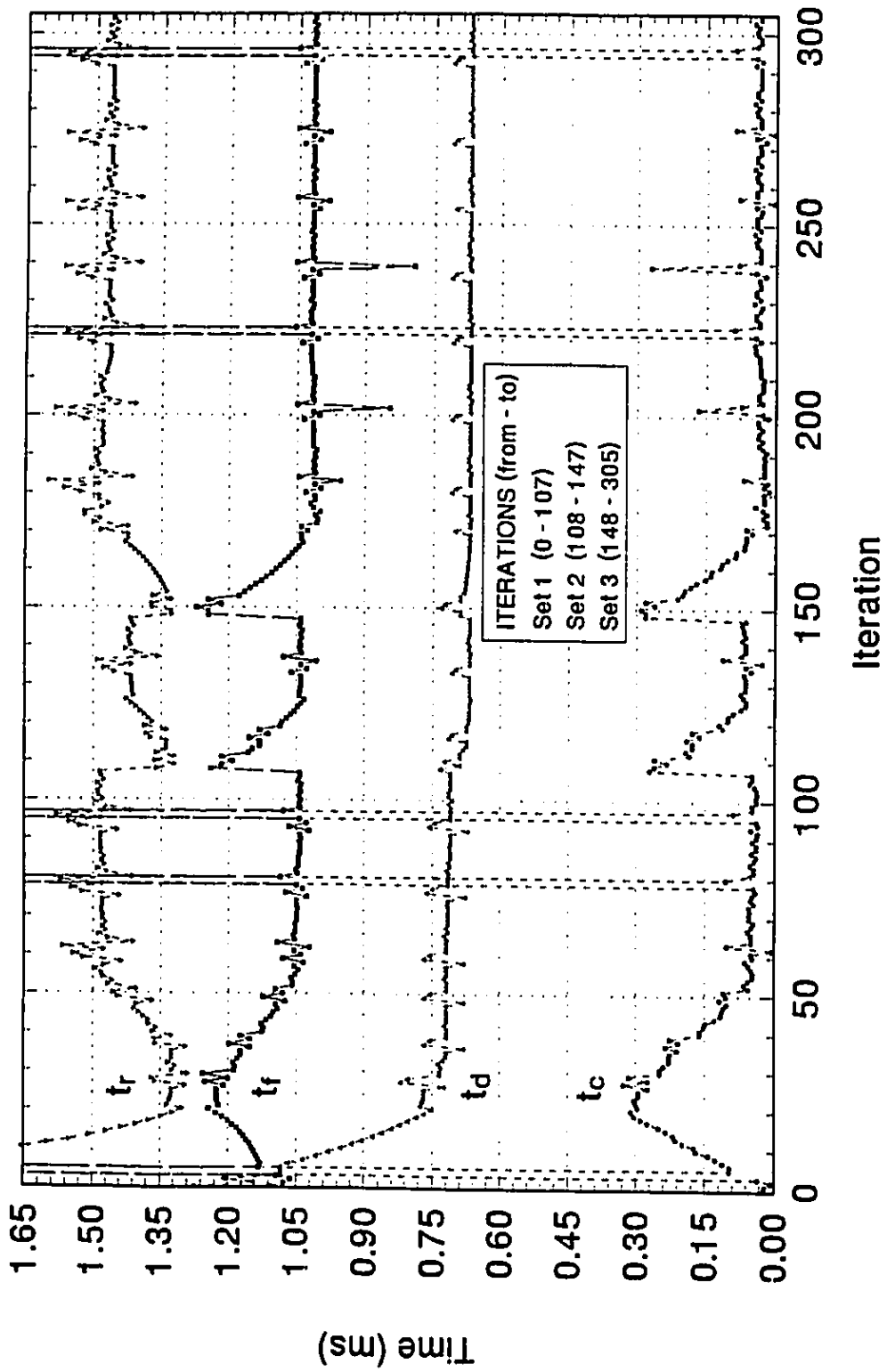


Fig. 6.3 Four time objectives w.r.t. iteration sequence

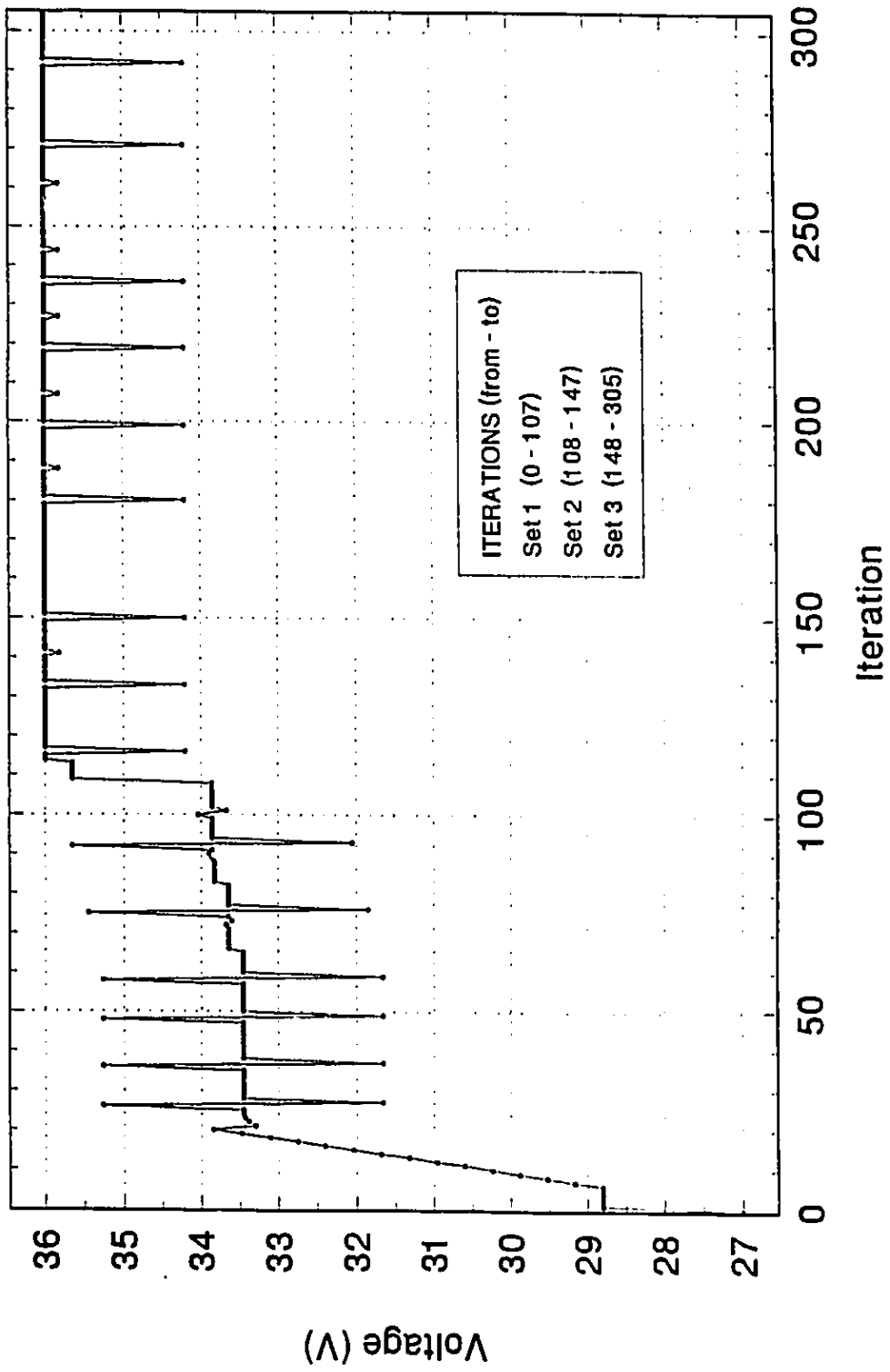


Fig. 6.4 Change in voltage w.r.t. iteration sequence

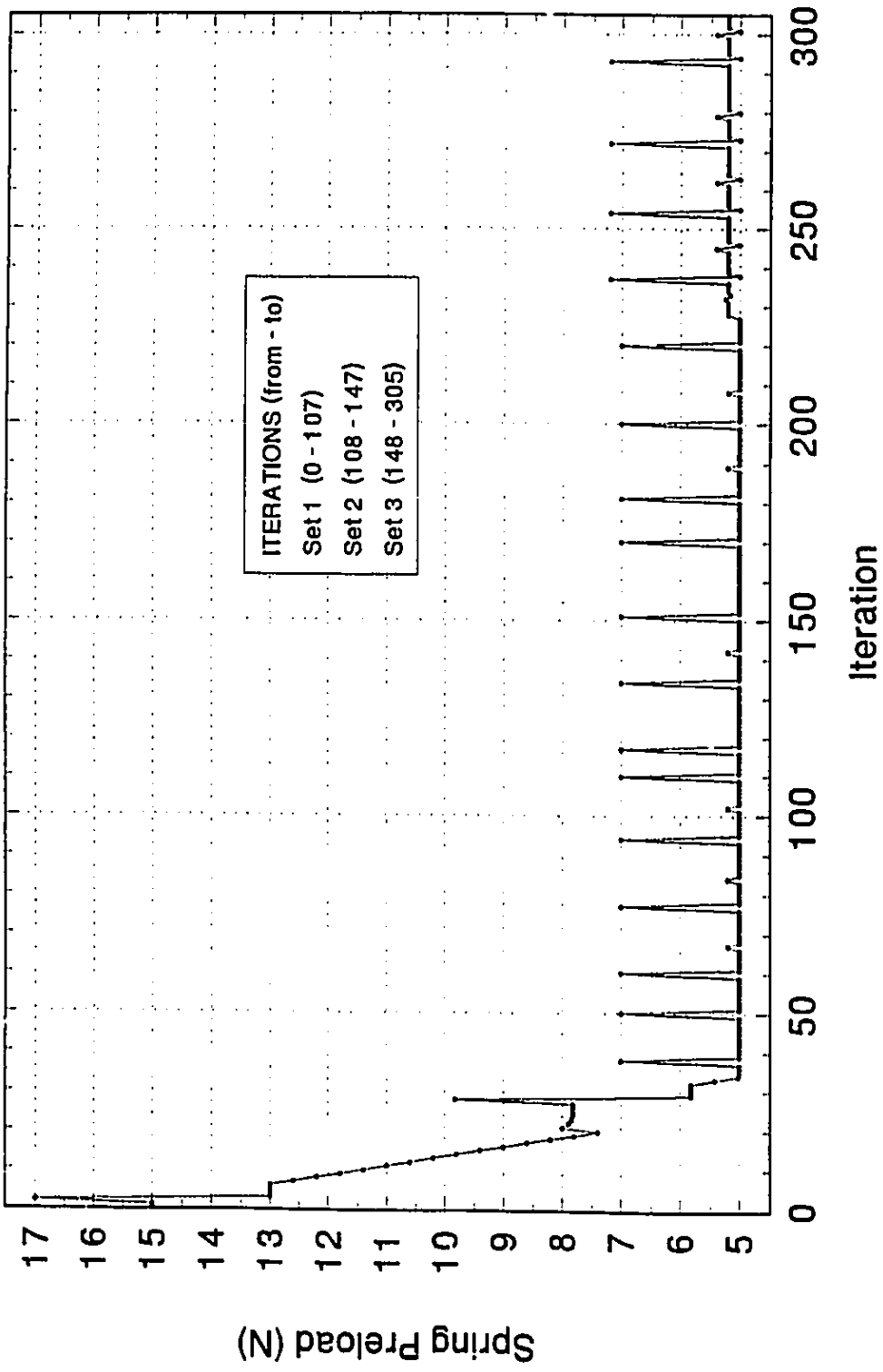


Fig. 6.5 Change in spring preload w.r.t. iteration sequence

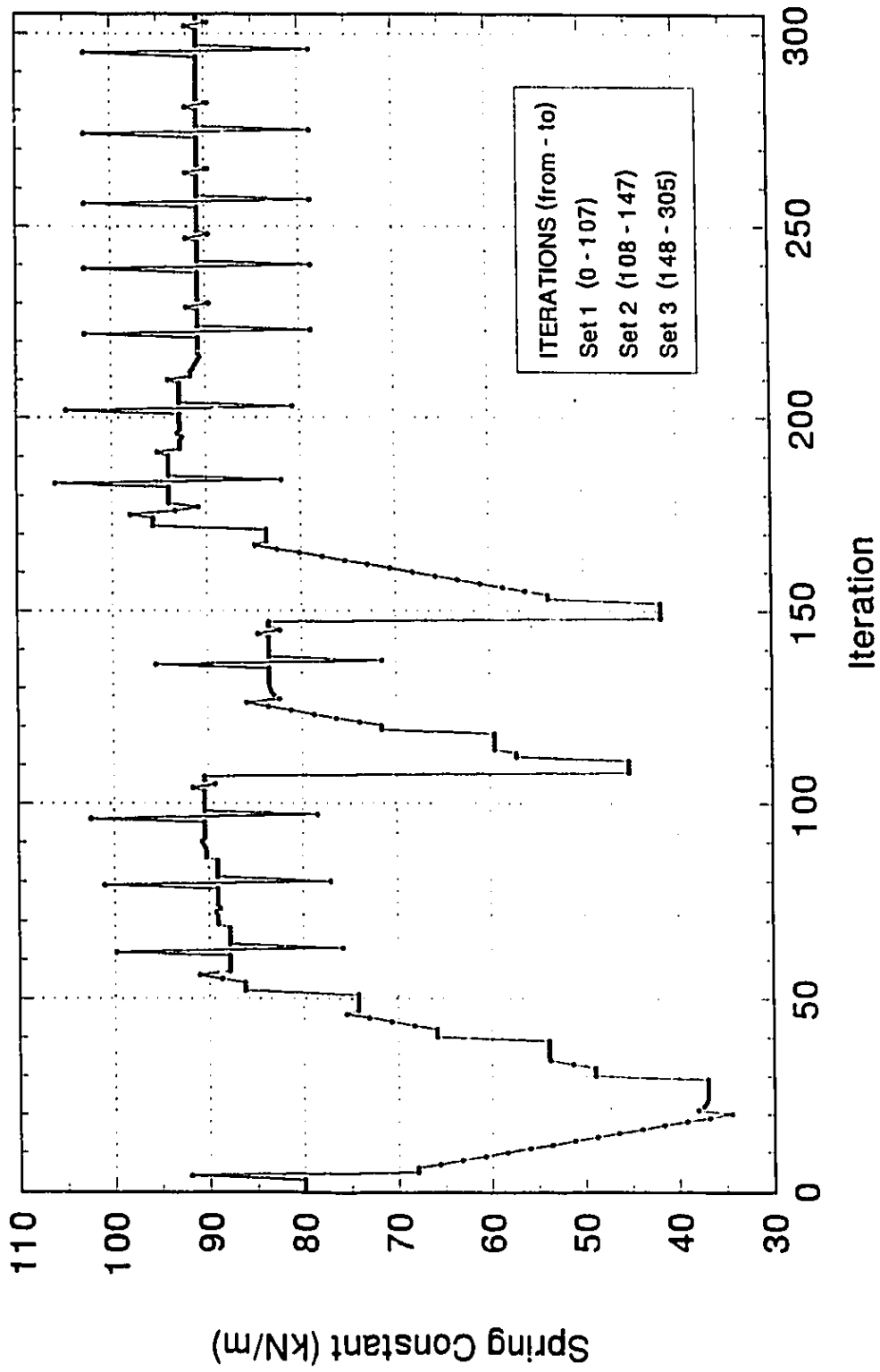


Fig. 6.6 Change in spring constant w.r.t. iteration sequence

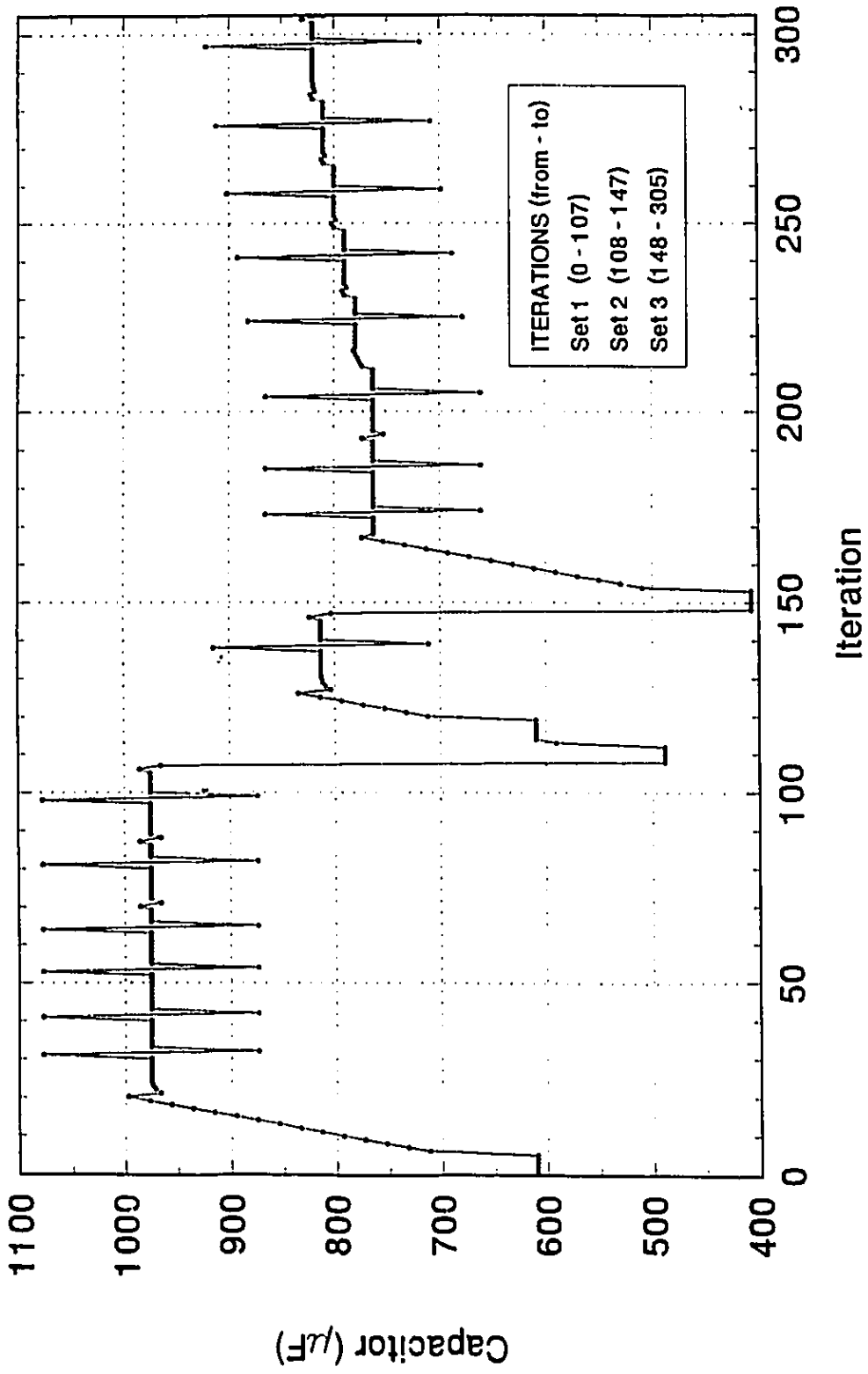


Fig. 6.7 Change in capacitance w.r.t. iteration sequence

only one design variable is changed at a time. At the end of the exploratory search, the pattern direction vector is defined and results in all variables to change simultaneously with iteration increment. When the objective function reaches a minimum along the defined direction, the pattern search is terminated and the exploratory search begins again. If the solution to any design variable reaches a boundary, the pattern direction component for this variable will be zero and there will be no corresponding variable change during the pattern search.

## **6.9 Injector Transient Performance Comparison for Optimum and Typical Design Variables**

The solenoid force and injector needle dynamic response, after the optimum design vector values are used to simulate the natural gas injection process, is shown in Figure 6.8. For comparison purposes, also shown in the same figure is the dynamic response for a typical set of not optimized design variables. The corresponding voltage and current characteristics for both optimized and typical systems, are shown in Figures 6.9 and 6.10, respectively. Numerical values for system design variables, the four important time delays ( $t_d$ ,  $t_r$ ,  $t_c$ ,  $t_f$ ) with zero time as reference, and the peak boost current and the time of occurrence, are tabulated in Table 6.2 for comparison.

With reference to Figure 6.8, both the optimized and typical system needle lift deviates from the ideal square wave motion profile corresponding to the pulse width shape. Although the pulse width command signal for both system simulations is 5 ms (starting at zero seconds), the injection time which is defined from the start of injector

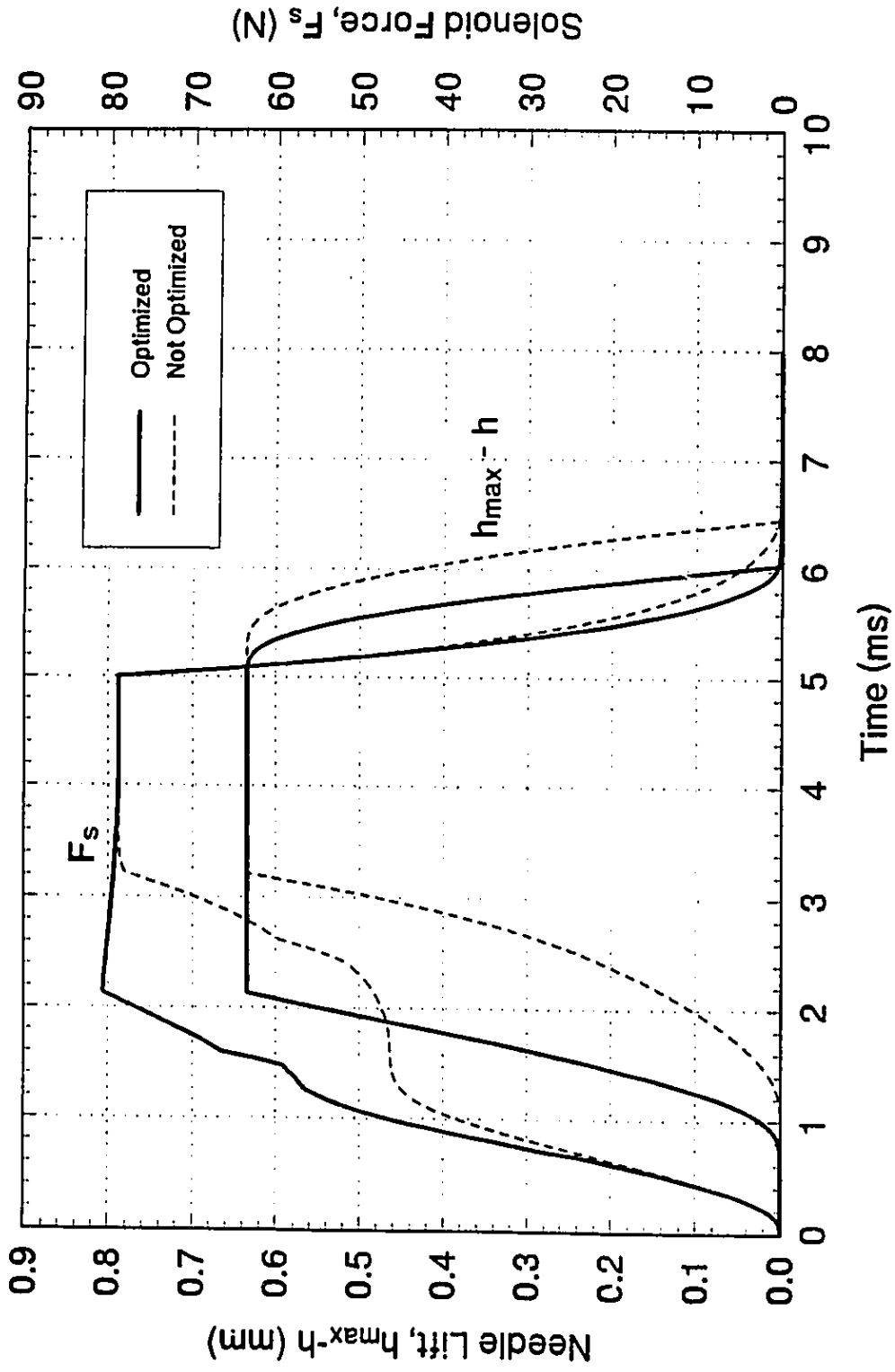


Fig. 6.8 Injector needle lift and solenoid force dynamic response for optimized and typical systems

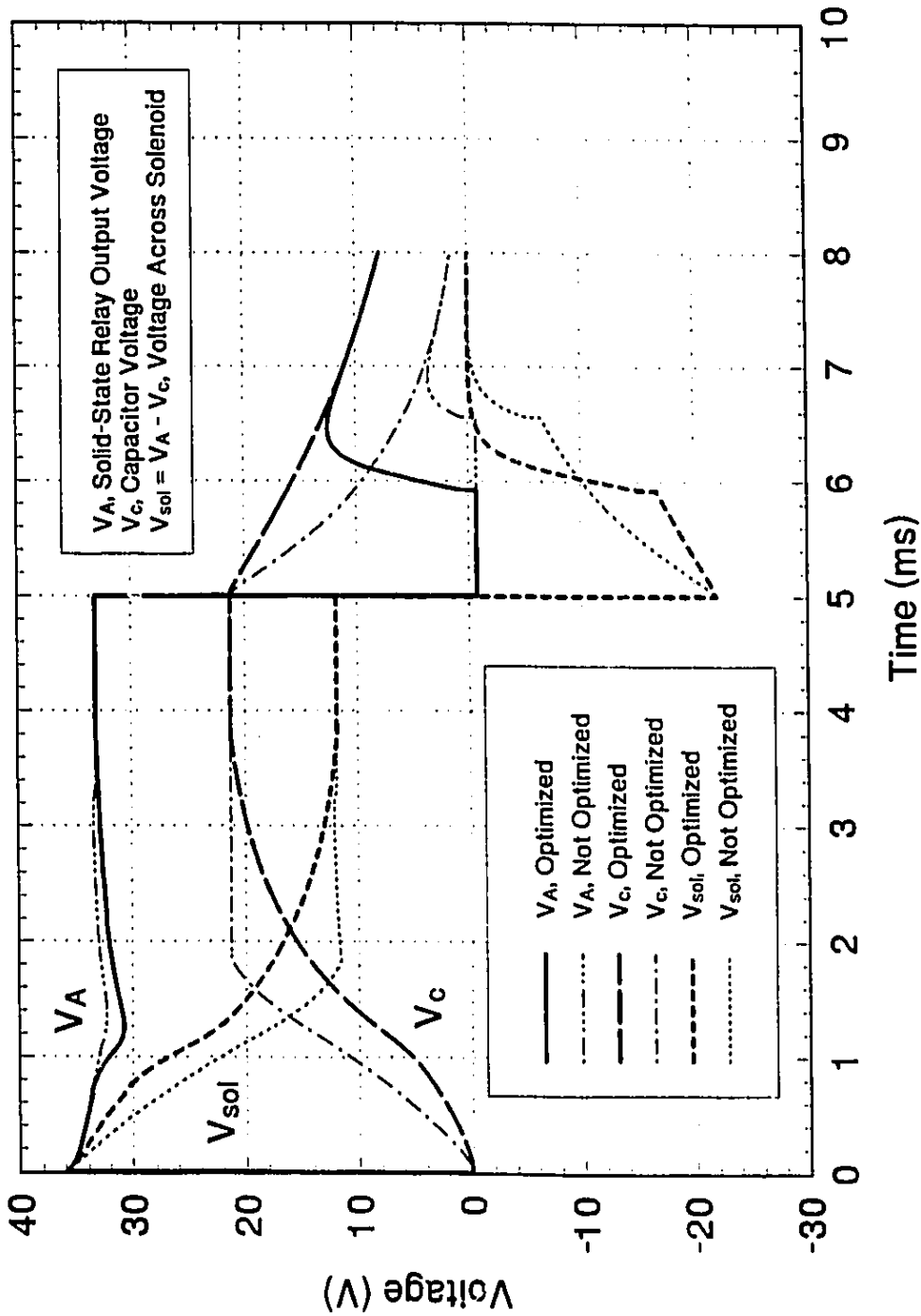


Fig. 6.9 Voltage transient characteristics for optimized and typical systems; for solid-state relay output, capacitor and across solenoid coil



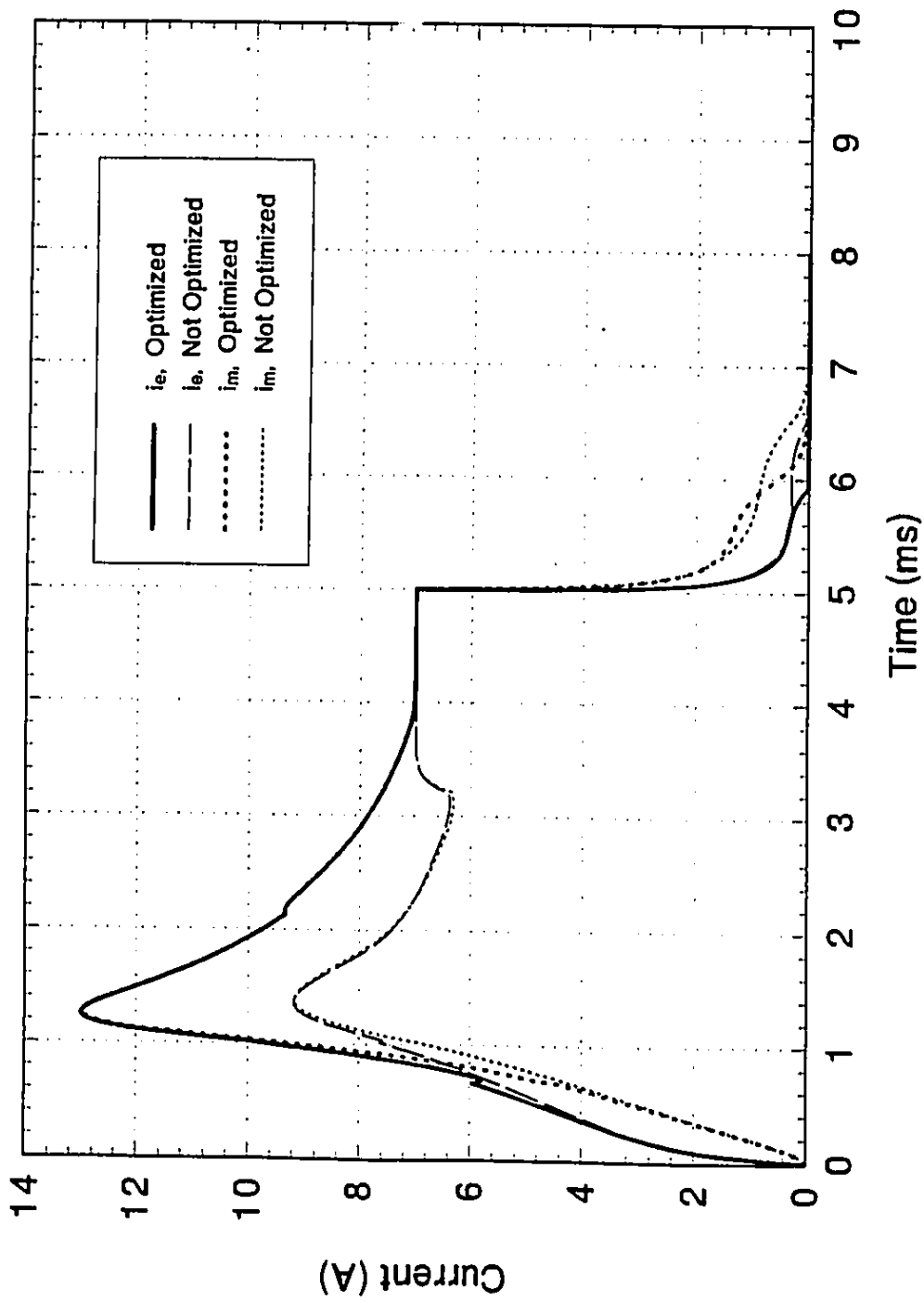


Fig. 6.10 Exciting current  $i_e$  and magnetizing current  $i_m$  transient responses for optimized and typical systems

opening to the end of closing, is 6.721 ms for the optimized system and 5.438 ms for the non-optimized system. The non-optimized system has the injection time being closer to the pulse width command signal time, but its needle motion profile has much more deviations and time delays when compared to the optimized system. These differences are due to the delays inherent to the second order spring-mass-damper needle system dynamics and to the delays resulting from the solenoid electro-magnetic force generation due to the coil inductance. It can be concluded that the optimized injection system minimizes the time delays and is shaping the profile of the needle motion, diminishing the deviation between the ideal and actual amount of the gas dosage. A presentation of the gas dosage for these two systems, as compared to the ideal square needle motion, for a maximum needle lift of 0.635 mm and with consideration of the sonic orifice flow, is given in Table 6.3. The gas dosage for both systems is of course less than for the ideal 'square' needle opening process. Since it is difficult to design a system to inject an exact amount of gas dosage because of the system dynamics, the system must first be designed for an excess gas dosage and then re-tuned to meet the exact requirement. It should be remembered that the engine under consideration is a four 1 litre per cylinder engine running at 2,000 rpm, which requires 80 mg of natural gas per injection. As Table 6.2 indicates, even if the injector is designed to provide excess gas dosage, a non-optimized system may not fulfil the requirement, while an optimized system can.

		OPTIMIZED	NOT OPTIMIZED	% DIFFERENCE w.r.t. OPTIMIZED
$\bar{X}$	$V$ (V)	36.0	36.0	0.0
	$F$ (N)	5.19	20.0	+285
	$K$ (kN/m)	90.786	20.0	-78
	$C$ ( $\mu$ F)	820	300	-63
$t_d$ (ms)		0.671	1.024	+52.6
$t_r$ (ms)		2.134	3.210	+50.4
$t_c$ (ms)		5.033	5.263	+4.6
$t_f$ (ms)		6.050	6.462	+6.8
<b>INJECTION TIME</b> (ms)		6.721	5.438	-19.1
<b>PEAK BOOST CURRENT, <math>i_e</math> (A)</b>		13.0	9.18	-29.4
<b>at AIR-GAP, <math>h</math> (mm)</b>		0.537	0.626	+16.6
<b>at TIME (ms)</b>		1.254	1.364	+8.8

Table 6.2 Optimized and non-optimized systems. Comparison showing design vector values, the four time objectives with time zero as reference, the injection time, and the peak boost current at corresponding time.

GAS DOSAGE (mg)		% DIFFERENCE FROM	
IDEAL (square shape)	102.37	IDEAL	ACTUAL
ACTUAL ENGINE REQUIREMENT	80.0		
OPTIMIZED	84.12	-17.8	+5.2
NOT OPTIMIZED	72.85	-28.8	-8.9

Table 6.3 Gas dosage comparison assuming: ideal square injection time corresponding to the pulse width, actual engine requirement, optimized and non-optimized system.

For an optimized system, the electromagnetic force generated by the solenoid has a rapid rise because of the large current boost created by the specially designed electrical switching circuit. The peak boost current is 13.0 A and occurs at 1.254 ms when the air-gap has been reduced to 0.537 mm, after which the current decays towards its nominal 7 A value, as is illustrated in Figure 6.10. Although, the current decays after it peaks, the solenoid force continues to rise because of the solenoid air-gap decrease, as the solenoid core mass continues to accelerate upwards.

Similarly, for the non-optimized system, the current also has a rapid rise but the peak boost current reaches only 9.18 A at 1.364 ms, which is 29.4 % less in magnitude, as compared to the optimized system. The current peaks too early when the needle is only slightly opened at an air-gap of 0.626 mm. Although the needle continues to accelerate upwards due to the electromagnetic force of attraction and to the mass inertia, the air-gap remains still too large to significantly increase the solenoid force as the current decays. This situation is clearly illustrated in Figure 6.8 between 1.2 ms and

2.0 ms, and reduces the force profoundly causing the injector needle to accelerate at a lower rate. After 2.0 ms, the decrease in the air-gap causes the solenoid force to accelerate more rapidly, despite the decreasing current.

The main factor affecting the peak value of the boost current and the rate of the current rise (and hence the rate and magnitude of the force generation), depends on the amount of capacitance in the switching circuit. With reference to Figure 6.9 for the non-optimized system, a small  $V_c$  capacitance value of 300  $\mu\text{F}$  forces the capacitor to charge-up very quickly; it does not permit the voltage differential  $V_{sol}$  across the solenoid to be maintained large enough and long enough to generate an effective peak current. As well, a high spring preload of 20 N delays the injector opening and hence delays the generation of a strong solenoid force. This is because for a given current, smaller air-gaps are contributing to larger forces than when the air-gap is large. It is now becoming clear that the opening delay caused by the preload cannot be compensated by earlier application of the command pulse, similar to adjusting the spark advance in gasoline engines. It is because the needle rise has already been deformed by the delay. On the contrary, when compared to the optimized system, the larger capacitor value of 820  $\mu\text{F}$  and small preload of 5.19 N provides the combined effect to produce a large peak current and rapid force generation. The advancing of the pulse width would be quite effective for the optimized system.

The drop in the current for the non-optimized system initially decays below its 7 A nominal value. This is not because of the voltage drop caused by the internal

resistance of the solid-state relay, in which the relay output voltage  $V_A$  is less than the supply voltage. The reason is because, as the air-gap gets smaller and with a fast velocity, the velocity induced voltage tends to reduce the magnetizing current  $i_m$ , as is described by Equation (4.16). Thus, electrical energy is converted to mechanical energy to attract the solenoid core towards its magnetic pole. Once the injector needle is fully opened, the velocity dependent voltage becomes zero and the current returns to its nominal 7 A value.

At 5 ms the supply voltage is removed to close the injector. As shown in Figure 6.9, the non-optimized system has a faster capacitor voltage decay than the optimized system because of a smaller capacitance. The capacitor should be able to sustain the voltage for a sufficient amount of time to oppose the forward exciting current  $i_e$ , to quickly reduce the solenoid force. As the result of the velocity induced voltage, the mechanical energy is converted into electrical energy and is supplied to the source. This produces an unwanted effect in that both exciting and magnetizing current tends to increase and to prolong the force decay. Still, for the optimized system, the spring with a constant of 90.186 kN/m has sufficient force to quickly close the injector needle within 1.017 ms, and with a delay of only 0.033 ms, as measured from the removal of the command voltage. For the non-optimized system, the spring constant of 20 kN/m does not provide such effective compression force and the delay before the needle starts to close is prolonged to 0.263 ms. However, once it starts to fall it quickly accelerates and completely closes within 1.199 ms.

## 6.10 Weight Assignment for Qualitative Comparison of System Performance

From a qualitative point of view, it is desired to have the rates of needle rise and fall as high as possible so that the injector needle movement approximates the ideal square shape motion profile. To perform this study, subjective weights ( $w_1, w_2, w_3, w_4$ ) are assigned, respectively, to the four individual time objectives ( $t_d, t_r, t_c, t_f$ ), as defined by Equation (6.7). In Sections 6.8 and 6.9 the situation was considered where all four objectives had equal importance. Solution results for the condition of relative equal weights 1:1:1:1, is summarized in Table 6.4 as sets 3 and 4. As stated in Section 6.8, solution set 4 is the global optimum. Set 3 is considered only as a local minimum which is very close to the optimum and is presented for comparison purposes because the spring preload is at its boundary constraint value of 5 N. Solution set 2 presented in Table 6.4 is for the relative weights of 1:3:1:3. This means that the rise time objective  $t_r$  and fall time objective  $t_f$  are three times more important as compared to the time delays  $t_d$  and  $t_c$ . Solution set 1 in Table 6.4 is for the relative weights of 0:1:0:1, i.e. the time objectives  $t_r$  and  $t_f$  are subjectively very much more important than the objectives  $t_d$  and  $t_c$ .

The optimization results summarized in Table 6.4 show that for all three systems, the best injection performance occurs when the applied voltage is at the maximum value of 36 V, the preload is at, or very close to its minimum value of 5 N, and the capacitor charge is between the small range of 813 to 821  $\mu\text{F}$ . The preload variation with respect to the optimum value is only -3.6 %, and affects slightly the delay before the injector begins to open  $t_d$  by less than -0.5 %. The capacitor percentage variation with respect

SET		1	2	3	4
WEIGHT ( $w_1, w_2, w_3, w_4$ )		0:1:0:1	1:3:1:3	1:1:1:1	1:1:1:1
$\bar{X}^*$	V (V)	36.0	36.0	36.0	36.0
	F (N)	5.0	5.0	5.0	5.19
	K (kN/m)	67.046	77.474	83.471	90.786
	C ( $\mu$ F)	821	817	813	820
$t_d$ (ms)	0.668	0.668	0.668	0.671	
$t_r$ (ms)	1.339	1.384	1.414	1.463	
$t_c$ (ms)	0.133	0.086	0.062	0.033	
$t_f$ (ms)	1.093	1.059	1.040	1.017	
$t_d + t_c$ (ms)	0.801	0.754	0.730	0.704	
$t_r + t_f$ (ms)	2.432	2.443	2.454	2.480	
$J^* = J'(\bar{X}^*)$ (ms)	3.233	3.197	3.184	3.184	

Table 6.4 Optimization results from the application of different weights ( $w_1, w_2, w_3, w_4$ ) corresponding respectively to the four important individual time objectives ( $t_d, t_r, t_c, t_f$ ). For each set of weights, the corresponding design vector values, the four time objectives, and the multiobjective function values are indicated.



to the optimum value is less than -1 %, and can be considered to have negligible effect on the system performance comparison. It is the spring constant design variable that shows the most change when compared to the optimum value, with a maximum variation of 26.2 %.

The impact of the spring constant should be expected because it affects the needle rise and fall times,  $t_r$  and  $t_f$ , respectively, as it is stipulated by the assignment of weights. From Table 6.4, it can be seen that when more importance is assigned to  $t_r$  and  $t_f$ , the spring rate decreases. This effect on the four important time objectives and on the optimum objective function values is summarized in the table, and is also recapitulated in Figure 6.11, where it is normalized against their optimum values from set 4. As the assigned weight is decreased resulting in an increase of spring constant, the rise time  $t_r$  increases, as shown in Figure 6.11. This trend is correct because there is higher spring force opposing the solenoid force against the injector needle opening. Consequently, the injector fall time  $t_f$  is shown to decrease for an increase in spring constant because there is more compressed spring force available to accelerate the needle closure. As well, this higher spring force helps to reduce the time delay  $t_c$  before the needle starts to close, as shown in the figure. It can be concluded that the weight assignment has a profound influence on  $t_c$ , which could be four time worst for a low spring rate, as compared to the optimum of set 4.

Although the assignment of increasing weights is to influence  $t_r$  and  $t_f$ , the figure shows that the overall objective function  $J^*$  decreases with an increase in the spring rate.

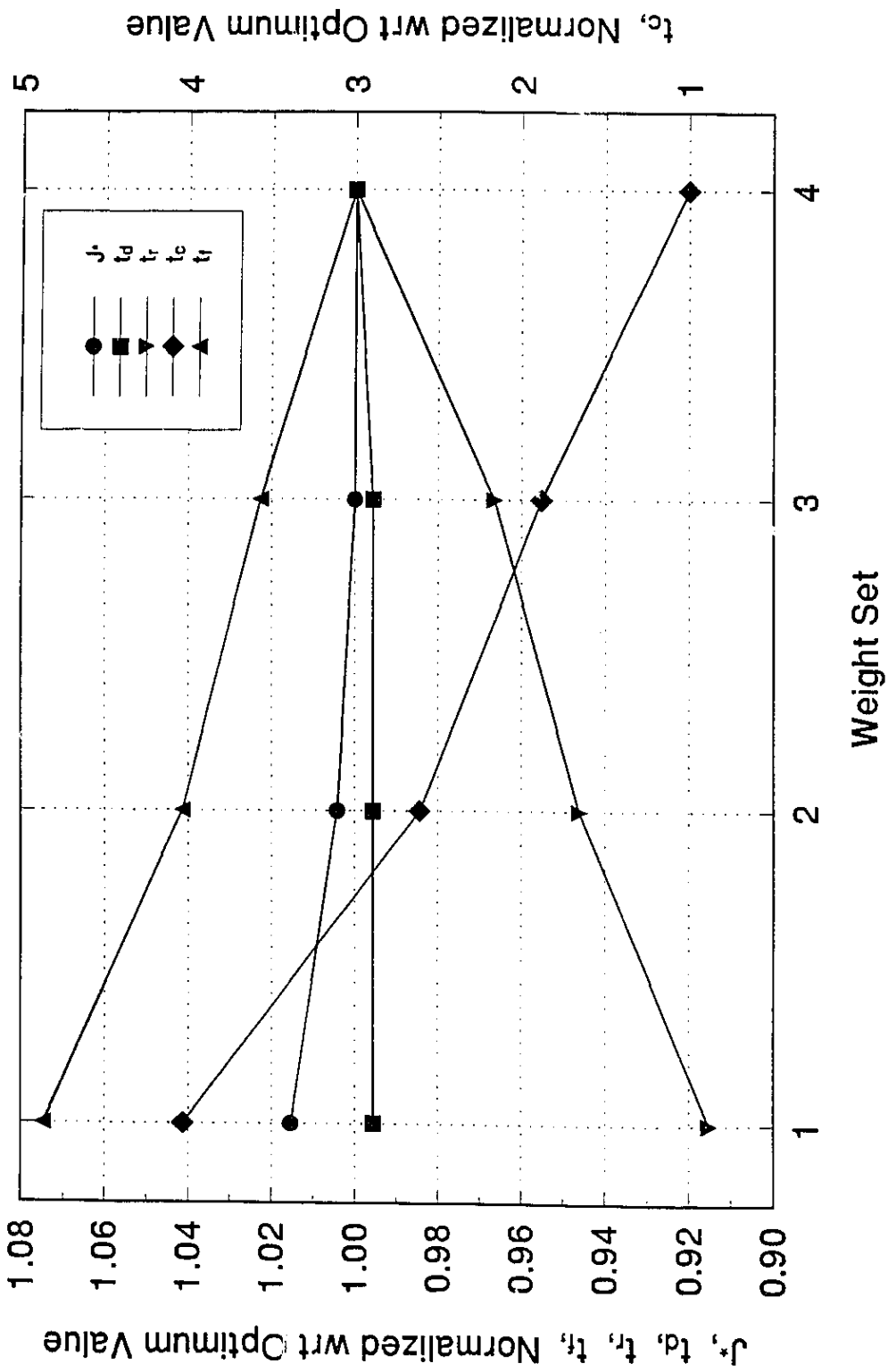


Fig. 6.11 Normalized objective function values as the result of variations in weight assignment

The impact of the weights assignment has to be considered as correct because the sum of  $t_r$  plus  $t_f$  reduces with their weight increase, as is shown by the numerical data in Table 6.4. And, since the delays  $t_d$  and  $t_c$  are of less importance, their total value is worst for larger weights, which is also shown in the table. In conclusion, from a qualitative point of view, the optimum design variables obtained from weight selection set 1 should be chosen because the combined needle rise and fall times produce a closer to square needle operating profile. However, from a quantitative point of view, the design vector from weight set 4 should be chosen because the objective function value is minimum.

## 6.11 Summary

A new technique to account for boundary constraints has been introduced into the Hooke and Jeeves unconstrained optimization method. The main modification to the Hooke and Jeeves method was to limit the design variable exploratory moves to their maximum or minimum values. These limit values act as a 'barrier' to keep the design vector to within the feasible region. The major contribution in the consideration of boundary constraints is attributed to the one-dimensional search for the optimum scalar step length along the pattern direction, where three successive objection function values and their corresponding step lengths are tracked. Whenever a design variable is about to violate its constraint, it is barred from the infeasible region by their maximum or minimum limits. An algorithm comparing these three sets of values is used to determine whether a design variable lying on the boundary is an optimum solution. In addition,

these values are required anyway for the concave bracketing to determine the optimum step length by the quadratic interpolation method when the optimum design variables are in the feasible region.

This new boundary constraint technique is general and should be compatible to other direct search optimization methods with some programming modifications, such as the Powell's method and Rosenbrock's method of rotating coordinates, which are considered as further improvements of the Hooke and Jeeves method [44<sup>(9)</sup>]. It is recommended that this new constraint procedure be further investigated and the algorithm optimized and tested on other direct search methods. The merits of this new approach should be thoroughly investigated and exploited because it avoids all the pitfalls encountered when the penalty function methods are used in optimization which are requiring systems simulation for objective function evaluation, as described in Section 6.2.

In Section 6.8, optimization of the injection system took 305 function evaluations before the optimum solution was reached. However, it should not be mistakenly concluded that the optimization method is inefficient. The reason for the large number of function evaluations is because the initial design vector starting point was taken arbitrarily at the centre of each of the boundary constraints, well away from the final solution vector and three complete optimizations were performed to ensure global optimality. These procedures were to illustrate that the same solution can be reached independently of the starting point. If the actual solution to the optimum design vector

was known approximately, and if this solution was known to be a global minimum, then starting the optimization search close to the solution with these 'a priori' knowledge would save much of computation time. The individual optimization sets shown in Figure 6.1 illustrate this fact.

It should be pointed out that the optimization technique by reducing the spring rate and capacitor values by one half and re-optimization to determine the optimum global solution set, is not a general method and is particular to this class of problem from 'a priori' knowledge of the system performances obtained from Chapter 5. Thus, the general procedure is to optimize the problem from many different starting points and then the comparison of all the local minimums for the global optimum becomes not necessary.

Application of the optimization procedure designates the optimum design vector as:

$$\bar{X}^* = [ 36 V, 5.19 N, 90.786 kN/m, 820 \mu F ]^T$$

The applied voltage should be large to provide a high current through the coil, since the solenoid force is a function of current. The spring preload force should be small, so as to keep the injector opening delay short. The spring constant should be large, so that when the applied voltage is removed the large spring force can quickly accelerate the injector needle to its closed position. Even though the spring constant might be large, the high solenoid force created by the current boost is much greater and can accelerate the injector needle to reach the nozzle opening quickly. The capacitor value should not be too small because, in such a case, the capacitor would charge-up too fast to provide

sufficient current boost at the beginning of the injector opening and would discharge too quickly to provide a sufficient voltage to oppose and help decelerate the current for a fast force decay. If the capacitance is excessively large, which is equivalent to no capacitor in the circuit, the current would be kept at high level too long and may cause damage to the solenoid; after the needle lift, the current should return to its nominal 7 A value.

An optimized injector design minimizes the time delays and improves the profile of the needle motion. This in turn, diminishes the deviation between the ideal and actual amount of the gas dosage supplied to the engine. The dynamics of the injection process is complex, and the injector performance depends on the interaction from many design variables. Only a systematic optimization procedure can establish the correct parameter values to meet the optimum system performance requirements.

## CHAPTER 7

### CONCLUSIONS AND RECOMMENDATIONS

#### 7.1 Conclusions

One of the objectives of this research was to develop a comprehensive mathematical model describing the dynamic characteristics of an electromagnetic solenoid. The ferromagnetic material effects due to the solenoid core and solenoid casing were included in the model equation as represented by the material reluctance. This is given by Equation (4.2), where the parameters  $a_1$  and  $a_2$  were derived from experimental 'steady-state' force and current data for a particular air-gap length. This led to a unique representation as given by the steady-state magnetization curves for the solenoid, shown in Figure 4.28 for different air-gaps.

The equivalent circuit for the solenoid is shown in Figure 4.21, which includes the representation of a flux leakage inductance term and an eddy current loss resistance term. The value of this circuit is that it models the solenoid force and current transients correctly as proved by the experimental results. However, such validation can only be achieved by a correct representation of the material steady-state magnetization curves and appropriately chosen parameters for the flux leakage and eddy current terms. The uniqueness of this model is even more profound, in that it also represents the dynamic hysteresis characteristics of the solenoid force, as shown in Figures 4.15 to 4.19. In conclusion, the objective to model and to derive the governing equations to represent the solenoid transient force and current characteristics has been achieved. It must be

emphasized that the mathematical model of the solenoid is both innovative and contributing to a better understanding of solenoid transient behaviour.

A comprehensive model of the solenoid contributes to the second objective of this research. With a better understanding of the solenoid characteristics, it became possible to use the solenoid in applications and performances beyond its nominal intended use. This was the purpose of the specially designed solenoid switching circuit, as shown in Figure 4.34. The purpose of the circuit is to provide a current 'boost' to create a large initial force to open the injector quickly. The current is then brought back to its nominal operating conditions because the voltage across the solenoid coil decreases as the capacitor is charged up. When the applied voltage is removed, the counter voltage provided by the capacitor helps to decelerate the current to quickly reduce the solenoid force for fast injector closing. In conclusion, application of the circuit has demonstrated that small off-the-shelf solenoids (or solenoids in general) can function in an "over-powered" mode to give a rapid rise in force without causing solenoid damage, provided that electric power is brought back to nominal conditions rapidly. It must be pointed out that this solenoid driving circuit performs as intended, is constructed with only few components, and its design is novel.

The comprehensive mathematical model for the solenoid provides the basis for a computer simulation of the solenoid/injector systems dynamic response for the design improvement purposes and a computer optimization method was developed for a systematic design approach. For the injector system under consideration, any adjustment



to one or more system parameters during the optimization procedure requires the complete model to be simulated again. In addition, information about the derivatives of the objective function cannot be expressed explicitly. Thus, after reviewing different optimization techniques, it was concluded that a 'direct search technique' is the most appropriate because derivatives of the objective function are not required. The Hooke and Jeeves optimization method was selected because the method is not difficult to implement as an algorithm, and because the other accepted direct search techniques are only extensions of this method, as a basis for their modifications. A new procedure was introduced to account for boundary constraints, which avoids all the drawbacks as encountered by using the penalty function method (fully described in Section 6.2). The procedure keeps track of three successive objective function values and their corresponding step lengths. These values are used 1) to determine if a boundary has been reached, and if so, the algorithm decides if this corresponds to the optimum design vector, and 2) to the bracketing of three function values that is required for the quadratic interpolation method. The technique to account for boundary constraints can be classified as a 'self-bounding' method, since the design variables are restricted to remain within the feasible region. The procedure is innovative, and can be applied to other direct search methods with minor programming modifications. The merits of this new approach should be thoroughly investigated and exploited because it avoids all the pitfalls encountered when the penalty function methods are used in the optimization procedures which are requiring systems simulation for objective function evaluation.

Results from application of the optimization procedure leads to the following conclusions about the performance of the injector:

The applied voltage should be large to provide a high current through the coil, since the solenoid force is a function of current. The spring preload force should be rather small, to keep the injector opening delay short. The spring constant should be large, so that when the applied voltage is removed the large spring force can quickly accelerate the injector needle towards its closed position. Even though the spring constant might be large it does not increase the spring force at the start of its lift; the high solenoid force created by the current boost is much greater and accelerates the injector needle to reach the nozzle opening quickly. The capacitor value should not be too small because, in such a case, the capacitor would charge-up too fast to provide sufficient current boost at the beginning of the injector opening and would discharge too quickly to provide a sufficient voltage to oppose and help decelerate the current for a fast force decay. If the capacitance is excessively large, which is equivalent to no capacitor in the circuit, the current would be kept at high level too long and may cause damage to the solenoid; after the needle lift, the current should return to its nominal 7 A value.

An optimized injector design minimizes the time delays at opening and closing and improves the profile of the needle motion. This in turn, diminishes the deviation between the ideal and actual amount of the gas dosage supplied to the engine. The dynamics of the injection process is complex, and the injector performance depends on the interaction from many design variables. Only a systematic optimization procedure

can establish the correct parameter values to meet the optimum system performance requirements.

In summary, the contributions from this research work are threefold:

1. A mathematical model of an electrical solenoid has been established that describes the solenoid current and force transients, as well as the force saturation characteristics. The model is based on the solenoid coil steady-state flux versus current magnetization characteristics and on a unique equivalent circuit representation which includes a flux leakage inductance and an eddy current resistance component. The solenoid model is innovative and contributes to a better understanding of solenoid transient behaviour.
2. A novel solenoid driving circuit has been designed that provides a boost current to rapidly generate the solenoid force for quick injector opening. The capacitor incorporated in the circuit design reduces the current through the solenoid to protect the coil from over-heating during the injector opening sequence, and is also used as a reverse voltage across the coil to rapidly decelerate the current for quick injector closing.
3. A numerical optimization procedure has been established to determine the complex set of system parameters for the injector/solenoid optimum performance. A new procedure to account for boundary constraints has been introduced to the Hooke and Jeeves optimization method. The procedure tracks three sets of

objective function and step length values and programming logic determines if the boundary solution is a possible minimum.

## **7.2 Recommendations for Future Work**

The presented work is based on some basic gas injection processes in a well defined environment, although not fully adapted to a real internal combustion engine. So, the differences that can affect the proposed gas injection system, when used in a real engine, should be further investigated and their impact should be found regarding the changes in performance of the injector. The following recommendations could be made regarding the follow-up of this research work:

1. The variations of the gas temperature in the injector as well as the duty cycle of the solenoid and their impact on the injector performance.
2. The variations of the combustion chamber temperature and pressure and their impact on the gas discharge characteristic.
3. The injector needle bouncing, both at the upper stop and in the seat and its impact on the gas discharge characteristic.
4. The specific changes of the gas discharge characteristics in cases of extreme variations of the injected gas dose (as for example, idling).

The above analysis has to be done when adapting the proposed gas injection system to a particular engine type. To optimize for a dedicated gas injection system, the

procedure described in this thesis can be still used; however, the weight assignments should be proposed depending on the engine development objectives and with regard to the expertise of the responsible project engineer.

## REFERENCES

1. Krepec, T., "Environmental Impact of Vehicle Design", Proceedings of CSME Forum 1992, 'Transport 1992+', Concordia University, Montreal, June 1 - 4, 1992, pp. 366-371.
2. Heywood, J.B., "Internal Combustion Engine Fundamentals", McGraw-Hill Book Co., pp. 37, Table D4, pp. 915, 1992.
3. Rivard, J.G., "Closed-loop Electronic Fuel Injection Control of the Internal Combustion Engine", SAE Paper No. 730005, 1973.
4. Gorille, I., Rittmannsberger, N. and Werner E., "Bosch Electronic Fuel Injection with Closed Loop Control", SAE Paper No. 750368, 1975.
5. Probst, C.O., "Bosch Fuel Injection and Engine Management", Robert Bentley, 1989.
6. De Grace, L.G. and Bata G.T., "The Bendix DECA Fuel Injector Series - Design and Performance", SAE Paper No. 850559, 1985.
7. Howes, P., "The New CAV Microjector Injector", SAE Paper No. 800509, 1980.

8. Smith, D.H. and Spinweber, D.A., "A General Model for Solenoid Fuel Injector Dynamics", SAE Paper No. 800508, February 1980.
9. Esperti, R.V., "Mathematical Model of a Throttle Body Fuel Injection System", SAE Paper No. 810449, 1981.
10. Henry, J.P. and Dennis, D.S., "Predicting Solenoid Transient Performance", SAE Paper No. 870473, February 1987.
11. Bata, G. and Sosa, M., "Application of the Taguchi Method to the Design of Bendix Electronics DEKA Fuel Injectors", SAE Paper No. 870079, 1987.
12. Lake, T.H., Christie, M.J., Stokes, J., Horada, O. and Shimotani, K., "Preliminary Investigation of Solenoid Activated In-cylinder Injection in Stoichiometric S.I. Engines", SAE Paper No. 940483, 1994.
13. Hames, R.J., Straub, R.D. and Amann, R.W., "DDEC Detroit Diesel Electronic Control", SAE Paper No. 850542, 1985.
14. Hames, R.J., Hart, D.L., Gillham, G.V., Weisman, S.M. and Peitsch, B.E., "DDEC II Advanced Design Diesel Control", SAE Paper No. 861049, 1986.

15. Frankl, G., Barker, B.G. and Timms, C.T., "Electronic Unit Injectors", SAE Paper No. 891001, 1989.
16. Bosch R. GMBH, "Bosch Worldwide: Your Partner in Diesel Technology" - A catalog of Bosch Diesel Systems, 1993.
17. Murayama, F. and Tanaka, Y., "The Nippondenso Electronic Control System for the Diesel Engine", SAE Paper No. 880489, 1988.
18. Yamada, K. and Oshizawa, H., "The Second Generation of Electronic Diesel Fuel Injection Systems - Investigation with a Rotary Pump", SAE Paper No. 860145, 1986.
19. Schechter, M.M., Levin, M.B. and Dutcher, W.R., "Electromagnetically Controlled Distributor-Type Fuel Injection System", SAE Paper No. 890477, 1989.
20. Shinoda, K., Koide, H., Kobayashi, F., Nagase, M., Ikeda, S., Takata, M. and Nakano, J., "Development of New Electronic Control System for a Diesel Engine", SAE Paper No. 860597, 1986.
21. Stockner, A.R., Flinn, M.A. and Camplin, F.A., "Development of the HEUI Fuel System - Integration of Design, Simulation, Test and Manufacturing", SAE Paper



No. 930271, 1993.

22. Fischer, W., Fuchs, W., Laufer, H. and Reuter, U., "Solenoid-Valve Controlled Diesel Distributor Injection Pump", SAE Paper No. 930327.
23. Krepec, T., Tebelis, T. and Kwok, C.K., "Fuel Control Systems for Hydrogen-Fuelled Automotive Combustion Engines -- a Prognosis", Int. Journal of Hydrogen Energy, Vol. 9, No. 1/2, pp. 109-114, 1984.
24. Tebelis, T. and Krepec, T., "A New Concept of Hydrogen Injector for High Speed Compression Ignition Engines", Paper presented at Second International Symposium on Hydrogen Produced from Renewable Energy, sponsored by the University of Miami in Cape Canaveral, Florida in October 22-24, 1985.
25. Giannacopoulos, T., Krepec, T. and Lisio, C., "Preliminary Investigations on a Microprocessor Controlled Gaseous Hydrogen Injector", Paper presented at the 1986 ASME International Computers in Engineering Conference in Chocago, July 20-24, 1986.
26. Krepec, T., Giannacopoulos, T. and Miele, D., "New Electronically Controlled Hydrogen-Gas Injector, Development and Testing", Int. Journal of Hydrogen Energy, Vol. 12, No. 12, pp. 855-861, 1987.

27. Miele, D., Krepec, T. and Giannacopoulos, T., "Electronic Injection System for Natural Gas in a Diesel Engine - Development and Testing", SAE Paper No. 890852, 1989.
28. Green, C.J. and Wallace, J.S., "Electronically Actuated Injection for Gaseous Fuels", SAE Paper No. 892143, 1989.
29. Georgantas, A., Hong, H., Krepec, T. (supervisor), Lisio, C., Miele, D., Pharand, M., Rohrauer, G., Rychter, T., Tummala, M. and Wojciechowski, J., "Research and Development of New Concepts for On-Board Storage, Direct Injection and Ignition of Gaseous Fuels in Automotive Internal Combustion Engines", Final report, Prepared for Bendix Avelex Inc., Concordia University, Mechanical Engineering Department, Centre for Industrial Control, Montreal, CIC Report No. 0049, March 1992.
30. Hong, H., Krepec, T. and Georgantas, A.I., "Design Optimization of Solenoid Operated Diesel Injectors for Gaseous Fuels", CSME Forum Transport 1992+, June 1992, and CSME Transactions, Vol. 17, No. 4A, pp. 865-880, 1993.
31. Hong, H., Krepec, T. and Cheng, R.M.H., "Optimization of Electronically Controlled Injectors for Direct Injection of Natural Gas in Diesel Engines", SAE Paper No. 930928, and SAE 1993 Transactions, Journal of Engines, Sec. 3, Vol.

102, pp. 1430-1439.

32. Hong, H., Krepec, T. and Cheng, R.M.H., "Optimization of Hydrogen Injectors Dynamic Response", Paper presented at 10-th World Hydrogen Energy Conference, Cocoa Beach, Florida, June 20-24, 1994.
33. Kekedjian, H. and Krepec, T., "Further Development of Solenoid Operated Gas Injectors with Fast Opening and Closing", SAE Paper No. 940450.
34. Glasson, N. and Green, R., "High Pressure Hydrogen Injection", Proceedings of the 9<sup>th</sup> World Hydrogen Energy Conference, Paris, June 22-25, 1992.
35. Giannacopoulos, T., "A Feasibility Study on an Electronically Controlled Hydrogen Gas Injector", A Thesis in The Department of Mechanical Engineering, Concordia University, Montreal, Quebec, 1986.
36. Seilly, A.H., "HELENOID Actuators - A New Concept in Extremely Fast Acting Solenoids", SAE Paper No. 790119, 1979.
37. B.W. Andersen, "The Analysis and Design of Pneumatic Systems", Robert E. Krieger Publishing Company, Huntington, New York, 1976.

38. L.A. Zalmanzon, "Components for Pneumatic Control Instruments - The Static and Dynamic Characteristics of Pneumatic Resistances, Capacitances and Transmission Lines", Pergamon Press, New York, 1965.
39. Brown, D. and Hamilton III, E.P., "Electromechanical Energy Conversion", Macmillan Publishing Company, New York, N.Y., 1984, pp. 17-29.
40. Gourishankar, V. and Kelly, D.H., "Electromechanical Energy Conversion", Intext Educational Publishers, New York, N.Y., 1973, pp. 93-100.
41. Hong, H., Krepec, T. and Cheng, R.M.H., "Transient Response of Fast Acting Solenoids in Automotive Applications", Journal of Circuits, Systems, and Computers, World Scientific Publishing Co., Vol.4, No.4, 1994.
42. W.T. Hunt, Jr. and R. Stein, "Static Electromagnetic Devices", Allyn and Bacon, Inc., Boston, 1963, pp.64-65.
43. Majmudar, H., "Electromechanical Energy Converters", Allyn and Bacon, Inc., Boston, 1965, Chapter 2.
44. Rao, S.S., "Optimization / Theory and Applications", Second Edition, Wiley Eastern Limited, New Delhi, India, 1984, pp. 271-273<sup>(1)</sup>, pp. 424<sup>(2)</sup>, pp. 391 & 393<sup>(3)</sup>, pp.

391<sup>(4)</sup>, pp. 392-402<sup>(5)</sup>, pp. 397-398<sup>(6)</sup>, pp. 274-292<sup>(7)(9)</sup>, pp. 234-242<sup>(8)</sup>.

45. Dixon, L.C.W., "Nonlinear Optimization", Crane, Russak & Company, Inc., New York, N.Y., 1972, pp. 65<sup>(1)(2)</sup>.

46. Gill, P.E. and Murray, W., "Numerical Methods for Constrained Optimization", Academic press, London, England, 1974, pp. 195-196<sup>(1)</sup>, pp. 191<sup>(2)</sup>, pp. 217<sup>(3)</sup>, pp. 184<sup>(4)</sup>.

47. Jacoby, S.L.S., Kowalik, J.S. and Pizzo, J.T., "Iterative Methods for Nonlinear Optimization Problems", Prentice-Hall, Englewood Cliffs, New Jersey, 1972, pp. 165-166.

48. Fox, R.L., "Optimization Methods for Engineering Design", Addison-Wesley Publishing Company, Reading, Massachusetts, 1971, pp. 135-136.

49. Arora, J.S., "Introduction to Optimum Design", McGraw-Hill Book Co., 1989, pp. 83 & 136.

## APPENDIX A

### CONICAL VALVE SEAT DESIGN AND MINIMUM GEOMETRIC FLOW AREA

The conical valve seat design is very important for the proper operation of the injector. Figure A.1 illustrates the cross-sectional view of the conical valve seat where the cone angle is greater than that of the conical needle. When the valve is closed, the contact to its seat is described by a circle of diameter  $\underline{mn}$ . When the needle is lifted, the minimum geometric flow area is given by the frustum area circumscribed by the line of length  $L$ . The curved surface of the frustum of a right cone, radius of base  $r_1$ , radius of top  $r_2$  and altitude  $z$ , is given by:

$$\pi (r_1 + r_2) \sqrt{z^2 + (r_1 - r_2)^2} \quad (\text{A.1})$$

From Figure A.1, the parameters to the equation are:

$$r_1 = \frac{d}{2}$$

$$r_2 = \frac{d}{2} - L \cdot \cos\theta$$

$$\sqrt{z^2 + (r_1 - r_2)^2} = L$$

$$L = h \cdot \sin\theta$$

Thus, the critical flow area is calculated as:

$$A_m = \pi \cdot (h \cdot \sin\theta) (d - h \cdot \sin\theta \cdot \cos\theta) \quad (\text{A.2})$$

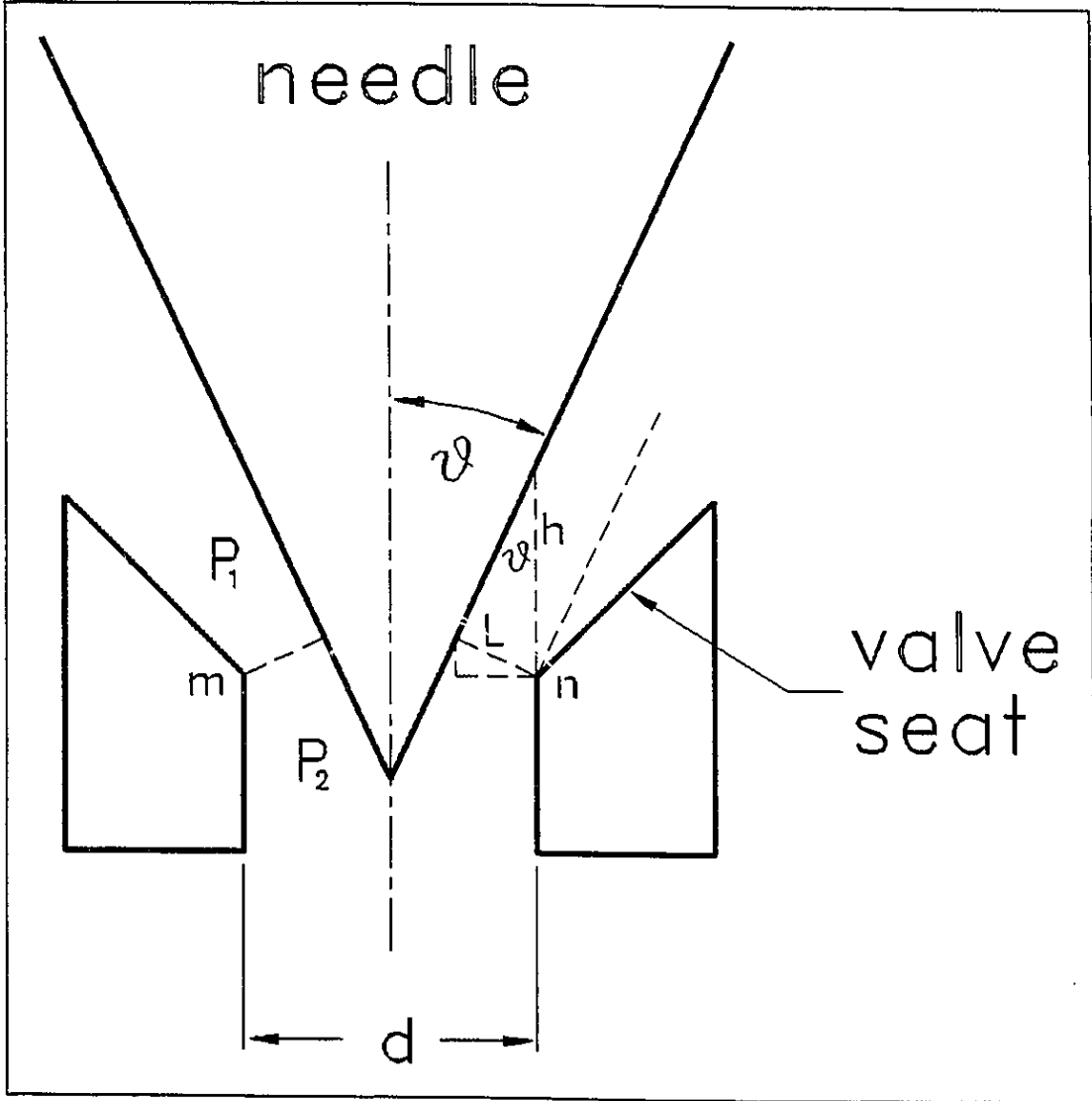


Fig. A.1 Valve seat with a conical angle greater than the needle angle

In the above equation,  $A_m$  represents the minimum geometric flow area after the needle has lifted to height  $h$ . The diameter of the nozzle orifice is represented by  $d$ .

This valve seat design will require lower solenoid force to lift the needle because more of the needle cone end area is exposed to the pressure above the circular contact line. Since the part of the needle within the injector housing is pressure balanced, the net closing gas force created by the pressure difference  $P_1-P_2$  on the seated needle acts on the needle projected area of diameter  $\underline{mn}$ , which is equal to the nozzle orifice diameter  $d$ .

When the needle is lifted and the gas is injected, it is assumed that the pressure acting on the conical end of the needle, is uniformly equal to  $P_1$  upstream of the critical flow area and uniformly equal to  $P_2$  downstream of the critical flow area. This assumption provides a base for an approximate calculation of the forces acting on the cone of the lifted needle. Hence, for the pressure balanced injector design, it can be concluded that the net force exerted by the gas pressure difference on the needle always tends to close the valve. That is, it acts against the solenoid force and in the same direction as the spring force.



## APPENDIX B

### DESCRIPTION AND CALIBRATION OF PIEZO-CELL FORCE TRANSDUCER

A piezo-electric load cell was used to measure the electromagnetic force of attraction in the experimental set-up shown in Figure 4.1. The load cell is a product of Kistler, type 9001, and the specifications are:

Range	: from 0 to 7500 N
Sensitivity	: -4.29 pC/N
Linearity	: $\leq \pm 0.4$ %FSO
Operating Temperature Range	: -196 to 200 °C

The converter used is the charge amplifier produced by Kistler, model 504E.

In the calibration of the force transducer, dead weights were gradually applied from 0 to 66.720 N to load the cell under compression, and the electrical output from the cell was recorded. Figure B.1 plots the calibration curve for the transducer. The numerical readings taken are also shown in the figure.

The static gain of the force transducer was found to be:

$$7.7698 \times 10^{-1} \frac{N}{mV}$$

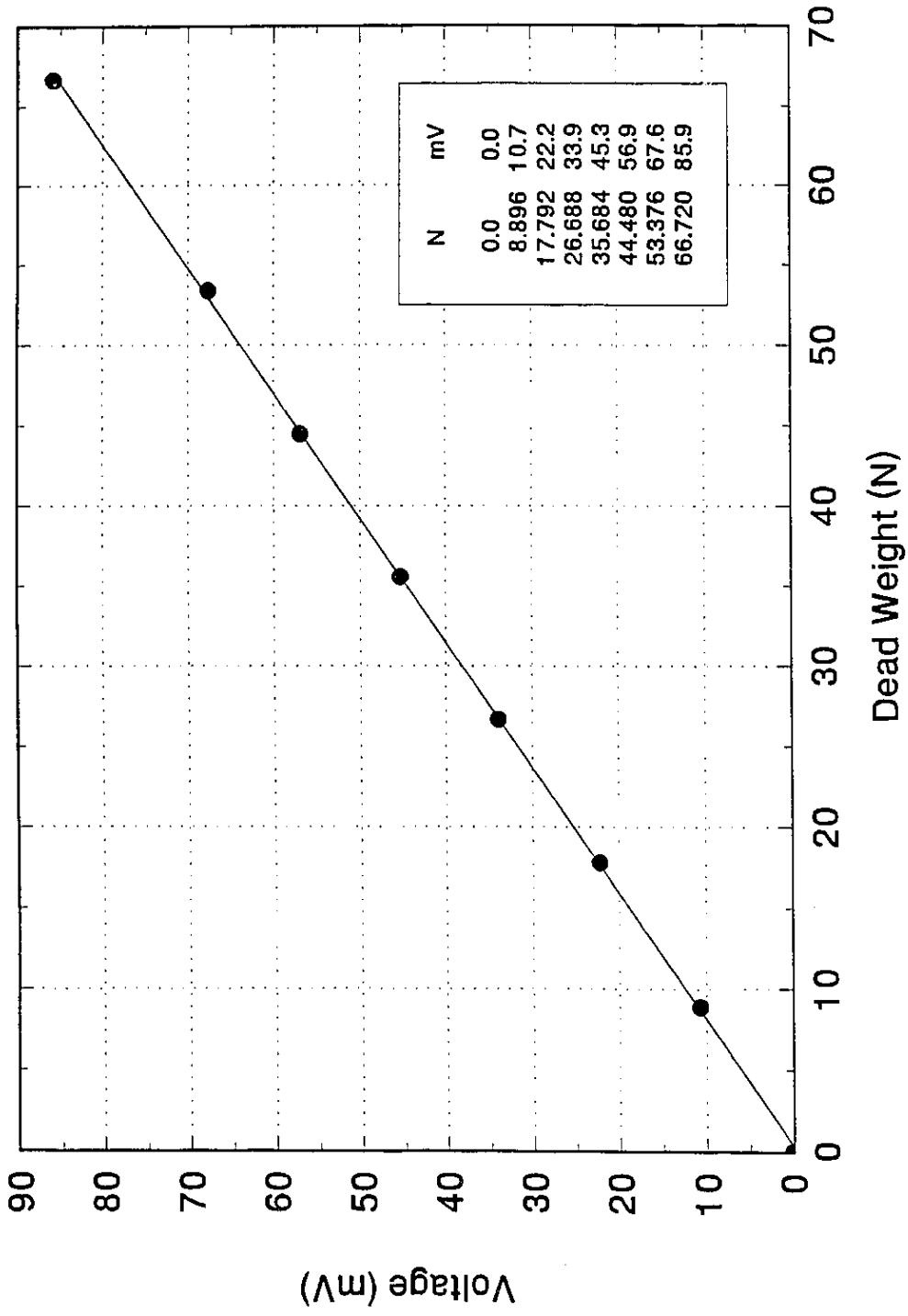


Fig. B.1 Piezo-cell force transducer calibration curve

## APPENDIX C

### DESCRIPTION OF CLAMP-ON CURRENT METER

A clamp-on current meter produced by Kyoritsu Electrical Instruments Works, Ltd., was used to measure the transient (exciting) current to the solenoid coil. The instrument is a model 8113 clamp-on AC/DC current /voltage converter that permits AC/DC current measurements from 1 mA to 200 A. The specifications of the instrument for DC current measurements are:

Range Switch Position	Measuring Ranges	Output	Accuracy
2A DC	0 -5A DC	0 - 500.0 mV DC	$\pm(1.5\% \text{ rdg} + 5\text{mA})$
20A DC	0 - 50A DC	0 - 500.0 mV DC	$\pm(1.0\% \text{ rdg} + 0.02\text{A})$
200A DC	0 - 200A DC 150 - 200A DC	0 - 200.0 mV DC	$\pm(1.5\% \text{ rdg} + 0.2\text{A})$ $\pm 3.0\% \text{ rdg}$

Frequency Range : DC to 1 kHz

Operating Temperature Range : -196 to 200 °C

## APPENDIX D

### DESCRIPTION OF SUBROUTINE MAXMIN

A descriptive flow chart is shown in the following page explaining the functions of subroutine MAXMIN. The subroutine returns to the calling program the flag BORDER set to TRUE and the new value for the step length  $\lambda$  if any boundaries have been violated. The step length  $\lambda$  is calculated from the variable that went the most into the infeasible region. Thus, the returned  $\lambda$  to the main program will recalculate the move for that variable to reach exactly to the boundary, where  $\lambda$  is acting as a barrier. All other variables will also move but will remain within the feasible region away from the boundary. If all variables are within or are lying on the boundary, subroutine MAXMIN only returns the flag BORDER set to FALSE. This means that no boundaries have been violated and there is no change to the step length  $\lambda$ .

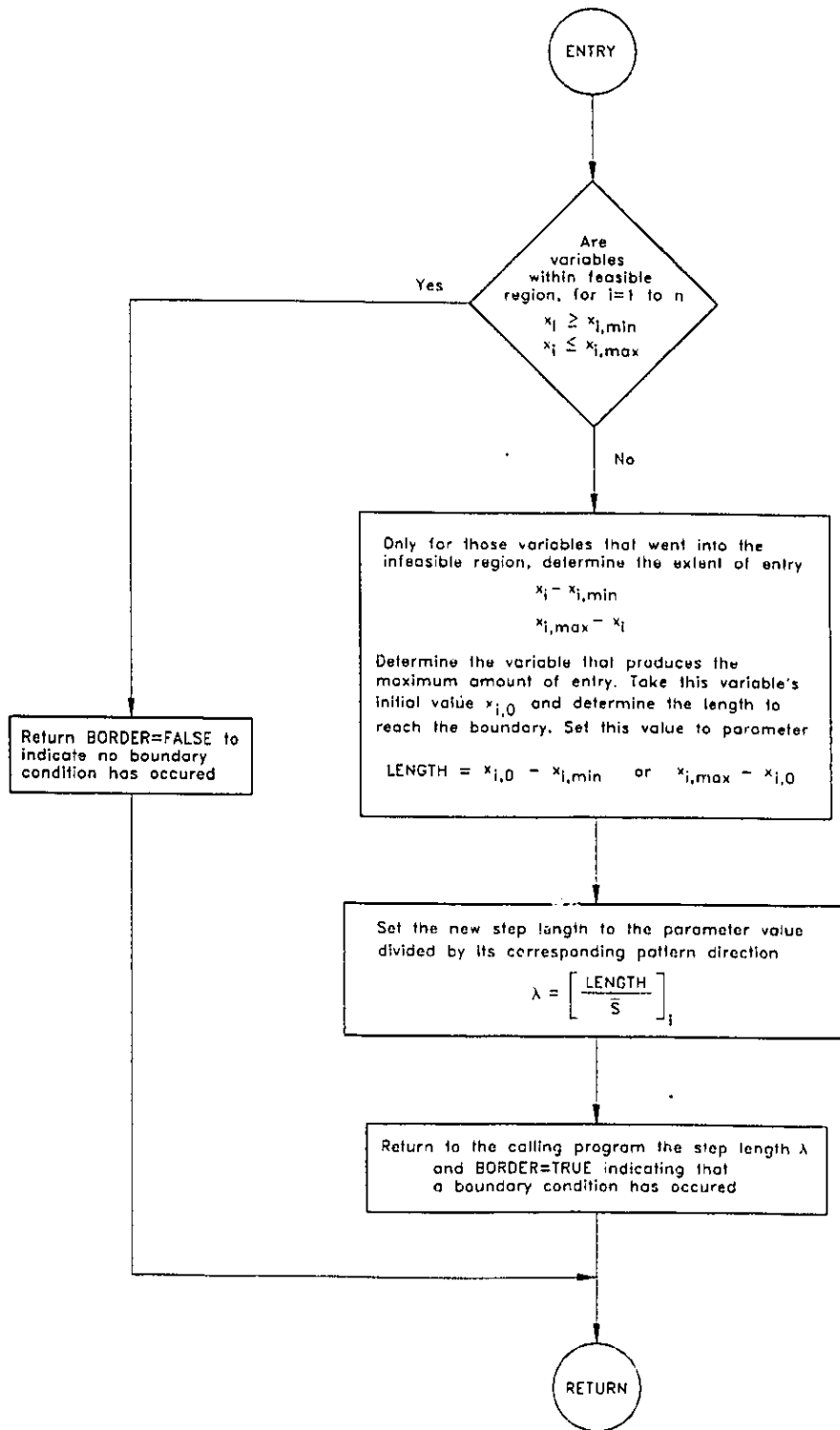


Fig. D.1 Functional flow chart for subroutine MAXMIN